Vibroacoustics of plates excited by water drop impacts

Thesis submitted in accordance with the requirements of
the University of Liverpool for the degree of Doctor of Philosophy
by

Yicheng Yu

Acoustics Research Unit
School of Architecture
University of Liverpool

June 2019

Abstract

Rainfall on windows and roofs of buildings, and the roofs and windscreens of cars can generate high levels of re-radiated sound that may adversely affect speech communication or other activities. This thesis concerns the prediction and experimental analysis of vibroacoustics of plates excited by water drop impacts.

The impact force applied by single raindrops on both dry and wet surfaces is quantified experimentally. Single liquid water drops with 2 and 4.5 mm diameter were tested at a range of drop velocities when the plate is dry and with a shallow water layer. Force transducer measurements and wavelet deconvolution were used to measure the time-dependent force. When the response signal has a low SNR value (<10 dB), wavelet deconvolution becomes less robust and the sparse representation method was used to improve the accuracy and preserve the initial phase of the impact force.

The validity of theoretical models for the impact force from a drop on a dry surface has been assessed through comparison with experimental data. The inability of these models to describe the time-dependent force provided the motivation to develop empirical formulae. Based on the experimental data, empirical formulae were developed for 2 and 4.5 mm drops falling at (a) different velocities up to and including terminal velocity onto a dry glass surface, (b) terminal velocity onto dry glass or glass with a shallow water layer up to 10 mm and (c) different velocities below terminal velocity onto dry glass or glass with a shallow water layer up to 10 mm. A correction to the empirical model for drop impacts at an oblique angle was accounted for by using the perpendicular velocity component, which was validated with experiments.

Numerical models have been validated using Statistical Energy Analysis (SEA) and Finite Transfer Matrix Method (FTMM) with the empirical model to estimate the vibration and sound radiation from a single glass plate and a multilayer plate represented by a plate-foam-plate system. To improve computational efficiency, an order reduced integral with travelling wave method for finite plate size correction of FTMM method has been proposed. An experiment with artificial rainfall was used to assess the accuracy of the numerical models for terminal velocity and the lower velocity (3.65 m drop height). The empirical model was used to quantify the power input into a plate from natural rainfall using numerical experiments.

Table of contents

List of tables

List of figures

Acknowledgement

I would like to express my sincere appreciation to my supervisor, Professor Carl Hopkins, for his constant support, guidance and encouragement throughout my four years study in the Acoustic Research Unit.

I would like to thank Dr. Gary Seiffert for his help and advice for my experiments and his continuing support throughout my research. I would also like to thank Dr. Pyoung-Jik Lee, Professor Emeritus Barry Gibbs, and Dr. Simone Graetzer for their useful advice and encouragement.

My colleagues and friends at the Acoustics Research Unit have always been there, providing advices personally and academically, for which I am very grateful.

I would like to gratefully thank Dr Luc Jaouen and Matthew Edwards from Matelys for kindly carrying out measurements to characterize the open cell foam. For kind assistance with the rain noise measurements, the author is grateful to Lawrence Barnes and Andy Snaylam from School of Engineering at the University of Liverpool.

I would like to gratefully acknowledge the scholarship and funding provided by the School of Arts, at the University of Liverpool.

Finally, my sincere gratitude goes to my dear family, for their support and love. To all my friends who got me through nearly four years of work I am very thankful.

List of symbols

a	Horizontal dimension of oblate spheroids (m)
$\bar{a}$	Dimensionless radius of wetted spot
b_1	Vertical dimension of lower side oblate spheroid (m)
b_2	Vertical dimension of upper side oblate spheroid (m)
c_L	Longitudinal wave speed of the plate (m/s)
c_0	Sound velocity in the air (m/s)
d	Water layer depth (mm)
D	Drop diameter (m)
D_i	Bending stiffness of plate i
δD	Drop diameter interval (m)
$\boldsymbol{e}$	Vector of acceleration response signal in the time domain (m/s^2)
$\boldsymbol{E}$	Vector of acceleration response signal in the frequency domain (m/s^2)
E_k	Kinetic energy (kgm^2/s^2)
E_s	Surface energy (kgm^2/s^2)
f	Frequency (Hz)
$f(t)$	Time dependent force (N)
$\boldsymbol{f}$	Vector dependent force (N)
$\boldsymbol{f}_w$	Vector of amplitude of force representation using wavelet functions (N)
g	Acceleration due to gravity (m/s^2)
G	Green function (-)
h	Thickness (m)
H	Falling height of drop (m)
$\boldsymbol{h}$	Vector of impulse response in the time domain(m/s^2)
$\mathbf{h}$	Matrix of impulse response (m/s^2)
$\boldsymbol{H}$	Vector of impulse response in the frequency domain (m/s^2)
i	Imaginary number, $\sqrt{-1}$
J_0	First order Bessel function
k_0	Acoustic wavenumber in the air (/m)
k_l	Acoustic wavenumber in the limp foam (/m)
k_f	Bending wavenumber in the plate (/m)
K_{eq}	Effective bulk modulus (Pa)
L_x	Dimension of plate on x-axis (m)

L_y Dimension of plate on y-axis (m)

m Mass of drop (kg)

$n(D)$ Raindrop number distribution ($mm^{-1}m^{-3}$)

$\boldsymbol{n}$ Vector of noise from measured acceleration in the time domain (m/s^2)

$\boldsymbol{N}$ Vector of noise from measured acceleration in the frequency domain (m/s^2)

$N(D)$ Number of natural raindrops (m^{-2} s^{-1})

$\bar{p}$ Dimensionless pressure (-)

p Pressure or distributed pressure field (Pa)

R_r Rainfall rate (mm/h)

R_h Horizontal radius of drop (m)

R_v Vertical radius of drop (m)

S Area of the plate (m^2)

v Velocity of vibrating plate (m/s)

v_d Drop velocity (m/s)

$v_{d,n}$ Perpendicular drop velocity (m/s)

v_T Terminal velocity of drop (m/s)

$<v^2>$ Mean square velocity (m^2/s^2)

r Radius of drop (m)

s Scale integer (-)

t Time array or instantaneous time (s)

t_n Time steps (s)

W_{in} Power input to the system (W)

W_{ij} Power transfer from subsystem i to j (W)

Z_{TMM} Impedance of the multilayer structure (Ns/m)

τ Dimensionless time factor (-)

σ Liquid surface tension (N/m)

σ_0 Radiation efficiency without damping (-)

σ_n Equivalent radiation efficiency from nearfield of a point force (-)

ρ_w Density of water (kg/m^3)

ρ_s Surface density of plate (kg/m^2)

ρ_0 Density of air (kg/m^3)

ρ_{limp} Density of limp foam (kg/m^3)

λ	Regularization parameter
η	Loss factor (-)
μ	Viscosity of water (Pa·s)
ω	Angular frequency (radians/s)
φ	Geometrical angle of velocity that bending wave propagates (degree)
$\mathbf{\Phi}$	Matrix of wavelet functions (-)

List of abbreviations

We	Weber number ($= \rho_w {v_\mathrm{d}}^2 D/\sigma$)
Re	Reynolds number ($= \rho_\mathrm{w} v_\mathrm{d} D/\mu$)
Eo	Eötvös number ($= \left(\rho_\mathrm{w} - \rho_0\right) g D^2/\sigma$)
Oh	Ohnesorge number ($=\mathrm{We}^{1/2}/\mathrm{Re}^{-1}$)
coifN	N^{th} order of Coiflets wavelet function
symN	N^{th} order of Symlets wavelet function
dbN	N^{th} order of Daubechies wavelet function
ESD	Energy Spectrum Density
FFT	Fast Fourier Transform
FRF	Frequency Response Function
FSI	Frame Stiffness Influence
FTMM	Finite Transfer Matrix Method
IFFT	Inverse Fast Fourier Transform
LMS	Least Mean Square
LTI	Linear Time-Invariant
LSE	Least Square Error
MAP	Maximum A Posteriori
ML	Maximum Likelihood
SEA	Statistical Energy Analysis
SNR	Signal-to-Noise Ratio
TMM	Transfer Matrix Method
TSVD	Truncated Singular Value Decomposition

1. Introduction

1.1. Background and motivation

The forces applied by liquid drops impact on dry or wet surfaces are important in many different areas of engineering such as blade erosion in steam turbines, soil splash from raindrops, and spray coating of paper (e.g. soil erosion [1-3], rain noise [4-7], and energy harvesting [8, 9]). For these applications, it is necessary to have knowledge of the force applied by a liquid drop upon impact to allow an assessment of erosion, damage, or the efficacy of the impact process.

The application considered in this thesis is in the field of engineering acoustics where rain falls on windows and roofs of buildings, and the roofs and windscreens of cars. When these relatively light weight structures are excited by raindrops, they can then generate high levels of re-radiated sound that can adversely affect speech communication or other activities [10].

Prediction of the sound and vibration resulting from the impact of raindrops on a plate-like surface initially requires knowledge of the time-dependent force that is applied to a structure when it is dry or covered with a shallow surface layer of water. The force arising from water drops impacting onto dry or wet surfaces is affected by impact velocity, drop shapes, surface texture, and environment temperature. However, previous work in building acoustics to predict rain noise has only considered models assuming a drop impacts on a dry surface [5]; hence there is a need to assess the effect of a wet surface.

The present theoretical models for the liquid drop impact force only consider the normal impact. For automotive roofs, (such as glass panoramic roofs in cars) the surface is flat; whereas the windscreen can be angled. For roof glazing in buildings, the roof lights are in the same plane as the sloped roof. Most buildings have roof slopes between 5° and 56°, although in the UK most roofs are between 40° and 50° [11]. For the testing of rain noise on building elements according to ISO 10140 [12] the standard configuration for the slope is 30°. Therefore, it is necessary to be able to predict the impact force for impact at an oblique angle.

With knowledge of the time dependant force from rain drop impact, the next step is to model the excitation that results in vibration and sound radiation from structures. The vibro-acoustic responses of plates with attached noise control material (e.g.

porous material like fibres, felts foams etc.) are classically modelled by using deterministic models such as the Finite Element Method (FEM) or Boundary Element Method (BEM), statistical models such as Statistical Energy Analysis (SEA), and analytical wave propagation models such as the Transfer Matrix Method (TMM). The accuracy and suitability of these models needs to be assessed for vibro-acoustic prediction of rain noise, particularly for multilayer plates.

1.2. Properties of rain

Natural rain is comprised of different size drops for which the distribution of drop sizes depends on the rainfall rate [13]. Light rain with a rainfall rate of 1 mm/h will rarely give rise to significant re-radiated noise problems; hence it is of more interest to consider moderate to heavy rain which typically has rainfall rates from 4 to 50 mm/h [14]. For light to heavy rain, raindrops can generally be described as spherical or ellipsoidal in shape by using the concept of an equivalent sphere [15]. In general, a drop shape is conveniently represented by the combination of two oblate semi-spheroids [15] although 2 mm drops at terminal velocity are approximately spherical (axis ratio is ≈0.9 [16]). In temperate climates there is rarely any need to consider equivalent drop diameters larger than 5 mm because such drops will break up into smaller drops as they fall [17]. Although natural rain contains a wide range of equivalent drop diameters, the structure-borne sound power it injects into a structure tends to be dominated by the fraction of larger diameter drops that apply a higher force due to their higher mass and terminal velocity [18]. The raindrop size distribution is typically considered to have equivalent drop diameters between 1 and 6 mm [14]; in this thesis it is assumed that 2 mm drops represent the smallest drop diameter of interest for rain noise.

1.3. Models for the time-dependent force applied by a liquid water drop on a rigid surface

Theoretical models to estimate the time-dependent force by drop impact are mainly based on simplified two-phase [19] impact dynamic models.

Idealized drop shape models have previously been used to predict the time-dependent force applied to a dry, rigid surface. Petersson [4] considered prediction models based on paraboloidal and cylindrical-hemispherical drop shapes for which comparison with measurements indicated that the former showed better agreement

than the latter. Photographic observations (e.g. [20]) indicate that a cylindrical-hemispherical model could be appropriate when the drop velocity on impact is low (i.e. ≈2 m/s). The deficiencies observed with this model were attributed to the assumption of constant velocity in the flow phase. Petersson's experiments appear to be the only published results that have attempted to quantify the force applied when there is a surface layer of water; however, the depth of this layer was described subjectively as either a 'thin' or 'thick' layer. Hence the experiments in this thesis are used to determine the forces for a specified range of surface water layer depths and different drop velocities.

In the idealized drop shape model described above, there is no consideration of the spreading lamella after impact [21]. Roisman *et al* [22] assumed a spherical drop shape model to estimate the spreading and receding phenomenon for a liquid drop on a dry surface from which the time-dependent force was derived, but it was not compared with measurements. Anantharamaiah *et al* [23] later compared the calculated force from Roisman *et al* with their CFD simulations which showed close agreement for a 4.9 mm diameter water drop with a velocity of 2.34 m/s (i.e. well-below terminal velocity). However, the 2002 Roisman *et al* model was noted as being incorrect in 2011 by Marengo *et al* [24]. In 2009, Roisman *et al* [25] determined an empirical curve for dimensionless pressure at the impact point from curve fitting of numerical predictions for a spherical liquid drop on a dry surface. Although Roisman *et al* didn't provide an explicit calculation equation for the impact force; the pressure can be multiplied by the drop's area to estimate the force.

Philippi *et al* [26] studied the initial phase of a drop impact in theory and with simulation for a dry surface. During the initial impact phase, the extent pressure field is proportional to $1/\sqrt{t}$, and consequently the impact force increases with $\sqrt{t}$ for short time as observed by Gordillo *et al* in experiments [27]. However, this formula doesn't describe the relatively long decay of the force in the whole impact process. Therefore, Mitchell *et al* [28] combined the early-time force model for impact force from Philippi *et al* [26] and the exponential post-peak decay to give the full force profile. However, this model assumes a spherical drop shape which is problematic for large raindrops (i.e. 4.5 mm diameter drops used in this thesis). Moreover, the present theoretical models only consider the normal impact on a dry surface, whereas

the impact on building roofs and vehicle windscreens are often at an angle and with a thin layer of water on the surface.

In this thesis, the aim is to avoid the problems and shortcomings of idealized drop shape models and models from fluid dynamics for different drop velocities by determining empirical formulae for the time-dependent force.

1.4. Experimental determination of the time-dependent force of a liquid drop impact

Previous experiments to measure the time-dependent force from liquid drops have used a variety of approaches mainly based on the use of pressure sensors and force transducer discs.

Nearing *et al* [2] used pressure sensors and noted that the time-dependent force and average pressure were not adequately predicted by theory based on incompressible mechanics or numerical techniques that do not account for compressional wave generation, surface tension, and viscosity. Nearing and Bradford [1] used a pressure transducer to measure the force although the sensing area was small with a diameter of only 6.45 mm which meant that many drops did not fall onto the sensor. Grinspan and Gnanamoorthy [29] used PVDF film to measure the impact force applied by a low velocity water drop and an oil droplet on a solid surface. This showed that the impact force depends on the drop velocity and liquid density. The main advantage of a pressure sensor is that the contact area of pressure sensor is large for the drop impact features that occur during impact process such as spreading and splashing.

Another measurement method is based on the force transducer with a receiver disc. Petersson [4] used a force transducer to measure the impact force of water drops on dry and wet surfaces. In his experiment, a thin titanium disc was attached on top of the force transducer as the impact surface. It was observed that water drop impact on a dry surface leads to an initial sharp rise to a maximum force followed by a gradual decay to zero. On a wet surface, the impact force has higher energy at low frequencies and lower energy at high frequencies compared with a dry surface. However, this wet surface effect on the measured impact force was only discussed in frequency domain and without quantifying the water layer depth. Also, it is not known whether the measured force on a wet surface is relevant to a large area on a wet plate when measuring constrained water on top of a force transducer. Soto *et al*

[30] used two different approaches to measure the force from a water drop: piezoelectric quartz and a thin glass lamella. The latter approach used mechanical equilibrium to determine the maximum force from the largest deformation of the lamella for a given impact. Li *et al* [31] used a force transducer to measure the impact force, however the measured force curve was corrupted by the structural resonances of the transducer disc at high frequencies (approximately 17k Hz).

The literature indicates that piezoelectric transducers can be problematic due to (a) resonances of the transducer disc (e.g. [31]), (b) drop impacts outside the small sensor area and (c) small sensors not being well-suited to the measurement of drop impacts on shallow water layers. Hence, an alternative approach using inverse approaches based on wavelet theory for impacts on a relatively large plate is considered in this thesis.

1.5. Inverse methods to reconstruct transient force in the time domain

This section reviews the force time history reconstruction based on time domain analysis approaches. Inverse methods for force reconstruction use the measured response signal (for example, displacement, velocity, acceleration or strain) to estimate the impact force indirectly [32]. However, this inverse process is often ill-posed which consequently leads to the instability of the solution. Therefore, approaches to try and overcome the ill-conditioning are a key step in impact force reconstruction, which is commonly optimized based on regularization or deconvolution methods [32-35].

One of the methods to improve the measurement of the transfer matrix (which is referred to the matrix that represents the linear relation between the excitation force and the response signal) to make it well-posed, for example using multiple responses [33, 34, 36] or selection of the response locations [37]. This is because response sensors located at different positions may be at nodal points force some modes. Therefore, using multiple sensors or careful choice of positions could compensate for this.

For ill-posed problems, a common approach to find a solution is deconvolution optimization: such as truncated singular value decomposition (TSVD [38]), l_2-norm regularization (also known as Tikhonov regularization [38]), Wiener filter [39]. The l_2-norm regularization method improves the estimate by reducing the effects of errors or noise on the small singular value of the transfer matrix.

Alternative techniques including state variable formulation (Kalman filter) [40, 41], Sum of Weighted Accelerations Technique (SWAT) [42], neural networks [43] and genetic algorithms [44]. State variable formulation is a commonly used approach for force estimation especially in-situ, however this technique requires that the system differential equations can be described adequately, which may be problematic when the plate is covered with a layer of water. SWAT also has a difficulty of determining the weighting factors. Other new techniques using large numbers of processing units like neural networks have been considered for impact force estimation on composite plates, particularly for non-linear response [45], which is computationally expensive.

Transient Statistical Energy Analysis (TSEA) has also been applied to estimate the time history of impact load [46] by assuming a typical half sine waveform for the force-time history. Hence after calculating the input energy with TSEA and obtaining the impact load spectrum, only two factors of the half sine waveform require optimization to identify the load time history. However, in general force identification problems, including rain drops, a priori information of the force curve shape is unknown, which increases the complexity of reconstructing the load time history.

In 1997, Doyle [33] developed a deconvolution method using wavelets for impact force estimation on a beam and plate. Compared with Fourier transform based on the linear combination of series of sinusoidal functions with infinite duration in time, wavelet basis functions are finite in time and suitable for transient drop impact forces. Moreover, the wavelet method can overcome the ill-conditioned problem by selecting the optimal scale and shift factors [33]. In this thesis, Doyle's wavelet method will be assessed and compared with other inverse methods in simulation and experiment for water drop impact force estimation. In order to assess the accuracy of Doyle's wavelet method, comparisons will be made with force transducer measurements.

1.6. Prediction of sound radiation by plates excited by rainfall

Natural rainfall has a statistical distribution of raindrop diameters that can be described by the Marshall-Palmer distribution [13]. This can be used to estimate the power input based on the rain fall rate. In laboratory investigations of the sound

radiation by plates under rain excitation, artificial rainfall apparatus is usually constructed to simulate natural rainfall [5, 7, 18, 47].

Suga and Tachibana [5] developed an empirical model for the relationship between the radiated sound power and the transmission loss (TL) under artificial rain fall, where the TL measured for 20 lightweight roofs and the power spectrum of natural rainfall was estimated using the paraboloidal drop shape model from Petersson [4]. Suga and Tachibana [5] also used the paraboloidal drop shape model [4] to estimate the injected power from natural rainfall but it was only used to calculate the change due to different raindrop diameters by comparing theory with laboratory measurements. Ballagh [18] also applied the paraboloidal drop shape model [4] to predict the sound radiation from plates with infinite size assumption. However, this assumption is problematic below the critical frequency as it does not represent the response of finite plates.

Numerical methods have also been applied to predict the sound radiation from rainfall excitation. Deterministic methods such as FEM and BEM [48] are commonly used in vibro-acoustic predictions. However, for broadband excitation like rainfall excitation, these methods become inaccurate and computationally expensive at mid- and high- frequencies. In contrast, SEA can be advantageous because it conveniently applies the statistical properties of rainfall excitation (for example, the random phase of raindrop impacts) and it is computationally inexpensive. Compared with numerical methods such as FEM and BEM, SEA provides estimates of the temporal and spatial average sound and vibration parameters for the components of the structure and allows analysis of the transmission paths between these components [49]. Hopkins [7] used the paraboloidal drop shape model and SEA to predict the radiated sound of a single sheet of glass plate which showed close agreement with measurements below 800 Hz and above 1.6k Hz. However, in the intermediate frequency range, there was a discrepancy that might be caused by the idealized drop shape model. Therefore, in this thesis, the idealized drop shape model will be assessed with other theoretical models and experimental measurement.

Roof structures such for cars and buildings are usually composite multilayer systems. SEA prediction models for multilayer structures are generally based on calculating an equivalent damping to account for the noise control treatment [50, 51]. This method includes the mass effect of the whole structure via a smeared added

mass by assuming that the layers are homogeneous [51]. However, the effects of the stiffness are usually neglected which can cause prediction errors at low frequencies [51]. An alternative method, the Transfer Matrix method (TMM) is better suited to sound radiation analysis for multilayer structures [50]. Similarly to SEA, TMM can also take advantage of the spatial and temporal incoherence of rainfall excitation, which can be analysed conveniently in the frequency and wavenumber domain. Guigou *et al* [10] used the TMM method combined with paraboloidal drop shape model to predict the rainfall noise on multilayer glazing that can be regarded as multilayer systems. The spatial windowing technique from Villot *et al* [52] has also been applied to account for the effect of the finite size of the plate. This thesis will assess the Finite Transfer Matrix Method (FTMM) for the prediction of vibration and sound radiation from a homogeneous and multilayer plate under rainfall excitation as well as using SEA for a homogeneous plate.

1.7. Aims and objectives

This thesis aims to predict the vibration and sound radiation of homogeneous plate and multilayer plate under excitation by single and multiple raindrop impacts.

The main objectives are as follows:

- Experimentally quantify the time-dependent force applied by a single liquid water drop impacting a glass plate (at normal and oblique angles) at different drop velocities when the plate is dry and with a shallow water layer.

- Assess the validity of idealized drop impact models for the time-dependent force through comparison with experimental data for impacts normal to the plate surface.

- Create empirical models from the experimental data for drop impacts normal to the plate surface for a single liquid water drop on a glass plate when dry and with a shallow water layer.

- Develop and validate correction terms for the empirical models so that they can be used to estimate the force from drop impacts on a plate at an oblique angle.

- Experimentally validate SEA and FTMM models which incorporate the empirical models to predict the sound radiated by single and multilayer plates that are excited by artificial rainfall.

- Simulate excitation from natural rainfall using numerical experiments.

1.8. Thesis structure

Chapter 2 reviews the physics of liquid drop impact on dry and wet surfaces, and the theoretical models for impact force prediction.

Chapter 3 contains the theory of the inverse methods based on Bayesian approach using wavelets for impact force estimation. This chapter also contains the simulation of wavelet deconvolution and the sparse representation using l_0-, l_1-, $l_{1/2}$-, l_2-norm with dictionaries.

Chapter 4 introduces SEA and FTMM models for the vibroacoustic analysis of a homogeneous plate and a multilayer plate represented by a plate-foam-plate system.

Chapter 5 contains the experimental set-ups and the measurement methods used in the experimental work.

Chapter 6 describes the measured time dependant force applied by water drops impacting onto a dry surface and a surface with a layer of water. The wavelet deconvolution estimation results are compared with the force transducer measurements. Sparse representation methods with l_0- and l_1-norm regularization is also used to estimate the impact force when the signal-to-noise ratio is low.

Chapter 7 contains the empirical model to estimate the impact force from 2 and 4.5 mm drops diameter at terminal velocity and a lower velocity onto a dry surface and a surface with a shallow water layer. The empirical model results are compared with the wavelet measurement data and the theoretical models (idealized drop shape model and other models).

Chapter 8 describes the experimental validation of FTMM method for the prediction of rain noise with artificial rainfall. A glass plate and multilayer plate experimental results are compared with SEA and FTMM numerical simulation.

Chapter 9 contains the numerical study of FTMM for the prediction of power input from natural rainfall on a glass plate. The Marshall-Palmer distribution is applied to analyse the power input associated with a range of drop diameters.

2. Theoretical models of liquid drop impact

This chapter reviews the liquid drop impact process and the force estimation models. The features of liquid drops impacting on dry and wet surfaces will be discussed in Section 2.1. Section 2.2 describes the Marshall-Palmer distribution of raindrop size for different rainfall rates. In Section 2.3 and Section 2.4, the shape of raindrops and the oscillation phenomenon will be considered. Then the force and pressure distribution of drop impact over the contact surface during the whole impact process will be described in theory using simplified idealized drop shape models (Section 2.5) and complex models from fluid dynamics (Section 2.6). Section 2.7 discusses about the angled impact force.

2.1. Overview of liquid drop impacts on a solid dry surface and a thin liquid layer

Worthington [53, 54] was one of the first researchers to investigate the impact dynamics of a liquid drop impact, producing many photographs of the phenomena of liquid drop impact on dry solid plates [53], as well as liquid drop and solid ball impact on deep liquid pools [54]. For more than ten decades, the physics of time-varying drop geometry and features during the impact process has been extensively investigated [15, 55, 56].

The impact phenomenon is governed by a large number of parameters. Figure 2.1, provided by Rein [55] gives an overview of different parameters that can affect drop impact phenomena. At the moment of impact, a drop may be spherical or deformed as ellipsoidal; the impact angle may be normal or oblique; and the surface can be dry or covered with a layer of liquid. All these parameters can affect the impact force.

This thesis mainly focuses on the structural vibration and noise radiation from rain drops impact on building and car roofs. Two different receiver surface conditions are assumed: 1) plane, smooth, unyielding dry surface, 2) a shallow flat layer of water.

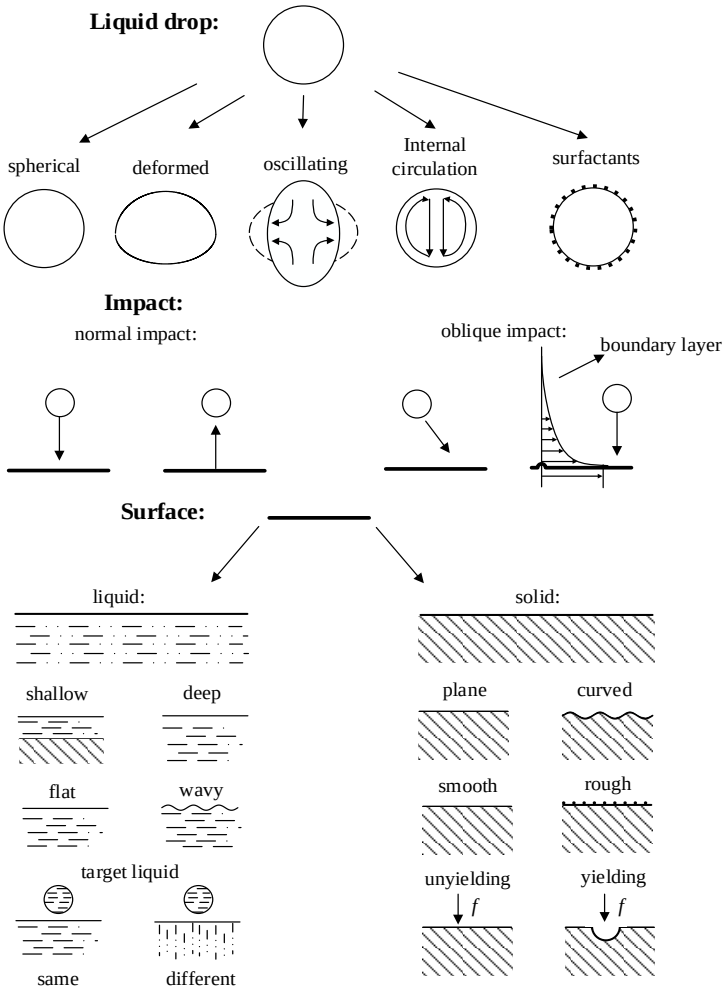

Figure 2.1. Survey of parameters governing the impact of a liquid drop from Rein [55].

2.1.1. Liquid drop impacts on dry surfaces

According to the experiments of Rioboo *et al* [57], there are six possible outcomes of a droplet impacting a dry surface as shown in Figure 2.2. The outcomes depend on the impact velocity, drop size, properties of the liquid (density, viscosity, viscoelasticity, and other non-Newtonian effects for rheologically complex fluids), surface or interfacial tension, roughness and wettability of the solid surface, non-isothermal effects (e.g., solidification and evaporation), and air entrapment [55, 58].

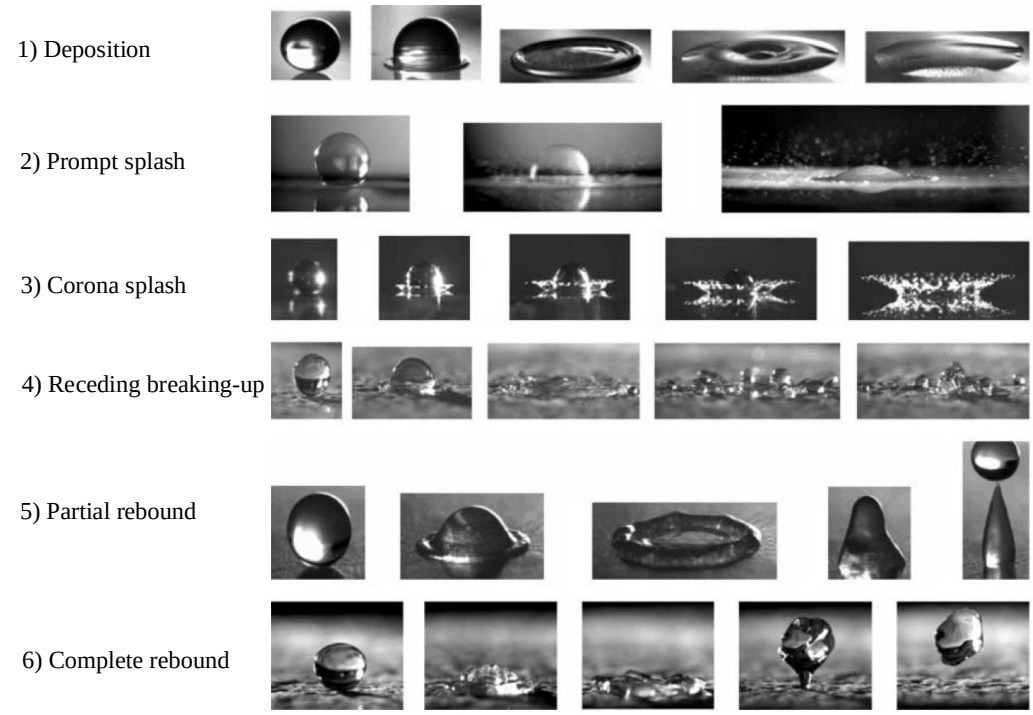

Figure 2.2. Six possible outcomes for a droplet impacting a dry surface. Images from Rioboo et al [57].

In terms of a drop impact on a solid dry surface, it is common that high impact velocities yield splashing whereas deposition is obtained at low-speed impacts [55]. This implies the importance role of droplet kinetic energy. During the impact, the kinetic energy of the droplet will be mainly transferred to the surface tension. Therefore, the surface tension can also affect the spreading and splashing phenomenon. Scaling the kinetic energy by the surface energy induces the Weber number. Weber number expresses the ratio of the kinetic energy on impact to the surface energy:

$$We = 12\frac{E_{\mathrm{k}}}{E_{\mathrm{s}}} = 12\frac{\pi\rho_{\mathrm{w}}D^3{v_{\mathrm{d}}}^2/12}{\pi D^2\sigma} = \rho_w{v_{\mathrm{d}}}^2D/\sigma \qquad 2\text{-}1$$

where ρ_w is the density of water, v_d is the drop velocity, D is the diameter of the drop, σ is the liquid surface tension. For rain drops of diameter D, at terminal velocity, v_d where 2 m/s<v_d<9 m/s and 1 mm<D<5 mm, the Weber number regime is 50<We<3500.

The impact phenomena can be significantly affected by the wettability and surface roughness [55]. Wettability indicates the maximum drop spreading area and spreading time for a moderate Weber number regime (30 < We < 200); However for

a high Weber number regime (We > 200), the effect of wettability is secondary because capillary forces are dominated by inertial effects [24, 59]. The effect of wettability on spreading is not negligible for rainfall with drop diameters smaller than 1.2mm.

The threshold Weber number of a water drop impact from the phenomenon of rebound or deposit to fragmentation is near 60 [24, 59, 60]. Below this Weber number, the liquid drop can deposit or rebound after impact which depends on the wettability as shown in Figure 2.2. At higher Weber numbers, the surface wettability effect is secondary, and a corona splash is usually observed as shown in Figure 2.2.

Surface roughness also affects the spreading and splashing phenomenon [61]. In this thesis, smooth surfaces are considered such as metal and glass plates such that the surface roughness effect on the impact force can be assumed to be negligible.

2.1.2. Liquid drop impacts on wet surfaces

Different phenomena occur for a liquid drop impact on a thin layer of liquid or a deep liquid pool. The collision of a drop with a deep liquid surface may result in floating, bouncing, coalescence and splashing [55] as shown in Figure 2.3.

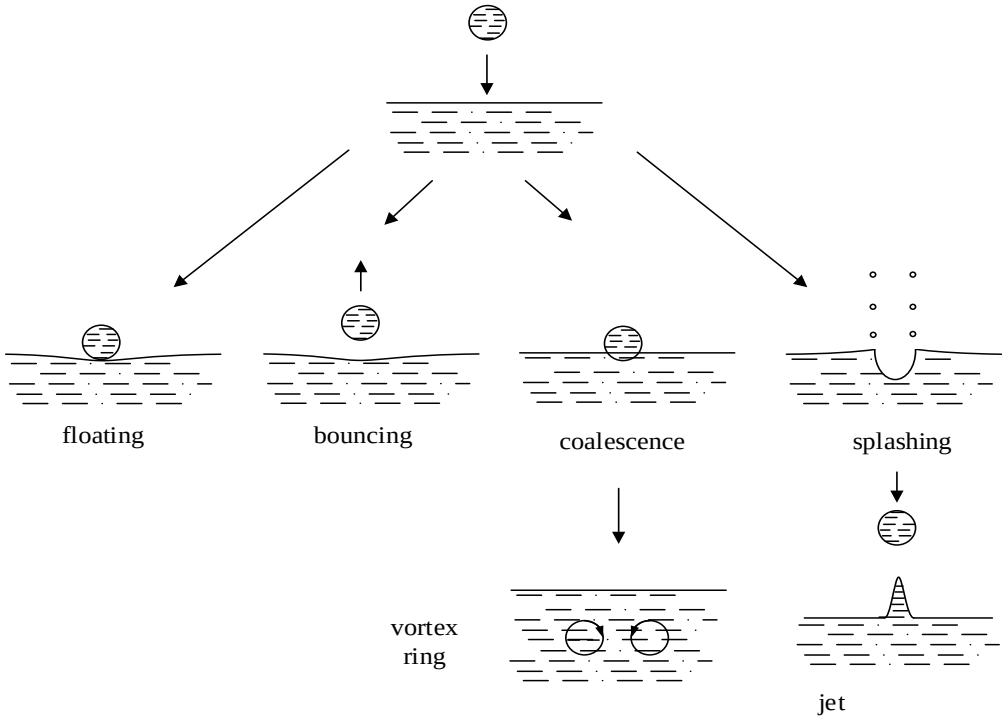

Figure 2.3. Impact of a drop on a liquid surface: floating, bouncing, coalescence and splashing from Rein [55].

Occasionally, after a liquid drop impact on a wet surface, it may float or bounce on the surface for several seconds and then disappear [55, 62].

The result of a collision that does not lead to floating or bouncing can be classified as coalescence or splash, respectively [55]. At low drop velocities, the impacting drop can coalesce with the water layer without making a splash, and without forming a jet, but making a vortex ring [63]. In this case, a small crater is formed but otherwise the impacted surface is hardly disturbed and the impacting drop disappears quickly in to the water layer. By contrast, the target surface is greatly deformed in the splashing case.

In contrast to splashing on dry surfaces where the formation of secondary droplets occurs, the conditions for splashing on a wet surface are not always consistent in literature. This is because the generation of secondary droplets can be different for different water layer depths.

For a deep pool impact, the liquid ejection from the crater is defined as splashing with or without formation of droplets at the rim of the crown as shown in Figure 2.3 [55]. Another example of splashing is where a droplet detaches from the central jet. For a drop impact on deep water (> 25 mm) with a sufficiently high drop velocity, the general features are the formation of a crater with a raised crown-like perimeter, followed by closure of the crater with a rising jet (often called the 'Rayleigh' or 'Worthington' jet) emanating from the centre of the aforementioned crater. A drop (or drops) may then detach from the top of the jet [64, 65]. The appearance of this central jet was used as a criterion for splashing by Rodriguez and Mesler [63]. Hobbs and Osheroff [65] note that for water depths less than 5 mm, the crown is more unstable than with impacts on deep liquid. Moreover, no drops detach from the jet for depths <3 mm [65]. Experimental work by Macklin and Hobbs [66] shows that the crater has a maximum depth of up to ≈3 drop diameters; hence for shallow water the crater depth is affected by the presence of the rigid plate which supports the water layer, and this flattens the bottom of the crater. When the depth of the water layer is approximately equal to two drop diameters, the jet height and the number of detached drops reaches a maximum [65, 66]. When the depth is similar to the drop diameter, the jet only reaches a very low height with no detaching drops [65].

In this thesis, two different drop sizes (2 and 4.5 mm diameter) with different velocities are used in the experimental work. For a drop impact on deep water

(>25 mm), a 2 mm drop would be expected to coalesce with drop velocities <1.4 m/s and 4.5 mm drops with velocities <0.8 m/s [65]; however such a deep water layer is not relevant to the situation on most roof structures.

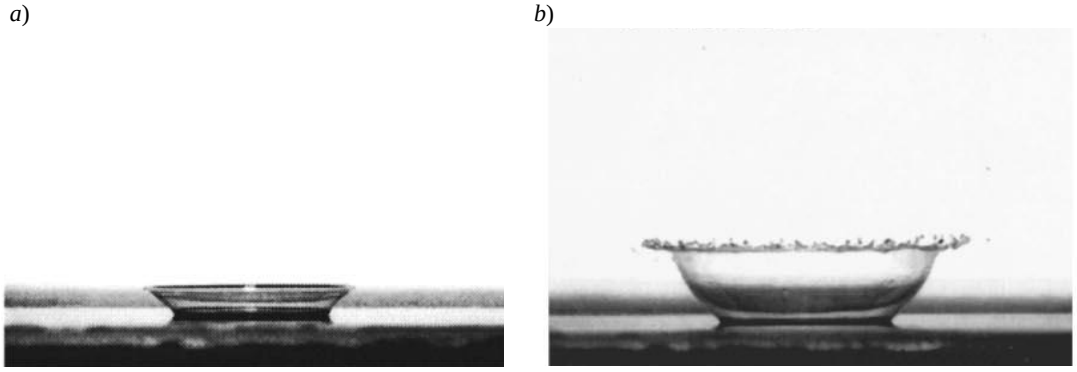

Figure 2.4. a) A non-splashing and b) a splashing crown of a drop impacting onto a thin layer of liquid from Wang and Chen [67].

In terms of drops impacting on a thin layer of liquid, the splashing phenomenon is usually defined by the secondary droplets generated from the rim of the crowns. When drops impact on a thin liquid layer with high velocities, numerous small secondary droplets are ejected from the free rim on top of the crowns [56], as shown in Figure 2.4b. At sufficiently low impact velocities the drops spread over the wall, taking the shape of lamellae with a visible outer rim (Figure 2.4a) [56]. At still lower impact velocities practically no rim is visible, which Rioboo *et al* [44] termed deposition [56].

2.2. Rain drop number and size distribution

Different from the artificial rain in laboratory, natural rainfall contains different size raindrops. There is a statistical distribution of raindrop diameters. The raindrop size and number can be modelled as the exponential distribution given by Marshall and Palmer [13] in terms of $n(D)$ $mm^{-1}m^{-3}$:

$$n(D) = 8000\exp(-4.1DR_r^{-0.21}) \quad 2\text{-}2$$

where D is the diameter of the rain drop size, R_r is the rain fall rate (mm/h). Then the number of drops, $N(D)$, with drop diameters between D and δD (in mm) that fall upon a unit area (1 m^2) per unit time (1 s) is:

$$N(D) = n(D)v_T\delta D \quad 2\text{-}3$$

where $v_T = 9.58\left\{1 - \exp\left[-\left(\frac{D}{1.77}\right)^{1.147}\right]\right\}$ is the terminal velocity, δD is the drop diameter interval (δD is assumed to be 0.03mm in this prediction model).

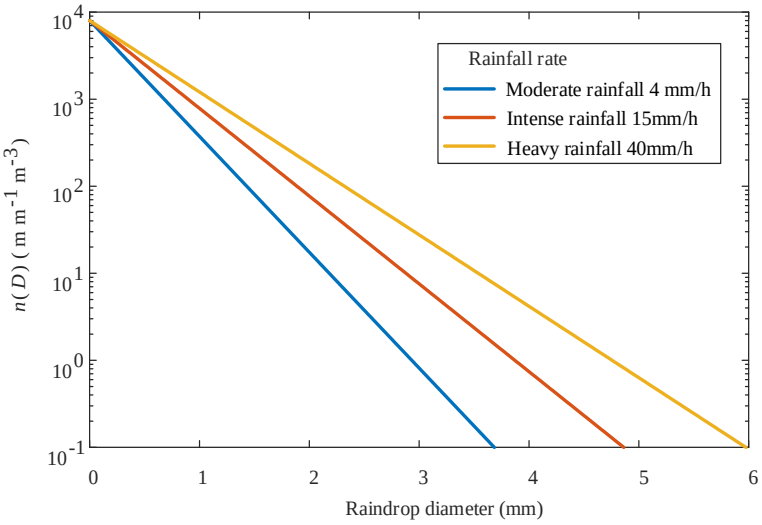

Figure 2.5. Marshall-Palmer distribution of raindrop diameters for different rainfall rates.

Figure 2.5 shows the number distributions of raindrop diameters for different rainfall rates. This emphasizes the effect from large rain drops especially for heavy rain fall (40mm/h). With small fraction from all the raindrops, the larger diameter drops apply higher forces due to the higher terminal velocity, and therefore dominate the power input into the collided structure. This will be discussed later in natural rain fall power input.

2.3. Drop shape

Most of the theoretical and numerical research tends to be based on the assumption that liquid drops are spherical, when moving in a homogeneous, unlimited ambient medium, and interfacial tension and/or viscous forces are much more important than inertia forces [16, 55]. However, as shown in Figure 2.1, the drop shape is not necessarily spherical before the impact. Specifically, for high Reynolds number (Re>10^3), the initial spherical drop shape becomes distorted [15], where the Reynolds number is given by $\rho_w v_d D/\mu$, where μ is the viscosity of water. Beard *et al* [68] calculated the equilibrium drop shape and the surface curvatures by an iterative adjustment of the pressure drag around the drop to the actual drop shape. This model has close agreement with several experimental photographic results on

the drop shape [16, 68]. The raindrop shapes without electrical stresses are shown in Figure 2.6.

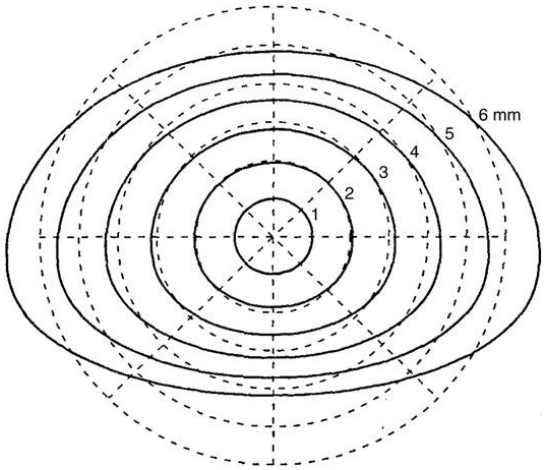

Figure 2.6. Numerical simulations of raindrop shapes for D=1, 2 3, 4, 5, and 6mm with origin at the centre of mass. Dashed circles are shown for comparison [16, 68].

For heavy rain, the diameter of raindrops is assumed to be 5 mm [7], which is close to the artificial drop of 4.5mm used in this thesis. For this drop diameter, (see Figure 2.6), the bottom of the drop is flattened. This may lead to difficulty in the theoretical models analysis, since the theoretical models are usually based on spherical shape assumption.

2.4. Drop oscillation

Oscillation can also affect the drop impact: 1) oscillation may be formed by the process of drop formation, the friction between a moving drop and the fluid surrounding it, and the wake of the drop, which causes the drop shape to deviate from the spherical shape [55], 2) oscillation can also occur when a drop spreads and recoils many times before coming to the rest [69]. Phase (1) is associated with a flow within the drop which can be affected by the surface tension [55]. Phase (2) is about the dynamic phenomenon due to the competition of the surface tension and inertia [2].

It has been observed that when a drop detaches from a needle, the damped shape oscillations stop after a free fall distance of approximately 15 mm [70]. Therefore, in this thesis which considers much longer drop distances, the oscillation effect on drop shape has been ignored.

2.5. Idealized drop shape model for estimation of the impact force on a dry surface

The idealized drop shape model proposed by Petersson [4] assumes that the impact of a liquid drop upon a surface can be considered in two phases. In the initial impact phase the mass of the drop remains unperturbed, and in the second phase the mass of the drop decreases as it jets out over the surface. Since the drop shape can be distorted and is "inevitably uncertain" after travelling through a varying ambient medium [4], one approach to prediction is to adopt idealized drop shapes.

Four idealised drop shape models are used to predict the time-dependent impact force on a dry surface; these correspond to paraboloidal, cylindrical-hemispherical, spherical and ellipsoidal shapes.

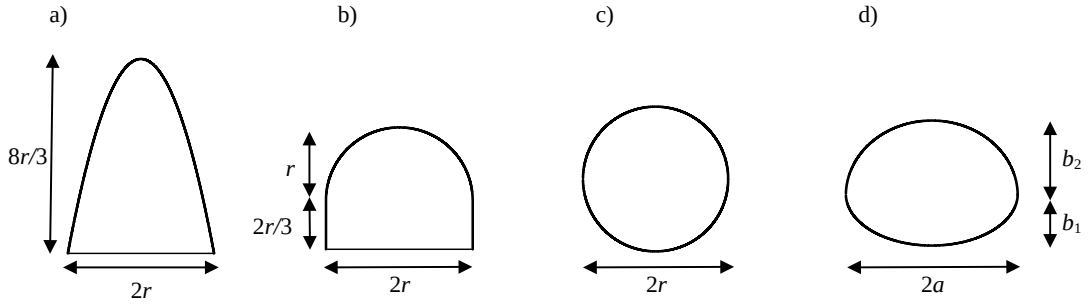

Figure 2.7. Idealised drop shape: a) paraboloidal, b) cylindrical-hemispherical, c) spherical, d) ellipsoidal.

The force from idealized drop shape model can be described by the change of momentum over time, which is given by Petersson [4]:

$$f(t) = \frac{\mathrm{d}(mv_\mathrm{d})}{\mathrm{d}t} \qquad 2\text{-}4$$

Assuming that the velocity is constant from the flow phase and the spreading lamella is negligible, the force can then be calculated using the residue mass-time function. For a spherical drop, the force can be given by:

$$f(t) = \frac{\mathrm{d}m}{\mathrm{d}t} v_\mathrm{d} = \frac{\rho_\mathrm{w}\pi\left[r^2 - (r^2 - v_\mathrm{d}^2 t^2)\right]v_\mathrm{d}\mathrm{d}t}{\mathrm{d}t} v_\mathrm{d} \qquad 2\text{-}5$$

From Petersson [4] the time-dependent force, $f(t)$, for a paraboloidal drop shape (Figure 2.7 (a)) is given by:

$$f(t) = \begin{cases} \rho_\mathrm{w}\pi r^2 {v_d}^2 (1 - \dfrac{3v_d t}{8r}) & 0 \le t \le 8r/3v_d \\ 0 & \text{for all other } t \end{cases} \qquad 2\text{-}6$$

where r is the drop radius, ρ_w is the density of water, v is the drop velocity.

For a cylindrical-hemispherical drop shape (Figure 2.7 (b)) the force is given by [4]

$$f(t) = \begin{cases} \rho_w \pi r^2 {v_d}^2 & 0 \le t \le \dfrac{2r}{3v_d} \\ \rho_w \pi r^2 {v_d}^2 \left[\dfrac{5}{9} + \dfrac{4v_d t}{3r} - \dfrac{{v_d}^2 t^2}{r^2}\right] & \dfrac{2r}{3v} \le t \le \dfrac{5r}{3v_d} \\ 0 & \text{for all other } t \end{cases} \qquad 2\text{-}7$$

As discussed in Section 2.3, it is more realistic to assume that the drop shapes are spherical and ellipsoidal. Therefore two additional drop shape models have been derived in this thesis using the approach of Petersson [4], a spherical drop shape model (Figure 2.7 (c)) giving:

$$f(t) = \begin{cases} 2\rho_w \pi r {v_d}^3 t - \rho_w \pi {v_d}^4 t^2 & 0 \le t \le 2r/v_d \\ 0 & \text{for all other } t \end{cases} \qquad 2\text{-}8$$

and an ellipsoidal drop shape model (Figure 2.7 (d)) giving:

$$f(t) = \begin{cases} \rho_w \pi {v_d}^2 \left[a^2 - \dfrac{a^2}{{b_1}^2}(b_1 - v_d t)^2\right] & 0 \le t \le b_1/v_d \\ \rho_w \pi {v_d}^2 \left[a^2 - \dfrac{a^2}{{b_2}^2}(b_1 - v_d t)^2\right] & \dfrac{b_1}{v_d} \le t \le \dfrac{b_1 + b_2}{v_d} \\ 0 & \text{for all other } t \end{cases} \qquad 2\text{-}9$$

The relationship between the dimensions a, b_1 and b_2 for the two oblate spheroids are [15]

$$b_1 = \frac{a}{[1 + 0.18(E_o - 0.4)^{0.8}][1 + 0.12(E_o - 0.5)^{0.8}]} \qquad 2\text{-}10$$

$$b_2 = \frac{2a}{1 + 0.18(E_o - 0.4)^{0.8}} - b_1; \qquad 2\text{-}11$$

where E_o is the Eötvös number which is defined as

$$E_o = (\rho_w - \rho_0) g D^2 / \sigma \qquad 2\text{-}12$$

in which g is the acceleration due to gravity, ρ_0 is the density of air, D is the drop diameter, and σ is the surface tension.

The paraboloidal idealized drop shape model has been validated by Petersson [4], and other researchers [5, 7, 10, 18] that have investigated rain noise prediction. However, the accuracy of this model is questionable. For example, Hopkins [7] observed a discrepancy between the measured rain noise and the prediction in the intermediate frequency range (800 Hz to 1.6k Hz). Moreover, there is no consideration of the spreading lamella [21] in idealized drop shape models.

Furthermore, the idealized drop shape models assume that raindrops fall on dry surface, which could be problematic for rain noise prediction when there is a layer of water over the surface during steady rainfall.

2.6. Theoretical models of liquid drop impact force from fluid dynamics

The idealized drop shape models are simplified models that do not consider parameters that affect the impact phenomenon such as the surface tension, roughness or wettability of the solid surface. More importantly, the effect from the other features during the impact process such as spreading lamella is ignored. Therefore, theoretical models for liquid drop impact force estimation established by researchers from fluid dynamics background are introduced here and will be compared with the idealised drop shape models.

In 2009, Roisman *et al* [25] used the volume-of-fluid method to simulate the pressure field during droplet impact on solid surface. The dimensionless pressure, $\bar{p}(t)$, at the impact point is given by:

$$\bar{p}(t) = 1.7\exp(-3.1t/(D/v_d)) \qquad \text{2-13}$$

This dimensionless pressure can also be calculated from the Bernouilli equation as proposed by Marengo *et al* [24] where:

$$\bar{p}(t) = \frac{1}{2} + \frac{1 - 2t/(D/v_d)}{\pi\sqrt{t/(D/v_d) - (t/(D/v_d))^2}} \qquad t/(D/v_d) < 0.5 \qquad \text{2-14}$$

Eqs. 2-13 and 2-14 are compared with the idealised drop shape models by converting the dimensionless pressure to force using

$$f(t) = \bar{p}(t)\bar{a}(t)^2\pi\rho_{\mathrm{w}}{v_d}^2D^2 \qquad \text{2-15}$$

where $\bar{a}(t)$ is the dimensionless radius of the wetted spot which can be obtained by assuming a spherical drop:

$$\bar{a}(t) \approx \sqrt{t/(D/v_d) - (t/(D/v_d))^2} \qquad \text{2-16}$$

Theoretical and numerical models of liquid drops impact pressure have also been investigated by Josserand and Zaleski [71] and Eggers *et al* [72], who found that the amplitude of pressure field $p(t)$ in this self-similar region (i.e. where the solution form is similar to itself if the independent and dependent variables are appropriately scaled) behaves like [72]:

$$\frac{p(t)}{\rho_{\mathrm{w}} {v_{\mathrm{d}}}^2} \propto \sqrt{\frac{\tau}{t}} \qquad 2\text{-}17$$

where $\tau = D/2v_{\mathrm{d}}$. This self-similar solution is for early stages of deformation (up to $t = \tau$). In 2016, Philippi *et al* [26] showed that the velocity and the pressure fields adhere to a self-similar form which is in agreement with Eq. 2-17. Furthermore, Philippi *et al* first derived the early evolution of the force, which is given by:

$$f(t) = \sqrt{27/2}\rho_w D^{3/2} {v_{\mathrm{d}}}^{5/2} \sqrt{t} \qquad 2\text{-}18$$

Gordillo *et al* [27] experimentally investigated the force profiles in a Reynolds number range of approximately $10^{-1} < Re < 10^4$, resulting in the discovery of visco-elastic, viscous and inertial regimes. When Re>200, self-similarity has been observed for all the measured force profiles in the inertial regimes. Additionally, the peak force is found to be approximately equal to $0.85\rho v^2 D^2$. However, the prediction of the initial-impact self-similar theory breaks down when Re<200, where viscous dissipation becomes important.

Because the model derived by Philippi *et al* [26] only provides the force evolution at early times, Mitchell *et al* [28] developed a model equation based on Eq. 2-18 from Philippi *et al* [26] and an exponential of the form e^{-t} to describe the post-peak decay, which is given by:

$$f(t) = \rho_{\mathrm{w}} v_{\mathrm{d}}^2 D^2 \sqrt{\frac{1000\pi v_{\mathrm{d}} t}{243D}} e^{-\frac{10 v_{\mathrm{d}} t}{3D}} \qquad 2\text{-}19$$

In addition, Mitchell *et al* [28] illustrated the interplay between the deformed droplet shape in images and its corresponding force. As shown in Figure 2.8, before the peak force is reached, the droplet side walls near the receiver surface are curved inward and the projected area onto the surface is less than the maximum area of a circle with diameter, *D*. At peak force, the side walls become perpendicular to the receiver plate and the projected area onto the surface has the maximum area. Therefore, the largest amount of momentum within the bulk droplet, which is purely in the direction normal to the plate, results in the largest normal force occurs at this time. After the peak force, the side walls of the droplet curved outward along with the spreading lamella which leads to less momentum directed in the normal direction towards the plate, although the projected area is larger. This spreading lamella consequently generates an exponential decay phase in the time dependent force.

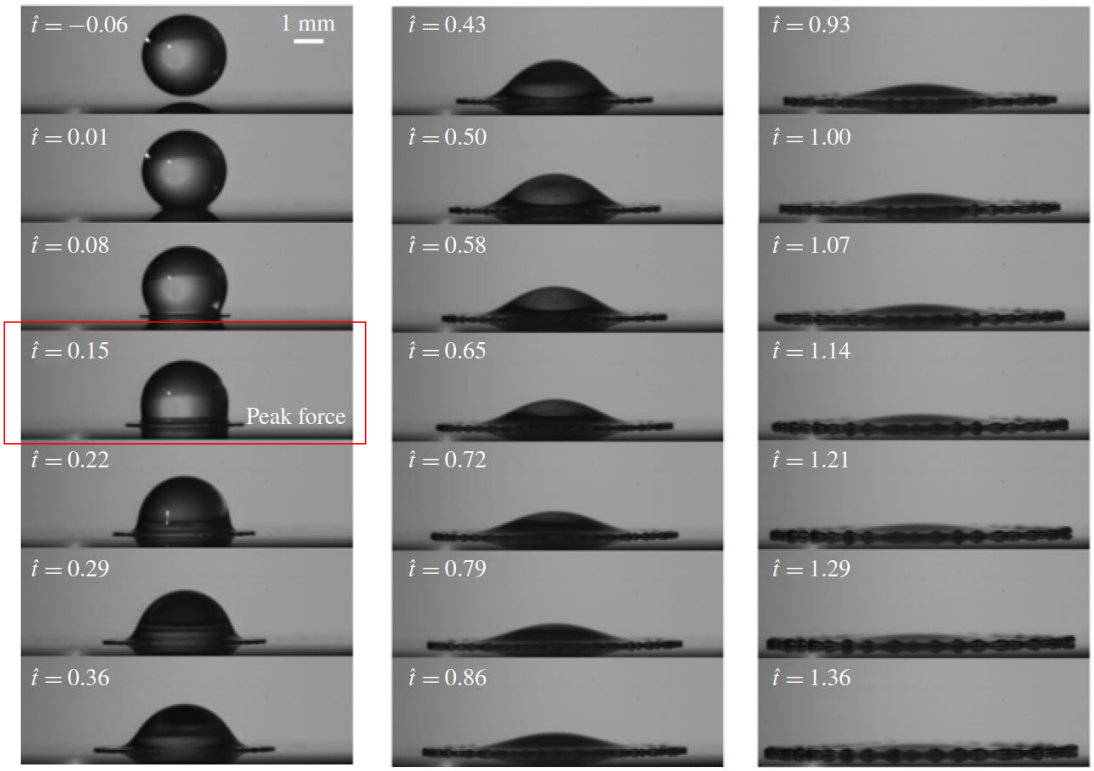

Figure 2.8. Impact process for a 2.9 mm diameter water drop impacting at 2.1 m/s from Mitchell *et al* [28].

2.7. Angled impact

In studies of liquid drop impact force, it is commonly assumed that the impact surface is horizontal. In practice, oblique impacts also occur such as a raindrop falling on sloped roof elements or droplets colliding with a turbine blade surface [73]. The pressure from angled impact of a liquid drop onto a dry surface has been previously researched [73, 74] with emphasis on the impact force by Zhang *et al* [75]. Zhang *et al* [75] show that the perpendicular component of the impact velocity dominates the impact force pulse due to momentum theory, and that the tangential component of the impact velocity may result in slip motion of the droplet but this has little effect on the impact force.

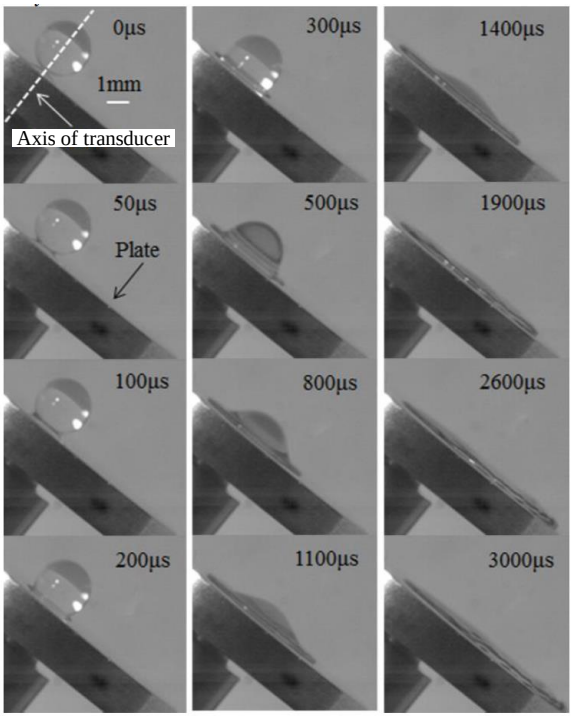

Figure 2.9. Images of water drop impact on an angled plate with 50°, D=2.44 mm, v_d=2.32 m/s from Zhang *et al* [75].

As shown in Figure 2.9, because the spreading velocity at the initial phase of the impact (before 800 μs in Figure 2.9 [75]) is larger than the slipping velocity $v_{d,t}$ of the drop, therefore, the impact process is similar to a horizontal surface. After 1100 μs in Figure 2.9, the slip motion becomes significant particularly for the lower side of the lamella which results in an asymmetric process. Zhang *et al* [75] also presented a fitted curve for the peak force with respect to the perpendicular velocity $v_{d,n}$.

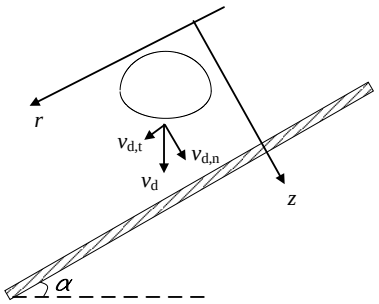

Figure 2.10. Illustration of 4.5 mm drop impact at terminal velocity 9.20 m/s on an angled surface.

Therefore, in order to account for the effect of the angle on the impact force as shown in Figure 2.10, only the perpendicular velocity $v_{\mathrm{d,n}}$ is used:

$$f(v_{\mathrm{d}}, t) = f\left(v_{\mathrm{d,n}}, t\right) = f(v_{\mathrm{d}} \cos \alpha, t) \qquad 2\text{-}20$$

However, in Zhang *et al*'s [75] experimental study, the drop shape is spherical. A non-spherical drop has a time-dependent force profile that is different from a spherical drop. For large raindrops at terminal velocity, the drop shape can be ellipsoidal with a flattened bottom (discussed in Section 2.3 and Section 2.5). A large drop impacting on a horizontal surface has shorter momentum transfer times and the larger projection area than oblique impact, which consequently results in higher force peak. The influence of drop shape on impact force has also been discussed by Zhang *et al* [76]. For 4.5mm ellipsoidal drop impact on an angled surface, as shown in Figure 2.10, the maximum projection area is smaller than the horizontal situation. In addition the perpendicular drop velocity is also smaller than the vertical drop velocity, which will result in lower force peak. Furthermore, the time-varying irregular projection area may lead to a more complex time-dependent force profile. However, the aim in this thesis is only to assess the accuracy of the correction based on the correction to the drop velocity.

2.8. Conclusions

Theoretical models for the force from a drop impact onto a horizontal surface that have been determined using simplified idealized drop shape or fluid dynamics have been reviewed in this chapter. The idealized drop shape models, which assumes that the drop shape is spherical, is suitable for small drops such as 2 mm drops used in this thesis. However this assumption is likely to be problematic for 4.5 mm drops that are used in this thesis to represent large raindrops, because the drop will have a flattened bottom at terminal velocity. Therefore, the idealized drop shape models based on spherical and ellipsoidal shapes are also developed.

Furthermore, the prediction models for the force only provide the time dependent force on dry surface. In practice, the assessment of first few raindrops on a dry roof is of less interest than the sound radiated during steady rainfall. This means there will be a thin water layer over the roof which can affect the impact phenomenon as well as the impact force. In addition, as most roof elements are sloped, the angled impact should also be accounted for. Therefore, this thesis focuses on the accuracy assessment of these theoretical models based on experiment, from

which an empirical model will be developed to estimate the force from drops impacting onto dry and wet surfaces.

3. Wavelet theory used for experimental force estimation from a single drop impact

3.1. Introduction

This chapter introduces the wavelet analysis used to quantify the force of a single water drop impact.

Section 3.2 reviews the conventional time domain and frequency domain deconvolution methods.

In Section 3.3, the force estimation method based on Doyle's wavelet deconvolution has been interpreted using the Maximum Likelihood method from Bayesian Estimation theory. To improve the force estimation in terms of robustness towards noise, the sparse representation theory is also introduced.

Section 3.4 describes the numerical experiments on force identification using wavelet deconvolution, and the sparse representation with wavelet dictionaries. The numerical experiments test the wavelet theory by using the force from the idealized paraboloidal drop shape model.

3.2. Inverse methods for force identification in the time and frequency domain

Inverse approaches have been established (e.g. see review paper [32]) to estimate the impact force from measurement of the response (e.g. displacement, velocity, acceleration) at points on the structure when it is subjected to an impact. The structure is assumed to be relatively thin compared to the wavelength, and only bending waves are considered. For a Linear Time-Invariant (LTI) system, the response $\boldsymbol{e}(t)$ at point A on the structure can be related to the impact force $\boldsymbol{f}(t)$ applied at point B on the structure by a linear convolution integral where the time domain response can be expressed as:

$$\boldsymbol{e}(t) = \int_0^t \boldsymbol{h}(t-\tau)\boldsymbol{f}(\tau)\,\mathrm{d}\tau + \boldsymbol{n}(t) \qquad 3\text{-}1$$

where $\boldsymbol{h}(t)$ is the impulse response of the linear system measured at point A with excitation at point B, and $\boldsymbol{n}(t)$ is the additive noise. The time domain equation Eq. 3-1 can be expressed in the discrete time-domain form from which the impact force can be calculated by solving the following equation [77]:

$$\boldsymbol{e} = \mathbf{h}\boldsymbol{f} + \boldsymbol{n} \rightarrow \begin{Bmatrix} e_1 \\ e_2 \\ \vdots \\ e_N \end{Bmatrix} = \begin{bmatrix} h_1 & & & \\ h_2 & h_1 & & \\ \vdots & \vdots & \ddots & \\ h_N & h_{N-1} & \dots & h_1 \end{bmatrix} \begin{Bmatrix} f_1 \\ f_2 \\ \vdots \\ f_N \end{Bmatrix} + \begin{Bmatrix} n_1 \\ n_2 \\ \vdots \\ n_N \end{Bmatrix} \quad 3\text{-}2$$

For an infinite structure, the response signal only consists of the forward propagating dispersive wave as shown in Figure 3.1 (a). For a finite structure, if the reflected waves can be windowed out from the incident wave in the time domain, then the force input can be deconvoluted straightforwardly by division, because the reflections contain redundant information which is already available in the incident wave. In practice, the reflections for a dispersive system are superimposed on the incident portion of the response and cannot be easily windowed out (compare Figure 3.1(a) and Figure 3.1(b)). The calculations in Figure 3.1 used modal summations of a rectangular 6mm glass plate in the frequency range from 1 Hz up to 6k Hz (for detailed theory see Ref. [7]). Properties of the glass plate are shown in Table 3-1.

Table 3-1. Properties of the glass plate

Density (kg/m^3)	2500
Thickness (mm)	6
Dimensions (m)	1.2×1
Young's modulus (GN/m^2)	74
Poissons ratio	0.3
Loss factor	0.003

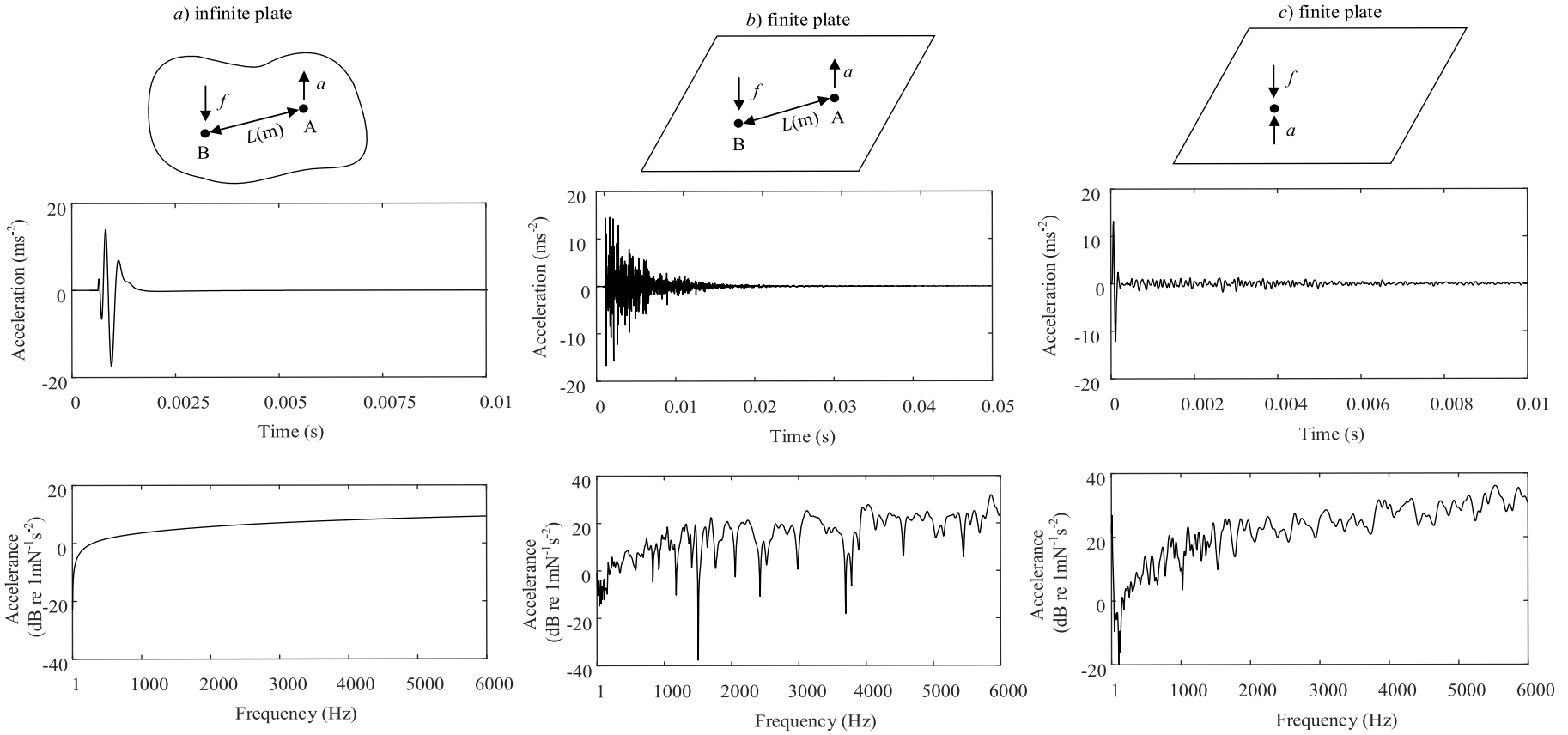

Figure 3.1. Illustration of the transient response in the time and frequency domain for an excitation position and response position separated by a distance *L* on (a) an infinite plate and (b) a finite plate, and (c) the driving-point response of the finite plate.

In order to improve the accuracy and stability of the estimation of the inverse estimation, many techniques have been applied in the literature [32] such as Least Square Error (LSE) [35, 36, 77], l_2 norm regularization methods (e.g. Truncated Singular Value Decomposition (TSVD) [78], and Tihkonov regularization [38]).

However, these time domain methods are computationally expensive to process the transfer matrix, such as the SVD decomposition of the transfer matrix [38, 78], or the iterative LSE [36]. During the development of these time-domain techniques in force identification problems, frequency domain methods have also been investigated. Compared with the time domain deconvolution or the transfer matrix decomposition, the frequency domain approach is computationally efficient.

The frequency domain method uses the Fourier Transform (FT) to transfer the convolution in Eq. 3-1 to multiplication at each frequency:

$$\boldsymbol{E}(\omega) = \boldsymbol{H}(\omega)\boldsymbol{F}(\omega) + \boldsymbol{N}(\omega) \tag{3-3}$$

where the uppercase symbols represent the frequency domain symbols corresponding to the time domain represented with lowercase in Eq. 3-1. The discrete form of the frequency domain can be obtained by Fast Fourier Transform (FFT) from Eq. 3-2. Therefore, when the excitation and the sensing are collocated, as shown in Figure 3.1(c), the frequency domain force can be estimated directly from division according to Eq. 3-3, with the knowledge of the Frequency Response Function (FRF), $\boldsymbol{H}(\omega)$, which is represented with the accelerance in Figure 3.1:

$$\widehat{\boldsymbol{F}}(\omega) = \frac{\boldsymbol{E}(\omega)}{\boldsymbol{H}(\omega)} - \frac{\boldsymbol{N}(\omega)}{\boldsymbol{H}(\omega)} \tag{3-4}$$

where $\widehat{\boldsymbol{F}}(\omega)$ is the estimated frequency domain force.

However, when the excitation and the sensing are not collocated [79], the FRF of the finite structure usually has smaller amplitudes at anti-resonances as shown in Figure 3.1(b) compared with the collocation case in Figure 3.1(c). This leads to missing information in the reconstructed input load and can make the division problematic particularly when the measurement noise in the response signal is significant. Additionally, the presence of sharp spectral peaks also leads to the loss of information as the response energy is dominant in some frequencies. Consequently, the deconvolution division can be problematic if there exists any mismatch between the response and the transfer matrix. This deconvolution method using direct division

was used in early research (e.g. Holzer [80]), from which it was noted that the noise tends to be amplified by the division of $\boldsymbol{E}(\omega)/\boldsymbol{H}(\omega)$ at high frequencies [80] such that a low-pass filter is required.

With a Fourier Transform there is a leakage problem caused by the truncated data from the time domain. This leakage is usually reduced by exponential windowing which incorporates the Fourier Transform resulting in the equivalent Laplace transform. Inoue *et al* used the Tikhonov regularization in the inverse Laplace transform for force estimation [81, 82]. However, the parameter for the exponential window is difficult to choose, especially when the signal is corrupted with noise [81, 82]. Other deconvolution methods has also been applied to solve the ill-posed problem such as Wiener filter [39], LSE [83], over-detection and singular value rejection method [84].

Since the frequency domain methods have this leakage problem and the conventional time domain methods are computationally expensive, another time domain method is investigated in this thesis which uses wavelets.

3.3. Inverse methods for force identification using wavelets

3.3.1. Wavelet deconvolution

An alternative method to solve the inverse problem for impact force identification is using wavelet deconvolution [85]. Impact force with finite time duration can be represented as a linear combination of wavelet basis functions with compact support (which means they are non-zero only over a limited time range). This is different from the Fourier transform expressed by a linear combination of sinusoidal functions with infinite durations. Use of the Fourier Transform requires a long stationary data to minimize the leakage problem and for fine resolution. This is likely to be problematic for non-stationary vibration such as transient excitation from a single water drop.

In 1997, Doyle [33] developed a deconvolution method using wavelets for impact force estimation on a beam and plate, and from the comparison with the frequency domain method, wavelet deconvolution was shown to give a more accurate solution. Li *et al* [86] proposed Daubechies wavelet for multi-resolution analysis to estimate the impact and sinusoidal forces. Compared with the conventional frequency method, the proposed wavelet method has better

identification ability and was robust to noise. Qiao *et al* [87, 88] also used cubic B-spline function for the basis function expansion methodology which is similar as wavelet deconvolution, resulting in superior estimation accuracy than TSVD. Therefore, in this thesis, the wavelet deconvolution method developed by Doyle [33] has been considered for the raindrop impact force determination.

Assuming that the impact force can be expanded by a series of basis wavelet functions [33], this is given by:

$$\boldsymbol{f} = \boldsymbol{\Phi}^{\mathrm{H}} \boldsymbol{f}_{\mathrm{w}} \tag{3-5}$$

where superscript H is the Hermitian, $\boldsymbol{\Phi}$ is an $M \times N$ matrix of wavelet functions. The elements of $\boldsymbol{\Phi}$ given by Doyle [33] are $\phi_m(t_n) = \exp\left[-\left(\frac{t_n - mt_0}{\alpha}\right)^2\right]$, t_n is the n^{th} sample in time (subscript w indicates wavelet), m is the time shift integer (also called shifting factor in the thesis), α is the parameter that can determine the width of the wavelet function (which is dependent on the frequency range of analysis). As illustrated in Figure 3.2, the collection of bell shaped wavelet basis functions $\phi_m(t_n)$ is used to represent the force pulse.

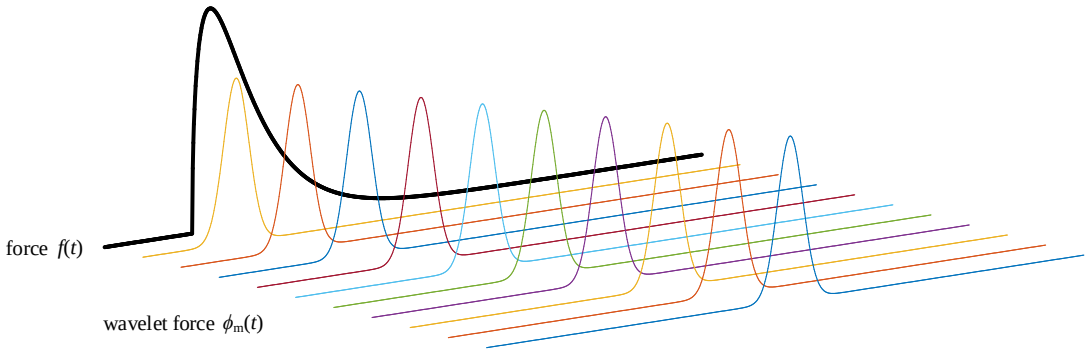

Figure 3.2. Illustration of wavelet functions to represent the force pulse.

The width of a smoothed triangle wavelet or bell shaped basis function is given by [33]:

$$\text{pulse width} = 4\alpha \text{ [s]} \tag{3-6}$$

In wavelet theory, α is usually chosen in the power of 2 [85], which in this thesis is $\alpha = 2^s \times 10^{-4}$, where s is the scale integer (also called scaling factor in the thesis) that can be chosen from the frequency content of the measured response. In Eq. 3-5, $\boldsymbol{f}_{\mathrm{w}}$ is a vector with dimension M to replace the original unknown vector $\boldsymbol{f}$ with dimension, N.

Doyle's wavelet deconvolution theory [33] does not consider noise in the derivation of the theory; hence, substituting Eq. 3-5 into Eq. 3-2 by ignoring the noise gives:

$$\boldsymbol{\Psi e} = \boldsymbol{\Psi\Psi}^{\mathrm{H}}\boldsymbol{f}_{\mathrm{w}} \tag{3-7}$$

$\boldsymbol{\Psi}$ is defined as:

$$\boldsymbol{\Psi} = \boldsymbol{\Phi}\mathbf{h}^{\mathrm{H}} \tag{3-8}$$

Then the unknown force is estimated according to [33]:

$$\boldsymbol{f} = \boldsymbol{\Phi}^{\mathrm{H}}\left(\boldsymbol{\Psi\Psi}^{\mathrm{H}}\right)^{-\mathbf{1}}\boldsymbol{\Psi e} \tag{3-9}$$

where the elements are a matrix of functions $\psi_m(t_n) = \sum_{k=0}^{n-1} x(t_n - \tau_k)\phi_m(\tau_k)$.

The system impulse response on a structure (e.g. plate) can be measured using force hammer excitation with accelerometers at several response positions. The unknown force applied by the real impact can then be related to the impact force, $\bar{\boldsymbol{f}}$, applied by the force hammer, and the associated acceleration signal, $\bar{\boldsymbol{e}}$, [36] by

$$\boldsymbol{e} * \bar{\boldsymbol{f}} = \bar{\boldsymbol{e}} * \boldsymbol{f} \tag{3-10}$$

where * denotes convolution. Eqs. 3-7 or 3-9 can then be solved by substituting $\boldsymbol{e} * \bar{\boldsymbol{f}}$ for $\boldsymbol{e}$ and $\bar{\boldsymbol{e}}$ for $\mathbf{h}$. However, depending on the experimental conditions and the selection of parameters of the wavelet function, $\boldsymbol{\Psi\Psi}^{\mathrm{H}}$ can be ill-conditioned which can lead to instability in the solution of Eq. 3-10. To overcome this problem, Eq. 3-7 can be solved using the LSQR algorithm [89] to give $\boldsymbol{f}_{\mathrm{w}}$. Note that the method for LSE solution in Eq. 3-9 is known as pseudo-inverse method, $(\boldsymbol{\Psi\Psi}^{\mathrm{H}})^{-1}\boldsymbol{\Psi}$ refers to the pseudo-inverse of the matrix $\boldsymbol{\Psi}$.

3.3.2. Maximum Likelihood Estimation from Bayesian theory

Since Doyle's approach [33] doesn't include noise in the derivation of the theory, this is addressed in this thesis by introducing the Maximum Likelihood (ML) approach from Bayesian theory.

Bayesian Estimation is a method that is usually used to estimate or predict a random process from a related observation signal, based on the prior knowledge of the probability distribution of the process. There are many classical estimators used in Bayesian philosophy such as: maximum-likelihood (ML), maximum a posteriori (MAP), LSE and minimum mean absolute value of error (MAVE). Under the

assumption of Gaussian likelihood function, the LSE solution is the same as ML solution [90].

From Eq. 3-2, the probability density function (pdf) of the vector $\boldsymbol{f}_{\mathrm{w}}$ from wavelet expansion given an observation response signal $\boldsymbol{e}$ can be described as [90]:

$$p_{\boldsymbol{f}_{\mathrm{w}}|\boldsymbol{e}}(\boldsymbol{f}_{\mathrm{w}}|\boldsymbol{e}) = \frac{f_{\boldsymbol{e}|\boldsymbol{f}_{\mathrm{w}}}(\boldsymbol{e}|\boldsymbol{f}_{\mathrm{w}}) f_{\boldsymbol{f}_{\mathrm{w}}}(\boldsymbol{f}_{\mathrm{w}})}{f_{\boldsymbol{e}}(\boldsymbol{e})} \tag{3-11}$$

The likelihood of the signal $\boldsymbol{e}$ given the parameter vector $\boldsymbol{f}_{\mathrm{w}}$ is the pdf of the random noise [90]:

$$p_{\boldsymbol{e}|\boldsymbol{f}_{\mathrm{w}}}(\boldsymbol{e}|\boldsymbol{f}_{\mathrm{w}}) = f_{\boldsymbol{n}}(\boldsymbol{n}) = f_{\boldsymbol{n}}(\boldsymbol{e} - \boldsymbol{\Psi}^{\mathrm{H}}\boldsymbol{f}_{\mathrm{w}}) \tag{3-12}$$

Assuming that $\boldsymbol{n}$ is random noise with a Gaussian distribution of mean, $\boldsymbol{\mu}_{\mathrm{n}}$, and a constant covariance σ_n, then the likelihood function is:

$$p_{\boldsymbol{e}|\boldsymbol{f}_{\mathrm{w}}}(\boldsymbol{e}|\boldsymbol{f}_{\mathrm{w}}) = \frac{1}{(2\pi\sigma_n)^{\frac{N}{2}}} \exp[-\frac{1}{2\sigma_n^2}(\boldsymbol{e} - \boldsymbol{\Psi}^{\mathrm{H}}\boldsymbol{f}_{\mathrm{w}} - \boldsymbol{\mu}_{\boldsymbol{n}})^{H}(\boldsymbol{e} - \boldsymbol{\Psi}^{\mathrm{H}}\boldsymbol{f}_{\mathrm{w}} - \boldsymbol{\mu}_{\boldsymbol{n}})] \tag{3-13}$$

The estimated force is obtained from maximization of the log-likelihood function, $\ln[f_{\mathbf{E}|\mathbf{F}_{\mathrm{w}}}(\boldsymbol{e}|\boldsymbol{f}_{\mathrm{w}})]$, with respect to $\boldsymbol{f}_{\mathrm{w}}$ and is given by [90, 91]:

$$\boldsymbol{\Psi}\boldsymbol{\Psi}^{\mathrm{H}}\boldsymbol{f}_{\mathrm{w}} = \boldsymbol{\Psi}(\boldsymbol{e} - \boldsymbol{\mu}_{\mathbf{n}}) \tag{3-14}$$

and when $\boldsymbol{\Psi}\boldsymbol{\Psi}^{\mathrm{H}}$ is well-posed,

$$\boldsymbol{f}_{\mathrm{w}} = (\boldsymbol{\Psi}\boldsymbol{\Psi}^{\mathrm{H}})^{-1}\boldsymbol{\Psi}(\boldsymbol{e} - \boldsymbol{\mu}_{\mathbf{n}}) \tag{3-15}$$

If $\boldsymbol{\mu}_{\mathbf{n}} = 0$ the added noise is white Gaussian noise with zero-mean value, Eq. 3-15 is then equivalent to the LSE solution given by Eq. 3-9.

3.3.3. Maximum A Posteriori estimation from Bayesian theory

Although Doyle's method [33] can provide close estimates for the force, the transfer matrix is likely to be ill-posed as observed by Qiao *et al* [92] especially when the parameters of the basis function (e.g. scaling and shifting factors) are not optimally chosen. The scaling and shifting factors work in a similar way to the regularization parameters to supress the noise [88, 93]. Moreover, the advantage of wavelet deconvolution method is essentially the same as l_2 regularization [88], regardless of the suitable finite time duration of wavelet function for the transient force. Selecting the optimal factors can also help to filter out the high-frequency components from the response and the force to improve the stability of estimation [86]. Unfortunately, Doyle did not provide a quantitative optimization method for

these parameters. Furthermore, Doyle produced the wavelet only by shifting the bell-shaped basis function, which makes the wavelets single resolution and non-orthogonal, although it can be orthogonalized using Gram-Schmidt orthogonalization [33]. The selection of a wavelet basis function can also affect the estimation accuracy [87, 88, 94]. Therefore, according to the theory of wavelets, it is likely to be more computationally efficient to use multi-level orthonormal wavelet functions, and apply the optimized orthonormal wavelet basis.

Gunawan *et al* [95, 96] used quadratic splines functions and B-splines functions as the basis functions to estimate the impact forces. For quadratic splines function, a uniform distribution of knots (the abscissas λ_j called nodes or knots of the B-splines functions control the smoothness of the profile or regularize the solution.) is assumed for the force identification [96]. For B-splines functions, the impact force within time interval [a, b] is divided into n-1 subintervals $a = \lambda_1 \leq \lambda_2 \leq ... \leq \lambda_n = b$. Gunawan *et al* proposed two steps to optimize the knots: 1) the knots are coarsely distributed to the entire domain of the analysis to capture the loading and the unloading stages of the impact; 2) the knots along the unloading stage are deleted and new knots are inserted along the loading stage.

Qiao *et al* [87] simplified the two-step regularization proposed by Gunawan *et al* [95] without calculating the slope at each knot, as well as the loading stage. Qiao *et al* admitted that corresponding to choose the number of singular values for the TSVD-based method, a smaller level j (the level of the wavelet decomposition) leads to an underestimated solution; conversely, for a larger level j, the solution will be overestimated.

These basis function expansion or wavelet deconvolution methods [33, 86-88, 95, 96] select the optimal parameters to supress the effect from noise, which are essentially similar as l_2 norm regularization parameters. Recently the sparsity representation algorithms based on l_1 norm [92, 97, 98] or $l_{1/2}$ norm [99], and adaptive l_q norm ($1<q<2$) [100, 101] regularization has led to investigations on load identification problems. These sparsity representation methods have been extensively researched in image or other signal processing, compressive sensing and machine learning [102-106]. Sparse representation is a method of reconstructing the input data (also known as sparse coding) in the form of a linear combination of basic elements as well as those basic elements themselves. These elements are called atoms and they

compose a dictionary [102-106]. Sparse representation applied for load identification using the regularization term mainly uses two different schemes: time domain force history identification (e.g. [92]) and frequency domain force localization (e.g. [99]).

This thesis mainly concerns time domain estimation of the force history from a water drop impact. For small water drops impacting at low velocities, the response signal might be corrupted with noise which results in low signal-to-noise ratios (SNR). Sparse representation force identification has considerable advantages for the sparse type solutions such as impacts, especially with low SNR [92, 97, 107]. Qiao *et al* [92] used the SpaRSA algorithm from l_1 norm regularization [108] to reconstruct the force from single and double impacts from highly noisy responses. Different basis functions like Dirac, Db6 wavelets, Sym4 wavelets, Cubic B-spline, and discrete cosine functions are used for representation. Compared with the traditional Tikhonov regularization using L-curve criterion [109], the l_1 norm shows better identification results when the response signal is corrupted with high level noise [92]. Later Qiao *et al* [97] applied the primal-dual interior point method (PDIPM) [110] to solve a large-scale ill-posed inverse force identification problem. Pan *et al* [111] used a weighted l_1 norm regularization to identify the moving force in the field of bridge structural health monitoring (SHM). In their research, both discrete trigonometric functions and discrete rectangular functions are used as a redundant dictionary so that the main features of the moving loads on the bridge are closely fitted.

Since the l_1 norm regularization tends to adjust for its sparsity-inducing effect, and given the condition that the prior information on the sparsity or continuity of the unknown force is implicit, Li and Lu [101] used a hierarchical Bayesian method to determine the force history, precision parameters, as well as q (in l_q norm). Their approach was to adaptively determine q which indicated that $1<q<2$ can lead to better reconstruction performance than other existing Bayesian methods with a pre-determined single value q. Another method of determining the adaptive q is proposed in Ref. [100]. In this thesis, since the force from a water drop impact is transient rather than steady-state, this hierarchical Bayesian method with adaptive q is not considered here.

These sparse representation methods are effectively applied to estimate the impact/sparse force time history in different cases, however, the time domain force estimation methods in the literature are based on convex optimization such as l_1 norm

regularization [92], or l_q norm [101] where $1<q<2$, instead of using the nonconvex l_q norm where $0\leq q<1$. A more natural sparse-inducing regularization method should be the l_0 norm, where the number of non-zero elements is considered. Furthermore, using l_1 norm regularization as a relaxation of the l_0 norm may underestimate the force [112]. Moreover, most of the research focuses on force identification using low SNR response signal, however, the sparse representation effect on the discontinuity or sharp edge of the impact force has not received so much attention. Based on the knowledge of the force applied by a single water drop impact from the literature (i.e. [26, 28]), the initial phase of the liquid drop impact process has instantaneous velocity redirection, which results in high pressure gradient around the edge of the spreading as well as a sharp edge in the time dependant force during the first millisecond, as shown in Figure 3.3.

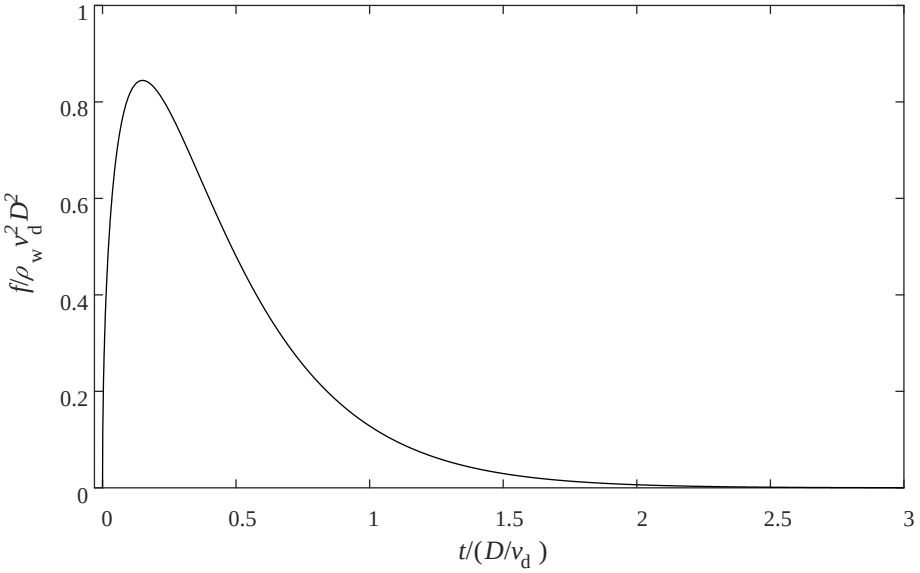

Figure 3.3. Time dependent force of liquid drop impact on a dry surface using the model from Mitchell *et al* [28] in terms of dimensionless force and dimensionless time.

It is observed by some researchers that the hard thresholding referred to as the l_0 norm is usually more robust towards noise than soft thresholding (referred to as the l_1 norm) for wavelet decomposition, particularly for sharp edged signals [113]. Therefore, three typical sparse representation methods l_0-, $l_{1/2}$-, l_1-norm regularization, have been utilized in this thesis to compare with the l_2 norm regularization method to estimate the impact force using numerical simulation. In the actual experiment, l_0 norm regularization will be validated for force estimation of 2mm drops impacting on dry surface with 2.57m/s velocity in Chapter 6. (Section 6.3.2). In the following

contents of this section, the MAP estimation based on Bayesian theory is used to describe l_0-, $l_{1/2}$-, l_1-, and l_2-norm regularization.

The MAP estimate $\hat{\boldsymbol{f}}_{MAP}$ is obtained as the parameter vector that maximises the posterior pdf:

$$\hat{\boldsymbol{f}}_{MAP} = \underset{\boldsymbol{f}}{arg\,max}\ p_{\boldsymbol{f}|\boldsymbol{e}}(\boldsymbol{f}|\boldsymbol{e}) = \underset{\boldsymbol{f}}{arg\,max}\ \frac{p_{\boldsymbol{e}|\boldsymbol{f}}(\boldsymbol{e}|\boldsymbol{f})p_{\boldsymbol{f}}(\boldsymbol{f})}{p_{\boldsymbol{e}}(\boldsymbol{e})} \tag{3-16}$$

Assuming that the estimated force $\boldsymbol{f}$ is also a Gaussian process with mean of $\boldsymbol{\mu}_{\mathbf{f}}$ and covariance of matrix $\boldsymbol{\Sigma}_{\boldsymbol{ff}}$, and $\boldsymbol{\mu}_{\mathbf{n}} = 0$, therefore the posterior distribution can be obtained by substituting Eq. 3-13 into Eq.3-16:

$$p_{\boldsymbol{f}|\boldsymbol{e}}(\boldsymbol{f}|\boldsymbol{e}) = \frac{1}{p_{\boldsymbol{e}}(\boldsymbol{e})}\frac{1}{(2\pi\sigma_n)^{\frac{N}{2}}}\frac{1}{(2\pi)^{\frac{N}{2}}\left|\boldsymbol{\Sigma}_{\boldsymbol{ff}}\right|^{\frac{1}{2}}}\exp\left[-\frac{1}{2\sigma_n^2}(\boldsymbol{e}-\mathbf{h}\boldsymbol{f})^H(\boldsymbol{e}-\mathbf{h}\boldsymbol{f})\right.$$
$$\left.-\frac{1}{2}\left(\boldsymbol{f}-\boldsymbol{\mu}_{\boldsymbol{f}}\right)^H\boldsymbol{\Sigma}_{\boldsymbol{ff}}^{-1}\left(\boldsymbol{f}-\boldsymbol{\mu}_{\boldsymbol{f}}\right)\right] \tag{3-17}$$

The MAP estimation of the impact force can then be obtained by differentiating the log-posterior pdf $\ln[f_{\boldsymbol{f}|\boldsymbol{e}}(\boldsymbol{f}|\boldsymbol{e})]$ and setting the derivative to zero:

$$\hat{\boldsymbol{f}}_{MAP} = \left(\left(\mathbf{h}^H\mathbf{h} + \sigma_n^2\boldsymbol{\Sigma}_{\boldsymbol{ff}}^{-1}\right)^{-1}\left(\mathbf{h}^H\boldsymbol{e} + \sigma_n^2\boldsymbol{\Sigma}_{\boldsymbol{ff}}^{-1}\boldsymbol{\mu}_{\boldsymbol{f}}\right)\right) \tag{3-18}$$

If the covariance of the Gaussian distributed force satisfy $\boldsymbol{\Sigma}_{\boldsymbol{ff}}^{-1} \to 0$, the Gaussian prior tends to a uniform prior, and then MAP estimation in Eq. 3-18 is the same as Eq. 3-9. On the other hand, when $\boldsymbol{\Sigma}_{\boldsymbol{ff}}^{-1} \to \infty$, which means the covariance of the Gaussian distributed force decreases, the pdf of $\boldsymbol{f}$ becomes peaked, and then the estimate tends towards $\boldsymbol{\mu}_{\boldsymbol{f}}$.

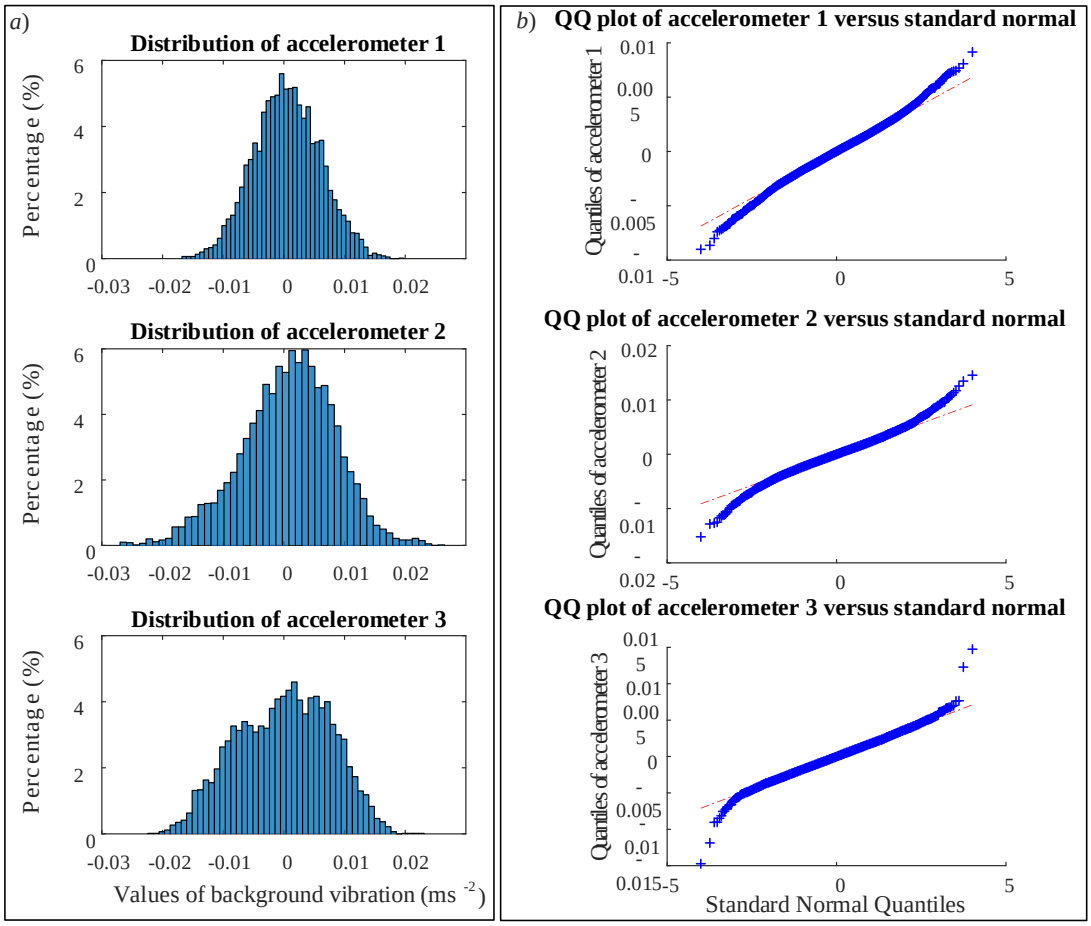

Figure 3.4. Examples of background vibration for three accelerometers mounted on a glass plate a) distribution histogram; b) QQ-plot.

An assessment is now made of the background noise in the experimental work in this thesis. Three accelerometers used for measuring the response signal are mounted on a glass plate (later described in Chapter 5, Figure 5.2). The white Gaussian assumption for the background noise is reasonable as shown in Figure 3.4. However, the prior knowledge of the mean value or the covariance of the force is unknown; therefore MAP estimation in Eq. 3-18 cannot be directly used for force identification.

The multivariate generalized Gaussian distribution [99, 114] is chosen here to estimate the force.

$$p_{\boldsymbol{f}}(\boldsymbol{f}) \propto \exp\left[-\frac{1}{2\Sigma_f}\|\boldsymbol{f}\|_q^q\right] \qquad 3\text{-}19$$

Substituting Eq. 3-19 into Eq. 3-16, the MAP estimate is given by:

$$\hat{\boldsymbol{f}}_{MAP} = \underset{\boldsymbol{f}}{arg\,min}\ \left\{\frac{1}{2}\|\mathbf{h}\boldsymbol{f}-\boldsymbol{e}\|_2^2 + \lambda\|\boldsymbol{f}\|_q^q\right\} \qquad 3\text{-}20$$

where λ is known as the regularization parameter $\lambda = \frac{\Sigma_f}{\sigma_n^2}$, and l_q-norm penalty function is given by $\|\boldsymbol{f}\|_q^q = \sum_{i=1}^{n} |\boldsymbol{f_i}|^q$. The probability distribution and the penalty function for different selection value of q are shown in Figure 3.5.

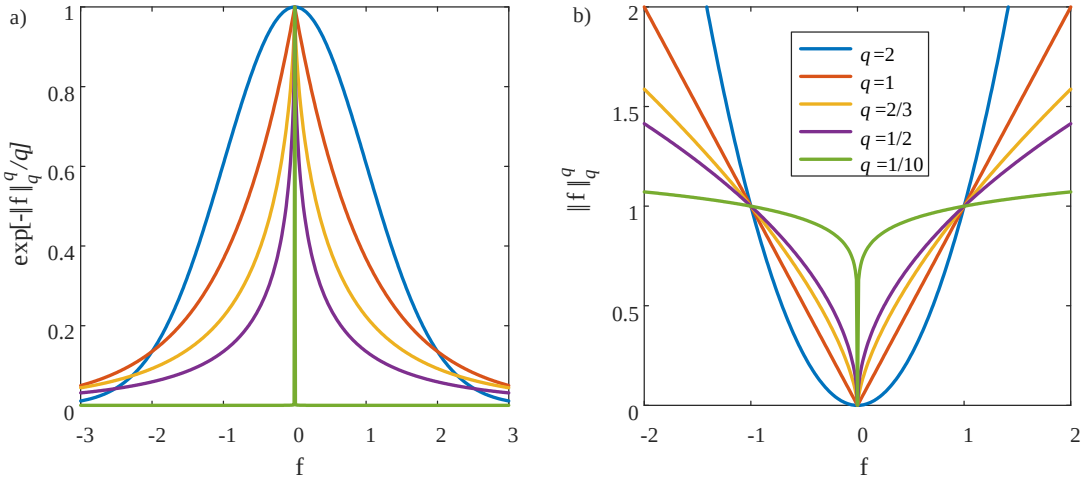

Figure 3.5. Geometric interpretation of probability distribution of (a) $\exp\left[-\frac{1}{q}\|\boldsymbol{f}\|_q^q\right]$ and (b) l_q–norm penalty function with different values of q.

When q=2, $\|\cdot\|_q^q$is called the l_2-norm or Euclidean norm, and the solution of Eq. 3-20 is the same as the solution in Eq. 3-18 (if the mean value of the force satisfy $\boldsymbol{\mu_f} = 0$). This l_2-norm regularization becomes the classical Tikhonov regularization which is well-known for its Gaussian smooth effect. This l_2-norm penalty function makes the solution stable in the least squares sense at the expense of allowing the original Eq. 3-2 not to be satisfied exactly. The l_2-norm regularization solution of minimizing the functional Eq. 3-20 is given by [32]:

$$\hat{\mathbf{f}}_{l_2} = \mathbf{V}\boldsymbol{\Sigma}^{\dagger}{}_{\lambda}\mathbf{U}^H\boldsymbol{e} \qquad 3\text{-}21$$

where $\mathbf{U}$ and $\mathbf{V}$ are unitary matrices, $\boldsymbol{\Sigma}$ is a diagonal matrix from the singular value decomposition (SVD) of the transfer matrix $\mathbf{h} = \mathbf{U}\boldsymbol{\Sigma}\mathbf{V}^H$, $\sum_{\lambda}^{\dagger}$ is a diagonal matrix whose elements are $\boldsymbol{\Sigma}_{i,i}/(\boldsymbol{\Sigma}_{i,i}{}^2 + \lambda)$, which is also known as the Tikhonov filter for supressing noise. The solution $\hat{\mathbf{f}}_{l_2}$ is unstable if λ is too small while it becomes inaccurate if λ is too large. The parameter λ is usually determined by using the L-curve method [109].

When q=1, it is called the l_1-norm, which describes the sum of absolute values of the elements of $\boldsymbol{f}$. The l_1-norm is usually used to induce sparsity in the optimal solution of Eq. 3-20. Another important advantage of the l_1-norm regularization as

opposed to the l_2-norm is that l_1 regularization is less sensitive to outliers (e.g. sharp edges in image processing applications) [115] which in this thesis corresponds to the sharp edges at the initial phase of the impact force from a single water drop. In this thesis the l_1-norm regularization is solved using the SpaRSA algorithm [108].

If the factor q is chosen as q<1, Eq. 3-20 becomes non-convex and a non-smooth optimization problem as shown in Figure 3.5, which is more difficult to solve. Moreover, to select an optimal q that can give the best estimation result is also a challenge. In signal processing areas such as image processing, it has been observed that the parameter q= ½ is a representative value for the selection of q: when $q \in \left(\frac{1}{2}, 1\right]$, the solutions subjected to l_q regularization are sparser with smaller q value, and no significant difference has been observed for the performance of l_q regularization when $q \in (0, 0.5]$ [116, 117]. Therefore, q= ½ is usually chosen as the representative parameter for 0<q<1. In this thesis the $l_{1/2}$-norm regularization is solved using the Half Proximal Thresholding Algorithm ([116, 117]).

When q=0, the penalty function is formally called l_0-norm, the number of non-zero components of the vector. Therefore, minimizing the penalty function $\|\boldsymbol{f}\|_0$ means minimizing the number of non-zero components of vector $\boldsymbol{f}$. The l_0-norm is probably the most intuitive and convenient for defining the sparse representation problem. In this thesis the Iterative Hard Thresholding (IHT [118]) is used to solve the l_0-norm regularization, which is efficient and suitable for high-dimensional problems.

In this thesis, four different parameters of q are chosen to recover the impact force applied by a water drop from the measured response signal: q=2, q=1, q=1/2 and q=0. Figure 3.6 shows the histogram of the impact force from 2mm and 4.5mm water drops impacting on a dry glass surface at terminal velocity using the paraboloidal drop shape model from Petersson [4]. The prior knowledge of the impact force distribution with centralized values of $\boldsymbol{f}$ and "heavy tails" seen in this figure shows that using sparse representation for l_1-, l_0- or $l_{1/2}$-norm regularization should give better estimation than the l_2-norm corresponding to the geometric interpretation in Figure 3.5.

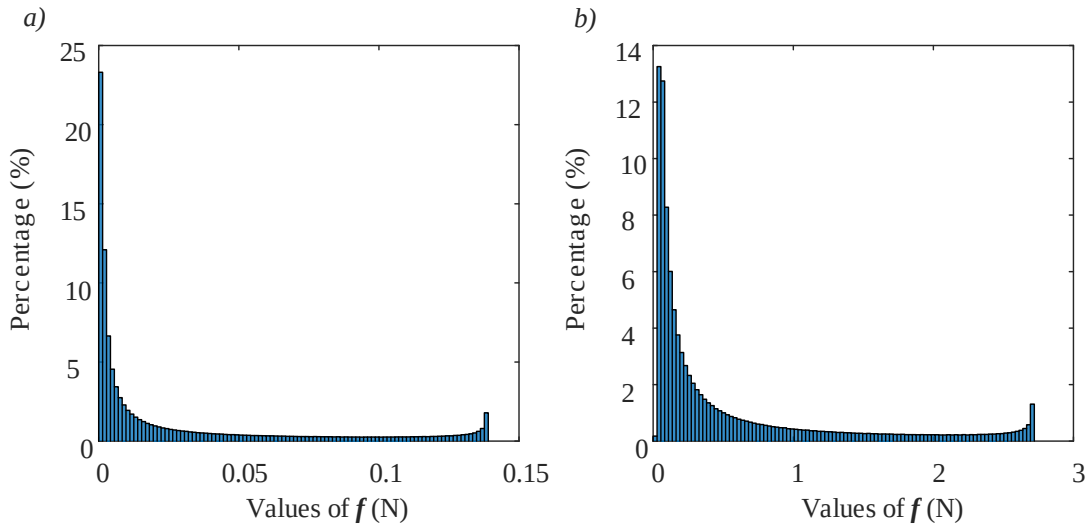

Figure 3.6. Histogram of force from water drop impacting on a dry surface at terminal velocity using the paraboloidal drop shape model from [4] for a) 2 mm diameter drops; b) 4.5 mm diameter drops.

3.4. Numerical experiments on force identification using wavelets

This section describes the numerical experiments on force identification using wavelet deconvolution and sparse representation methods.

3.4.1. Simulation of deconvolution using Doyle's wavelet method

3.4.1.1 Optimal sensing position(s)

The stability of the wavelet deconvolution method is determined by the transfer matrix and the SNR of the response signal. It can improve the estimation accuracy and stability by selecting the sensing positions for transfer matrix with small condition number and response signal with high SNR. Therefore, in this section, the optimal sensing positions for wavelet deconvolution have been assessed in simulation.

Khoo *et al* [37] observed that the multiple impact force identification can be reliable and robust by using LSE method estimation (specifically pseudo-inverse method) for over-determined or even-determined cases when good positions are selected from the averaged minimum condition number. Since only the single raindrop impact force is estimated in this thesis and multiple sensing positions are available, which can be interpreted as even- or over- determined cases.

In this simulation, the transfer matrix is obtained based on a modal summation [7] for a simply supported 6mm glass plate using 10000 bending mode shapes between

10 and 8k Hz. The excitation position is at $p_e\left(\frac{1}{3}L_x, \frac{1}{3}L_y\right)$ so that most of the modes are excited, and a 40×40 grid of different sensing positions is compared.

The structural damping is an important factor that can influence the singular frequencies of the response signal as well as the conditional number of the transfer function. As shown in [119], applying a dynamic damper at a suitable location can minimise the ill-conditioned nature of the frequency response function (FRF) matrix especially near the resonance frequency. Therefore, with low damping, the inverse problem becomes more difficult. In order to assess the condition number of the transfer matrix in the worst case, the loss factor of the glass plate is 0.003 in this section, which is the lowest possible damping that could be achieved in a measurement [7] and that the perimeter support for the plate would increase the damping. Parameters of the glass plate are shown in Table 3-1.

In order to estimate the ill-conditioning problem of the transfer function, the natural logarithm of the condition number is shown in Figure 3.7. Condition number of a matrix is defined as the ratio of the largest to smallest singular value in the singular value decomposition. The natural logarithm of the condition number is used to estimate the precision of an inverse solution. In this simulation, the transfer matrix is obtained using the impulse response (Eq. 3-1), which is obtained by the inverse Fast Fourier Transform (IFFT) from the frequency domain with summed mode shape functions of the plate as mentioned above.

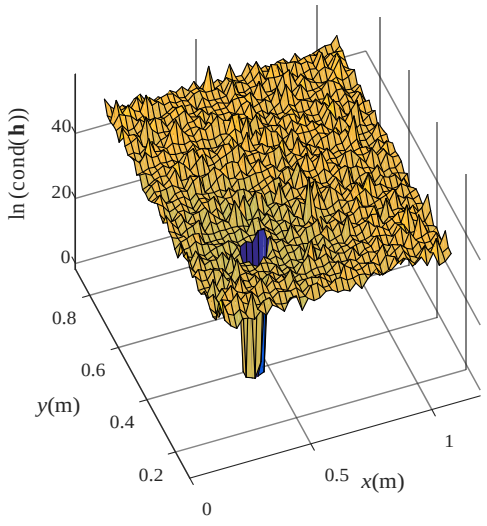

Figure 3.7. Logarithm of condition number of the transfer matrix for single response points over the 6mm glass plate surface.

As shown in Figure 3.7, the transfer matrix is well-conditioned near the excitation position. One reason for this can be seen by comparing Figure 3.1(b) and Figure 3.1(c) as discussed in Section 3.2. One possibility to obtain a well-conditioned matrix is to use a sensor position underneath the excitation position. However, drop impacts from at least a few metres do not always lead to impacts at exactly the same position. Hence an alternative is to choose a number of sensor positions that are randomly selected away from the excitation position which is the same as suggested by Doyle *et al* [33].

3.4.1.2 Comparison between l_2 norm regularization and wavelet deconvolution

In this section, the l_2 norm regularization is compared with the wavelet method for numerical determination of a transient impact force in the presence of noise in the response. In order to obtain the optimal value of regularization parameter, L-curve principle [109] has been used. L-curve principle requires plotting log-log scale l_2 norm of the regularization term (i.e. $\|\boldsymbol{f}\|_2^2$) versus the l_2 norm of the residual term (i.e. $\|\boldsymbol{e}-\mathbf{h}\boldsymbol{f}\|_2^2$) for different regularization parameters, as shown in Figure 3.8(a), which is in L-shape curve. The optimal regularization parameter is the value that gives the maximum curvature of the L-shape curve. In order to illustrate the regularization parameter conveniently, the curvature of the L- curve is also plotted in Figure 3.8(b) as an example.

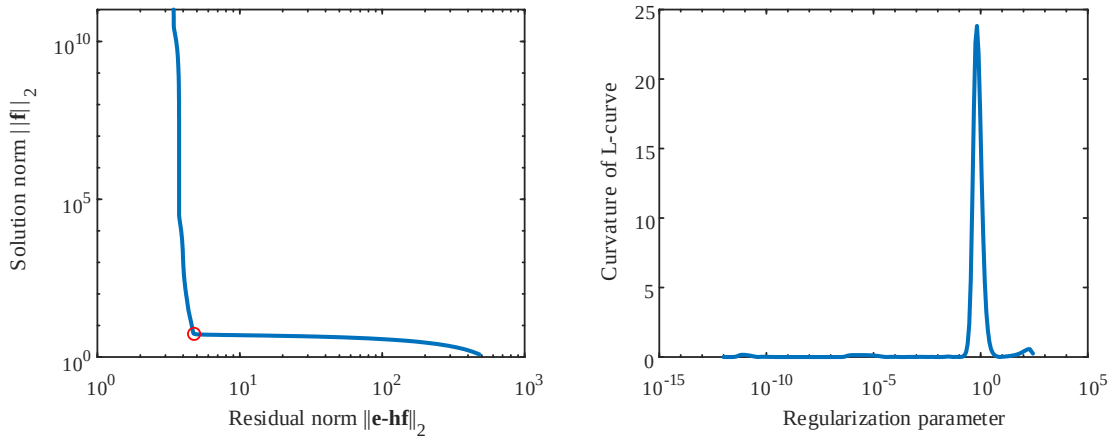

Figure 3.8. L-curve method to identify the parameter for l_2-norm regularization a) plot of the L-curve b) curvature of the L-curve versus the regularization parameter.

The comparison between the idealized half-sine force and the estimation result using wavelet deconvolution and the l_2-norm regularization is shown in Figure 3.9. In this simulation, the response signal is obtained by convolution between the impulse response (at position ($0.41L_x$, $0.22L_y$)) and the impact force ($1/3L_x$, $1/3L_y$). White Gaussian noise is added into the response signal with 30 dB SNR.

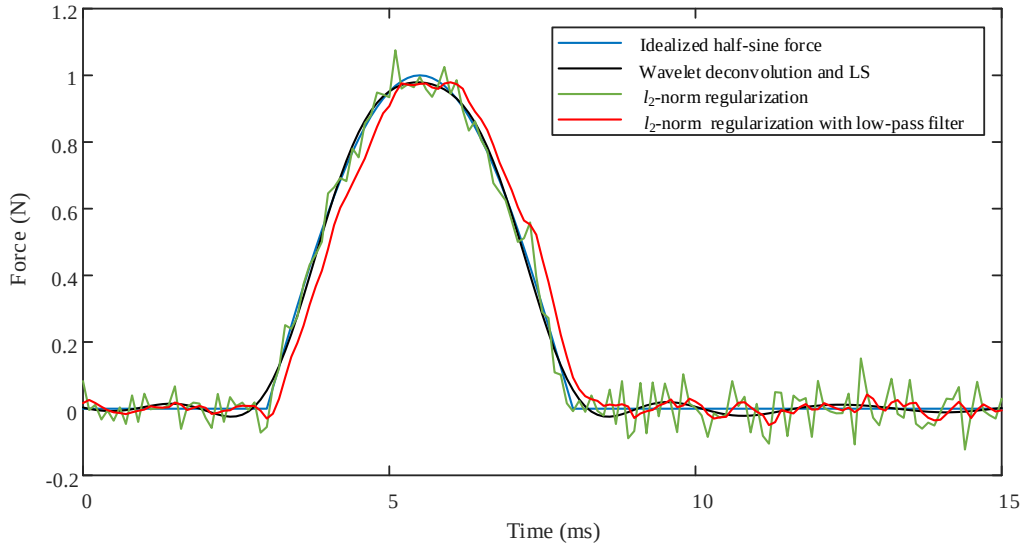

Figure 3.9. Comparison between the wavelet deconvolution method and the l_2 norm regularization.

The l_2-norm regularization is commonly used in inverse problems, however, for low SNR response signal, l_2 norm regularization is not reliable for the transient excitation because the solution is smoothed and supressed in the whole time history [92, 107]. As shown in Figure 3.9, combining the wavelet deconvolution method and the LSQR can estimate the impact force robustly against the additive noise. Conversely, the l_2 norm regularization method is more sensitive to noise. The small ripples in the l_2 norm regularization estimation curve occur due to high frequency components when the FRF is close to zero which is amplified by the added noise in the inverse process. Although those components can be supressed by choosing a larger regularization parameter, this leads to underestimation of the force,

particularly at low frequencies where the main energy of the impact force locates. An alternative solution is to filter out the high frequency components with a low-pass filter. However, there are two main disadvantages of using a low pass filter: 1) it will reduce the valid impact force components beyond the cut-off frequency, rather than those singular frequencies of the FRF only. Due to the Gibbs phenomenon [90] of the frequency domain expansion, the time history of the impact force can be inappropriately smoothed especially when there are sharp edges. 2) As shown in Figure 3.9, a low-pass filter can induce a phase shift or time delay in the impact force. Therefore, wavelet deconvolution is a more robust option to inversely estimate the force from the rain drop impact.

3.4.1.3 Implementation of wavelet deconvolution

As mentioned above, when the shifting factor and the scaling factor are optimally chosen, the system transfer matrix can be well-posed [33, 87, 88, 94, 95]. However, Doyle didn't provide the quantitative method to optimize these parameters. Hence in this thesis, the effect of scaling factor and the shifting factor on estimation has been assessed.

It is observed that when the structure is lightly damped, the wavelet deconvolution combined with the LSQR algorithm can improve the robustness of the inverse force estimation, thus in this section, two coefficients [86, 88, 95]: correlation coefficient and estimation relative error are utilized to assess the error of impact force identification using wavelet deconvolution and iterative LS algorithm.

$$\text{Correlation coefficient} = \frac{\text{cov}(\mathbf{f}, \hat{\mathbf{f}})}{\sigma_{\hat{\mathbf{f}}}\sigma_{\mathbf{f}}} \tag{3-22}$$

$$\text{Estimation error} = \frac{\left\|\mathbf{f} - \hat{\mathbf{f}}\right\|_2}{\|\mathbf{f}\|_2} \tag{3-23}$$

where cov(.) is the covariance and σ is the standard derivation.

In this section, three main factors are concerned: the scaling factor, the shifting factor, and the amplitude of additive white noise corrupted into the signal (assessed by SNR).

In single resolution one-dimensional wavelet deconvolution, if the scaling factor is chosen too small (approximately <3), the basis function will be close to a Dirac function, which doesn't improve the condition number of the transfer matrix. On the other hand, if the scaling factor gets too large (approximately >6), the high frequency

components of the impact force can be filtered out by the basis function. Therefore, it is critical to select the optimal scaling factor for the estimation accuracy. On the other hand, using a relatively larger shifting factor (approximately >2) can significantly decrease the size of the transfer function matrix, so that its condition number can be reduced. However, the shifting factor cannot be too large since the impact force may no longer be completely represented by the summation of a few basis functions.

For high SNR value, the optimal scaling factor or the pulse width of the basis function is selected to be relatively small, so that the solution can be more accurate due to the broader frequency range for calculation. As shown in Figure 3.10, a scaling factor around 3 is an optimal selection when the SNR is 30 dB. With a relatively small scaling factor, the shifting factor has an upper limit, because significant shifting of the single resolution wavelet basis function leads to the incapability of representing the force time history. In contrast, if the shifting factor is too small, the condition number of the transfer function cannot be reduced. Fortunately, when the scaling factor is small, increasing the shifting factor slightly can rapidly reduce the condition number, which improves the robustness of the solution.

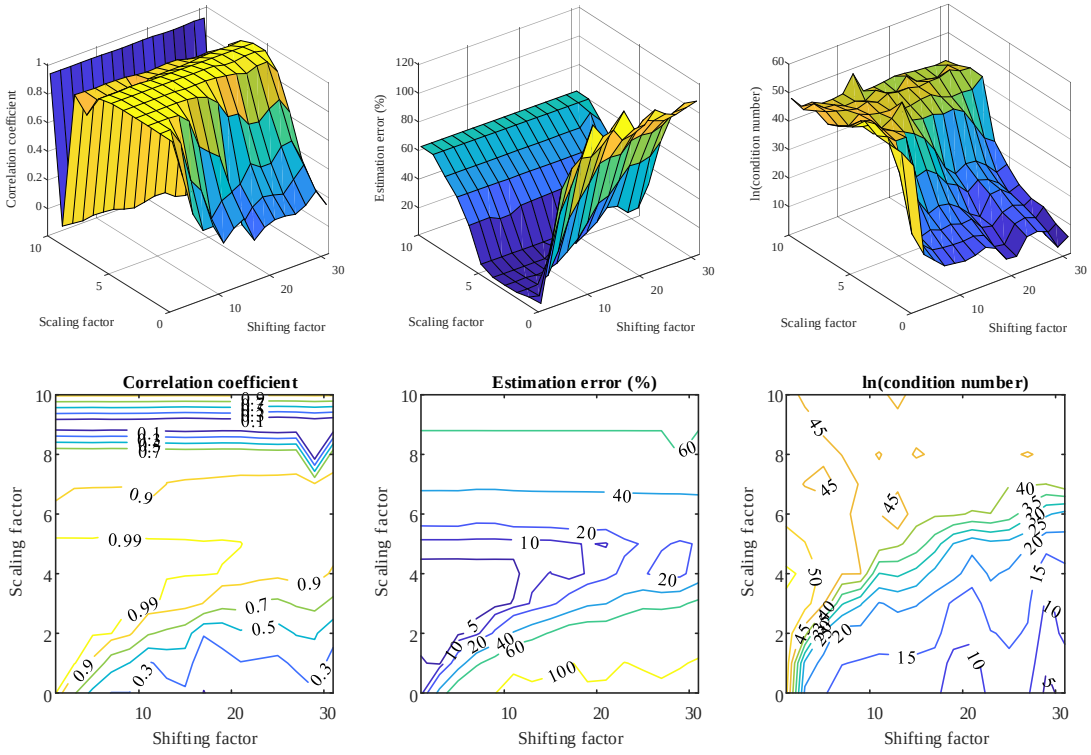

Figure 3.10. Optimal shifting factors and scaling factors for wavelet deconvolution and LS method assessed using the correlation coefficient (first column), estimation error (second column), and the condition number of the matrix in log scale (third column) when SNR is 30 dB. The first row shows the 3D plot and the second row shows the contour plot.

For 30dB SNR, when the scaling factor is selected as three and the shifting factor is 10, then the shift of the basis function corresponds to approximately half the pulse width as shown in Figure 3.11, which results in the same proposal made by Doyle *et al* [33].

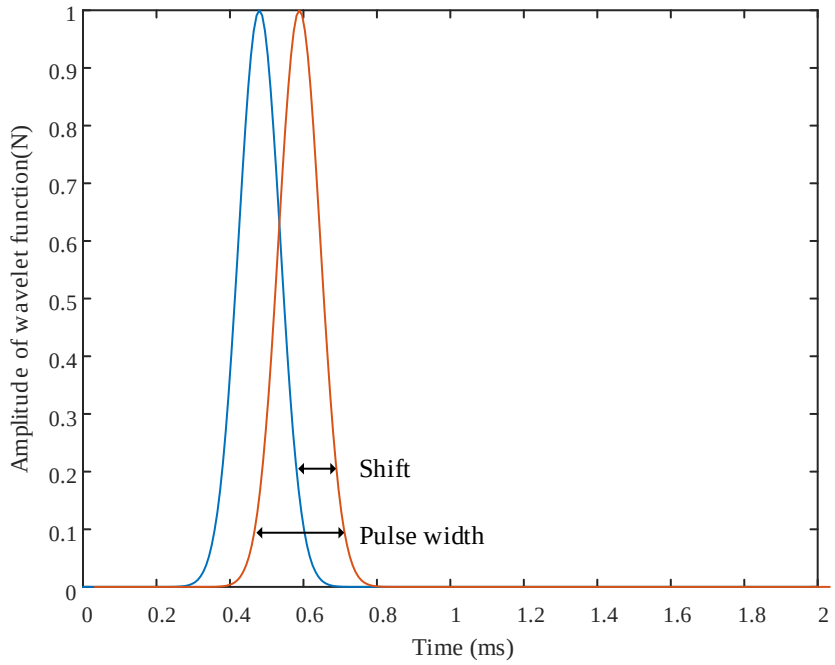

Figure 3.11. Relation between the optimal shift and pulse width for 30dB SNR.

Figure 3.12 shows the effect of these two factors on the estimation accuracy with 20 dB SNR for comparison with the previous 30 dB SNR. In Figure 3.12, although the condition number of the transfer matrix is the same as shown in Figure 3.10, it is replotted for viewing convenience. Compared with Figure 3.10, when the additive noise energy increases from 30 dB to 20 dB SNR, the optimal scaling factor gets slightly higher (approximately 4) to suppress the noise effect, in order to minimize the estimation error or maximize the correlation coefficient. For high SNR response signal, using a scaling factor of ≈ 3 can help to reduce the condition number by shifting the base functions slightly, which enhances the stability of solution process. However, for 20 dB SNR response signal, this can lead to an estimation error due to the noise effect on response signal. This is one of the reasons to use the

iterative LSE method together with the wavelet to improve the estimation robustness. The optimal scaling factor can be selected to be ≈ 4, although the condition number is not reduced significantly.

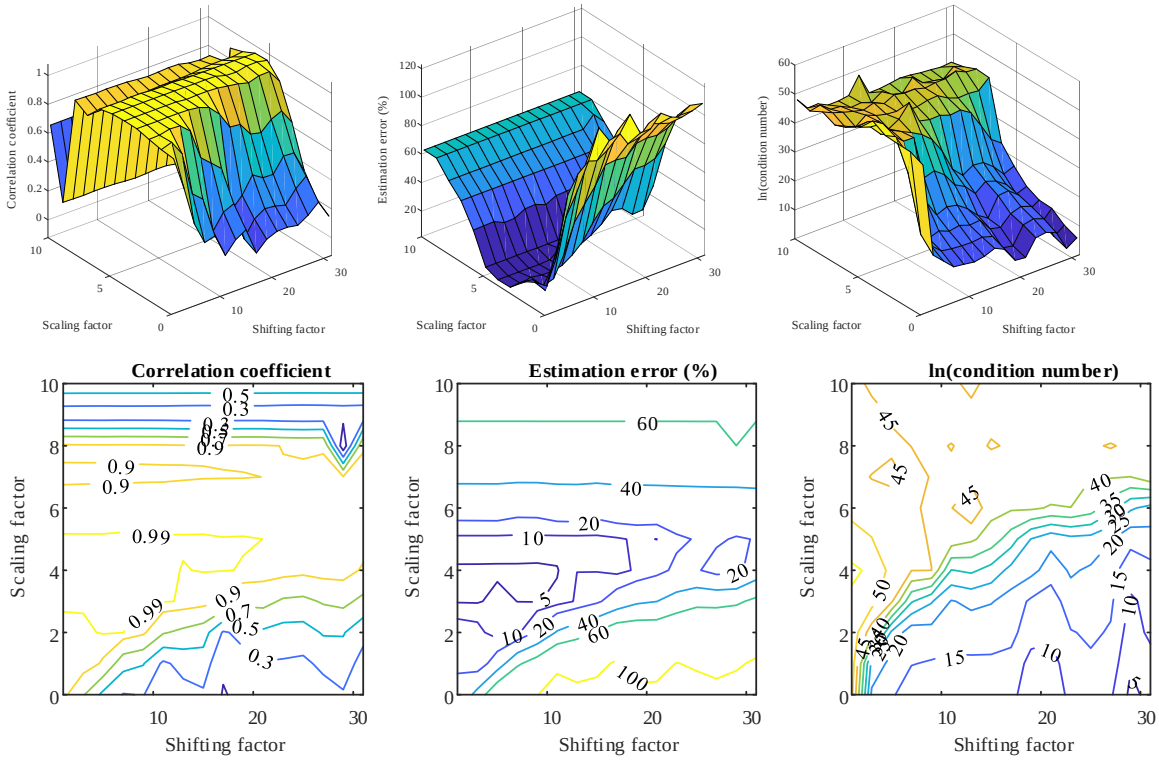

Figure 3.12. Optimal shifting factors and scaling factors for wavelet deconvolution and LS method assessed using the correlation coefficient (first column), estimation error (second column), and the condition number of the matrix in log scale (third column) when SNR is 20 dB. The first row shows the 3D plot and the second row shows the contour plot.

As shown in Figure 3.13, the optimal scaling factor becomes ≈5 when the SNR value decreases to 10 dB. This can be explained by interpreting the filtering effect in the frequency domain, as the pulse width of the basis function becoming longer with a higher scaling factor, which can consequently filter out more high frequency components from the noise.

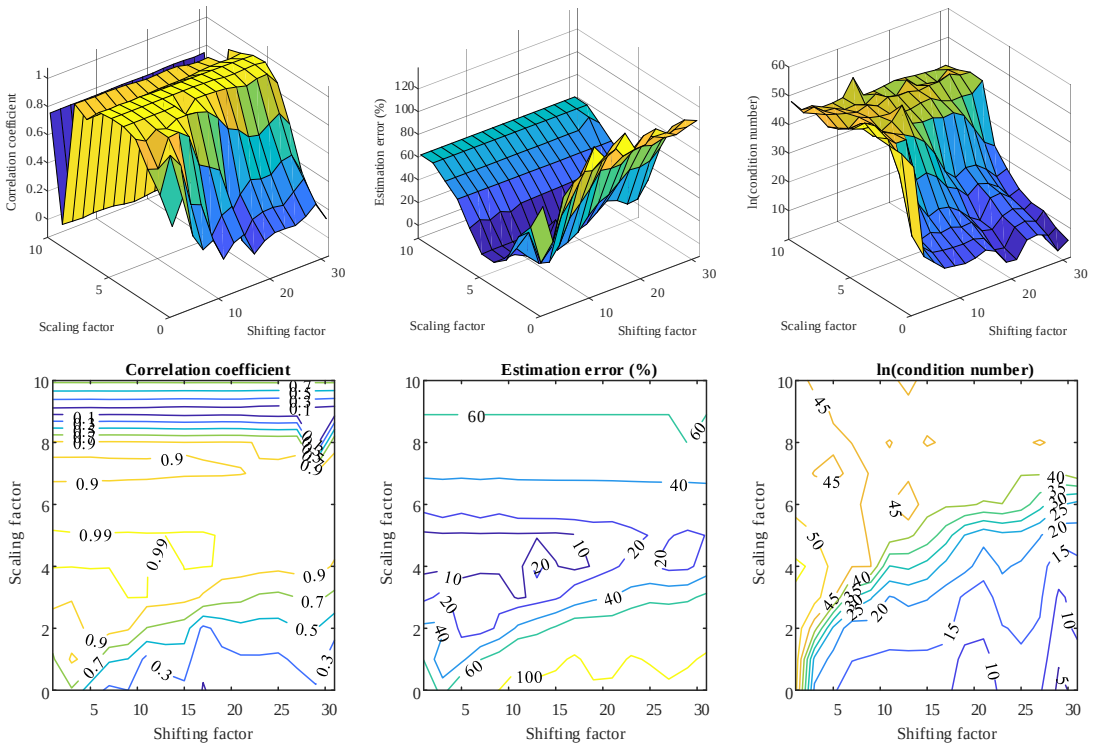

Figure 3.13. Optimal shifting factors and scaling factors for wavelet deconvolution assessed using the correlation coefficient (first column), estimation error (second column), and the condition number of the matrix in log scale (third column) when SNR is 10 dB. The first row shows the in 3D plot and the second row shows the contour plot.

It should be noted that these two coefficients from Eq. 3-22 and Eq. 3-23 are calculated using the time interval 50 ms, which is longer than the duration of the impact force pulse (5 ms). Most of the references [86, 88, 95] also used the relative error in a larger time scale than the force pulse width. There could be three reasons for this: 1) the estimation result out of the impulse duration to some extend reveals the stability of the deconvolution method, for instance the estimation of the impact force becomes unstable from the end of the pulse if using only $H_1(\omega) = \frac{S_{xy}}{S_{xx}}$ as the transfer function [120]; 2) the force and the shape of the force is unknown in most force identification cases, which makes it difficult to define the start and end point of the force (although in this research the force is classified to be the impulse force without much ringing); 3) some specific estimation procedures can shift, dilate or shrink the force pulse, meaning that the relative error cannot be calculated directly at the interval of the pulse width.

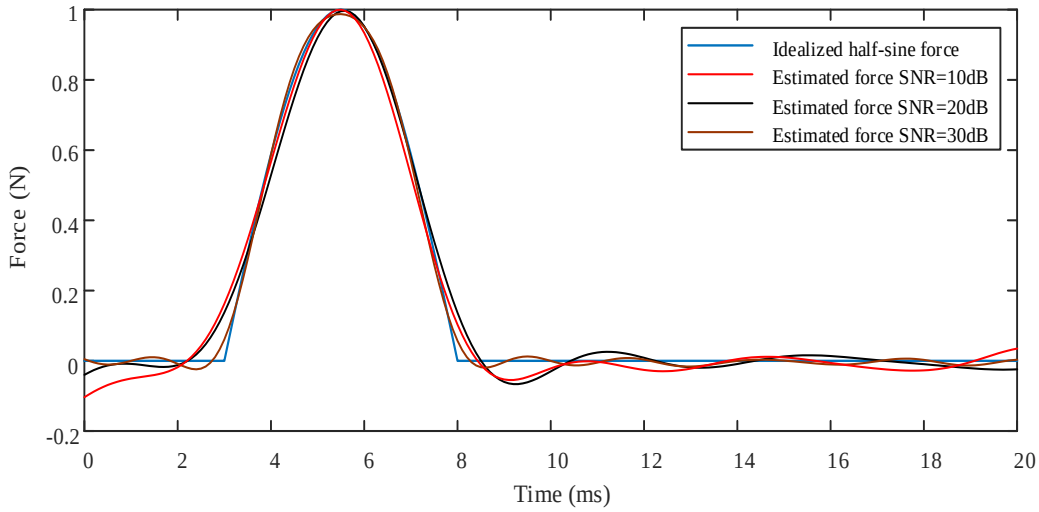

Figure 3.14. Comparison between the idealized half-sine force and the estimated force using wavelet deconvolution and LSE method using optimal scaling factor and shifting factor for different SNR values when only one sensor at ($0.41L_x$, $0.22L_y$) is used.

As shown in Figure 3.14, the estimation becomes more inaccurate with higher noise levels, and the estimated force pulse width gets longer than expected. This is because the optimal scaling factor gets larger with the increasing noise level in order to cancel the noise at high frequencies, which induces the Gibbs phenomenon and extend the length of the force pulse.

It is worth noting that wavelet deconvolution doesn't introduce new information for the system at anti-resonances. The reason that Doyle's wavelet deconvolution method can improve the robustness of the inverse problem is because the impact force has been smoothed at high frequencies by the basis function. If only one sensing position is measured to inversely estimate the single impact force which is also known as the even-determined case, the estimation using Doyle's wavelet may not be stable. Therefore, Doyle [33] suggests using multiple sensing positions to compensate for the lack of information of anti-resonances at each sensing position. This is particularly important for those anti-resonances within the frequency range of the impact force.

As shown in Figure 3.15, with 10 dB SNR, using three sensors at ($0.41L_x$, $0.22L_y$), ($0.21L_x$, $0.43L_y$) and ($0.36L_x$, $0.70L_y$) can improve the estimation results compared to only one sensor. The usage of multiple sensors compensates for the lack of information in the transfer matrix especially those anti-resonances.

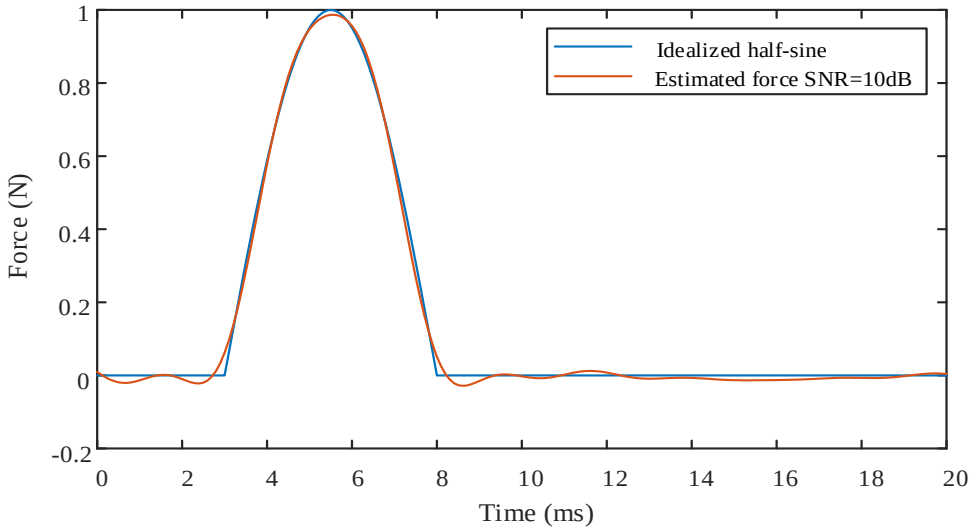

Figure 3.15. Comparison between the idealized half-sine force and the estimated force using wavelet deconvolution and LSE method using optimal scaling factor and shifting factor for 10 dB SNR when there are three sensors at ($0.41L_x$, $0.22L_y$), ($0.21L_x$, $0.43L_y$), and ($0.36L_x$, $0.70L_y$).

3.4.1.4 Summary

When the analysed structure is finite, the interference of reflecting waves may cause total loss of information at certain frequencies, i.e. at the anti-resonances in the frequency response function. A conventional Fourier transform can be problematic when the inverse calculation is implemented directly.

The advantage of the wavelet method is that the wavelet basis functions are finite in time which is suitable for a transient impact signal. Doyle's wavelet deconvolution [33] can be interpreted as suppressing the size of the ill-posed transfer matrix to reduce its condition number from the expansion on the basis functions (i.e. Doyle's bell shaped function [33]). According to Nyquist sampling principle, the time domain signal contains redundant information especially when the signal frequency range of the impact force is significantly less than the Nyquist frequency. Therefore, it is possible to filter off unnecessary high frequency components by expanding the impact force with a series of the basis function when the optimal scaling factor is selected. Moreover, increasing the shifting factor or decreasing the basis function overlap within a limited range can significantly compress the representation of impact force. Consequently, the condition number of the matrix expansion of the basis function can be significantly reduced.

There exist optimal scale and shift factors for the estimation process. The optimal scaling factor can be determined from the requirement that the frequency bandwidth of the basis function should exceed that of the impulse and response signal. The shift must correspond approximately to half of the width of the pulse Doyle *et al* [33].

Although wavelet deconvolution helps to reduce the condition number of the transfer matrix, combining the wavelet deconvolution with iterative LSE method can be more robust towards Gaussian noise. Using multiple sensors is also necessary to improve the stability and accuracy for the estimation.

3.4.2. Simulation of sparse representation using different wavelet dictionaries

In order to determine the water drop impact force with a sharp edge at the initial impact phase using low SNR response signal (in Chapter 6 it will be shown that this is particularly important for 2 mm drops impacting at a drop velocity 2.57 m/s), sparse representation algorithms have been utilized in this section. Recently the sparsity representation method with dictionaries based on l_1 norm [92, 97, 98] regularization has been investigated on force time history estimation. It has been concluded that using the l_1 norm regularization can lead to more robust estimation results than using l_2 norm regularization especially for low SNR response. However, the l_1 norm regularization can lead to an underestimate solution of the force. Existing applications of sparse representation for force time history estimation are based on the l_1 norm regularization in literatures; hence this thesis also applies non-convex optimization such as l_0 norm, $l_{1/2}$ norm regularizations. The algorithms for different regularization methods using different orthogonal wavelet basis function (*sym2*, *coif1* and *db2*) will also be shown in this section.

3.4.3.1 Selection of the optimal wavelet dictionary

Selecting an effective dictionary can affect the accuracy of the reconstructed force. In order to select an optimal dictionary, the classic result on linear approximation of random vector process is reviewed first. Consider a vector process $\boldsymbol{X} = [\boldsymbol{X}_0, \boldsymbol{X}_1 \ldots \boldsymbol{X}_{N-1}]^T$, where $\boldsymbol{X}$ is an independent identically distributed (IID) process with zero mean $E[\boldsymbol{X}_i] = 0$, and the covariance $E[\boldsymbol{X} \cdot \boldsymbol{X}^T] = \boldsymbol{R}_{\boldsymbol{X}}$, assumed that $\boldsymbol{R}_{\boldsymbol{X}}$ is known as a prior.

Consider now the linear representation of the vector process using an orthonormal basis or dictionary atoms, $\{\boldsymbol{w}_0, \boldsymbol{w}_1 \ldots \boldsymbol{w}_{M-1}\}, M < N$, therefore the approximation of $\boldsymbol{X}$ can be given by [121]:

$$\widehat{\boldsymbol{X}}_M = \sum_{m=0}^{M-1} < \boldsymbol{w}_m, \boldsymbol{X} > \boldsymbol{w}_m \qquad 3\text{-}24$$

where $<\cdot>$ denotes the inner product of two vectors. The approximation error can then be written as [121]:

$$\left\|\boldsymbol{X} - \widehat{\boldsymbol{X}}\right\|_2^2 = \sum_{m=M}^{N-1} \boldsymbol{w}_m^T \boldsymbol{X}\boldsymbol{X}^T \boldsymbol{w}_m \qquad 3\text{-}25$$

Therefore, the mean square error can be expressed as:

$$E\left[\left\|\boldsymbol{X} - \widehat{\boldsymbol{X}}\right\|_2^2\right] = \sum_{m=M}^{N-1} \boldsymbol{w}_m^T E[\boldsymbol{X}\boldsymbol{X}^T]\boldsymbol{w}_m = \sum_{m=M}^{N-1} \boldsymbol{w}_m^T \mathbf{R}_X \boldsymbol{w}_m \qquad 3\text{-}26$$

Given the covariance matrix of the vector process, the best basis can be chosen as the set of eigenvectors of $\mathbf{R}_X$ ordered with decreasing eigenvalues [121]. The geometric intuition behind this result is that the eigenvectors are the principal axes of the *N*-dimensional distribution and the best *M*-dimensional subspace gathering most energy corresponds to the principal axes with largest eigenvalues [121].

Since the prior knowledge of the covariance matrix of the force is generally unknown, it is necessary to propose another method to select the optimal basis. A common dictionary optimization method is dictionary learning methods that is motivated from sparse representation, such as K-SVD algorithm [104]. However, unlike the application in compressive sensing of minimizing the number of atoms so that the data can be most effectively represented, the impact force identification concerns the estimation stability and accuracy. Another method to choose the optimal base function is proposed by Coifman and Wickerhauser [122], using an entropy-based algorithm to adaptively pick a single orthogonal best-basis from many bases function. However, when the signal is composed of a moderate number of highly non-orthogonal components, the method may not deliver sparse representations [123].

If there is any prior information or experience of the force time history shape, this can be used to select the dictionary. For example, Pan *et al* [111] used the over-complete dictionary that consist both of the discrete trigonometric functions and

discrete rectangular functions so that the main features of the moving loads on the bridge are closely fitted. This can be understood intuitively by selecting the dictionary atoms that have a similar shape to the objective force curve. Furthermore, the optimal basis should have the minimum direction difference to the principal axes of the *N*-dimensional vector. Because cross correlation coefficient can be interpreted as the cosine function of the angle between the vectors, therefore, it is reasonable to choose this parameter to select the optimum dictionary. For example, Singh *et al* [124] used the maximum cross correlation between an ECG signal and the selected wavelet filter to determine the selection of the optimal wavelet.

In this section, the estimated impact force from Petersson's [4] paraboloidal drop shape model of 4.5mm diameter drop at terminal velocity is used to calculate the correlation with the wavelet dictionaries. In this section, the correlation coefficient (using Eq. 3-22) between the estimated force and the wavelet reconstructed force with the largest 15 wavelet decomposition coefficients was calculated using orthogonal wavelet basis functions in Matlab. As an illustration, Figure 3.16 shows the first order *coif* wavelet function, *coif1* which is orthogonal with compact support.

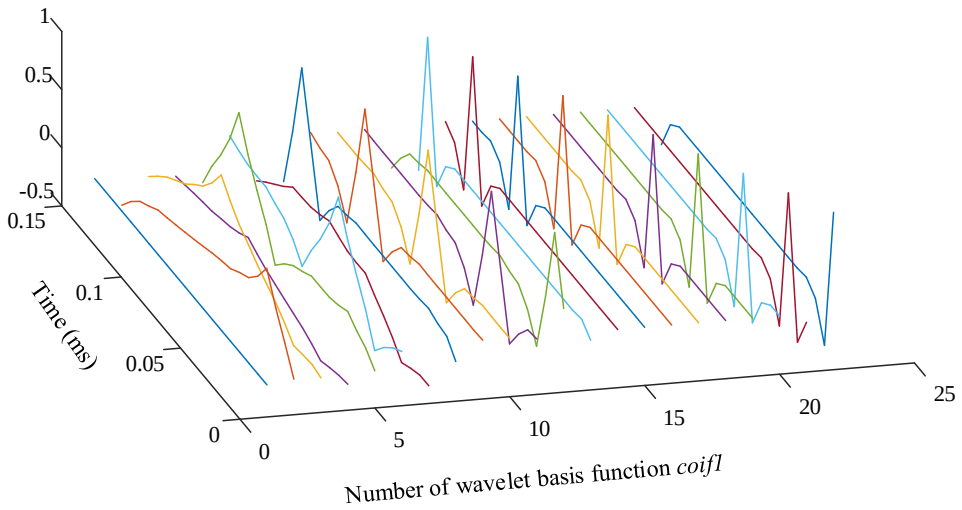

Figure 3.16. First order basis functions of *coif1*

In Figure 3.17(b), the additional information of the reconstruction error (Eq. 3-23) is presented. The correlation coefficient achieves the maximum value using the first order of *coif* wavelet function, which corresponds to the minimum value of the reconstruction error. As shown in Figure 3.17, using *db2* or *sym2* wavelet gives suitable representation. Therefore, in this section, these three wavelet filters have

been used in simulation to assess the validity of the approach for the optimal wavelet function selection.

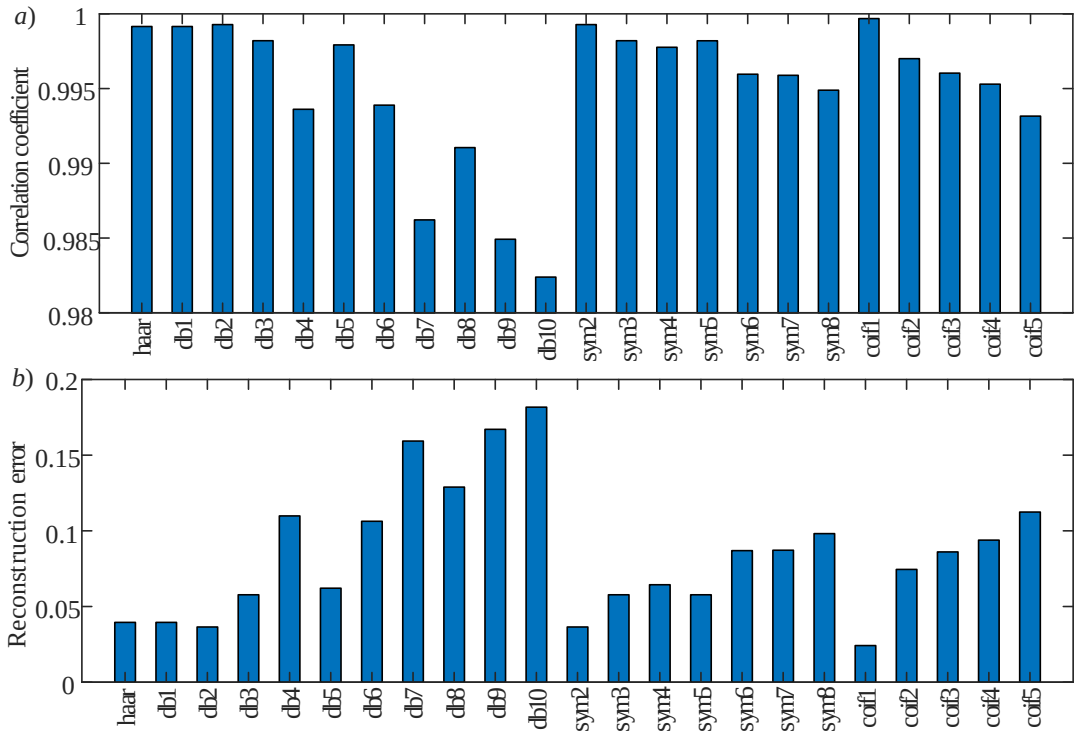

Figure 3.17. Cross correlation coefficient *a*) and the reconstruction error *b*) between the estimated impact force and the wavelet reconstructed force with the largest 15 wavelet coefficients.

3.4.3.2 Algorithms used for sparse representation

The algorithms of the sparse representation used in this thesis are introduced in this section. Since the impact force is of finite non-zero duration, which can be well fitted with wavelet dictionary, using the orthogonal wavelet can improve the sparsity than Fourier transform or the Dirac basis. In this section, the algorithms of SpaRSA (for l_1-norm regularization), IHT (for l_0-norm regularization), and half-thresholding (for $l_{1/2}$-norm regularization) with the wavelet dictionary representation have been summarised in Table 3-2, Table 3-3 and Table 3-4.

Table 3-2. Algorithm of Sparse Reconstruction by Separable Approximation (SpaRSA [108]) for l_1-norm regularization

Task: To solve the problem $\hat{\boldsymbol{f}} = \arg\min \frac{1}{2}\|\mathbf{hW}\boldsymbol{\alpha} - \boldsymbol{e}\|_2^2 + \lambda\|\boldsymbol{\alpha}\|_1$
Input: Response signal $\boldsymbol{e}$, transfer matrix $\mathbf{h}$, wavelet dictionary $\mathbf{W}$, parameter $\lambda = 0.001$
Initialization: k=1, $\mathbf{A} = \mathbf{hW}$, $\boldsymbol{e}_1 = \boldsymbol{e}$, $\tau_1\mathbf{I} = \mathbf{A}^T\mathbf{A}$, tolerance $\varepsilon = 10^{-5}$
Iteration: 1. $\lambda_k = \max\{0.2\|\mathbf{A}^T\boldsymbol{e}_k\|_\infty, \lambda\}$.
2. Exploit soft shrinkage: $\boldsymbol{\alpha}_{k+1} = soft(\boldsymbol{\alpha}_k - \mathbf{A}^T(\mathbf{A}\boldsymbol{\alpha}_k - \boldsymbol{e})/\tau_k, \lambda/\tau_k)$ (where $\text{soft}(s_i, \lambda) = \text{sign}(s_i)\max\{|s_i| - \lambda, 0\}$)
3. Update the step size: $\tau_k = \frac{(\boldsymbol{\alpha}_{k+1}-\boldsymbol{\alpha}_k)^T(\nabla\vartheta(\boldsymbol{\alpha}_{k+1})-\nabla\vartheta(\boldsymbol{\alpha}_k))}{(\boldsymbol{\alpha}_{k+1}-\boldsymbol{\alpha}_k)^T(\boldsymbol{\alpha}_{k+1}-\boldsymbol{\alpha}_k)}$
4. If $\frac{\|\boldsymbol{\alpha}_{k+1}-\boldsymbol{\alpha}_k\|}{\boldsymbol{\alpha}_k} \leq \varepsilon$, go to step 5**.** Otherwise, return to step 2
5. $\boldsymbol{e}_{k+1} = \boldsymbol{e} - \mathbf{A}\boldsymbol{\alpha}_{k+1}$
6. If $\lambda_k = \lambda$, stop**;** Otherwise k=k+1, and return to step 1.
Output: $\hat{\boldsymbol{f}} = \mathbf{W}\boldsymbol{\alpha}_k$

Table 3-3. Iterative Hard Thresholding Algorithm **(**IHT [118]) for l_0-norm regularization .

Task: To solve the problem $\hat{\boldsymbol{f}} = \arg\min \frac{1}{2}\|\mathbf{hW}\boldsymbol{\alpha} - \boldsymbol{e}\|_2^2 + \lambda\|\boldsymbol{\alpha}\|_0$
Input: Response signal $\boldsymbol{e}$, transfer matrix $\mathbf{h}$, wavelet dictionary $\mathbf{W}$, step size $\mu = 0.001$, sparse level K
Initialization: k=1, $\mathbf{A} = \mathbf{hW}$, $\boldsymbol{e}_0 = \boldsymbol{e}$, $\mathbf{I}/\tau_0 = \mathbf{A}^T\mathbf{A}$, tolerance $\varepsilon = 10^{-5}$
While not converged do: 1. $\boldsymbol{\alpha}_{k+1} = hard(\boldsymbol{\alpha}_k + \mathbf{A}^T(\boldsymbol{e} - \mathbf{A}\boldsymbol{\alpha}_k))$ where $hard(x)$ is the non-linear operator that sets all but the largest (in magnitude) K elements of x to zero 2. k=k+1
Output: $\hat{\boldsymbol{f}} = \mathbf{W}\boldsymbol{\alpha}_k$

Table 3-4. Half Proximal Thresholding Algorithm ([116, 117]).

Task: To solve the problem $\hat{\boldsymbol{f}} = \arg\min \frac{1}{2}\|\mathbf{hW}\boldsymbol{\alpha} - \boldsymbol{e}\|_2^2 + \lambda\|\boldsymbol{\alpha}\|_{1/2}^{1/2}$
Input: Response signal $\boldsymbol{e}$, transfer matrix $\mathbf{h}$, wavelet dictionary $\mathbf{W}$, parameter $\lambda = 0.001$, sparse level K
Initialization: k=1, $\mathbf{A} = \mathbf{hW}, \varepsilon = 10^{-2}, \tau = \frac{1-\varepsilon}{\|\mathbf{A}\|^2}$
While not converged do:
1. $\boldsymbol{\theta}(\boldsymbol{\alpha}_k) = \boldsymbol{\alpha}_k - \tau\mathbf{A}^{\boldsymbol{T}}(\mathbf{A}\boldsymbol{\alpha}_k - \boldsymbol{e})$
2. $\lambda_k = \frac{\sqrt{96}}{9\tau}\|[\boldsymbol{\theta}(\boldsymbol{\alpha}_k)]\|^{\frac{3}{2}}$
3. The representation solution is solved by $\boldsymbol{\alpha}_{k+1} = half\big(\boldsymbol{\theta}(\boldsymbol{\alpha}_k)\big)$, where $half(s_i) = \begin{cases} g_{\lambda,\frac{1}{2}}(s_i), & \text{if } \lvert s_i\rvert > \frac{\sqrt[3]{54}}{4}(\lambda\tau)^{\frac{2}{3}} \\ 0, & \text{otherwise} \end{cases}$, $g_{\lambda,\frac{1}{2}}(s_i) = \frac{2}{3}s_i\left[1 + \cos\left(\frac{2\pi}{3} - \frac{2}{3}g_\lambda(s_i)\right)\right]$, $g_\lambda(s_i) = \arccos\left(\frac{\lambda}{8}\left(\frac{\lvert s_i\rvert}{3}\right)^{-\frac{3}{2}}\right)$
4. k=k+1
Output: $\hat{\boldsymbol{f}} = \mathbf{W}\boldsymbol{\alpha}_k$

3.4.3.3 Comparison between different regularization methods

This section compares three different sparse representation methods with l_2 norm regularization in simulation. The transfer matrix is obtained based on a modal summation [7] for a simply supported glass plate (the properties are shown in) using 10000 mode shapes between 10 to 10k Hz. An idealized transient force is used to simulate the drop impact excitation from a paraboloidal drop shape model [4] with a second order low-pass Butterworth filter (cut-off at 10k Hz).

As shown in Figure 3.18, for high SNR response signal (30 dB SNR), sparse representation (with l_1-norm, l_0-norm and $l_{1/2}$-norm) methods can lead to more accurate results than l_2-norm regularization, especially at the sharp rising edge. Additionally, from l_2-norm regularization method, the estimation result contains ringing after the force pulse whereas the sparse representation results are zero. This is because the penalty function of l_1-norm, l_0-norm and $l_{1/2}$-norm in Eq. 3-20 induce sparsity into the solution which concentrates the energy of the time-dependent force within a short period. However, the l_2-norm regularization under the Gaussian

distribution assumption of the force has a smoothing effect over time. This smooth effect results in the underestimate of the force and the ringing before and after the force pulse.

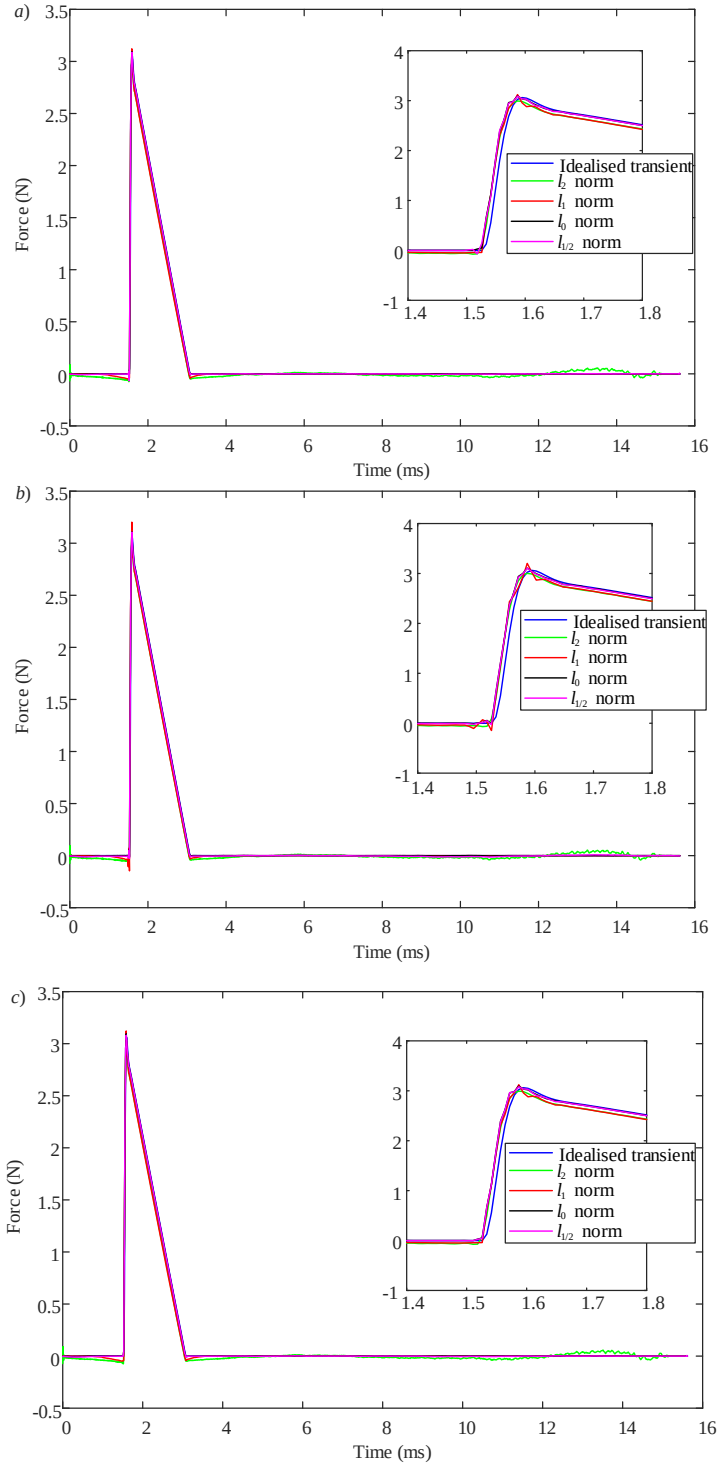

Figure 3.18. Representation of the impact force using different regularization algorithms with the wavelet dictionaries (a) *sym2*, b) *coif1*, c) *db2* when the SNR is 30 dB.

In Figure 3.19, the correlation coefficient (between the idealized transient force and the estimated force) and the estimation error is presented. Compared to l_1-norm regularization, l_0 –norm and $l_{1/2}$-norm regularization have lower estimation error, although the correlation coefficient of l_0 -norm using the *db2* dictionary is slightly higher than the other two sparse representation methods. The reason that the non-convex regularization ($l_{1/2}$-norm, and l_0 –norm regularization) gives better estimates is possibly because the iteration of these algorithms is stopped when the objective function starts to increase so that the solution is stable.

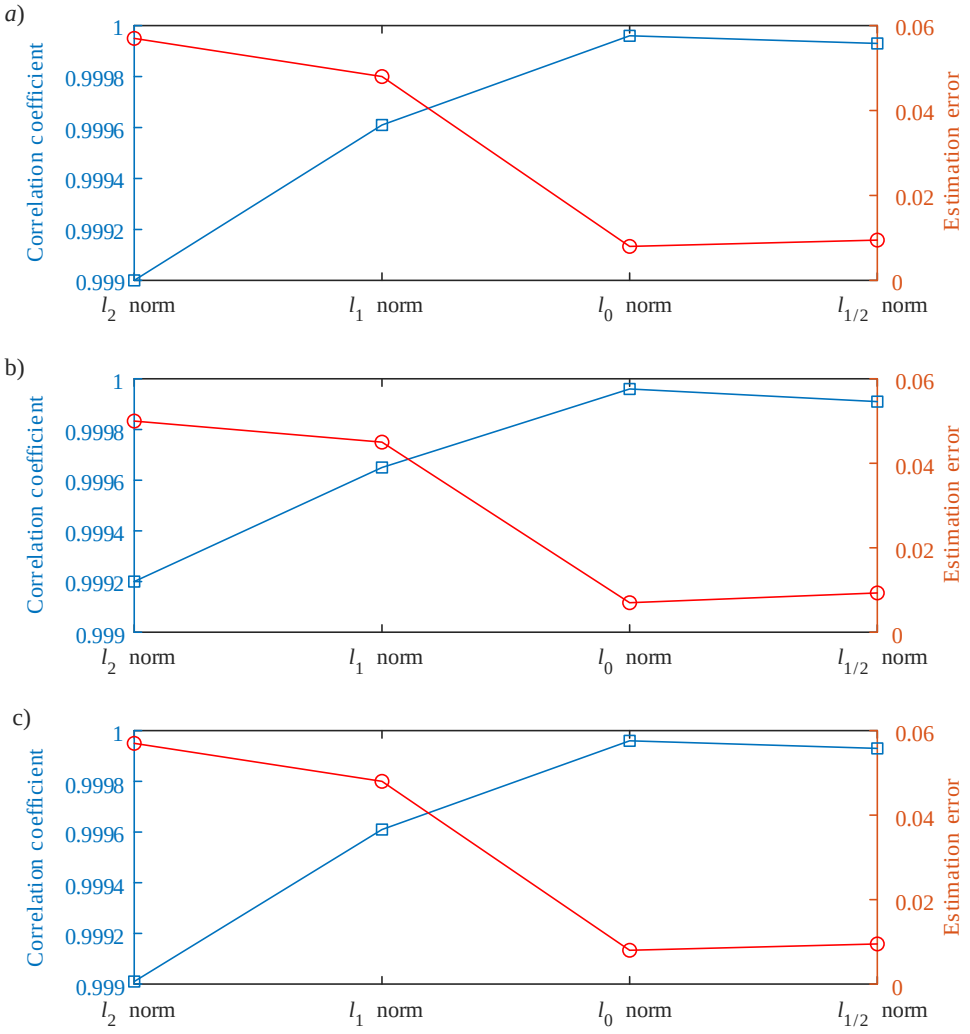

Figure 3.19. Correlation coefficient and estimation error between the idealised transient force and the represented force using different regularization algorithms with the wavelet dictionaries a) *sym2*, b) *coif1*, c) *db2* when the SNR is 30 dB.

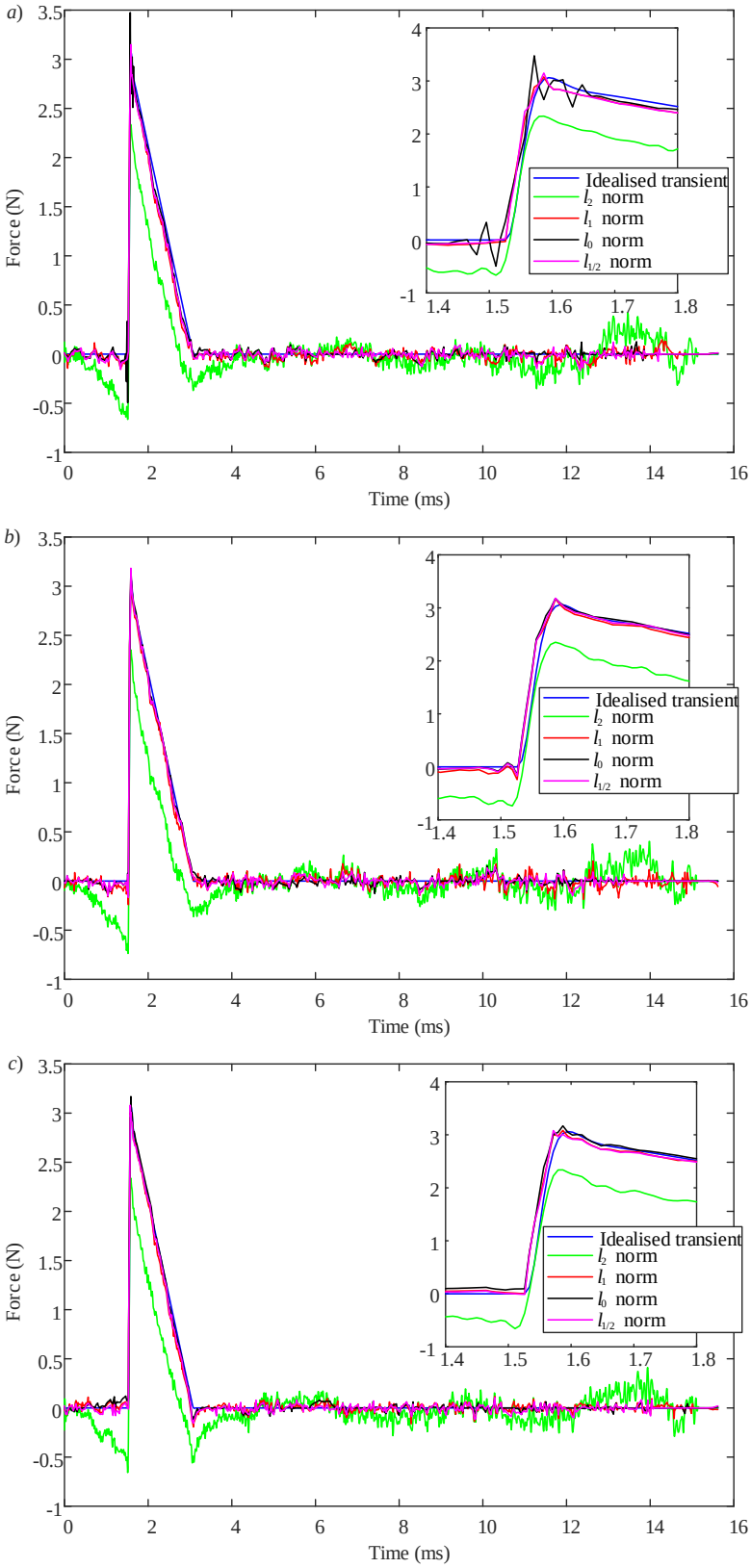

Figure 3.20. Representation of the impact force using different regularization algorithms with the wavelet dictionaries (a) *sym2,* b) *coif1*, c) *db2* when the SNR is 10 dB.

When the noise becomes more significant with 10dB SNR, the result from the l_2 –norm regularization underestimates the force peak because the regularization

parameter was chosen by the L-curve method to compromise the trade-off of suppressing noise. However, sparse representation is much more robust towards noise, and the *coif1* wavelet basis function can estimate the impact force shape with the lower error, which confirms its selection as an optimal wavelet.

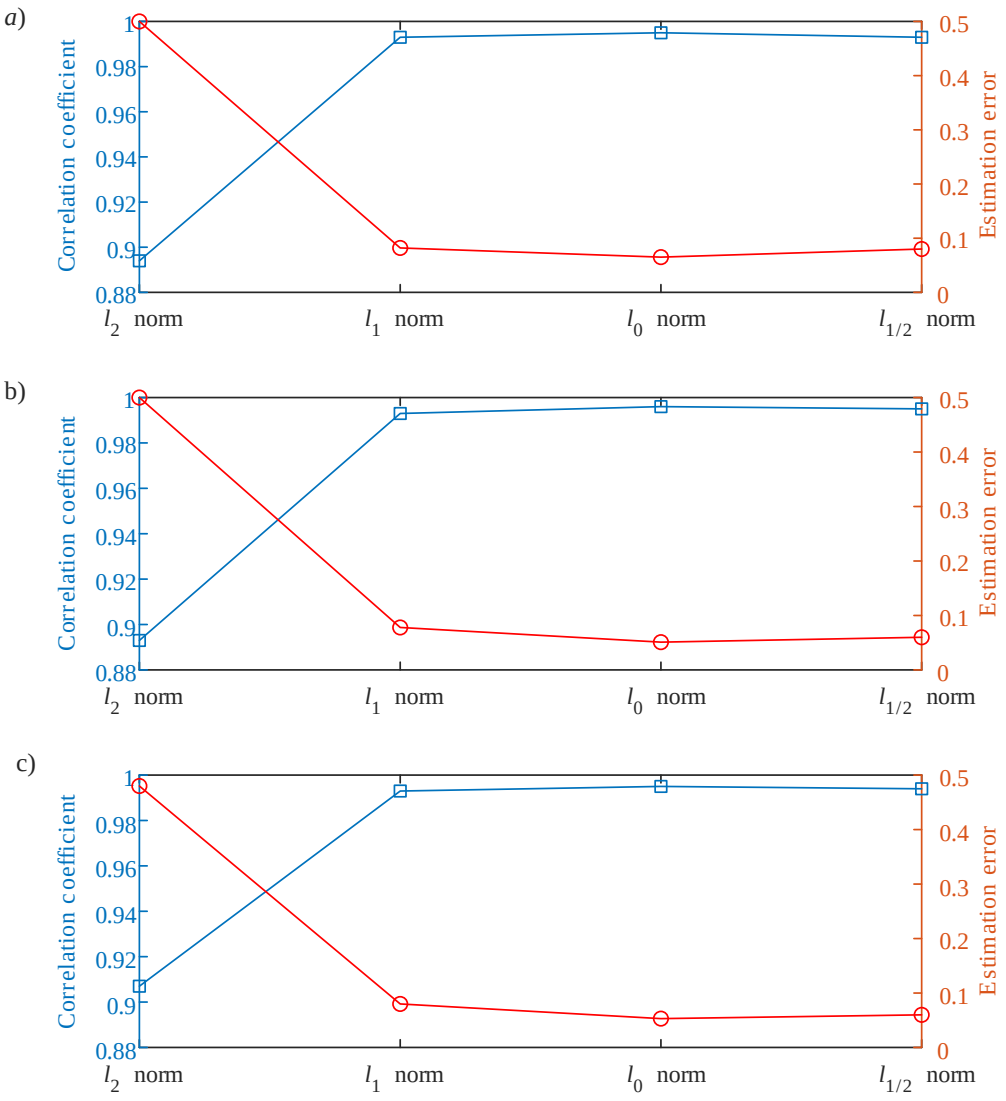

Figure 3.21. Correlation coefficient and the estimation error between the idealised transient force and the represented force using different regularization algorithms with the wavelet dictionaries (a) *sym2*, b) *coif1*, c) *db2* when the SNR is 10 dB.

3.4.3.4 Summary

In this section, the simulation of the sparse representation with three dictionaries has been implemented. The correlation coefficient between the idealized time-dependent force and the reconstructed force using the largest 15 wavelet

decomposition coefficients has been proposed to select the optimal wavelet basis function for force identification, and this has been tested with an idealised paraboloidal drop shape model. The estimation results show that with low or high SNR response signal, the sparse representation estimation with l_0-, l_1- and $l_{1/2}$-norm regularization using dictionaries is more robust towards noise and edge-preservation of a transient than using l_2 norm regularization. Compared with the l_1- and $l_{1/2}$-norm regularization, the l_0-norm regularization has closer agreement with the idealized force curve.

3.5. Conclusions

This chapter describes the inverse methods for force identification used in this thesis. Since the conventional time domain method is computationally inefficient and the frequency domain method has leakage problems, the time domain method based on wavelet theory has been investigated.

Doyle's approach to wavelet deconvolution has been validated using simulation. The optimal sensing positions are assessed using the condition number of the transfer matrix which indicates that response positions away from the excitation position lead to similar condition numbers. Three random selected positions will be used in the raindrop impact force experiment. Selecting the optimal scaling factor and the shifting factor of the wavelet basis function can significantly improve the ill-conditioned problem of the transfer matrix and provide superior solution than the Tikhonov method. Doyle's wavelet method incorporating the LSQR algorithm will be used in the water drop impact force identification experiment.

Sparse representation methods using l_0-, l_1- and $l_{1/2}$-norm regularization with dictionaries have been investigated in simulation, which shows more accurate and robust estimation results compared with the l_2-norm regularization methods particularly when the response signal has low SNR. Furthermore, l_0-norm regularization gives the closest estimate for the idealized time-dependent force curve compared with l_1- and $l_{1/2}$-norm regularization. Therefore, the l_0-norm regularization will be applied in the water drop impact force experiments for 2mm drops impacting at low velocity (2.57 m/s) where the SNR is the lowest. In this chapter, a method of maximizing the correlation coefficient has been proposed for the selection of the optimal wavelet function; hence the optimal wavelet basis function *coif1* will be used for the experimental force reconstruction.

4. Prediction of sound radiation from point-excited plates

4.1. Introduction

In this thesis, the prediction of sound radiation from point excited plates is considered using SEA for an isotropic, homogeneous plate and a more flexible model, TMM that can be used for a multilayer plate.

The prediction of vibration and sound radiation using SEA is described in Section 4.2, and in Section 4.3 using the TMM method for the specific multilayer plate of a plate-foam-plate structure.

The calculation of radiated sound power from infinite plates is described in Section 4.4, and from finite plates in Section 4.5, where the travelling wave method has been used to obtain an order reduced integral that can improve computational efficiency.

4.2. SEA for vibroacoustics prediction of homogeneous isotropic plates

SEA was introduced in the 1960s and is a framework of analysis for predicting the transmission of sound and vibration between coupled spaces and structures [49]. SEA uses a statistical approach based on temporal and spatial averages and therefore it doesn't require detailed geometrical information. This approach is suitable to multi-modal systems, where the eigen-frequencies and eigen-functions can be sensitive to small perturbations in the structural geometry and material properties, but there is uncertainty in this information at the design stage. SEA is based on frequency domain analysis using spatial averaged energy as the primary variable, which is convenient for the analysis of temporally and spatially random excitation points on plates, such as with rain noise problems. In this thesis, a two-subsystem SEA model is required for structural vibration and sound radiation prediction as shown in Figure 4.1 for a plate excited by rainfall that radiates into an enclosed volume of air.

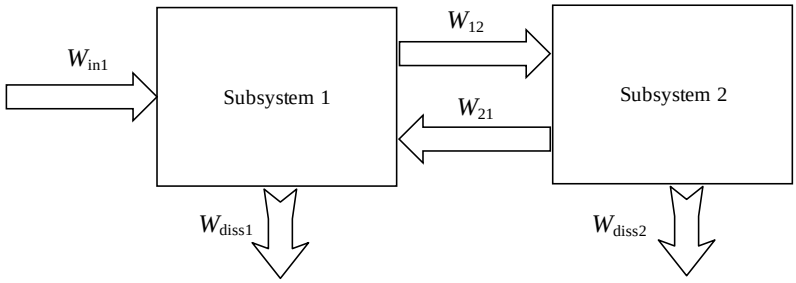

Figure 4.1. Two subsystem SEA model.

SEA requires knowledge of the power input into the subsystems, and the fraction of energy transferred per radian cycle in the form of loss factors. From conservation of energy, the power balance equation for subsystems 1 and 2 is [49]:

$$W_{\text{in1}} + \omega\eta_{21}E_2 = \omega\eta_{11}E_1 + \omega\eta_{12}E_1 \quad 4\text{-}1$$

$$\omega\eta_{12}E_1 = \omega\eta_{22}E_2 + \omega\eta_{21}E_2 \quad 4\text{-}2$$

where E_1 and E_2 are the energies of subsystems 1 and 2, respectively. There are three types of loss factors to be defined: total loss factors for each subsystem (i.e. η_1 and η_2), coupling loss factors between subsystems (i.e. η_{12} and η_{21}), and internal loss factors for each subsystem (i.e. η_{11} and η_{22}). Internal loss factors give rise to the dissipated power as shown in Figure 4.1 (i.e. W_{diss1} and W_{diss2}).

The power input W_{in1} represents the power injection from continuous rainfall excitation into subsystem 1 which represents the plate where subsystem 2 represents the enclosed volume of air into which the plate radiates. Equations 4-1 and 4-2 can be solved to determine the energy of the plate and room to give the vibration and sound pressure respectively.

Assuming that the energy returning from the air volume to the vibrating structure is negligible $\omega\eta_{21}E_2 = 0$, and the total loss factor ($\eta_1 = \eta_{11} + \eta_{12}$) of the plate can be measured, then Eq. 4-1 can be rewritten as:

$$W_{\text{in1}} = \omega\eta_1 E_1 \quad 4\text{-}3$$

where

$$E_1 = m\langle v^2 \rangle \quad 4\text{-}4$$

where $\langle v^2 \rangle$ denotes the mean-square velocity of the plate. Therefore, the radiated sound power, W_{12} is given by:

$$W_{12} = \omega\eta_{12}E_1 = \eta_{12}\frac{W_{\text{in1}}}{\eta_1} \quad 4\text{-}5$$

Note that Eq. 4-5 for the radiated sound power can be derived without using SEA theory, since the energy returning from subsystem 2 has been ignored. The impedance of the source can affect the power input to the plate [7]. For excitation by artificial or natural rainfall, the power input into a plate with driving-point impedance Z_{dp} is calculated by [4]:

$$W_{\mathrm{in1}} = \frac{N(D)S|F(\omega)|^2}{Z_{\mathrm{dp}} + Z_{\mathrm{f}}} \tag{4-6}$$

where $N(D)$ is the number of drops that fall on a unit area per unit time (in /m^{2}s) given by Eq. 2-3 for natural rainfall, S is area of the plate surface, $|F(\omega)|^2$ is the auto-spectrum of the single raindrop impact, Z_{f} is the flow impedance of the drop [4]:

$$Z_{\mathrm{f}} = \rho_{\mathrm{w}}\pi r^2 v_{\mathrm{d,T}} \tag{4-7}$$

whereρ_{w} is the density of water, r is the radius of the equivalent spherical drop and $v_{\mathrm{d,T}}$ is the terminal velocity of the raindrops.

For a thin plate of infinite extent, the driving-point impedance for excitation of bending waves is given by [7]:

$$Z_{\mathrm{dp}} = 2.3\rho c_{\mathrm{L}} h^2 \tag{4-8}$$

where c_{L} is the longitudinal wave speed of the plate, ρ is the density of the plate and h is the thickness of the plate.

The total loss factor of a plate η_1 is usually obtained from measurement, and the coupling loss factor from a plate to the surrounding fluid on one side can be predicted by the radiation efficiency. The radiation efficiency, σ, is defined as the ratio of the radiated acoustic power from the plate to that of a large baffled piston of radius a vibrating with the same average mean-square velocity where $k_0 a \gg 1$ [48].

$$\sigma = \frac{W_{12}}{\rho_0 c_0 S\langle v_1^2\rangle} \tag{4-9}$$

where W_{12} is the radiated sound power, $\langle v_1^2\rangle$ is the mean square velocity of plate subsystem 1, ρ_0 is the density of the air, c_0 is the phase velocity of the fluid, S is the surface area of the plate. Combining Eq. 4-2 and Eq. 4-4 and Eq. 4-9 gives the relation between the coupling loss factor and the radiation efficiency [7]:

$$\eta_{12} = \frac{\rho_0 c_0 \sigma}{\omega \rho_{\mathrm{s}}} \tag{4-10}$$

where ρ_{s} is the surface density of the plate.

Maidanik [125] proposed formulae for the calculation of modal radiation resistance as a function of frequency and extended this to the practical situation of multi-modal vibration. In contrast, Wallace [126] analysed the radiation efficiency for individual modes of a rectangular plate based on the far-field acoustic intensity using Rayleigh integral. Gomperts [127, 128] investigated the boundary conditions effects on the modal radiation efficiency of a rectangular plate.

The single mode radiation efficiency is not relevant when many modes of a palte are excited simultaneously, for which a frequency-averaged radiation efficiency [129, 130] is appropriate. Leppington *et al* [129, 130] determined a frequency-average radiation efficiency for a rectangular plate which is based on high modal density and continuous wavenumber assumption. The radiation efficiency from Leppington's asymptotic formula is given by [7, 129, 130]:

$$\sigma = \begin{cases} \left(0.5 - \dfrac{0.15L_1}{L_2}\right)\sqrt{kL_1} & f = f_c \\ \dfrac{(L_1 + L_2)}{\pi S k \mu \sqrt{\mu^2 - 1}}\left[\ln\left(\dfrac{\mu+1}{\mu-1}\right) + \dfrac{2\mu}{\mu^2-1}\right]\left[C_{\mathrm{BC}}C_{\mathrm{OB}} - \mu^{-8}(C_{\mathrm{BC}}C_{\mathrm{OB}} - 1)\right] & f < f_c \\ \dfrac{1}{\sqrt{1-\mu^2}} & f > f_c \end{cases} \qquad \text{4-11}$$

where C_{BC} is a constant for the plate boundary conditions ($C_{\mathrm{BC}} = 1$ for simply supported boundaries, $C_{\mathrm{BC}} = 2$ for clamped boundaries), C_{OB} is a constant for the orientation of the baffle that surrounds the edges of the plate ($C_{\mathrm{OB}} = 1$ when the plate lies within the plate of an infinite rigid baffle, $C_{\mathrm{OB}} = 2$ when the rigid baffles along the plate perimeter are perpendicular to the plate surface), $\mu = f_c/f$, and L_1 and L_2 are the smaller and larger rectangular plate dimensions respectively.

Note that the cross-modal coupling should be taken in to account for the radiated power if a particular force excitation position is considered [131]. As this thesis focuses on the sound radiation due to point force excitation over an area, this averages the cross-modal coupling to zero [132].

For multilayer structures, SEA models are generally based on calculating an equivalent damping to account for the noise control treatment [50, 51]. This method includes the mass effect of the whole structure via a smeared added mass by assuming that the layers are homogeneous [51]. However, the effects of the stiffness are usually neglected which can cause prediction errors at low frequencies [51]. An alternative method, the Transfer Matrix method (TMM) is better suited to sound radiation analysis for multilayer structures [50, 51]. Similar to SEA, TMM can also

take advantage of the spatial and temporal incoherence of rainfall excitation, which can be analysed conveniently in the frequency and wavenumber domain.

Note that SEA can also incorporate TMM as a hybrid method for vibroacoustic prediction [133, 134]. However, this thesis focuses on prediction of the radiated sound power; therefore it is feasible to consider TMM rather than hybrid SEA-TMM, although it might be useful for sound radiation into car cabins due to low modal densities in these small acoustic volumes.

4.3. TMM for a plate-foam-plate structure

TMM allows calculation of sound propagation across a stratified structure such as a multilayer plate. Each layer of the stratified media is homogeneous, isotropic and laterally infinite. In 1977, Folds and Loggins [135] modelled the plane ultrasound waves propagation in layers of fluid and elastic solid material; this appears to be one of the first applications of TMM to a sound propagation problem in the literature. Brouard *et al* [136] introduced a more general theory of TMM for modelling acoustic fields in stratified media with not only fluid and elastic solid layers but also porous materials. In Allard and Atalla's book [50], a detailed and complete framework of TMM method for different multilayer media is provided under acoustic and mechanical excitation.

As the multilayer structure used in this thesis is a plate-foam-plate (see Figure 4.2), only the vibration and sound propagation theory from Allard and Atalla [50] for thin elastic plates and a limp porous material representing the foam are shown here. Assuming excitation of plate 1 with distributed pressure p_1, the aim is to calculate plate velocity v_4 from which the radiated sound power can be calculated.

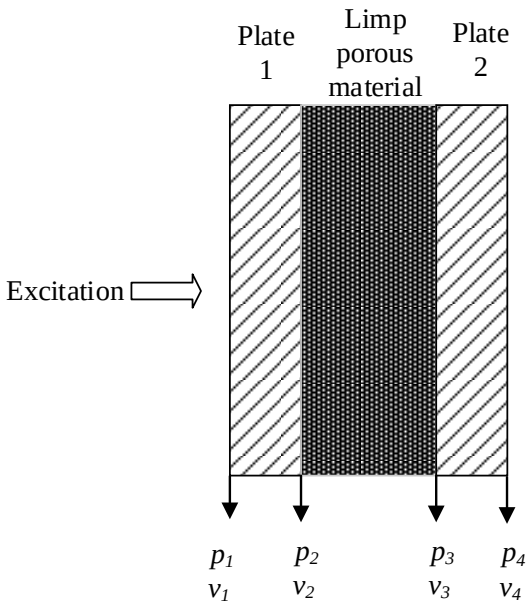

Figure 4.2. Diagram of the multilayer plate indicating the notation of the pressure and velocity at the boundary of each layer.

4.3.1. Modelling for the thin elastic plate

Assuming thin plate bending wave theory, the normal velocity of the plate on both sides is assumed to be the same [50]. Hence taking plate 1 as an example:

$$\begin{bmatrix} p_1 \\ v_1 \end{bmatrix} = [T_{\mathrm{p1}}] \begin{bmatrix} p_2 \\ v_2 \end{bmatrix} = \begin{bmatrix} 1 & -i\omega\rho_{\mathrm{s1}}(1 - \dfrac{D_1 k_{\mathrm{f}}^4}{\omega^2 \rho_{\mathrm{s1}}}) \\ 0 & 1 \end{bmatrix} \begin{bmatrix} p_2 \\ v_2 \end{bmatrix} \quad \text{4-12}$$

where $[T_{\mathrm{p1}}] = \begin{bmatrix} 1 & -Z_{\mathrm{s1}} \\ 0 & 1 \end{bmatrix}$ and $Z_{\mathrm{s1}} = i\omega\rho_{\mathrm{s1}}(1 - \frac{D_1 k_{\mathrm{f}}^4}{\omega^2 \rho_{\mathrm{s1}}})$, ρ_{s1} is the surface density of plate 1, D_1 is the bending stiffness of plate 1, and k_{f} is the wavenumber of the bending waves in plate 1.

4.3.2. Modelling the limp porous material

A model for the limp porous material can be derived from Biot theory assuming that the stiffness of the frame is negligible, for which the equivalent fluid equation for limp material is given by [50]:

$$\Delta p + \frac{\rho_{\mathrm{limp}}}{K_{\mathrm{eq}}} \omega^2 p = 0 \quad \text{4-13}$$

where ρ_{limp} is an equivalent effective density accounting for the inertia of the frame, given by [137]:

$$\rho_{\text{limp}} \approx \frac{\rho_{\text{t}}\rho_{\text{eq}} - \rho_0^2}{\rho_{\text{t}} + \rho_{\text{eq}} - 2\rho_0} \quad \text{4-14}$$

where

$$\rho_{\text{t}} = \rho_l + \phi\rho_0 \quad \text{4-15}$$

where ϕ is the porosity, ρ_l is the density of the material, ρ_0 is the density of air, and ρ_{eq} is given by [50]:

$$\rho_{\text{eq}} = \left[\phi\rho_0 + \rho_a - i\sigma_0\phi^2\frac{G(\omega)}{\omega}\right]/\phi^2 \quad \text{4-16}$$

where

$$G(\omega) = \sqrt{1 + \left(\frac{2\alpha_\infty q_0}{\phi\Lambda}\right)^2 \frac{i\omega}{\upsilon'}} \quad \text{4-17}$$

and

$$\rho_a = \frac{\phi^2\rho_0\upsilon G(\omega)}{i\omega q_0} + \phi\rho_0(\alpha_\infty - 1) \quad \text{4-18}$$

where σ_0 is the flow resistivity of the foam, $q_0 = \varsigma/\sigma_0$, with viscosity ς, and tortuosity α_∞, $\upsilon = \frac{\varsigma}{\rho_0}, \upsilon' = \frac{\upsilon}{\text{Pr}_0{}^2}$, Pr_0 is the Prandtl number. and Λ is the viscous characteristic dimension of the porous material [50].

K_{eq} in Eq. 4-13 is the effective bulk modulus that can be represented as R/ϕ^2, [50]

$$R = \frac{\phi \text{P}_0}{1 - \frac{\gamma - 1}{\gamma\alpha'}} \quad \text{4-19}$$

$$\alpha' = \frac{8\upsilon'}{\text{i}\omega\Lambda'^2}\left[1 + \frac{i\omega}{\upsilon'}\left(\frac{\Lambda'}{4}\right)^2\right]^{1/2} + 1 \quad \text{4-20}$$

with Λ' representing the thermal characteristic dimension [50].

The wavenumber in the limp porous material can be obtained from Eq. 4-13 which is given by [50]:

$$k_l = \sqrt{\rho_{\text{limp}}\omega^2/K_{\text{eq}}} \quad \text{4-21}$$

As it is assumed that the stiffness of the limp frame is negligible, the transfer matrix of the limp porous layer is given by [50]:

$$[T_l] = \begin{bmatrix} \cos k_l h & i\dfrac{\omega\rho_{\text{limp}}}{k_l}\sin k_l h \\ i\dfrac{k_l}{\omega\rho_{\text{limp}}}\sin k_l h & \cos k_l h \end{bmatrix} \quad 4\text{-}22$$

Note that the limp foam model is derived from the Biot theory by assuming that the bulk stiffness is negligible. Doutres *et al* [138] proposed a criterion to identify the validity of modelling the porous material as limp model. In their research, a new parameter Frame Stiffness Influence (FSI) has been proposed to assess the influence of the frame-borne wave on the fluid phase displacement, which can be calculated from the porous material properties. Comparing the parameter FSI with a critical value 0.16 determined by the confidence rate of 95% from 256 simulated porous materials [138], the validity of the one-wave limp model can be assessed.

4.3.3. Transfer matrix for the plate-foam-plate system under point excitation over an area

The transfer matrix $[T]$ between the input matrix $\begin{bmatrix} p_1 \\ v_1 \end{bmatrix}$, and the output matrix $\begin{bmatrix} p_4 \\ v_4 \end{bmatrix}$ in given by $[T] = [T_{\text{p1}}][T_l][T_{\text{p2}}]$:

$$\begin{bmatrix} p_1 \\ v_1 \end{bmatrix} = [T_{\text{p1}}][T_l][T_{\text{p2}}]\begin{bmatrix} p_4 \\ v_4 \end{bmatrix} \quad 4\text{-}23$$

Combining Eq. 4-12 and Eq. 4-22, the components of $[T]$ are given by [50]:

$$T_{11} = \cos(k_l h) - \frac{iZ_{\text{s1}}k_l \sin(k_l h)}{\omega\rho_l}$$

$$T_{12} = -Z_{\text{s2}}\left[\cos(k_l h) - \frac{iZ_{\text{s1}}k_l \sin(k_l h)}{\omega\rho_l}\right] - Z_{\text{s1}}\cos(k_l h) + \frac{i\omega\rho_l \sin(k_l h)}{k_l}$$

$$T_{21} = \frac{ik_l \sin(k_l h)}{\omega\rho_l}$$

$$T_{22} = \cos(k_l h) - \frac{iZ_{\text{s2}}k_l \sin(k_l h)}{\omega\rho_l} \quad 4\text{-}24$$

With pressure excitation $f(x, y, t)$ on plate 1, its vibration is described by:

$$D_1\nabla^4 w_1 + \rho_{s1}\frac{\partial^2 w_1}{\partial t^2} = f(x, y, t) + p_1 - p_2 \quad 4\text{-}25$$

where w_1 is the displacement. Therefore Eq. 4-23 can be rewritten as:

$$\begin{bmatrix} f + p_1 \\ v_1 \end{bmatrix} = [T]\begin{bmatrix} p_4 \\ v_4 \end{bmatrix} \quad 4\text{-}26$$

4.4. Calculation of radiated sound power from infinite plates

The radiation efficiency of an infinite plate on the emission side, σ_{E}, and the same as on the receiver side is σ_{R}, which is given by:

$$\sigma_{\mathrm{E}} = \sigma_{\mathrm{R}} = \frac{p_1}{-\rho_0 c_0 v_1} = \frac{p_4}{\rho_0 c_0 v_4} = \frac{k_0}{\sqrt{k_0^2 - k_{\mathrm{f}}^2}} \qquad 4\text{-}27$$

for $f > f_c$, where $k_0 = \omega/c_0$. The wavenumber of the plate can be written in terms of the *x* and *y* wavenumber components k_x and k_y:

$$k_{\mathrm{f}} = \sqrt{k_x^2 + k_y^2} \qquad 4\text{-}28$$

From Eq. 4-26 and 4-27, the velocity on the receiver side of the multilayer structure can be obtained:

$$v_4 = \frac{f}{Z_{\mathrm{TMM}}} \qquad 4\text{-}29$$

where:

$$Z_{\mathrm{TMM}} = T_{11}\rho_0 c_0 \sigma_{\mathrm{R}} + T_{12} + T_{21}\rho_0^2 c_0^2 \sigma_{\mathrm{E}}\sigma_{\mathrm{R}} + T_{22}\rho_0 c_0 \sigma_{\mathrm{E}} \qquad 4\text{-}30$$

Using wave-based approach [51], the spatial domain load can be represented in wavenumber domain using a Fourier integral transform from:

$$F(k_x, k_y, \omega) = \int_{-\infty}^{+\infty}\int_{-\infty}^{+\infty} f(x, y, \omega)\exp\left[-i(k_x x + k_y y)\right]\mathrm{d}x\mathrm{d}y \qquad 4\text{-}31$$

In order to estimate the radiated sound power from point excitation over an area, the input pressure or the impact force distribution is assumed as temporally random and spatially uncorrelated. Here it is assumed that the applied force position randomly varies over time so that spatial-temporal coupling can be ignored, then the force can be written as [139]:

$$f(x, y, t) = f_{\mathrm{s}}(x, y) f_{\mathrm{t}}(t) \qquad 4\text{-}32$$

where $f_{\mathrm{s}}(x, y)$ and $f_{\mathrm{t}}(t)$ denote the spatial and temporal components of force loading respectively. The second assumption of the spatially uncorrelated force can be expressed as:

$$f_{\mathrm{s}}(x, y) = \delta(x - x_0)\delta(y - y_0) \qquad 4\text{-}33$$

where (x_0, y_0) is the excitation position. Hence, the auto-spectrum of the point force excitation can be obtained as:

$$\left|F(k_x, k_y, \omega)\right|^2 = N(D)S|F(\omega)|^2 \qquad 4\text{-}34$$

where $N(D)$ is the number of raindrops per second per unit area and $|F(\omega)|^2$ is the auto-spectrum of the single raindrop impact.

According to Parseval's theorem, the mean-square velocity of the plate 1 in the spatial domain is equal to the wavenumber domain average square velocity $V_1(k_x, k_y)$, which is given by [50]:

$$\langle v_1^2 \rangle = \frac{1}{8\pi^2 S} \int_{-\infty}^{+\infty} \int_{-\infty}^{+\infty} \left| V_1(k_x, k_y) \right|^2 \mathrm{d}k_x \mathrm{d}k_y \qquad 4\text{-}35$$

The radiated sound power is given by [50]:

$$W_{12} = \frac{\rho_0 c_0}{8\pi^2 S_1} \int_{-\infty}^{+\infty} \int_{-\infty}^{+\infty} \frac{\left| F(k_x, k_y, \omega) \right|^2 \sigma_{\mathrm{R}}(k_x, k_y, \omega)}{\left| Z_{\mathrm{TMM}}(k_x, k_y, \omega) \right|^2} \mathrm{d}k_x \mathrm{d}k_y \qquad 4\text{-}36$$

Substituting Eqs.4-30, 4-34 and 4-35 into Eq. 4-36, the radiated sound power of the plate- foam-plate structure under point force excitation can be obtained.

The Transfer Matrix Method (TMM) is extensively used in industry to predict the structural borne or airborne response of a structure with attached noise control layers in both single- and double-walls [50, 51, 136]. However, the assumption of an infinite plate can lead to considerable errors in prediction at low- and mid-frequencies [50] because below the critical frequency, the influence of the edge diffraction on the sound radiation is important [52].

4.5. Calculation of radiated sound power from finite plates

In order to correct the radiated sound power from a finite size plate, the radiation efficiency from Eq. 4-27 is usually modified by an equivalent baffled window. Ghinet and Atalla [140] used the travelling plane wave as the basis function to predict the radiation efficiency, which can be equivalently expressed as "spatial windowing" in the wavenumber domain by Villot *et al* [52]. However, these equations have fourth or even fifth order integrals which require considerable computation time. Although Atalla and his colleagues improved the integral analytically to reduce the integral order [141], it is still time consuming and the equation given in the literature didn't always converge when used with adaptive integral routines. Bonfiglio *et al* [142] developed the integration based on Ref. [141], and assumes the rectangular plate is square to simplify the integration and remove the singularities in the equation.

Davy *et al* [143] rewrites the integral equations for the travelling wave case that removes the singularities from the radiation efficiency, however it is still computationally costly. They proposed an approximate formula that combines the travelling and mode shapes method, which was shown to significantly reduce calculation times.

In this thesis, the travelling wave method from Ghinet and Atalla [140] for a rectangular plate is considered. Based on the azimuthally averaged radiation impedance equation, the fifth order integration is proposed to be reduced significantly into single integral equation without the singularities as given in Ref. [141] and without the assumption of using a square plate from Ref. [142].

4.5.1. Spatial domain travelling wave method and wavenumber domain spatial windowing for radiation efficiency

In order to calculate the radiation efficiency, there are two commonly used methods: integrate the far-field sound power that encloses the plate on a hemispherical surface; or integrate the sound power over the surface of the plate [132]. The second method is applied in this thesis due to the lower computational cost. Furthermore, the second method can provide the complex radiation impedance.

Considering a baffled plate with dimension L_x by L_y, the radiated pressure over the surface of the plate can be given by [50]:

$$p_{\mathrm{rad}}(M) = -\int_s \frac{\partial p(M_0)}{\partial n} G(M, M_0) dS(M_0) \qquad 4\text{-}37$$

where $M(x, y)$ and $M_0(x_0, y_0)$ are the coordinates on the plate. The Green function is $G(M, M_0) = \exp(-ik_0 R)/2\pi R$, $R = \sqrt{(x - x_0)^2 + (y - y_0)^2}$, $k_0 = \omega/c_0$ and n is the outward normal to the radiation surface S that points into the receiving domain.

Let v denote the normal surface velocity [50]:

$$v = -\frac{1}{i\omega\rho_0}\frac{\partial p}{\partial n} \qquad 4\text{-}38$$

Therefore the radiated (transmitted) power can be calculated from Eq. 4-37 and Eq. 4-38 as given by [50]:

$$\mathrm{W}_{\mathrm{rad}} = \frac{1}{2} Re\left[\int_S p_{\mathrm{rad}}(M) v^*(M)\, \mathrm{d}S(M)\right]$$

$$= \frac{1}{2} Re\left[\iint_S \frac{i}{\omega\rho_0}\frac{\partial p}{\partial n}(M_0)G(M,M_0)\frac{\partial p^*}{\partial n}(M)\mathrm{d}S(M_0)\mathrm{d}S(M)\right] \quad 4\text{-}39$$

$$= \frac{1}{2} Re\left[i\omega\rho_0 \int_S \int_S v(M_0)G(M,M_0)v^*(M)\mathrm{d}S(M_0)\mathrm{d}S(M)\right]$$

Consider a flat in-plane baffled panel that is forced to vibrate with velocity [50]:

$$v(x,y) = |v|\exp[-ik_\mathrm{f}(x\cos\varphi + y\sin\varphi)] \quad 4\text{-}40$$

where k_f is the bending wavenumber, φ is the geometrical angle on the vibrating plate as shown in Figure 4.3.

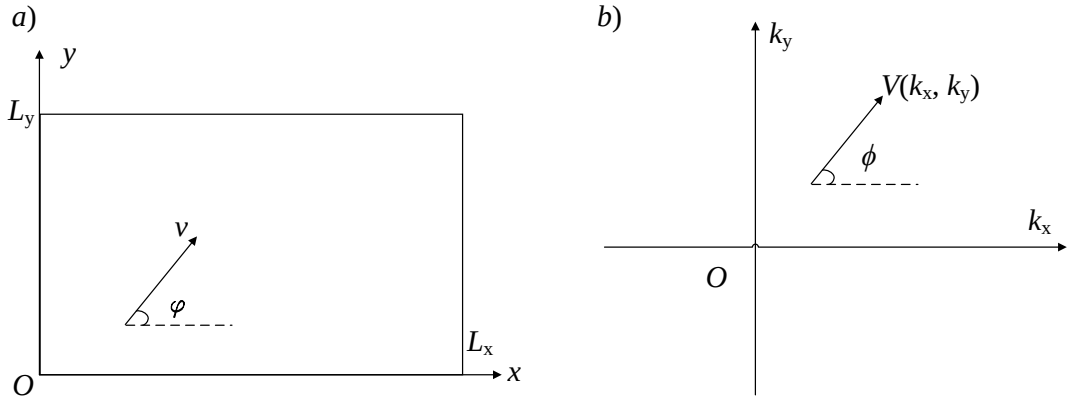

Figure 4.3. Geometrical angle of velocity in a) spatial and b) wavenumber domain.

Assuming that $|v|$ is constant over the surface, the radiated sound power can be calculated from [50]:

$$\mathrm{W}_\mathrm{rad} = \frac{|v|^2}{2} Re\left[i\omega\rho_0 \int_S \int_S \exp[-ik_\mathrm{f}(x_0\cos\varphi + y_0\sin\varphi)]\frac{\exp(-ik_0R)}{2\pi R} \cdot \exp[ik_\mathrm{f}(x\cos\varphi + y\sin\varphi)]\,\mathrm{d}x\mathrm{d}y\mathrm{d}x_0\mathrm{d}y_0\right] \quad 4\text{-}41$$

Therefore the radiation efficiency can be calculated from Eq. 4-9 given by [50]:

$$\sigma = Re\left[\frac{ik_0}{S}\int_S \int_S \exp[-ik_\mathrm{f}(x_0\cos\varphi + y_0\sin\varphi)] \cdot \frac{\exp(-ik_0R)}{2\pi R}\exp[ik_\mathrm{f}(x\cos\varphi + y\sin\varphi)]\,\mathrm{d}x\mathrm{d}y\mathrm{d}x_0\mathrm{d}y_0\right] \quad 4\text{-}42$$

The damping effect is ignored here. It should be noted that even if the damping of the plate is assumed to be relatively small, the damping effect cannot be simply accounted for by replacing D with $D(1+j\eta)$ where η is the loss factor. This is because there is a conjugate process in Eq. 4-42, which will be discussed in Section 4.5.3. The radiation efficiency from Eq. 4-42 can be simplified as [140]:

$$\sigma = Re\left[\frac{ik_0}{4\pi}L_y\int_0^2\int_0^2 (2-\mathrm{u})(2-\mathrm{u}')K(u,u')F_n(u,u')\mathrm{d}u\mathrm{d}u'\right] \quad 4\text{-}43$$

where $K(u,u') = \frac{\exp\left[i\frac{k_0 L_x}{2}\sqrt{u^2+u'^2/r_L^2}\right]}{\sqrt{u^2+u'^2/r_L^2}}$; $F_n(u,u') = \exp\left[-i\frac{k_\mathrm{f}L_x}{2}(u\cos\varphi + \frac{u'}{r_L}\sin\varphi)\right]$, where r_L is defined as the dimensional ratio $r_L = L_x/L_y$.

Eq. 4-42 can be implemented in the wavenumber domain, given by [52].

$$\sigma = \frac{L_x L_y}{2\pi^3}\int_0^{2\pi}\int_0^{k_0}\int_0^{2\pi}\frac{1-\cos[(k_\mathrm{r}\cos\phi - k_\mathrm{f}\cos\varphi)L_x]}{[(k_\mathrm{r}\cos\phi - k_\mathrm{f}\cos\varphi)L_x]^2} \cdot\frac{1-\cos[(k_\mathrm{r}\sin\phi - k_\mathrm{f}\sin\varphi)L_y]}{[(k_\mathrm{r}\sin\phi - k_\mathrm{f}\sin\varphi)L_y]^2}\cdot\frac{k_0 k_\mathrm{f}}{\sqrt{k_0^2-k_\mathrm{f}^2}}\mathrm{d}\phi\mathrm{d}k_\mathrm{r}\mathrm{d}\varphi \quad 4\text{-}44$$

where k_r is the wavenumber variable after Fourier Transform, with the associated geometrical angle ϕ. By assuming that the aspect ratio of the structure $L_x/\,L_y$ or $L_y/\,L_x$ is less than 1:2, Vigran *et al* [144] reduced the spatial window to one dimension using $L = \sqrt{L_x L_y}$:

$$\sigma = \frac{Lk_0}{2\pi}\int_0^{k_0}\frac{\sin^2\left[(k_\mathrm{r}-k_\mathrm{f})\frac{L}{2}\right]}{\left[(k_\mathrm{r}-k_\mathrm{f})\frac{L}{2}\right]^2\sqrt{k_0^2-k_\mathrm{r}^2}}\mathrm{d}k_\mathrm{r} \quad 4\text{-}45$$

Bonfiglio *et al* further investigated the integration in Ref. [142], and presented a reduced-order integral formula to predict the radiation efficiency for a square plate:

$$\sigma = Re\left\{\frac{ik_0}{4\pi}L_y\left\{\int_0^2 e^{ikA}\left(4\xi - \frac{k^2\cos^2\xi}{2} + 2k\cos\xi - 2k\sin\xi\right)\Big|_0^{\frac{\pi}{2}} \cdot Re\{I_0(iCk)\}\mathrm{d}k + \int_2^{2\sqrt{2}} e^{ikA}\left(4\xi - \frac{k^2\cos^2\xi}{2} + 2k\cos\xi - 2k\sin\xi\right)\Big|_{\xi_1}^{\xi_2} \cdot Re\{I_0(iCk)\}\mathrm{d}k\right\}\right\} \quad 4\text{-}46$$

where $\xi_1 = \tan^{-1}(\sqrt{k^2/4-1})$, $\xi_2 = \tan^{-1}(2/\sqrt{k^2-4})$, $C = k_\mathrm{f}L_x/2$, and $I_0(\cdot)$ is the modified Bessel function of the first kind.

4.5.2. Order reduction of radiation efficiency integral

In this section, an order reduction of the finite plate size correction integral is proposed for TMM based on the travelling wave method. From Eq. 4-42, the azimuth average can be derived:

$$\sigma(k_{\mathrm{f}},\varphi)=Re\left\{\frac{ik_0}{S}\int_S\int_S G(x,y;x_0,y_0)\cdot\exp\{ik_{\mathrm{f}}[(x-x_0)\cos\varphi+(y-y_0)\sin\varphi]\}\,\mathrm{d}x\mathrm{d}y\mathrm{d}x_0\mathrm{d}y_0\right\} \tag{4-47}$$

Assuming that $\tilde{x}=x-x_0=R\cos\vartheta$, $\tilde{y}=y-y_0=R\sin\vartheta$, the heading averaged geometrical radiation efficiency, $\bar{\sigma}$, is now analytically calculated, instead of implementing the spatial integral as in other literature [50, 142, 143]:

$$\begin{aligned}\bar{\sigma}(k_{\mathrm{f}})&=Re\left\{\frac{1}{2\pi}\int_0^{2\pi}\sigma(k_{\mathrm{f}},\varphi)\mathrm{d}\varphi\right\}\\&=Re\left\{\frac{ik_0}{2\pi S}\int_S\int_S G(R)\mathrm{d}x\mathrm{d}y\mathrm{d}x_0\mathrm{d}y_0\int_0^{2\pi}\exp\{ik_{\mathrm{f}}[\tilde{x}\cos\varphi+\tilde{y}\sin\varphi]\}\,\mathrm{d}\varphi\right\}\\&=Re\left\{\frac{ik_0}{2\pi S}\int_S\int_S G(R)\mathrm{d}x\mathrm{d}y\mathrm{d}x_0\mathrm{d}y_0\int_0^{2\pi}\exp\{ik_{\mathrm{f}}[R\cos\vartheta\cos\varphi+R\sin\vartheta\sin\varphi]\}\,\mathrm{d}\varphi\right\}\\&=Re\left\{\frac{ik_0}{2\pi S}\int_S\int_S G(R)\mathrm{d}x\mathrm{d}y\mathrm{d}x_0\mathrm{d}y_0\int_0^{2\pi}\exp[ik_{\mathrm{f}}R\cos(\theta-\varphi)]\,\mathrm{d}\varphi\right\}\\&=Re\left\{\frac{ik_0}{S}\int_S\int_S J_0(k_{\mathrm{f}}R)G(R)\mathrm{d}x\mathrm{d}y\mathrm{d}x_0\mathrm{d}y_0\right\}\end{aligned} \tag{4-48}$$

Considering the symmetry of first order Bessel function $J_0(k_{\mathrm{f}}R)$ and the Green function $G(R)$, the order of integration in Eq. 4-48 can be reduced:

$$\int_0^{L_y}\int_0^{L_x}\int_0^{L_y}\int_0^{L_x} f(|x-x_0|,|y-y_0|)\mathrm{d}x\mathrm{d}y\mathrm{d}x_0\mathrm{d}y_0\Leftrightarrow 4\int_0^{L_y}\int_0^{L_x}(L_x-\tilde{x})(L_y-\tilde{y})f(\tilde{x},\tilde{y})\mathrm{d}\tilde{x}\mathrm{d}\tilde{y} \tag{4-49}$$

Accordingly, Eq. 4-49 can be rewritten as

$$\bar{\sigma}(k_{\mathrm{f}})=Re\left\{\frac{4ik_0}{S}\int_0^{L_y}\int_0^{L_x}(L_x-\tilde{x})(L_y-\tilde{y})J_0(k_{\mathrm{f}}R)G(R)\mathrm{d}\tilde{x}\mathrm{d}\tilde{y}\right\} \tag{4-50}$$

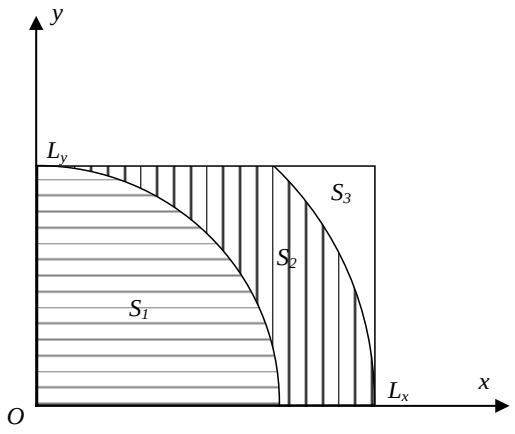

Figure 4.4. Diagram of integration districts.

Without losing the generality, it is assumed that $L_x > L_y$, therefore the integration of the rectangular plate can be divided into three parts as shown in Figure 4.4. Eq. 4-50 is rewritten as:

$$\begin{aligned}\bar{\sigma}(k_{\mathrm{f}}) = Re\{&\frac{4ik_0}{S}\int_0^{L_y}\int_0^{\frac{\pi}{2}}(L_x - R\cos\theta)\,(L_y - R\sin\theta)J_0(k_{\mathrm{f}}R)G(R)R\mathrm{d}R\mathrm{d}\theta \\ &+\frac{4ik_0}{S}\int_{L_y}^{L_x}\int_0^{\arcsin\frac{L_y}{R}}(L_x - R\cos\theta)\,(L_y - R\sin\theta)J_0(k_{\mathrm{f}}R)G(R)R\mathrm{d}R\mathrm{d}\theta \\ &+\frac{4ik_0}{S}\int_{L_x}^{\sqrt{L_x^2+L_y^2}}\int_{\arccos\frac{L_x}{R}}^{\arcsin\frac{L_y}{R}}(L_x - R\cos\theta)\,(L_y - R\sin\theta)J_0(k_{\mathrm{f}}R)G(R)R\mathrm{d}R\mathrm{d}\theta\}\end{aligned} \quad 4\text{-}51$$

This can be simplified to:

$$\begin{aligned}\bar{\sigma}(k_{\mathrm{f}}) = Re\{&\frac{2ik_0}{\pi S}\int_0^{L_y}\left(\frac{L_xL_y\pi}{2} - L_yR - L_xR + \frac{R^2}{2}\right)J_0(k_{\mathrm{f}}R)e^{-ik_0R}\mathrm{d}R \\ &+\frac{2ik_0}{\pi S}\int_{L_y}^{L_x}(L_xL_y\arcsin\frac{L_y}{R} - \frac{L_y^2}{2} + L_x\sqrt{R^2 - L_y^2} - L_xR)J_0(k_{\mathrm{f}}R)e^{-ik_0R}\mathrm{d}R\end{aligned} \quad 4\text{-}52$$

$$+\frac{2ik_0}{\pi S}\int_{L_x}^{\sqrt{L_x^2+L_y^2}}\left[L_xL_y\left(\arcsin\frac{L_y}{R}-\arccos\frac{L_x}{R}\right)+L_y\sqrt{R^2-L_x^2}+L_x\sqrt{R^2-L_y^2}\right.$$
$$\left.-\frac{L_x^2+L_y^2+R^2}{2}\right]J_0(k_fR)e^{-ik_0R}\mathrm{d}R\}$$

Up until this step, the fifth order integration in Eq. 4-47 has been reduced to a single integral. Taking the same assumption from Vigran *et al* [144] that the aspect ratio of the structure L_x/L_y or L_y/L_x is less than 1:2 and defining $L=\sqrt{L_xL_y}$ allows the integral of the radiation efficiency to be simplified into a single integral as:

$$\bar{\sigma}(k_f)=Re\left\{\frac{4ik_0}{\pi S}\left[\int_0^L\left(\frac{\pi}{4}L^2-LR+\frac{1}{4}R^2\right)J_0(k_fR)e^{-ik_0R}\mathrm{d}R+\right.\right.$$
$$\left.\left.\int_L^{\sqrt{2}L}\left(\frac{\pi-2}{4}L^2-L^2\arccos\frac{L}{R}-\frac{1}{4}R^2+L\sqrt{R^2-L^2}\right)J_0(k_fR)e^{-ik_0R}\mathrm{d}R\right]\right\} \quad 4\text{-}53$$

Substituting the radiation efficiency in Eq. 4-52 or Eq. 4-53 into Eq. 4-36 gives the prediction of finite size corrected sound power from a rectangular plate.

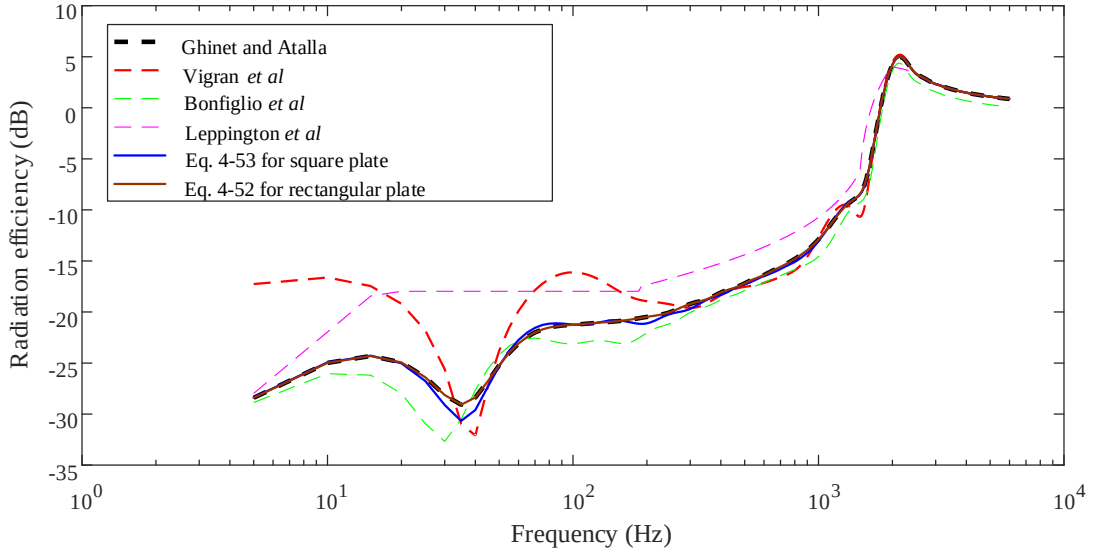

Figure 4.5. Comparison between different radiation efficiency calculation methods of a 6 mm thick glass plate with dimensions 1.5 m×1.25 m.

In the spatial domain integration such as Eq. 4-42 and Eq. 4-43, there is a singular point in the Green function term $G(R) = \frac{\exp(-ik_0R)}{2\pi R}$ when $R = 0$. In the wavenumber domain calculation using Eq. 4-44 or Eq. 4-45, there is also a singular point at $k_r = k_0$. Using the adaptive quadrature integration from Matlab, the singular point can make the calculation time-consuming and occasionally it does not converge.

A comparison of the different radiation efficiency calculations is shown in Figure 4.5, Atalla's method overlaps with Eq. 4-52 calculated by adaptive algorithm (function integral2 in Matlab). Bonfiglio *et al*'s method has 2 to 3 dB differences from the proposed method using Eq. 4-52, since the plate is not square. Additionally, the error can be even more significant when the ratio of the plate dimensions is significantly different to one.

It should be noted that the difference between the travelling wave case (Ghinet and Atalla) and the modal approach (Leppington *et al*) is ≈ 3 dB from 100 to 1k Hz, which corresponds to Davy *et al*'s conclusion in Ref. [143].

Table 4-1. Computation time using different calculation methods (operated on Intel(R) Core (TM) i3-4130 CPU 3.4GHz):

Methods for radiation efficiency calculations	Computation time (s)
Ghinet and Atalla [140]	>3600
Vigran *et al* [144]	0.79
Bonfiglio *et al* [142]	2.12
Leppington *et al* [129, 130]	0.008
Eq. 4-53 for square plate	1.9
Eq. 4-52 for rectangular plate	2.8

The proposed method gives the same results as Ghinet and Atalla's method but without the computational cost. In addition, compared to Bonfiglio *et al* or Vigran *et al* 's methods, Eq. 4-52 is not limited to a square plate.

4.5.3. Additional factors that influence the radiation efficiency

4.5.3.1. Angled baffle correction

Since the baffle conditions in buildings or car roofs are not usually represented by a planar baffle in the same plane as the plate, a correction factor for angled baffle conditions can be estimated using the geometry shown in Figure 4.6, where Q_ψ in Figure 4.7 is the correction factor when $c_B \ll c_0$ [145, 146], and ψ is the baffle angle.

Note that the angled baffle correction factor is based on the assumption that the rectangular plate has the same baffle angle at all four edges. In this thesis the baffle angle at four edges are not identical, therefore, the averaged ψ is used.

.

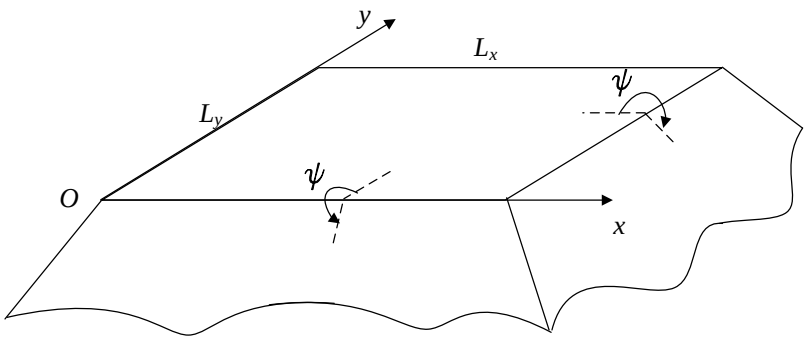

Figure 4.6. Rectangular plate placed in a rigid angled baffle.

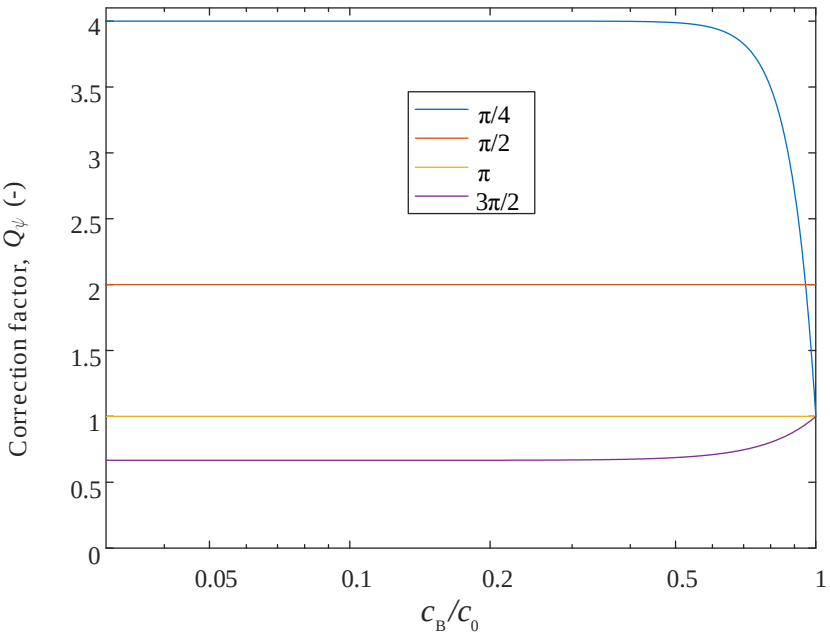

Figure 4.7. Radiation efficiency: correction factor for different angles where π radian represents the in-plane baffle.

4.5.3.2. Plate boundary conditions

The effect of boundary conditions effect on the vibro-acoustic response of the panel has been investigated using a modal approach [129, 130, 145, 147-149]. The correction for simply supported or clamped plate is shown in Eq. 4-11. However, in TMM, the finite correction approach using spatial windowing or the travelling wave method neglects the modal behaviour of the structure. An alternative method is developed by hybrid modal-TMM approach [133, 150, 151], assuming that the rectangular plate structure is simply supported, so that the plate radiation efficiency can be calculated at each mode using the mode-shape dependent wavenumber (i.e. [150]). In this thesis, the plate is assumed as simply supported so that the correction term of the boundary condition is one.

4.5.3.3 Nearfield radiation

In Section 4.5.1 and Section 4.5.2, the damping is assumed to be negligible. In this thesis, the Perspex plate used in the multilayer plate has an internal loss factor of ≈ 0.075. For this reason, it may be necessary to consider the effect of damping on the radiation efficiency. Kou *et al* [152] reported that when a plate has 5% to 10% loss factor, the radiation efficiency from the undamped plate could increase by 4 to 6 dB below the critical frequency. However, this was not validated experimentally.

Xie *et al* [132] accounted for the damping effect by using the equivalent radiation efficiency from the nearfield of a point force, which can be expressed as:

$$\sigma_n = \frac{4f}{\pi f_c}\eta \qquad \text{for } f < f_c \tag{4-54}$$

Hence the overall radiation efficiency of a damped point-excited plate can be given by:

$$\sigma = \sigma_0 + \sigma_n \qquad \text{for } f < f_c \tag{4-55}$$

where σ_0 is the radiation efficiency without damping.

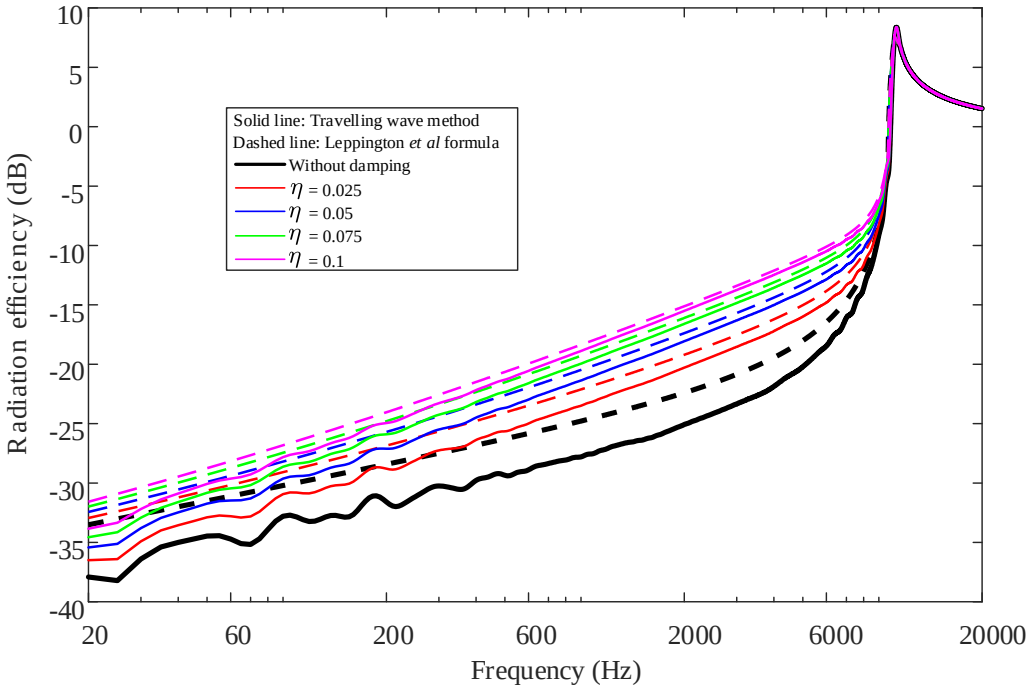

Figure 4.8. Radiation efficiency of a Perspex plate with or without damping.

In Figure 4.8, the effect of the loss factor on radiation efficiency has been assessed using Eq. 4-55. The radiation efficiency without damping effect is calculated using the Leppington *et al* formula [7, 129, 130] from Eq. 4-11, and the travelling wave method using Eq. 4-52. Properties of the Perspex plate are shown in Table 5-6; but to assess the effect of damping, different loss factors are used in Figure 4.8. The difference between the Leppington *et al* formula and travelling wave method without damping has about 3 dB difference over the frequency range from 50 to 6k Hz, which is similar to the result for glass plate (refer back to Section 4.5.2). However, with the 0.075 loss factor considered, the difference between these two methods is <1 dB from 100 to 6k Hz, because the nearfield radiation becomes

significant compared with the non-damped radiation efficiency. These results show that the loss factor on Perspex is likely to affect the rain noise prediction frequency range 20 to 6k Hz; hence it is included in the calculation in Chapter 8.

4.6. Conclusions

In this chapter, the theory of SEA and FTMM has been presented for the prediction of radiated sound from plates undergoing point excitation. The theory of a two subsystem SEA model has been introduced to predict the sound radiation from a homogenous glass plate. However, SEA is less well-suited to accurate modelling of multilayer plates. Therefore, the TMM method is used for both a homogeneous glass plate and a multilayer plate. To improve computational efficiency, an order reduced integral with travelling wave method for finite plate size correction of TMM (FTMM) has been proposed to calculate the radiation efficiency. This is significantly more efficient than the equation from Ghinet and Atalla [140], and unlike the equations from Bonfiglio *et al* [142] and Vigran *et al* [144], it applies to non-square plates. Using artificial rain excitation on a glass plate and a multilayer plate in Chapter 8 will allow a comparison of radiation efficiency formulae from FTMM developed in this thesis and the formulae from Leppington *et al*. In order to account for the damping effect on radiation efficiency from a Perspex plate, nearfield radiation from the point force excitation is considered. Other factors that affect the radiation efficiency such as the angled baffle condition are also considered as these are necessary to model practical situations.

5. Experimental set-ups and procedures

5.1. Introduction

This chapter describes the experimental set-ups for single drop impact force estimation and the vibroacoustic measurement of rectangular plates under rainfall excitation.

Section 5.2 describes the general setup for impact force measurement from a single water drop using a force transducer, the wavelet deconvolution method and the sparse representation method. This section includes the details on general system setup, generation of the water drops, and signal processing in force transducer measurement.

Section 5.3 describes the experimental setups for artificial rain noise measurement using a glass plate and a multilayer plate. The properties of these two plates are described in Section 5.4.

Section 5.5 describes measurement of the total loss factor of the glass plate using structural reverberation times and Morlet wavelet filter approach.

5.2. Experimental setup to measure the impact force for a single water drop

Doyle's wavelet method [33] and the sparse representation method are used to determine the impact force from the response signal on the plate. In the experiment, a matrix of transfer accelerances, **h**, is determined by applying an impact force at the excitation position, p_e, using a force hammer with a 3 mm diameter steel tip (Brüel & Kjær Type 8203). The acceleration at sensing positions, $p_1(0.41L_x, 0.22L_y)$, $p_2(0.21L_x, 0.43L_y)$, and $p_3(0.36L_x, 0.70L_y)$), was measured using three accelerometers (Brüel & Kjær Type 4375) fixed with cyanoacrylate glue to the underside of the glass plate at randomly located positions. Ten hits were averaged to give each transfer accelerance value. As shown in Figure 5.1, the auto-spectrum of the force hammer excitation on a glass plate is flat up to 8k Hz which covers the analysed frequency range of raindrop impact (up to 6k Hz [7]).

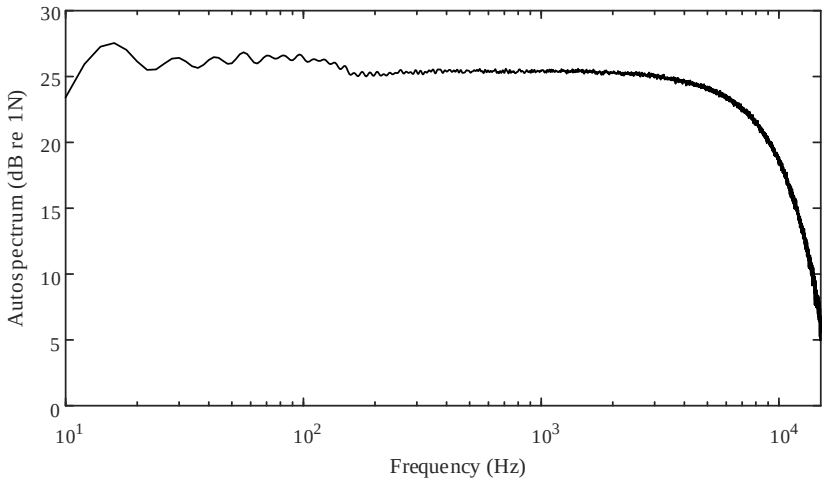

Figure 5.1. Force auto-spectrum of the force hammer excitation on a glass plate.

When the drop impacts upon the plate, Eqs. 3-9 and 3-15 are used to calculate the time-dependent forces from the acceleration measured at the same three accelerometer positions that are used to determine the matrix **h**. Impacts from eight drops are averaged in the time-domain. Note that for the glass with a surface water layer, the underside of the glass was used to apply the force and to fix the accelerometers. A piezoelectric force transducer (Brüel & Kjær Type 8200) is also used to determine the force.

The experimental set-ups used for force transducer and wavelet measurements are shown in Figure 5.2 (a) and Figure 5.2 (b) respectively. In both set-ups the drops are released from a burette. Apart from drops travelling at terminal velocity (15 m falling height), each drop travels inside rigid plastic tubing (up to 7 m in length, 200 mm diameter) to minimise any influence from any air movement in the laboratory. The lower end of the tubing was ≈0.4 m above the point of impact and was grounded through its supporting connections. The tubing improved the repeatability of both the drop velocity on impact and the drop position on impact. It was not possible to support a long length of tubing for the 15m height used for terminal velocity.

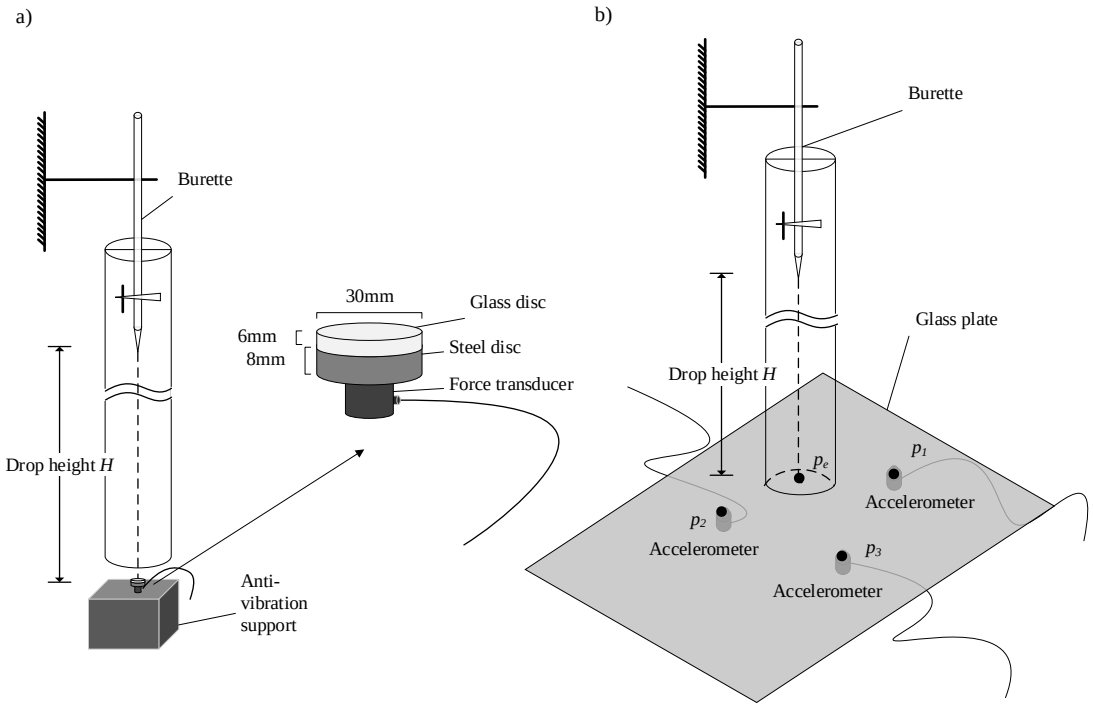

Figure 5.2. Measurement set-ups: (a) force transducer disc, (b) glass plate used for wavelet deconvolution.

The force transducer set-up (Figure 5.2 (a)) uses a 6 mm thick glass disc fixed with cyanoacrylate glue to a 8 mm thick steel disc to ensure that the surface condition is identical in terms of wettability and roughness to the wavelet deconvolution measurements. The maximum spreading diameter can be predicted by a semi-empirical equation provided by [153]:

$$D_{\max} = 0.61\left(\frac{We}{Oh}\right)^{0.166} \qquad 5\text{-}1$$

where *Oh* is the Ohnesorge number ($= We^{1/2}Re^{-1}$). Therefore, for *D*=5 mm, v_d=7 m/s raindrop, the maximum spreading diameter is calculated to be 34 mm. The force transducer disc has a 30mm diameter to minimize the ringing effect and support the spreading water flow. The steel disc is screwed to a force transducer which is mounted on an isolated 20 kg mass to reduce the background vibration.

In the experimental set-up for wavelet deconvolution (Figure 5.2 (b)), the drops impact upon a plate of 6 mm thick glass (1.2 m × 1 m). Glass typically has an internal loss factor of 0.006 [7]; hence, to increase the overall damping of the plate (up to a loss factor of ≈0.05), 50 mm wide strips of 13 mm thick Sylomer SR55 are

positioned on both sides of the glass around the entire perimeter with the upper layer of Sylomer compressed under a static load applied by 13 mm thick steel.

For the glass with water layers, the following water depths, *d*, are used: 1, 2, 4, 6, 8, and 10 mm. The variation of the water depth over the surface is estimated to be at most ±0.5 mm. For the force transducer measurement, thin plastic tape is wrapped around the perimeter of the glass disc to contain the water on top of the disc. Before each measurement, all glassware was cleaned and dried.

During all experiments the temperature was between 21 and 25^{o}C, with relative humidity between 40 and 60% to minimize their effect on surface tension.

5.2.1. Drop generation

Liquid water drops are formed from reverse osmosis water to minimize the effect from dissolved substances on surface tension. A burette produces 4.5 mm diameter drops, to which a needle is attached to produce 2 mm diameter drops. To ensure repeatable drops of approximately constant weight, Guigon *et al* [9] used relatively slow drop formation times ranging from 10 to 60 s; in this thesis, times ranging from 10 to 30 s are used. To achieve a range of drop velocities up to terminal velocity, the fall heights were 0.41, 0.81, 1.63, 3.25, 6.5 and 15 m.

5.2.2. Drop shape

For 2mm diameter drops, the drop shape can be assumed to be approximately spherical (refer back to Figure 2.6). For artificial “heavy rain” with a drop diameter typically assumed to be 5 mm [7], this thesis used 4.5mm artificial drops. These 4.5 mm drops travelled at 8.2 m/s which is slightly slower than their terminal velocity of 9.0 m/s. However, assuming that their shape would be similar to those at terminal velocity, their shape was estimated by combining two halves of different oblate spheroids according to [15].

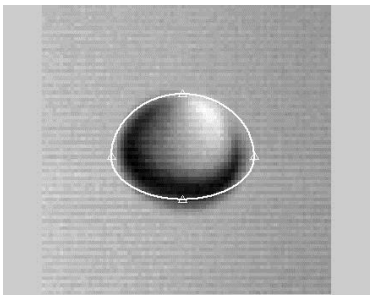

Figure 5.3. Estimated drop shape for a 4.5 mm water drop from [15] at terminal velocity of 9.0 m/s (white line), and an actual drop captured by high speed camera in the experiments with a velocity of 8.2 m/s.

Figure 5.3 shows a photograph of the 4.5 mm drop captured by high-speed camera and the estimated shape by combining two different oblate spheroids; they are slightly different which is attributed to the slightly different velocities. The axis ratio is defined as the ratio of the largest vertical and horizontal chords of the drop commonly used to describe the equilibrium drop shape [15]. According to [19], the axis ratio of 2 mm drops at terminal velocity is about 0.91, which is approximately spherical. Therefore, in these experiments only the axis ratios for 4.5 mm drops are shown in Table 1. For drop heights of 0.41, 0.81 and 1.63 m (corresponding to drop velocities of 2.69, 3.77, 5.18 m/s) the drops are approximately spherical (within experimental error and variation due to drop oscillations), but the underside of the drop becomes increasingly flattened at heights of 3.25 and 6.5 m (corresponding to 6.73 and 8.20 m/s).

Table 5-1. Axis ratio of 4.5mm drops (average of seven measurements) at different drop heights, *H*.

	H = 0.41m	H = 0.81m	H = 1.63m	H = 3.25m	H = 6.5m
Mean axis ratio	0.98	0.96	0.95	0.86	0.79
Standard deviation	0.072	0.034	0.039	0.045	0.064
Maximum axis ratio	1.08	1	1.06	0.93	0.93
Minimum axis ratio	0.93	0.93	0.93	0.81	0.73

5.2.3. Signal capture and signal processing

Force and acceleration signals are recorded using a Brüel & Kjær PULSE Analyser with a sampling rate of 131k Hz, and low-and high-frequency cut-offs of

10 and 10k Hz respectively (although the high-frequency cut-off is extended to 100k Hz in the Nexus when measuring bubble entrainment). The frequency resolution is 0.5 Hz for the FFT data after zero-padding in time domain and these narrow bands are used for the comparison of measured data. However, to determine and assess the empirical formulae the narrow bands are combined into one-third octave bands because (a) the smoother curves in the frequency domain are better suited to curve fitting and (b) these bands are typically used to assess human response to noise.

For the force transducer, the first structural mode of the transducer-disc system causes ringing between 7.5k and 8.5k Hz. Hence a second-order, band-stop Butterworth filter (low- and high-frequency cut-off at 7k and 9k Hz respectively) is used to remove the ringing without significantly changing the measured force below 6k Hz.

Li *et al* [154] used a low-pass filter to try and remove the ringing signal from the transducer disc. However, there are two problems in using the low pass filter with the force transducer: 1) The resonance is around 8k Hz, so higher frequency data will be lost, and using high order low pass filter can induce the Gibbs phenomenon in the filtered signal. 2) A low pass filter could also remove the high frequency components from the original force pulse.

Instead of using low-pass filter, two different notch or band stop filters have been tested in this thesis. These have been compared to wavelet deconvolution measurements which are assumed to be more accurate. The band stop filter is a 2nd order Butterworth filter with a cut-off frequency at $f_{c1} = 6\text{k Hz}$, and $f_{c2} = 12\text{k Hz}$. As shown in Figure 5.5, using a band stop filter can reduce the effect of the resonance significantly without changing the low frequency components, and high frequency components of the force pulse are preserved. An alternative filter is the adaptive notch filter. In this thesis, the adaptive notch filter as shown in Figure 5.4 is designed using the LMS (Least Mean Square) algorithm [155]. The centre frequency is set to 8k Hz which corresponds to the ringing resonance of the steel-glass disc and force transducer system. The convergence factor μ is determined by the notch band width $\mu C^2\Omega/\pi$ [155], which is equal to 0.18.

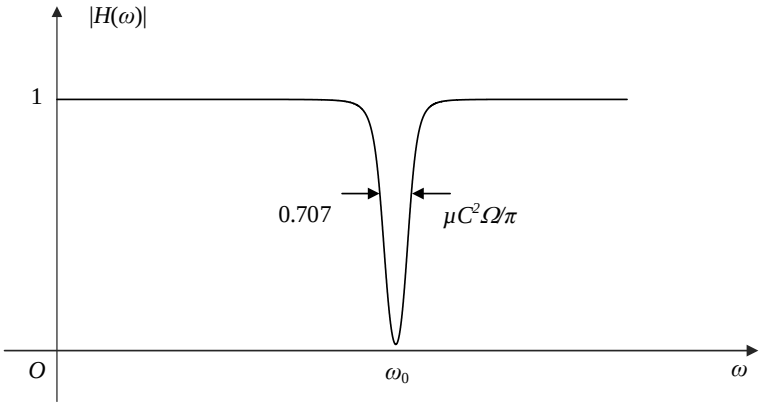

Figure 5.4. Frequency response function of adaptive notch filter.

As shown in Figure 5.5 (a), the adaptive notch filter in this thesis leads to over estimation of the force peak, and in the frequency domain, the adaptive notch filter increases the low frequency energy of the impact force pulse by about 1 dB. This is possibly because the adaptive filter is slightly slow to adjust the notch to remove the ringing signal. The resonance of the transducer disk not only induces a ringing signal around 8k Hz, but also increases the mid-frequency energy below the ringing centre frequency (3k to 6k Hz). Although this ringing signal can be cancelled by the adaptive filter, the stiffness effect cannot be filtered out. Combining an adaptive notch filter with a low-pass filter can cope with this stiffness effect as shown in Figure 5.5 (b). However the adaptive notch increases the ESD curve by 1dB at low frequencies. This is possibly because the ringing signal is so strong that the convergence parameter is slightly too large to suppress the resonance.

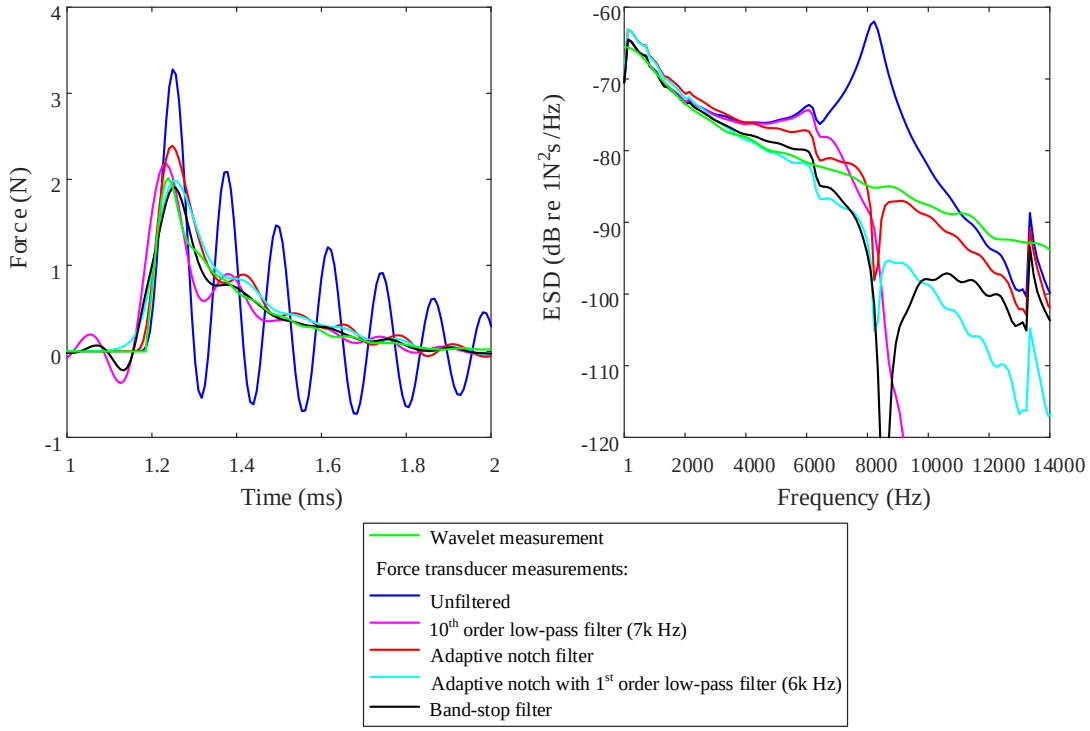

Figure 5.5. Effect of filtering on force transducer measurement: (left) time domain and (right) frequency domain.

The band-stop filter is applied in this thesis as the results are closest to the wavelet results up to 6k Hz. The reason for using the second order filter is because higher order filter may also reduce the components from the true force signal and generate ripples in the force curve. In this thesis, the ripples before the force pulse which are caused by the Gibbs phenomenon are zero-padded before carrying out FFT analysis.

5.2.4. Drop diameter measurement

The drop diameter is measured using two different approaches: (1) calibrating the pixel dimension of a high-speed camera (Lambda Mega Speed HHC X2) to capture an image of the drop just before impact, and (2) measuring the total mass of 200 drops and calculating the diameter. The difference between the drop diameter determined using these two methods is <0.05 mm; however, the quoted drop diameters in this thesis correspond to those measured with the high-speed camera. The measurement of the drop diameter, *D*, from the high-speed camera uses the calculation [61]:

$$D = 2\left(R_h^2 R_v\right)^{1/3} \quad 5\text{-}2$$

where R_h and R_v are the horizontal and vertical radius of the droplet respectively.

5.2.5. Drop velocity measurement

The drop velocity on impact is measured using a high-speed camera (Lambda Mega Speed HHC X2). In order to determine the physical frame dimension and the frame number for the velocity calculation, the velocity calculation error is estimated based on the empirical velocity equation provided by Range and Feuillebois [61]:

$$v_d = \sqrt{\frac{g}{A}(1 - \exp(-2AH))} \quad 5\text{-}3$$

$$A = \frac{3c_f \rho_{air}}{8\rho_{drop} R_0} \quad 5\text{-}4$$

where H is fall height of the drop, c_f is the friction coefficient which in this formula (for high Reynolds numbers) has been taken to be $c_f = 0.796$ [61], and R_0 is the equivalent radius of the droplet, which can be obtained from the diameter using Eq. 5-2.

The maximum frame rate of the available high-speed camera is 2000 frame/s; therefore, the time interval is Δt = 0.5 ms. Considering a drop at the velocity of v=9 m/s, the distance, Δs ,that the drop travels during this time interval is 4.5 mm.

The distance that the water drop travels in the digital image is measured with reference to a ruler in the image. Because of the limitation of ruler's scale, Δs has an error of Δs_{error}=± 0.5 mm, assuming that there are n frames captured for drop velocity calculation, which gives the error in the velocity as:

$$v_{\text{d,error1}} = \Delta s_{\text{error}} / \, n\Delta t = 1/\text{n m/s} \quad 5\text{-}5$$

Therefore increasing the number of frames can reduce the measurement error. However, when the water drop is not at terminal velocity, the drop velocity during the n frames cannot be regarded as constant according to Eq. 5-3. The drop velocity is related to the falling height, which gives the estimated error in the velocity as:

$$v_{\text{d,error2}} = v_{\text{d,measure}} - v_d$$

$$= \frac{\sum_{i=0}^{n} \sqrt{\frac{g}{A}\left(1 - \exp\left(-2A(H - u_0 i\Delta t)\right)\right)}}{n+1} - \sqrt{\frac{g}{A}(1 - \exp(-2AH))} \quad 5\text{-}6$$

Combining Eq. 5-5 and Eq. 5-6, the total error of the measured velocity is estimated using:

$$v_{\mathrm{d,error}} = v_{\mathrm{d,error1}} + v_{\mathrm{d,error2}} \qquad 5\text{-}7$$

In Figure 5.6, the error in the drop velocity measurement from two different water drops with different velocities is assessed. As shown in Figure 5.6, the number of frames can be chosen to minimize by minimizing the velocity measurement error. For the same drop size, higher velocity leads to lower estimation error because the acceleration is small when water drops get close to the terminal velocity.

With the optimal camera frame dimension, the estimated velocity error can be limited to 3%.

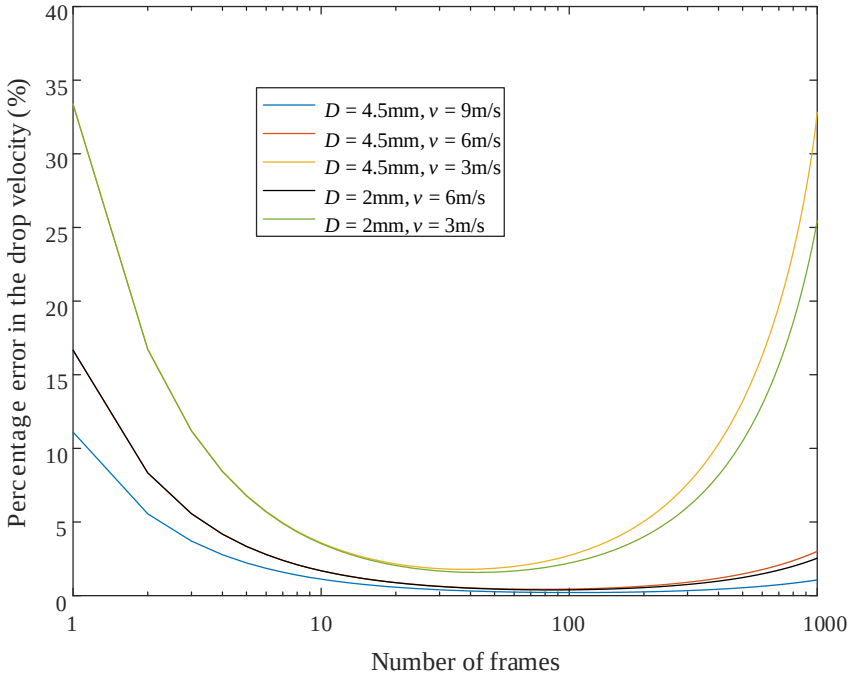

Figure 5.6. Error in the drop velocity measurement for different number of frames.

The drop velocity just before impact is measured using the high-speed camera with an average velocity calculated from ten drops at each fall height. The frame rate is 2000 frames/s for which the drop velocity on impact is estimated using between 10 and 20 frames up to the last frame before impact. The total error in the velocity is estimated to be <5%.

The drop velocity results determined for different fall heights are shown in Table 5-2. These can be compared with the empirical equation from Range and Feuillebois [61].

The friction coefficient used in Eq. 5-4 is given by Serafini's equation [156] and is a function of the Reynolds number but this equation is only valid over a limited range where Re<1000; hence for a range of fall heights from 0.25 to 1.75 m, Range and Feuillebois [61] adjusted the friction coefficient to fit their measurements with 3.6 mm diameter drops which resulted in c_f=0.796. For the range of fall heights in the present experiment where 350<Re<892 for 2 mm drops and 824<Re<2808 for 4.5 mm drops, the mean-square error was minimised to give c_f=0.533 for which the empirical equation is compared with measured data in Figure 5.7. Additional measurements were carried out without a tube around the 4.5 mm drops with fall heights between 0.42 and 5.5 m. These confirm the use of c_f=0.533 and demonstrate that the presence of the tube has negligible effect on the drop velocity. The reason for the difference compared with c_f from Range and Feuillebois is likely to be due to the wider range of fall heights and the two different drop sizes considered in the current experiment.

Table 5-2. Drop velocity on impact estimated from high-speed camera measurements for the different fall heights.

		Fall height (m)					
Drop diameter (mm)		0.41	0.81	1.63	3.25	6.5	15
2	Mean velocity (m/s)	2.57	3.49	4.62	5.71	This height was not measured	6.55
	Standard deviation (m/s)	0	0.04	0.18	0.18		0.15
4.5	Mean velocity (m/s)	2.69	3.77	5.18	6.73	8.20	9.17
	Standard deviation (m/s)	0.01	0.01	0.05	0.07	0.15	0.25

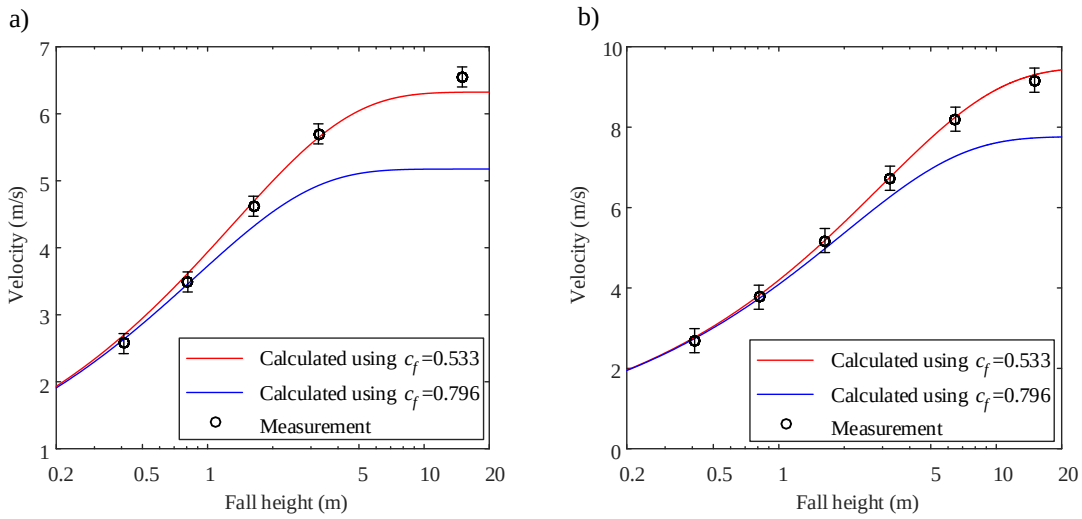

Figure 5.7. Comparison of measured and calculated drop velocity at different fall heights: (a) 2 mm drops, (b) 4.5 mm drops.

5.3. Artificial rainfall experiment

The artificial rainfall is generated from a rain box that is made from PVC plastic plates and plastic nozzles. The size of the rain box is 1.3 m×1.25 m as described in the standard rain noise measurement setup from ISO 10140-5 [12].

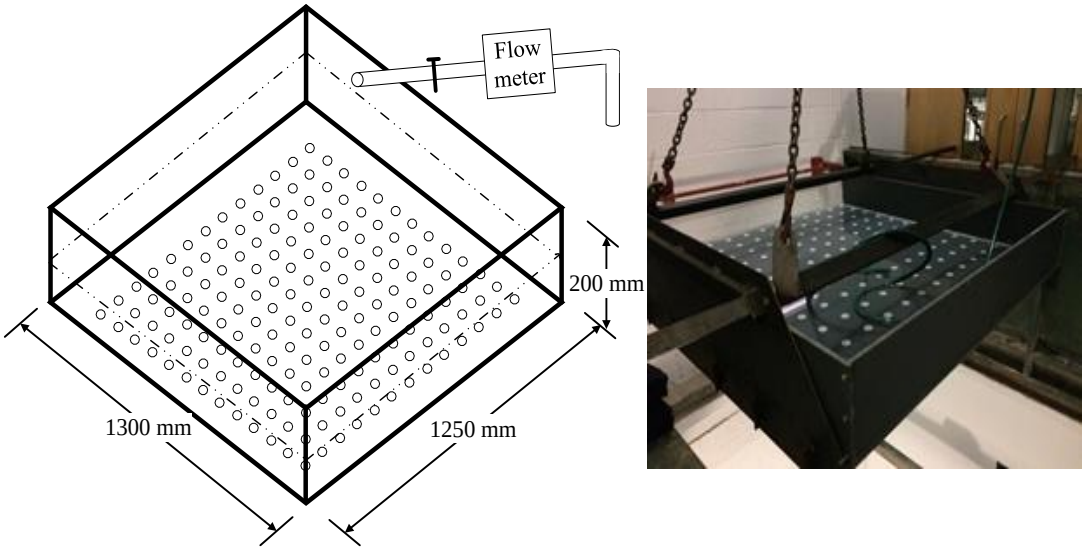

Figure 5.8. Artificial rain box.

As shown in Figure 5.8, the rain box is suspended using a hoist crane and two horizontal steel bars for stabilization. Since the rainfall rate is determined by the head of water which provides the pressure for raindrop generation, it is critical to control the water supply so that the water flow is stable over time. The water supply is connected to the tap water with controlled flow rate that can be instantaneously

measured by flow meter. For heavy rain fall (40 mm/h), the required water flow rate is 1.07 l/min. However, as the size of the nozzle hole is small (with 0.5 mm diameter see Figure 5.9), dirt/dust particles can block the holes during the experiments which resulted in a lower rainfall rate. For this reason the water flow rate was monitored during the experiment. There are 169 nozzles which were designed and tested in isolation to generate 4.6 mm diameter rain drops with the required rainfall rates see Figure 5.9.

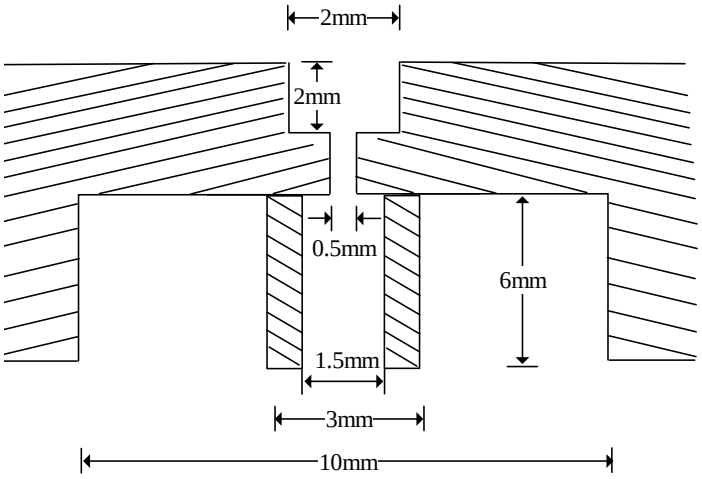

Figure 5.9. Design of the nozzle to generate 4.6 mm water drops.

The rain noise system is installed in a tower, so that the terminal velocity can be achieved with an average falling height of 11.4 m as shown in Figure 5.11 (a). A lower falling height around 3.65 m as proposed in ISO 10140-5 [12] is also used for measurements (Figure 5.11 (b)).

A glass plate and a multilayer plate rest upon a "baffle box" (see Appendix. A for the diagrams) with a 30^{o} slope. Flanking transmission was minimized by a layer of resilient foam attached to the top of the baffle box. The box is constructed from a double layer of 18mm thickness chipboard with a 12 mm air gap between them to reduce extraneous background noise inside the box see Figure 5.10b.

Both of the plates are fixed into frames as shown in Figure 5.10, with silicone sealant to minimize water penetration into the wooden frame (see Figure 5.10b). For the multilayer plate, two layers of the silicone sealant were applied between the plate and the frame gap to minimize flanking transmission via the frame.

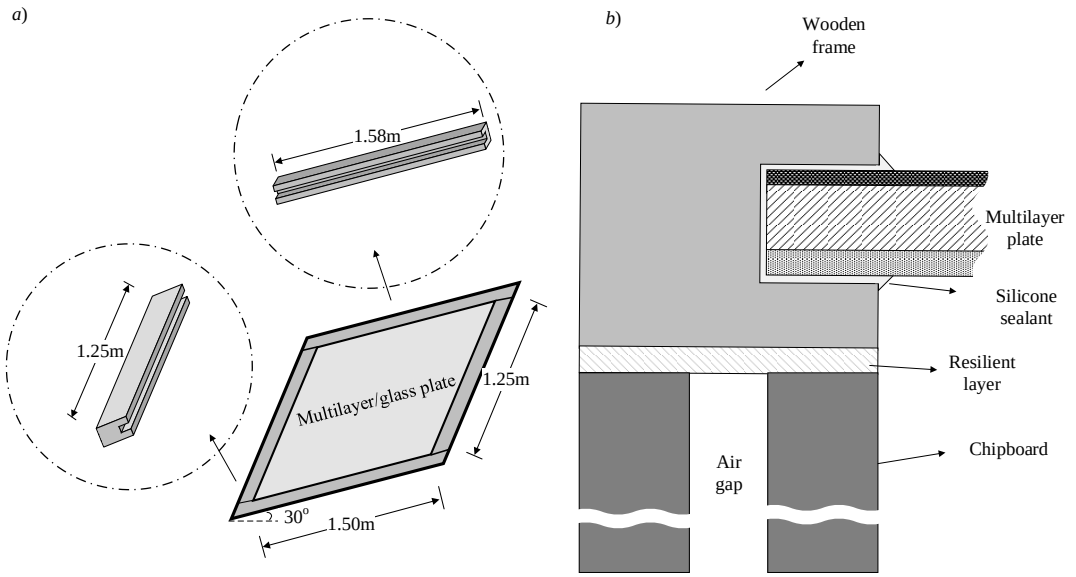

Figure 5.10. (a) Wooden frame for a glass plate and a multilayer plate, (b) detailed showing fixing of the multilayer plate into the frame that rests on the baffle box.

The plate vibration and the radiated sound power have been measured after measuring the background vibration and noise. The vibration of the plate has been measured using six accelerometers (DELTA TRON Type 4517) that were located randomly over the plate surface. The sound radiation from the plate has been measured using a sound intensity probe (B&K Type 3519 and 4183 phase matched microphones) positioned on a grid of discrete points based on ISO 9614-1 [157]. The measured frequency range is from 40 to 5.7 kHz, to cover one third octave bands from 50 to 5k Hz.

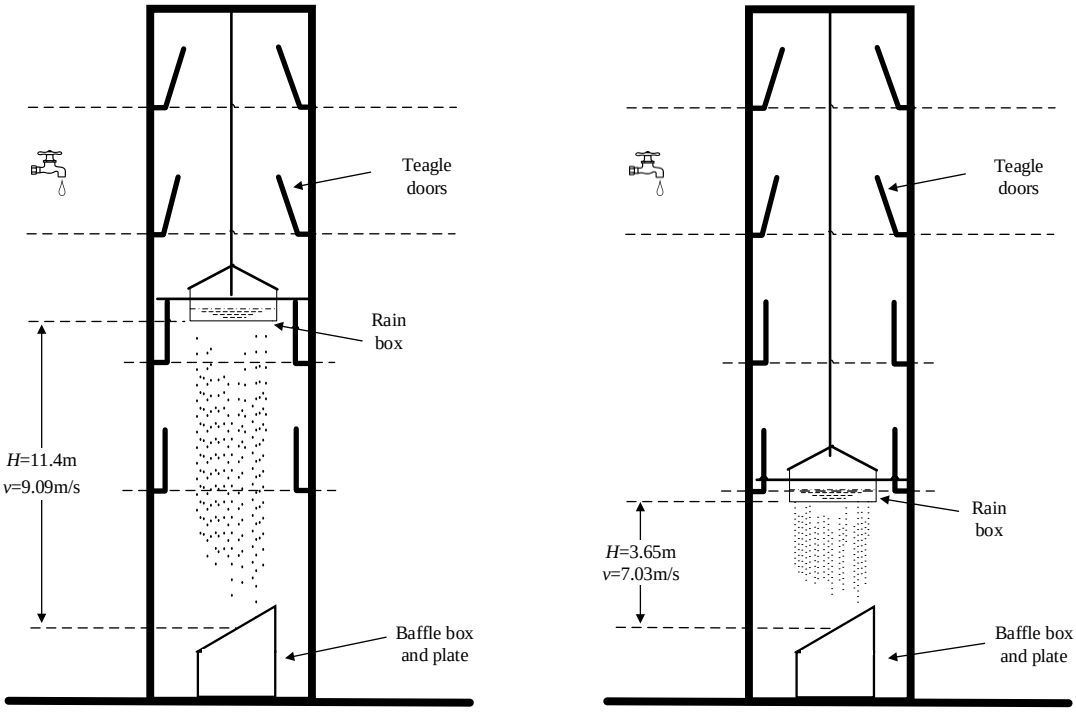

Figure 5.11. Artificial rain noise measurement system showing the two different drop heights.

5.4. Glass plate and multilayer plate structure

A single sheet of glass with properties shown in Table 5-3, has been used for the artificial rainfall experiment at both 11.4 and 3.65 m drop heights.

The multilayer plate is three-layer laminate plate constructed from aluminium plate, foam and Perspex plate as shown in Figure 4.2. The three layers are superglued together to avoid any air gaps. The foam was a high density open cell foam from Acefoam [158]. The material properties of the foam were measured by Matelys (France), and are shown in Table 5-4. A criterion of the limp model proposed by Doutres *et al* [138] has been applied to assess the validity of limp model. The parameter Frame Stiffness Influence (FSI) [138], based on the porous material properties, has been calculated to be smaller than the critical value 0.16 (determined by the confidence rate of 95% from 256 simulated porous materials [138]) as shown in Figure 5.12. Therefore, the one-wave limp model can be used for this foam as described in Section 4.3.2 instead of the poro-elastic Biot model.

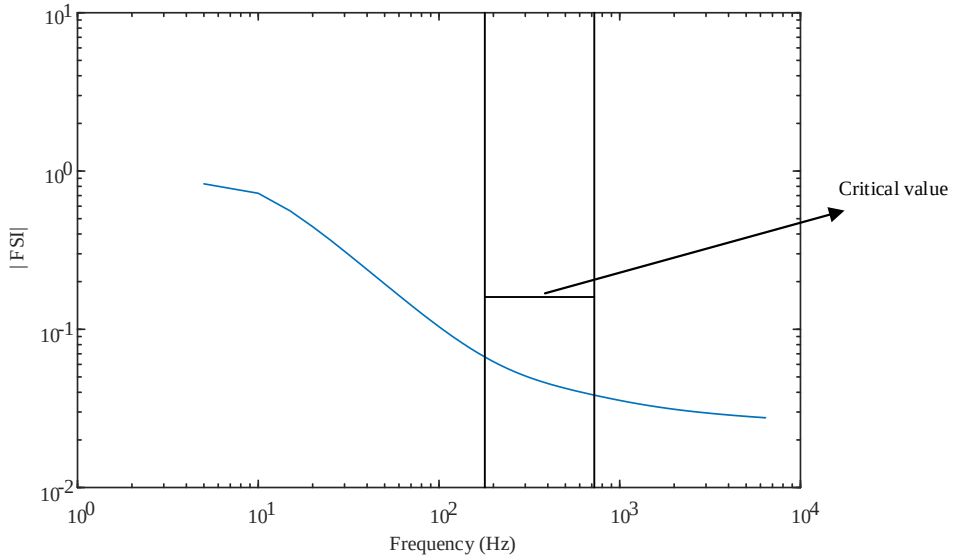

Figure 5.12. FSI curve and critical value

Table 5-3. Properties of the glass plate

Thickness (mm)	6
Dimension (m)	1.53×1.28
Density (kg/m^3)	2500
Young's modulus (GN/m^2)	74
Poisson ratio (-)	0.3
Internal loss factor (-)	0.003

Table 5-4. Properties of the foam

Thickness (mm)	11.4
Porosity (-)	0.98
Flow resistivity (Ns/m^4)	2900
Tortuosity (-)	1.26
Viscous characteristic length (μm)	195
Thermal characteristic length (μm)	197
Density(kg/m^3)	79
Young's Modulus (N/m^2)	1079400
Poisson ratio (-)	0.45
Internal Loss factor (-)	0.35

Table 5-5. Properties of the aluminium plate

Thickness (mm)	1.5
Dimension (m)	1.51×1.26
Density (kg/m^3)	2700
Young's modulus (GN/m^2)	34.8
Poisson ratio (-)	0.34
Internal loss factor (-)	0.0009

Table 5-6. Properties of the Perspex plate

Thickness (mm)	2.9
Dimension (m)	1.526×1.276
Density (kg/m^3)	1218
Young's modulus (GN/m^2)	Shown in Figure 5.14
Poisson ratio (-)	0.3
Loss factor (-)	0.073 (shown in Figure 5.15)

The material properties of Aluminium are taken from measurements in the literature [159], and are shown in Table 5-5. For Perspex, the Young's modulus and the internal loss factor are experimentally determined using the method described in ISO/PAS 16940:2004 for glass specimens [160]. The point input impedance at the centre of a strip specimen made from the material as shown in Figure 5.13.

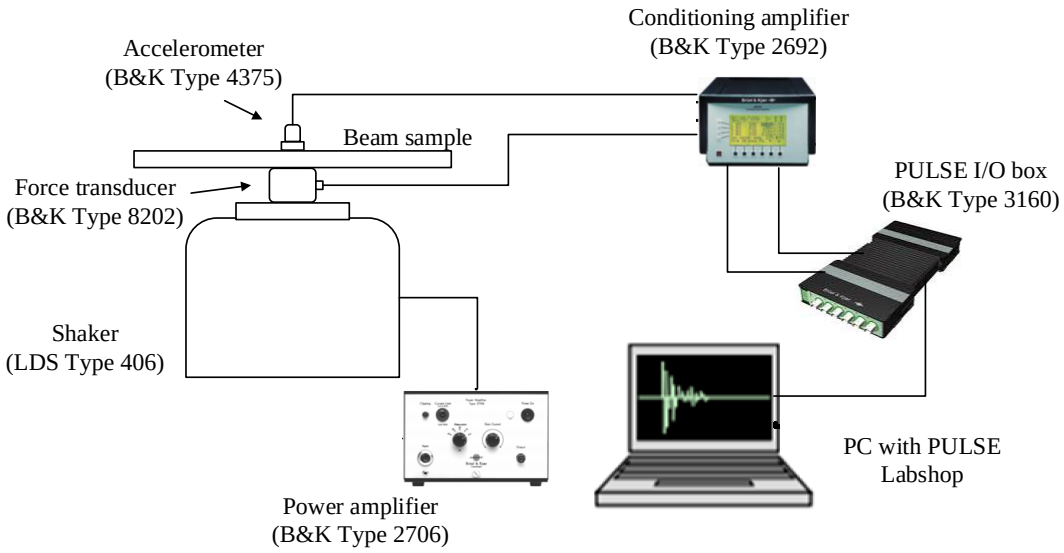

Figure 5.13. Experimental setup for the measurement of the impedance of a beam sample.

The resonance frequencies of different lengths of beam can be used to calculate the bending stiffness for a plate of the same material [7]. The relationship between the bending stiffness and the resonance frequencies is given by [160]:

$$B_{p,i} = \rho_s \left(\frac{\pi L^2 f_i}{2C_i^2} \right)^2 \qquad 5\text{-}8$$

where L is the length of the beam, ρ_s is the surface density, and f_i is the i^{th} resonant frequency, C_i is a parameter given by: C_1=1.87510, C_2=4.69410, C_3=7.85476 and C_4=10.99554. The measurement results from different resonances of 0.1, 0.2, 0.25 and 0.3 length beams are shown in Figure 5.14. Because the Young's modulus varies with frequency, therefore the fitted curve is used for the Young's modulus in this thesis.

The internal loss factor is estimated from the half power bandwidth [7]:

$$\eta_i = \frac{\Delta f_{3\text{dB},i}}{f_i} \qquad 5\text{-}9$$

where $\Delta f_{3\text{dB},i}$ is the 3 dB bandwidth associated with each resonant peak. As shown in Figure 5.15, the damping has been averaged to give a frequency-independent value.

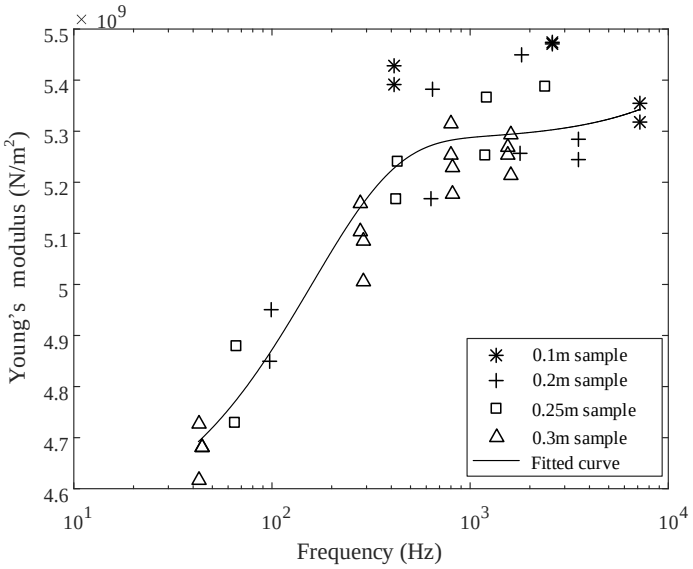

Figure 5.14. Experimentally determined Young's modulus and the fitted curve for Perspex plate.

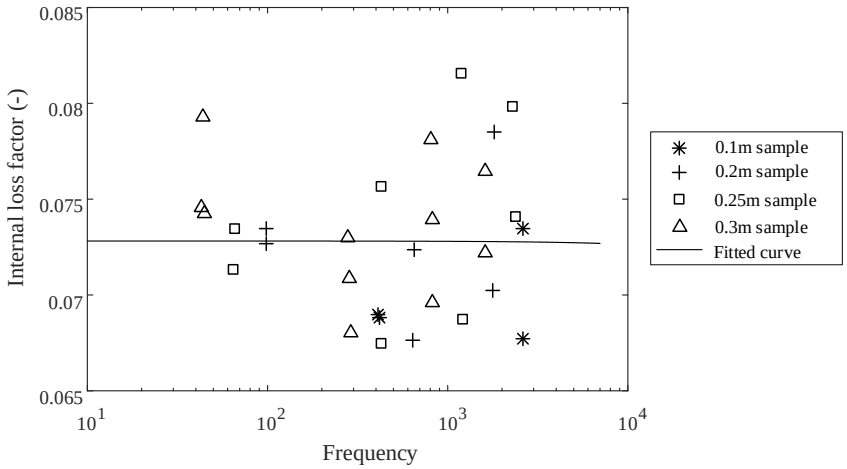

Figure 5.15. Experimentally determined internal loss factor and the fitted curve for Perspex plate.

5.5. Measurement of the total loss factor of glass fixed in a frame

The glass plate is fixed into a wooden frame with silicone sealant which affects the damping; hence measurement of the total loss factor is needed for the SEA and TMM models.

The structural damping can be calculated from the reverberation time using the equation given by [7]:

$$\eta = \frac{2.2}{fT_{60}} \qquad 5\text{-}10$$

The integrated impulse response method described in ISO 3382 [161] is used to determine the structural reverberation time. This method was introduced by Schroeder [162] to estimate the vibrational energy decay using reverse-time integration of an impulse response. To carry out this method, a Maximum Length Sequence (MLS) is generated internally using B&K DIRAC system. This signal is then fed into a shaker (LDS Type 406) via a power amplifier (B&K Type 2706) to excite the plate, and the response is measured with an accelerometer (B&K Type 4375). The impulse response is then obtained from the cross-correlation between the excitation signal which is pseudo-random white noise and the response signal. After the one-third octave or octave band filtering, the impulse response is integrated in the time domain and results in a time-decaying curve representing of the vibration levels. As a result, the reverberation time can be estimated using straight line regression over the initial part of the decay curve.

As a filter also has its own impulse response, the decay time of the filter must be shorter than the actual structural decay time to avoid filter affecting the decay curve [7]. Jacobsen [163] proposed using the BT_{60} product to assess the effect of the filter on the decay curve, where B is the filter bandwidth, and T_{60} is the actual reverberation time. ISO 3382 [161] requires that $BT_{60}>8$ in order to ensure that the measured decay curve is unaffected by the impulse response filter. As the bandwidth of a filter varies with band centre frequency, f_c, for one-third octave bands, the bandwidth $B=0.236f_c$.

In order to minimize the distortion induced by the filter, Lee [164] proposed the continuous band wavelet transform (CWT) method for the impulse response decomposition. The third-octave wavelet filter bank used in their method is the modified Morlet wavelet, whose envelope decays exponentially and has significantly less “ringing” in the tail than a typical Butterworth bandpass filter.

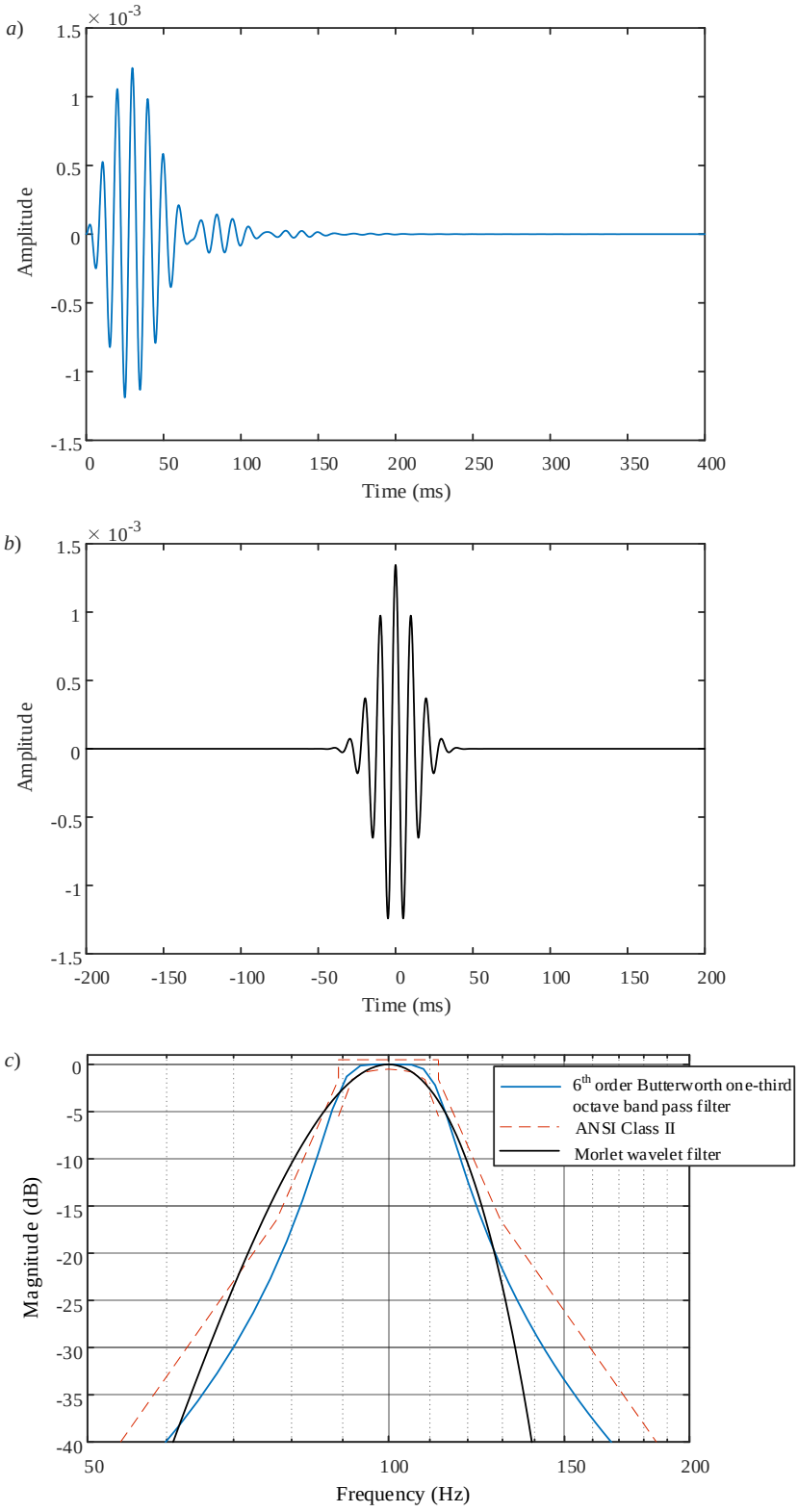

Figure 5.16. (a) impulse response of the 6th order Butterworth one-third octave bandpass filter with centre frequency at 100 Hz; (b) impulse response of the Morlet wavelet filter with centre frequency at 100 Hz; (c) frequency response of these two filters for comparison with the ANSI Class II limits.

Figure 5.16 shows a comparison between the one-third octave band 6th order Butterworth filter and the Morlet wavelet filter. The Morlet wavelet is modulated from the Gaussian function [164]. As shown in Figure 5.16, the Morlet wavelet has no "ringing" in the tail after the exponential decay. In the frequency domain, the slope of the Morlet filter has different attenuation compared with the Butterworth filter. Note that the shape of the Morlet wavelet filter is slightly out of the range of the ANSI Class II recommendation.

The effects of both filters are analysed using an idealized impulse response of the structural system which is defined as:

$$x(t) = \begin{cases} \cos(2\pi f t)\exp\left(-\frac{3t\ln 10}{T_{60}}\right) + \sigma n(t) & \text{for } t > 0 \\ 0 & \text{for all other } t \end{cases} \qquad 5\text{-}11$$

where T_{60} is the actual reverberation time, σ is the standard deviation of the white Gaussian noise.

Figure 5.17 shows the resulting energy decay analysis using a one-third octave band Butterworth filter and Morlet wavelet filter. The plot of the decay curve associated with the filter itself is shown alongside the plot of the decay curves for the idealized impulse response with $BT_{60} = 1.5$. When the reverberation time is shorter than the length of the filters, those ripples from the impulse response of the Butterworth filter also appear in the filtered energy decay curve. In order to obtain an acceptable decay curve using the Butterworth filter, BT_{60} should be at least 8 [161]. However, this distortion phenomenon can be significantly reduced using the wavelet filter bank even when BT_{60} is less than 4 [164].

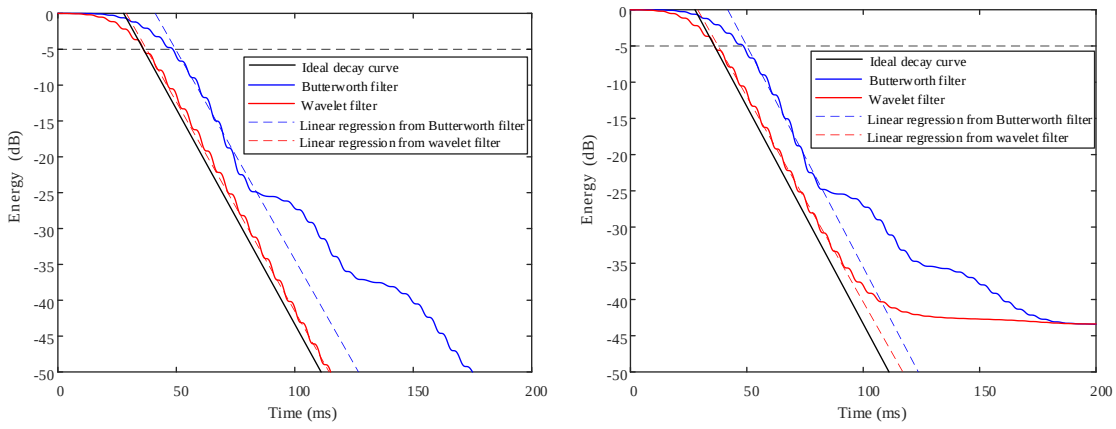

Figure 5.17. Energy decay curve calculated by one-third octave band Butterworth filter and the wavelet filter with *BT*=1.5. (a) standard deviation of background white Gaussian noise is 0.001; (b) standard deviation of background white Gaussian noise is 0.01.

Measurements on the glass plate used two excitation positions and three accelerometer positions per excitation position. Figure 5.18 shows the comparison between the measured damping using B&K DIRAC system and the wavelet filter. The main differences are at 100 and 200 Hz. The mean value of the total loss factor from six measurements over the frequency range from 100 to 5k Hz using the wavelet filter is ≈0.022.

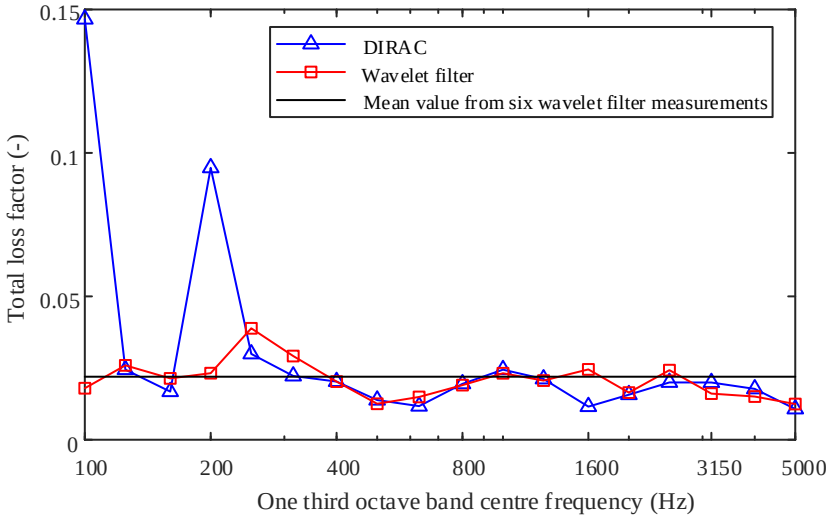

Figure 5.18. Comparison between the measured total loss factor from Dirac and the wavelet filter method for the glass plate.

5.6. Conclusions

This chapter described the experimental set-ups for the single water drop and artificial rainfall experiments.

For single drops, a wide range of falling heights has been used to estimate a new friction coefficient that can be used to estimate the drop velocity; this coefficient has wider applications to situations involving raindrops than previous work.

The force from a liquid drop impact measured by a force transducer disc is corrupted by ringing due to a resonance of the sensor system near 8k Hz. Although this ringing signal can be filtered by a band-stop filter, drops may fall outside the small sensor area, therefore small force sensors are not well-suited to the measurement of drop impacts on shallow water layers. For this reason, wavelet deconvolution method will be assessed for the force estimation and compared against the force transducer where possible.

In order to measure the total loss factor of the glass plate, Morlet wavelet filter has been applied to determine the structural decay time instead of using a typical Butterworth one-third octave band filter.

For the artificial heavy rainfall experiment, a rain box for 4.6mm diameter drops has been designed along with a baffle box to support a glass plate and multilayer plate. Two different drop heights have been implemented to obtain approximately terminal velocity and a lower drop velocity measurement required for artificial rain noise measurements according to ISO 10140-3.

6. Experimental results for the force from a single drop impact on dry and wet surfaces

6.1. Introduction

This chapter describes the experimental results for the force from a single drop impact on dry and wet surfaces.

Section 6.2 assesses the vibration signal-to-noise ratio (SNR) from a single drop impact on dry glass plate.

Section 6.3 compares the impact force estimation on a dry glass plate using force transducer measurements with wavelet measurement methods including the wavelet deconvolution from Doyle's method and the sparse representation methods.

Section 6.4 describes the impact force estimation from water drops on a shallow water layer using wavelet deconvolution and force transducer measurement.

6.2. SNR for vibration from a single drop impact on a dry glass plate

The SNR can affect the accuracy and the stability in force estimation using wavelets. The SNR of the response signal with 2 and 4.5 mm drops impacting on a dry glass plate at different drop velocities is shown in Figure 6.1. A Hanning window has been used for SNR calculation which covers the response pulse and ends when the amplitude of signal is approximately the same amplitude as the noise. Only the 2 mm drop with the lowest velocity (2.57 m/s) has <10 dB SNR over the frequency range from 10 to 6k Hz. All the other signals have a SNR>10 dB; hence it is expected that the estimation result from the wavelet deconvolution and sparse representation will be approximately the same. For this reason it is only the 2 mm drop at 2.57 m/s drop velocity that is likely to benefit from using the sparse representation approach.

When a 2 mm drop at drop velocity 2.57 m/s impacts on different water layer depths ranging from 1 to 10mm, the SNR of the response signal is >10 dB at low frequencies (10 to 3k Hz) as shown in Figure 6.2. However, the SNR is <10 dB at high frequencies (3k to 6k Hz) for $d \leq 4$mm.

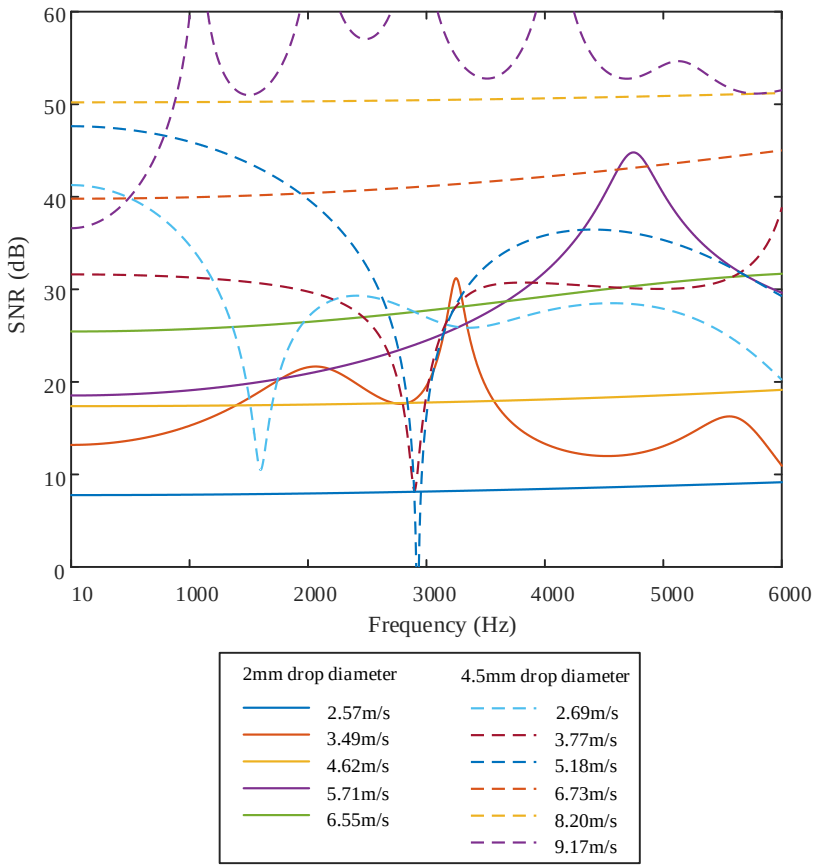

Figure 6.1. SNR for the vibration signal on a dry glass plate for 2 and 4.5 mm drops with different drop velocities.

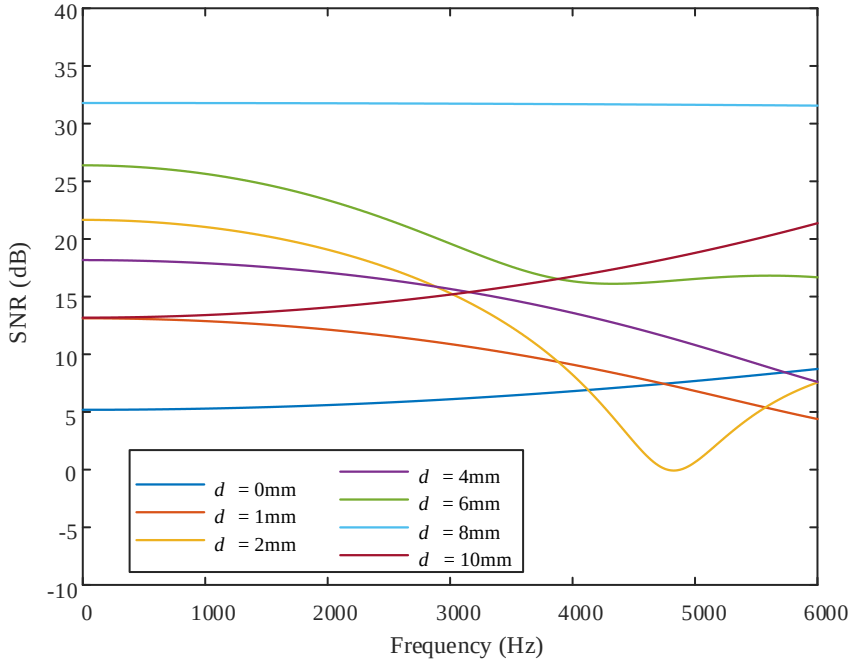

Figure 6.2. SNR for the vibration signal for a 2 mm drop impacting at velocity 2.57 m/s on a glass plate with a dry surface (d=0 mm) and different water layer depths ranging from d=1 to 10 mm.

6.3. Impact force from water drops on a dry surface

6.3.1. Comparison between wavelet deconvolution and force transducer measurements

Wavelet deconvolution describes the method using Eq. 3-9 from Doyle's method [33] in Section 3.3.1 and is compared with force transducer measurements.

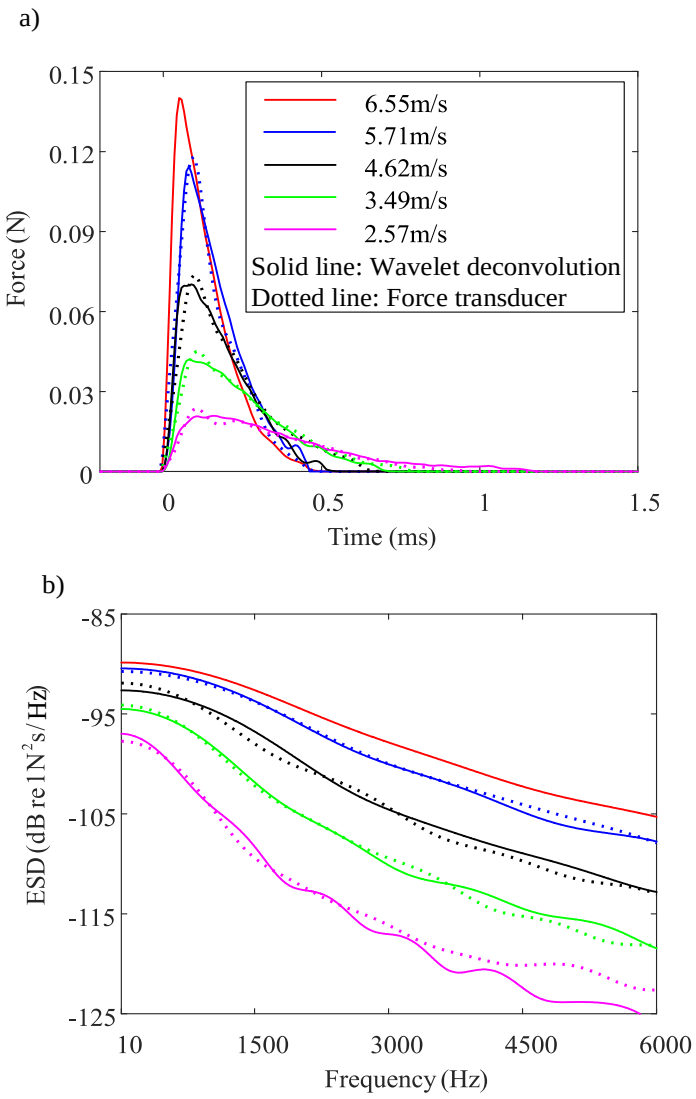

Figure 6.3. Measured force using the wavelet deconvolution approach and the force transducer for 2 mm drops with different drop velocities impacting a dry glass surface: (a) time-dependent force (b) ESD.

For 2 and 4.5mm drops, Figure 6.3 and Figure 6.4 show wavelet deconvolution and force transducer measurements for a dry glass surface in terms of the time-dependent force and the corresponding Energy Spectral Density (ESD) in the frequency domain. Note that force transducer measurements were not possible at

terminal velocity due to the variability in the position of the drop impact. This was not problematic for the wavelet approach because the impact position on the glass could be marked after the drop had impacted to allow subsequent accelerance measurements for the transfer matrix.

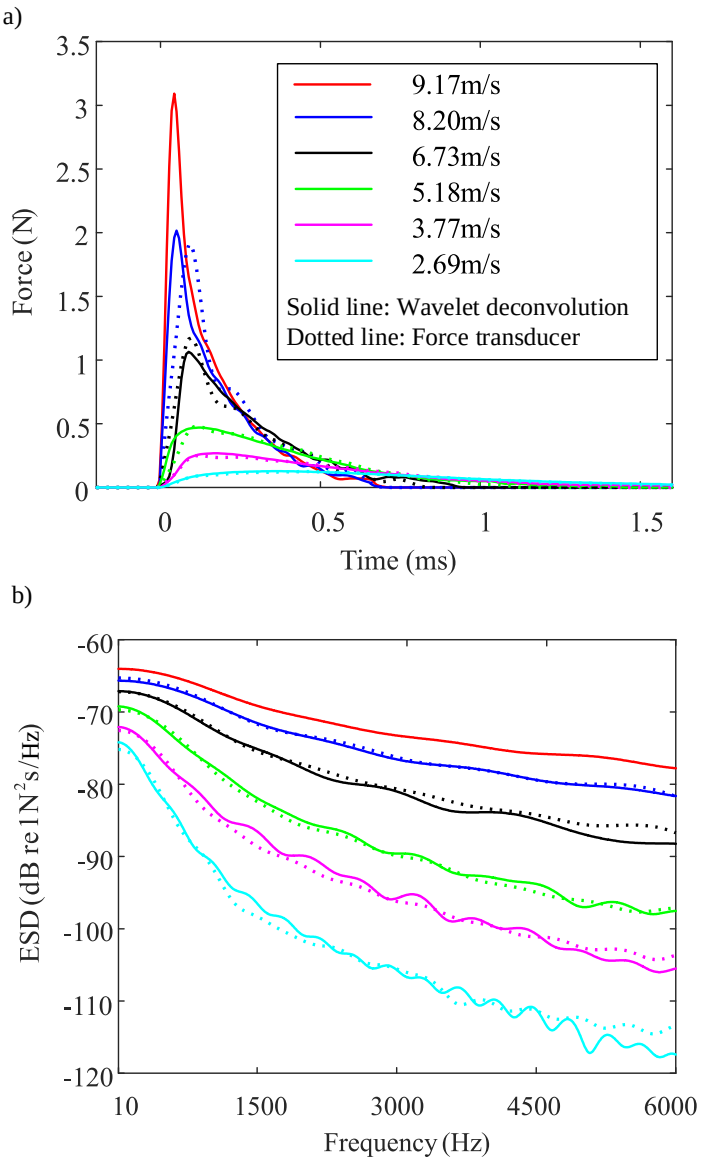

Figure 6.4 Measured force using the wavelet deconvolution approach and the force transducer for 4.5 mm drops with different drop velocities impacting a dry glass surface: (a) time-dependent force (b) ESD.

In the time domain, the peak force increases, and the pulse width decreases with increasing drop velocity. In the frequency domain, the differences between wavelet and force transducer measurements are <1.6 dB except for 2 mm drops at the lowest velocity where the former is up to 3.7 dB lower than the latter above 4.5k Hz. These

small differences are likely to be caused by the modal response of the force transducer-disc system even though a band-stop filter was used to minimise any effect. Another possible reason for this disagreement is that wavelet deconvolution is less robust for low SNRs. This is because of the compromise between noise cancellation and estimation accuracy when selecting the optimal scaling factor.

In general, the close agreement between the wavelet deconvolution approach and the force transducer measurement provides validation of the wavelet deconvolution approach. However, for the 2 mm drops at 2.57 m/s velocity, there is the potential to use a more robust method based on sparse representation.

6.3.2. Sparse representation methods based on l_1- and l_0-norm regularizations

Sparse representation methods based on l_1 norm [92] or l_p norm ($1<p<2$) [100, 101] have been validated for time history force estimation under low SNR conditions. However, l_0 norm regularization does not seem to have been applied for time history force identification. Therefore, this section discusses the validation of l_0 norm regularization method, compared with the l_1- and l_2-norm regularization.

Note that the selection of dictionary can affect the estimation accuracy [87, 88, 94], however Doyle's theory only used the bell-shaped wavelet with single resolution based on their experience in the force. In this thesis, an optimization method for the dictionary selection is proposed by the maximization of the cross correlation between the paraboloidal drop shape model and the wavelet filters, as discussed in Section 3.4.2. The sparse representation method based on l_1 norm and l_0 norm regularization applies the level 5 *coif1* wavelet as the basis function.

For a 2 mm drop at a drop velocity of 2.57m/s, the estimation results using wavelet deconvolution for 13 drop impacts are shown in Figure 6.5. As discussed in Section 3.4.1, a decrease in the SNR for the response signal can lead to a lower value of the scaling factor so that the noise can be filtered by the basis function. However, this filtering effect can possibly cancel the valid high frequency components of the force which consequently causes underestimation of the peak force. In addition, the sharp edge in the rising force curve can also be inaccurate. This can be explained by a lower value of the scaling factor having a smaller valid frequency range that can filter off the high frequency components of the noise, but also induce the Gibbs

phenomenon to the force signal. As shown in Figure 6.5(a), this Gibbs phenomenon is associated with ringing before the force pulse.

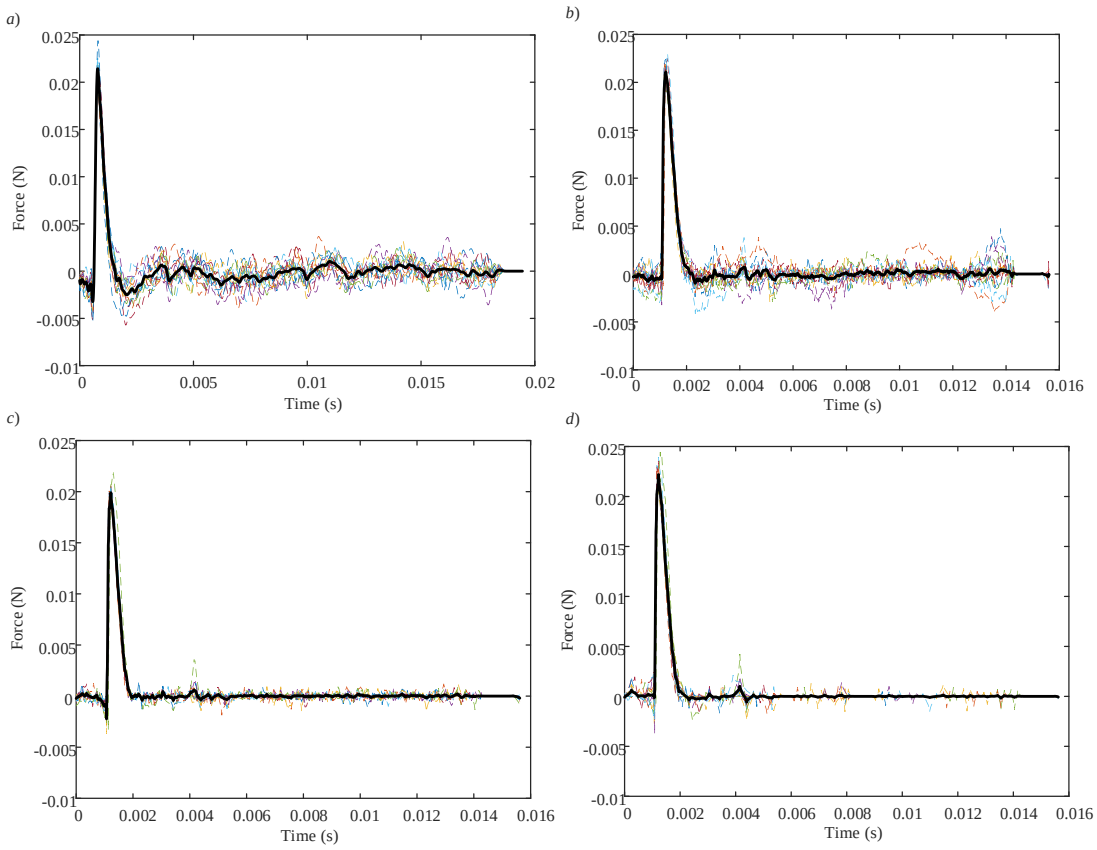

Figure 6.5. Results of the time dependent force for a 2 mm drop at a drop velocity of 2.57 m/s from 13 drop impact force estimations (thin dashed lines) and the time averaged result (solid black line) using a) wavelet deconvolution, b) l_1 norm regularization with $\lambda = 3$, c) l_1 norm regularization with $\lambda = 10$, d) l_0 norm regularization.

Figure 6.5 (b) shows the estimation result of using l_1 norm regularization based on SpaRSA algorithm [75] with $\lambda = 3$. Compared with the wavelet deconvolution, l_1 norm regularization shows better edge-preservation. Moreover, the estimation error after the initial impact has been significantly reduced. This error can be suppressed by increasing the regularization parameter, so that the sparsity level can be increased. As shown in Figure 6.5 (c), the error has been significantly suppressed by using a higher regularization parameter ($\lambda = 10$). However, the shape edge of the initial impact has been smoothed which results in an underestimate of the peak force and a negative component before the force pulse.

Therefore, l_1 norm regularization can help improve the estimation robustness compared to the wavelet deconvolution method, especially when the regularization parameter is relatively high. However, there still exists a trade-off between the estimation accuracy on the sharp edge and noise suppression.

As shown in Figure 6.5 (*d*), l_0 norm regularization has better edge-preservation at the initial impact phase, and also supresses the noise over the whole processing time interval.

The calculation time of wavelet deconvolution is more than 1 minute for each impact, whereas the l_1 norm using SpaSRA takes about 30 seconds for each impact, and l_0 norm regularization using the IHT algorithm takes only 1 second.

The results for the 2 mm drop impact on a dry surface at a 2.57 m/s drop velocity using wavelet deconvolution, sparse representation based on l_1 norm and l_0 norm regularization, and force transducer measurement are shown in Figure 6.6 and in Figure 6.7 with and without zero-padding respectively. All these curves are averaged from 13 impacts. Compared with wavelet deconvolution, sparse representation based on l_1 norm and l_0 norm regularization gives closer agreement with force transducer measurement, particularly at high frequencies. Furthermore, using sparse representation, the parameters of the wavelet basis function can be optimized in the algorithms without selecting the shifting and scaling factors.

In Figure 6.6, the sparse representation using l_0 norm regularization has the lowest ringing level in time domain and the smoothest curve in the frequency domain. The agreement between the force transducer and the l_0 norm regularization result below 6k Hz validates the use of l_0 norm regularization. l_1 and l_0 norm regularization estimation have similar result, except that the peak force from l_1 norm is lower and there is more ringing before and after the initial force pulse. Compared with l_0 norm regularization results, wavelet deconvolution methods also overestimate the peak force which increases the ESD at low frequencies.

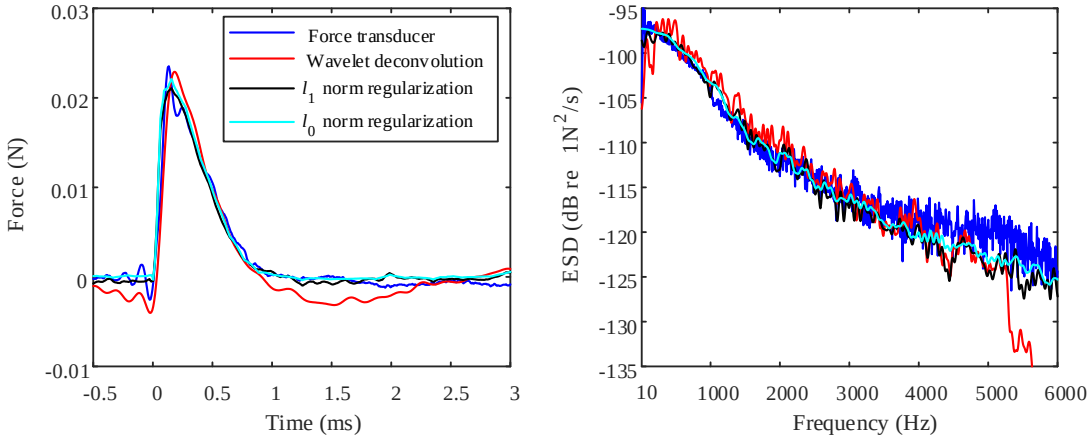

Figure 6.6. 2mm drop at a drop velocity of 2.57m/s: time domain (left) and frequency domain (right) estimation results of the impact force from different methods without zero-padding.

As shown in Figure 6.7, the sparse representation methods using l_1 and l_0 norm regularization provide steeper rising edge at the force pulse. This steep rising edge contains high frequency components which conversely have been filtered off by the wavelet deconvolution method. Therefore, using Doyle's wavelet deconvolution for this low SNR situation can lead to problematic estimation, particularly at high frequencies. This is because when the SNR is low, the values of scaling factors of the bell-shaped basis function tend to be larger so that the high-frequency noise can be significantly averaged and filtered out. This may also result in the cancelling of the high frequency components of the force signal.

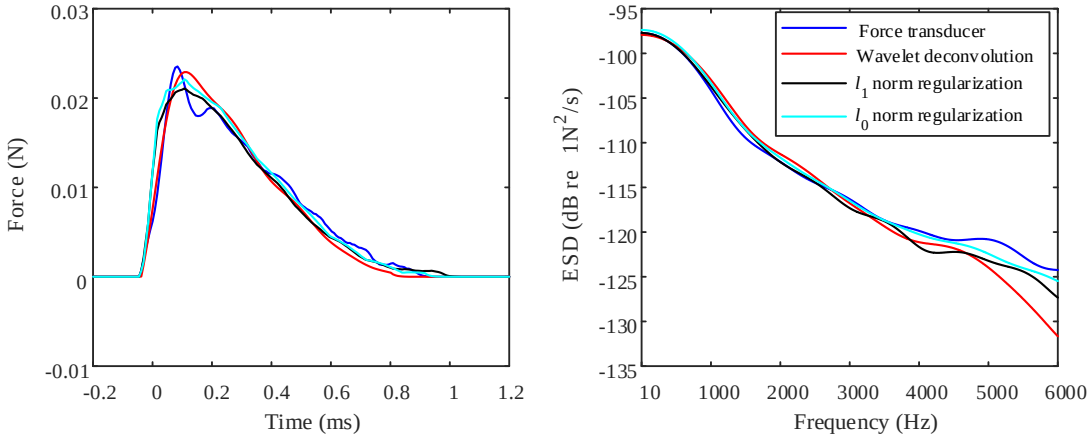

Figure 6.7. 2mm drop at a drop velocity of 2.57m/s: time domain (left) and frequency domain (right) estimation results of the impact force from different methods with zero-padding.

Figure 6.8 shows the comparison between the impact force of 2 mm drop impact on a dry glass plate with different velocities between the wavelet deconvolution, force transducer measurement and the l_0 norm regularization. It is observed that these three methods have less than 1.6 dB difference between them from 1 to 6k Hz, except for the lowest velocity in this experiment.

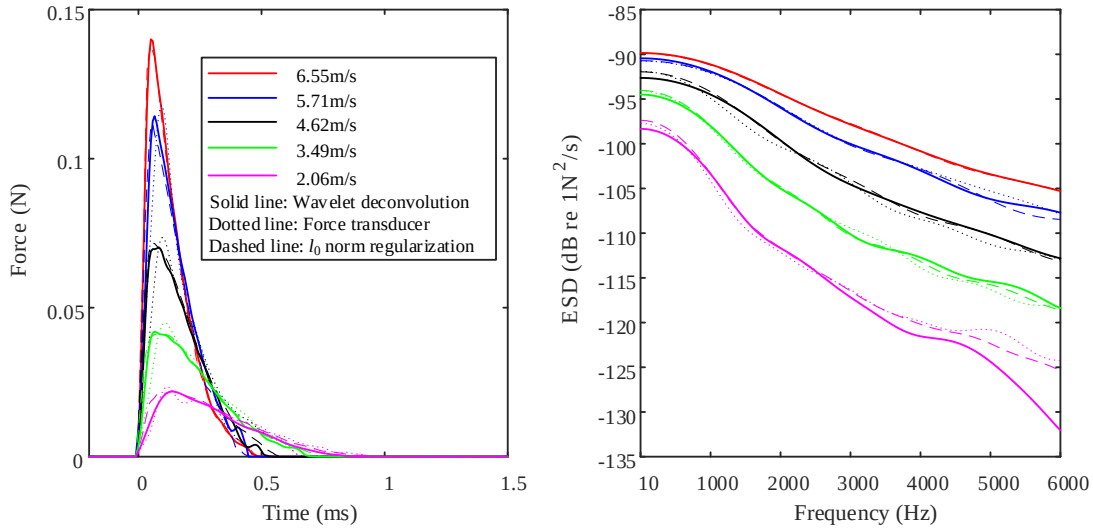

Figure 6.8. Comparison of 2 mm drop impact force on dry surface at different velocities from wavelet deconvolution, force transducer measurement and l_0 norm regularization with zero-padding.

6.4. Impact force from water drops on a shallow water layer

6.4.1. Analysis of the drop impact

For drops falling on a shallow water layer, the forces applied after the initial impact are not all applied at the same position. After the crater in the water layer has reached its maximum diameter, capillary waves propagate outwards over the water layer and these can be expected to exert low-level forces over a wide area. To illustrate the various phenomena that occur with different water layers and drop velocity, high-speed camera images are now analysed alongside the forces measured using the wavelet approach.

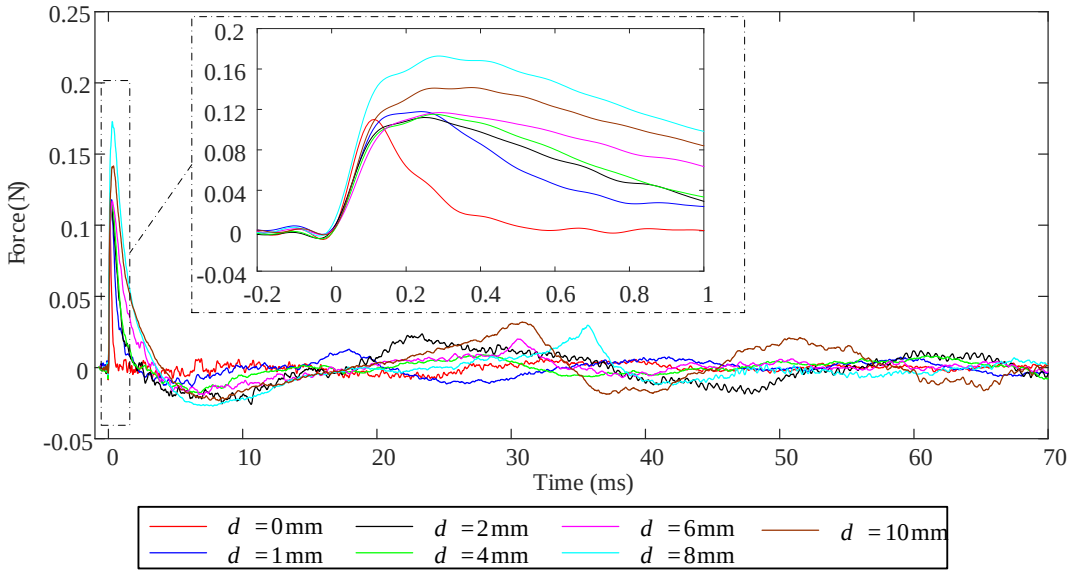

Figure 6.9. 2 mm drop impacting a water layer on glass with velocity 5.71 m/s: force measurements using the wavelet approach with a dry glass surface (d=0 mm) and different water layer depths on the glass ranging from d=1 to 10 mm (average of ten drops).

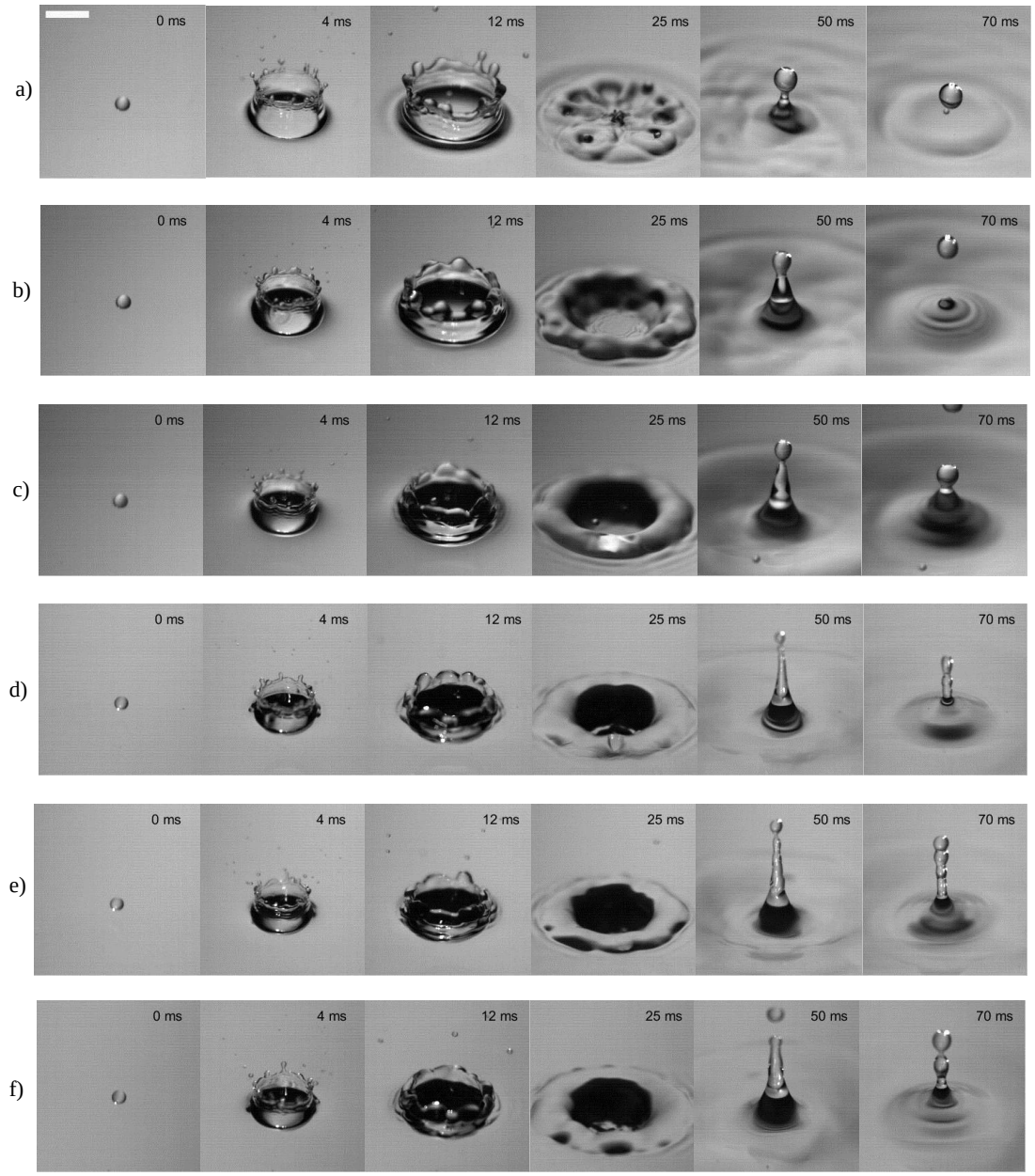

Figure 6.10. 2 mm drop impacting a water layer on glass with velocity 5.71 m/s: high-speed camera images of a 2 mm drop impact on a water layer depth of (a) 1 mm, (b) 2 mm, (c) 4 mm, (d) 6 mm, (e) 8 mm, (f) 10 mm. Time is shown in milliseconds after impact. White image scale bar is 6mm long.

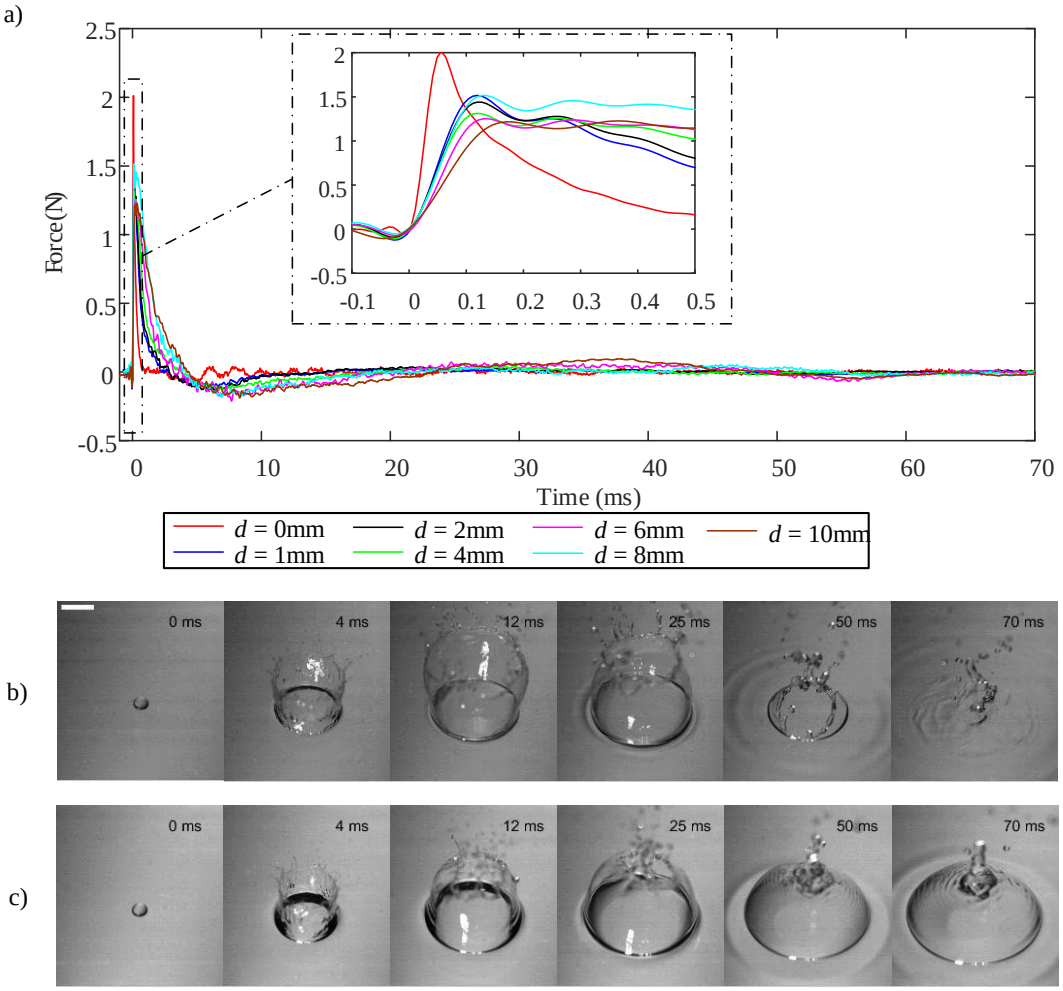

Figure 6.11. 4.5 mm drop impacting a water layer on glass with velocity 8.2 m/s: (a) Force measurements using the wavelet approach with different water layer depths on the glass ranging from *d*=1 to 10 mm (average of ten drops). High-speed camera images of a single example of a 4.5 mm drop impact on a water layer depth of (b) 1 mm and (c) 2 mm. Time is shown in milliseconds after impact. White image scale bar is 10mm long.

For the 2 and 4.5 mm drops shown in Figures 6.9, 6.10, and Figure 6.11 respectively there are distinct features relating to the splash that occur with relatively high drop velocities. During the formation of the raised crown-like perimeter after the initial impact, a negative force occurs as the water moves upwards, and drops detach from the tines around the perimeter of the crown (see Figures 6.9, 6.10). The crown diameters are ≈15 mm and ≈31 mm for the 2 and 4.5 mm drops respectively. Between 15 and 40 ms when the crater is formed, there is a slight peak in the force that occurs at different times depending on the depth of the water layer. Another feature occurs with the 4.5 mm drop that has a drop velocity of 8.2 m/s. For a 1 mm water depth, Figure 6.11 (b) shows a large bubble starting to form although it never

makes a complete hemisphere. However, for depths between 2 and 10 mm, a large hemispherical bubble is formed above the crater with a diameter between 40 and 50 mm; an example is shown in Figure 6.11 (c) for a 2 mm layer as the images are similar for thicker water depths. These large bubbles tend to rupture after 180 ms; hence whilst this is an interesting feature relating to a single drop, these bubbles are less likely to form with real rainfall due to motion of the water layer from other nearby drop impacts, and other drops falling into and breaking the surface of the bubble.

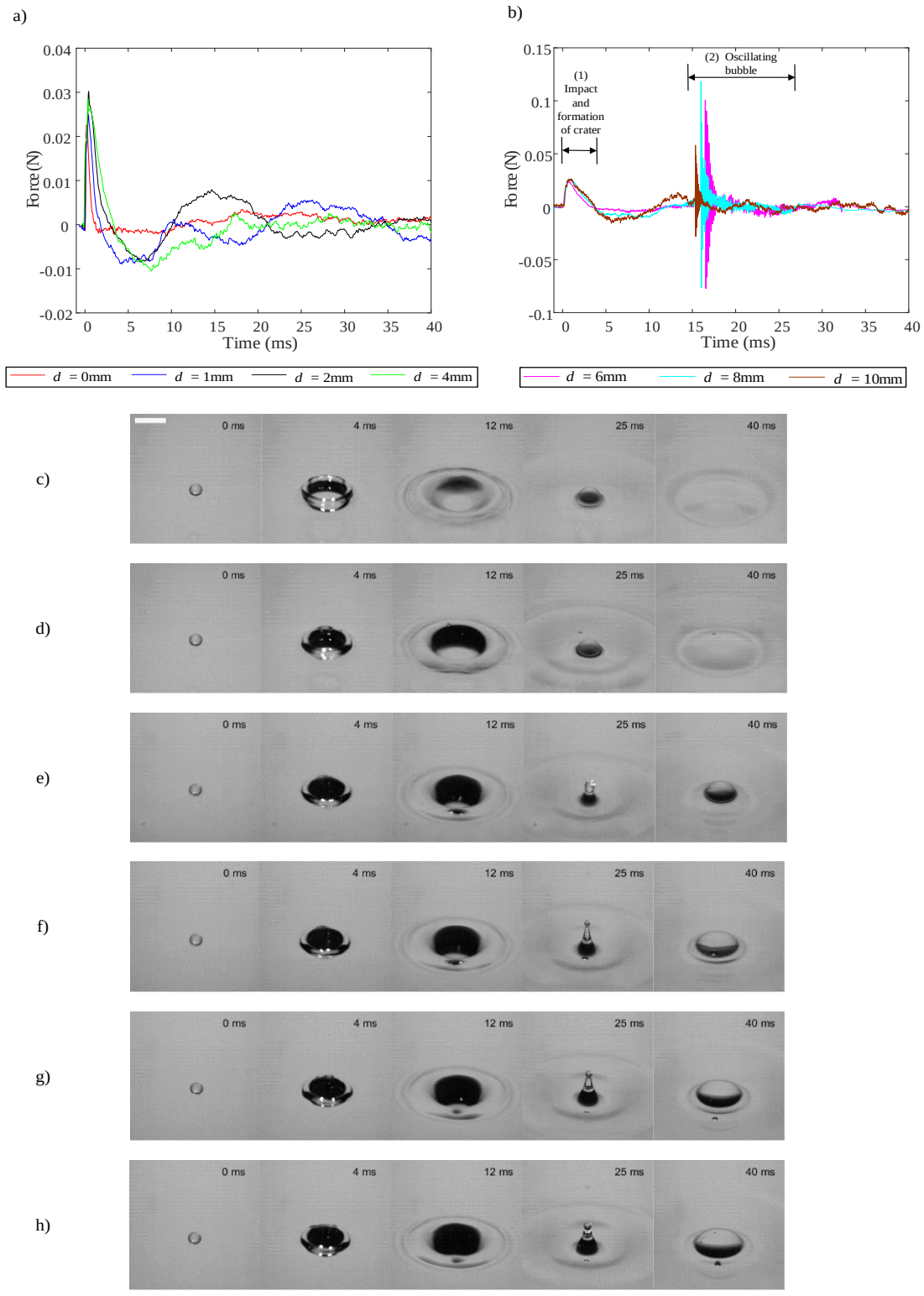

Figure 6.12. 2 mm drop impacting a water layer on glass with velocity 2.57 m/s. Force measurements using the wavelet approach (a) with a dry glass surface (d=0 mm) and water layer depths on the glass of d=1, 2 and 4 mm (average of ten drops) and (b) with water layer depths on the glass of d=6, 8 and 10 mm (average of ten drops). High-speed camera images of a single example of a 2 mm drop impact on a water layer depth of (c) 1mm, (d) 2 mm, (e) 4 mm, (f) 6 mm, (g) 8 mm, (h) 10 mm. Time is shown in milliseconds after impact. Time is shown in milliseconds after impact. White image scale bar is 5mm long.

For a 2 mm drop with a relatively low velocity of 2.57 m/s, the impacting drop coalesces without a splash. The measured forces are shown on Figure 6.12(a) and (b) depending on whether there are bubbles that are regularly entrained in the water layer [58]. In the centre of the crater a hemispherical dome is produced for 1mm and 2 mm water layer depths, whereas a short jet is produced for 4, 6, 8 and 10 mm depths although no drops detach from these jets. For 2 mm drops falling on 6, 8, and 10 mm water layers, bubbles are regularly entrained underneath the surface which are pinched off from the bottom of the crater. For lower depths, the water layer is not deep enough to allow complete formation of a crater, so bubbles are not entrained at the bottom of the crater. As shown in Figure 6.12(b), the oscillating bubble acts as an exponentially decaying high-frequency sinusoid that can produce significantly higher forces than the initial impact. The importance of the force applied by the oscillating bubble compared to the initial impact is assessed by windowing and zero padding (a) the initial impact, and (b) the pulse associated with the oscillating bubble. This gives the ESD for the initial impact and the bubble as shown in Figure 6.13. Below 200 Hz the force from the initial impact tends to be at least 9, 7 and 20 dB higher than the bubble-induced force for the 6, 8 and 10 mm water layers respectively. However, above 700 Hz the bubble-induced force tends to become significantly higher than that from the initial impact with high peak levels at 6.5k, 8.3k and 18.8k Hz corresponding to the bubbles generated for the 6, 8 and 10 mm water layers respectively. The frequencies, acoustic pressure and the directivity of sound radiation generated by these drops depends on the bubble size and their proximity to the surface of the water and the glass [58].

Note that the force hammer has a flat spectrum up to 8k Hz (refer back to Figure 5.1), therefore the initial impact force is reliable below 8k Hz. At higher frequencies up to 20k Hz, the transfer matrix is measured by normalizing the acceleration over the force, therefore, the force can still be determined when the SNR of the acceleration and force signals is sufficient.

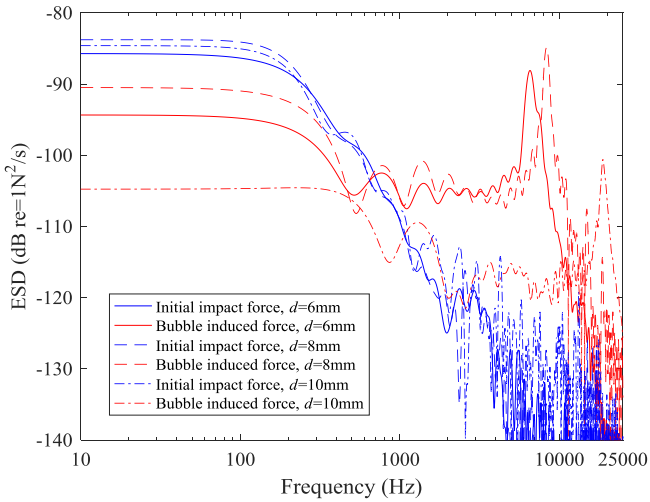

Figure 6.13. Comparison between the ESD of the initial impact force and the bubble induced force: 2 mm drop with velocity of 2.57 m/s impacting onto a 6 mm water layer (average of the response from 10 drops), 8 mm water layer (average of the response from 10 drops), and 10 mm water layer (one drop).

6.4.2. Validity of the wavelet approach for forces applied after the initial impact

For the initial impact the force transducer and wavelet approach give similar results (which will be seen in Section 6.4.3). After the initial impact it is evident that trying to contain a shallow water layer over a small area will introduce errors in the force that is measured during the formation of the crown up to the point that rebounding drops from the jet return to make impact. This partly occurs because the diameter of the glass disc on the force transducer is 30 mm, which is similar to the largest diameter of the crown or crater. It is also because the water that is displaced is constrained and capillary waves are not able to propagate freely away from the impact zone, they are reflected from the tape around the perimeter which is used to contain the water layer above the force transducer. In fact, sometimes water spills over the edge of the tape. This provides reasons to consider the validity of the inverse method after the initial impact.

The wavelet approach requires measured transfer accelerances with point excitation at the same position as the drop impact. These measurements used a force hammer with a 3 mm diameter tip, which is approximately mid-way between the 2 and 4.5 mm drop diameters. Hence the accelerance measurements are considered valid for the initial impact force because the excited areas are very similar. However,

the forces that occur after the initial impact are not all applied at the same position. The features that occur after the initial impact such as the formation of the crater apply forces over the perimeter of a circle with a diameter up to 7 mm, whereas the crown or vortex ring would apply forces over the perimeter of a circle with diameters between 15 and 31 mm. The jet emanates from a point that is close to the drop impact position; hence any forces associated with it should be reasonably estimated with point excitation. Some, but not all of the rebounding drops emanating from this jet will fall within the maximum crater diameter.

To make an assessment of the potential error in the forces applied after the initial impact it is assumed that in-phase forces are applied around the perimeter of a circle. Assuming an infinite plate, the driving-point accelerance with a response point at a distance, R_0, can be calculated for in-phase forces around the perimeter of a circle with radius, r_c, and for point excitation. The ratio of these two accelerances is given by

$$\frac{\int_0^{2\pi} H_0^{(1)}(k_B R(\theta)) - H_0^{(1)}(ik_B R(\theta))\,\mathrm{d}\theta}{2\pi\left[H_0^{(1)}(k_B R_0) - H_0^{(1)}(ik_B R_0)\right]} \qquad 6\text{-}1$$

where k_B is the wavenumber for bending waves, $H_0^{(1)}$ represents the Hankel function of the first kind and

$$R(\theta) = \sqrt{(R_0 + r_c \cos\theta\,)^2 + r_c^2 \sin^2\theta} \qquad 6\text{-}2$$

a) b)

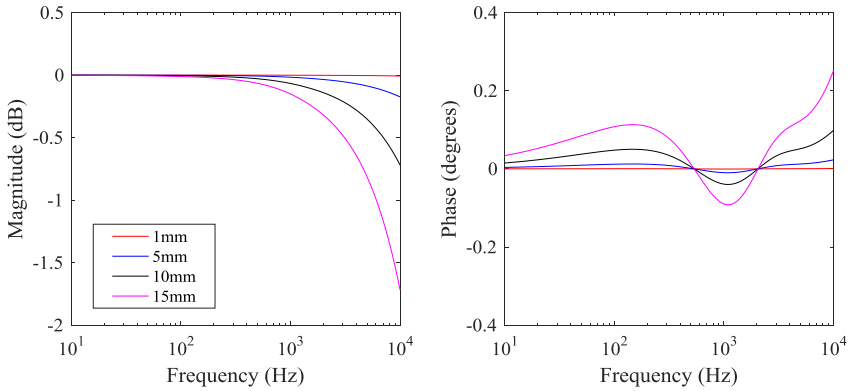

Figure 6.14. Ratio of accelerance for a circle of in-phase force with radius, *r*, to point excitation (a) magnitude and (b) phase.

Results from Eq. 6-2 are shown in Figure 6.14 that can be interpreted in the light of expected measurement errors. For the magnitude, it is reasonable to assume that the maximum measurement uncertainty in narrow band accelerance would be 1 dB and that for the phase the variation between different accelerometers would be <0.4° [7]. On this basis, an error of 1 dB in the accelerance would give an error in the impact force of ≈1 dB below 6k Hz. For this reason, it is concluded that after the initial impact the wavelet approach can still be used to estimate the forces (within 1 dB) that are applied by the crater, crown, jet, vortex ring, or oscillating bubbles. However, rebounding drops can fall at many different positions on the plate and therefore it is difficult to assess the accuracy for these forces. The low-level forces applied by capillary waves propagating away from the crater will not be correctly estimated by the wavelet approach. For rebounding drops these forces tend to be negligible in comparison with the initial impact and the oscillating bubble, but this may not always apply to the capillary waves. For this reason, the focus in Section 6.4.3 will be on comparing force transducer and wavelet approaches for the initial impact on different depths of water layer and then developing an empirical formula for the initial impact based on measurements using the wavelet approach in Chapter 7.

6.4.3. Comparison of initial impact forces

As discussed above in Figure 6.8, using the wavelet deconvolution and l_0 norm regularization has very similar estimation result for high SNR value response signal in terms of the dry surface condition.

For a wet surface with 1, 2, 4, and 6 mm water layers, the difference between wavelet deconvolution and l_0 norm regularization is <2 dB over the frequency range from 10 to 1k Hz as shown in Figure 6.15. This is because the water layer increases the initial energy of the impact force which results in higher response signal. Therefore, the SNR is sufficient for the force identification problem when there is water layer at low frequencies (<1k Hz). At high frequencies (>3k Hz), the energy of the impact force with water layer is lower than the dry surface situation, which may result in -1 dB<SNR<10 dB as shown in Figure 6.2. Therefore, due to the significance of noise, the high frequency signal cannot be cancelled from the filter-bank based on wavelet basis, which consequently presents the small amplitude ripples in the time dependant force curves and significant difference at high

frequencies, as shown in Figure 6.15. However, the difference of the estimation result from wavelet deconvolution and l_0 norm regularization is <±2.5 dB which can be considered negligible.

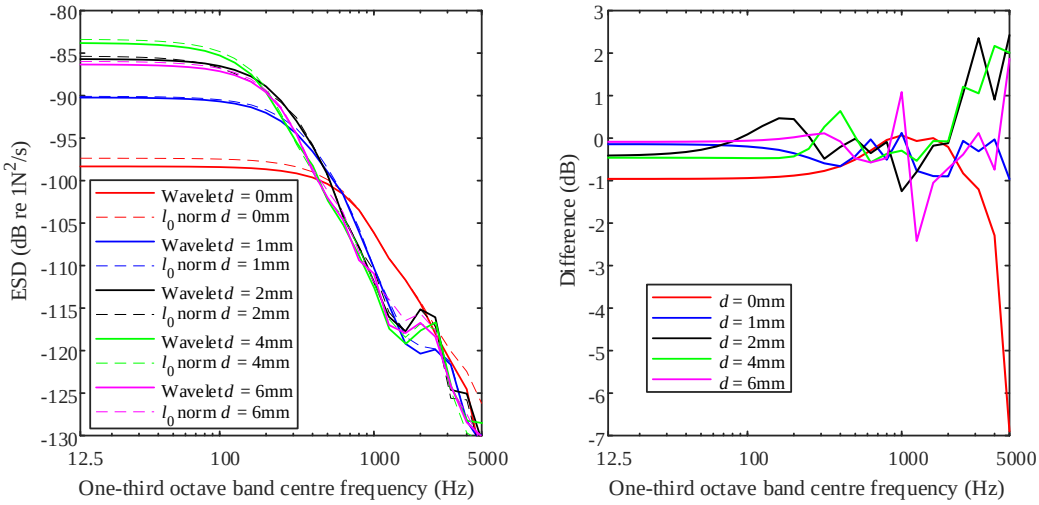

Figure 6.15. Comparison between the wavelet deconvolution and the l_0 norm regularization for 2mm drops impact on 1, 2, 4, and 6 mm water layers with a 2.57 m /s drop velocity.

Figure 6.16 and Figure 6.17 allow comparison of the initial impact forces determined using the force transducer and wavelet approach with and without a water layer for 2 and 4.5 mm drops respectively. This is carried out by zero padding the time signal after the initial impact. Note that for terminal velocity, there is significant variation in the drop impact position which prevents use of the force transducer disc due to too many 'misses'; however, the wavelet approach can be used because the excitation point can be identified after each impact. With a water layer, there are differences between the force transducer and wavelet approach in terms of the peak force and pulse width in the time domain but these only result in differences less than 3 dB between 10 and 2k Hz in the frequency domain. The differences between the force transducer and wavelet approach are more apparent with deeper water depths. Considering the errors due to the modal response of the force transducer-disc system and the effect of artificially constraining a water layer on the 30 mm disc, the wavelet approach is considered to be more accurate and is the only one discussed in the remainder of this section.

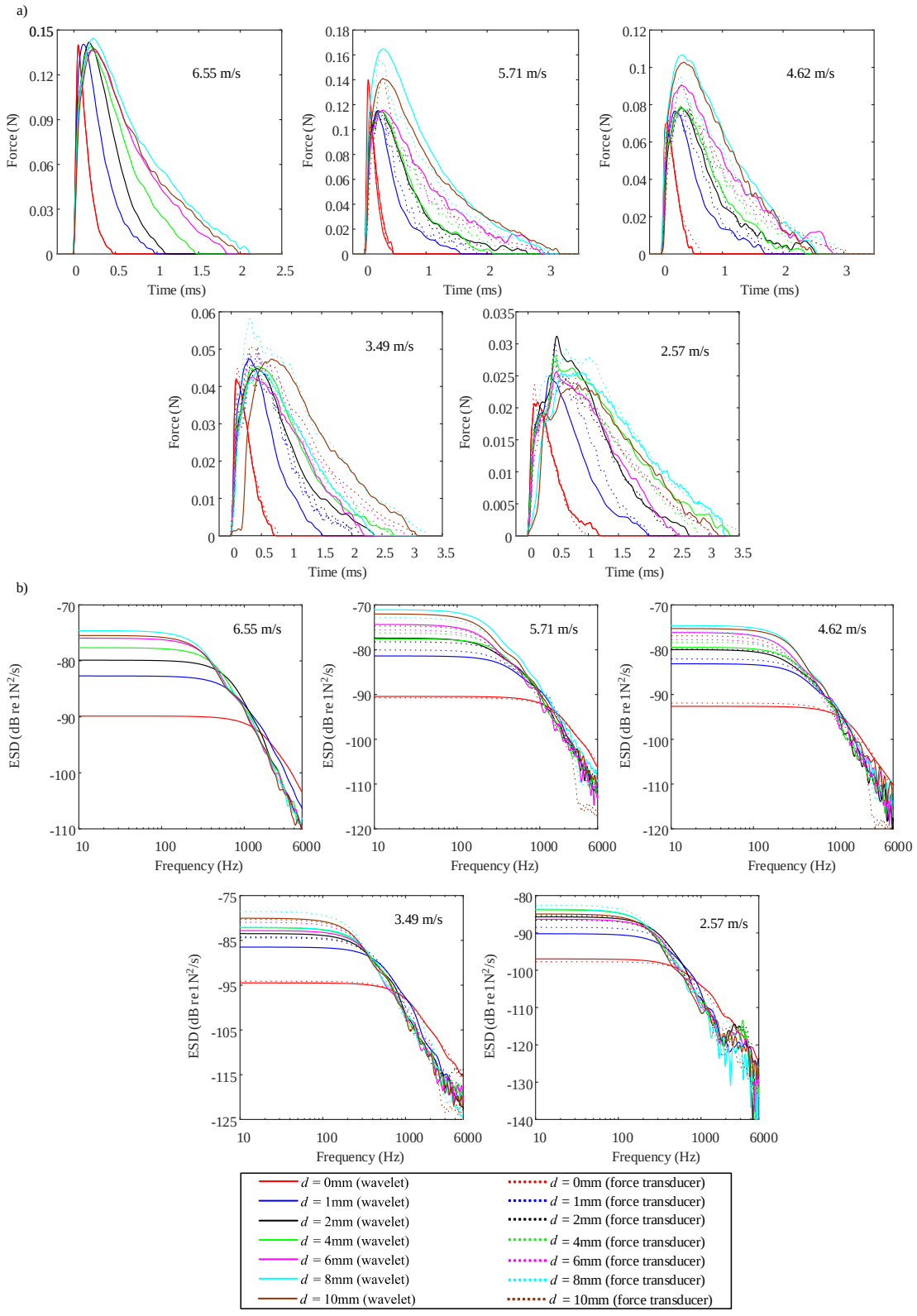

Figure 6.16. Measured time dependent force (a) and ESD (b) for 2 mm drops with different drop velocities impacting the dry glass surface (d=0 mm) and different water layer depths on the glass from d=1 mm to d=10 mm. Force measurements use the wavelet approach (solid line) and force transducer (dotted line).

Compared with dry glass, water drops impacting the various water layers apply higher forces below 500 Hz. For drops at terminal velocity, just a 1 mm water layer increases the force by ≈7 dB for 2 mm drops and ≈5 dB for 4.5 mm drops; the general trend is that as the water layer becomes deeper, the peak force decreases and the pulse width broadens. This results in higher forces at low frequencies; for drops at terminal velocity this increase is up to ≈15 dB for 2 mm drops and ≈12 dB for 4.5 mm drops. Below terminal velocity the presence of a water layer also increases the force at low-frequencies; however, in the time-domain the presence of a water layer can either increase or decrease the peak force. Petersson [4] also noted that a water layer could increase the force at low frequencies and attributed it to the energy of the drop being transferred to the water layer on the surface. However, this explanation does not seem to be sufficient to explain the differences in the peak force (time-domain) with different drop velocities because it takes no account of the effect of drop velocity on coalescence with different water layer depths and the area over which the force is applied on the glass. At high frequencies there is evidence that, compared with dry glass, the water layer gives lower forces above 2k Hz. However, this change is not as significant as the increase that is observed at low frequencies which has practical implications for noise control from rain on the roof in buildings because roofs and roof glazing will have a surface water layer during the rainfall period, albeit a moving layer of water.

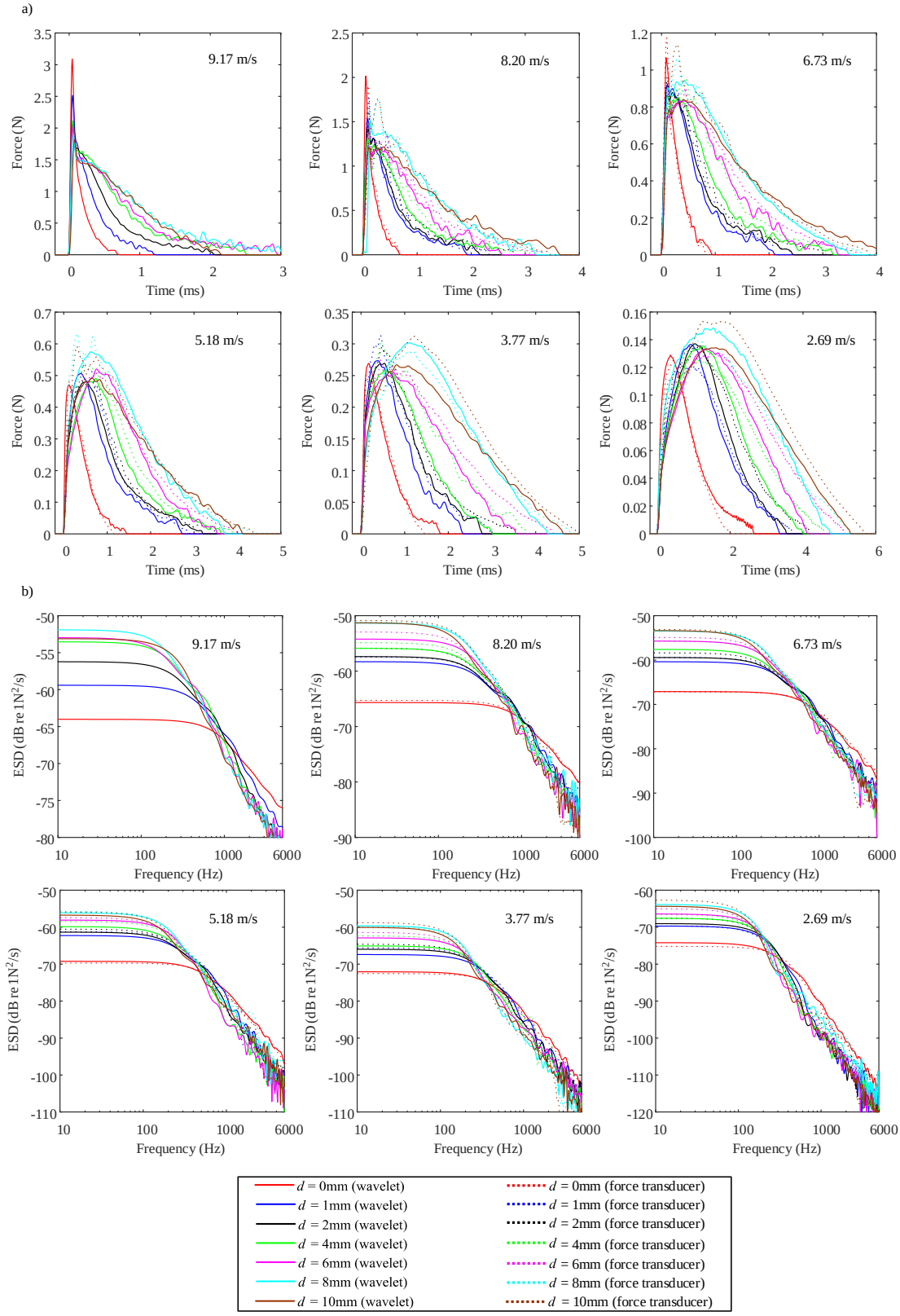

Figure 6.17. Measured data for (a) time dependent force and (b) ESD for 4.5 mm drops with different drop velocities impacting the dry glass surface (d=0 mm) and different water layer depths on the glass from d=1 mm to d=10 mm. Force measurements use the wavelet approach (solid line) and force transducer (dotted line).

6.5. Conclusions

The impact force applied by 2 and 4.5 mm liquid water drops impacting on an elastic plate with or without a still shallow water layer at a range of drop velocities has been determined using wavelet deconvolution.

For drops on dry glass, the peak force increases and the pulse width of the impact force decreases with increasing drop velocity. Wavelet deconvolution was validated by its close agreement with force transducer measurements in the frequency domain.

For drops on a shallow water layer, high-speed camera images were used to identify distinct features relating to the splash that apply forces on the plate that occur after the initial impact, such as the crater, crown, and jet as well as bubble entrainment underneath the surface of the water. This leads to measurement problems when using a force transducer with a constrained water layer because some features of the splash such as crater formation and outgoing capillary waves are no longer representative of the natural phenomena with a large area of surface water. Analysis of the measurement errors indicates that the wavelet approach can be used to estimate forces applied by the crater, crown, jet, vortex ring, or oscillating bubbles within 1 dB. However, there will be some low-level forces that cannot be accurately determined such as those from rebounding drops falling far from the original impact position, or capillary waves propagating away from the crater; fortunately their low-level makes them of little interest for the purpose of noise control. For 2 mm drops falling on 6, 8, and 10 mm layers, bubbles are regularly entrained in the water layer. Whilst the force from the initial impact tends to be significantly higher than the bubble-induced force below 200 Hz, the bubble-induced force above 700 Hz tends to become significantly higher than the initial impact with high peak levels at or above 6.5k Hz. Whilst these high forces from entrained bubbles are noteworthy, they are less critical when evaluating rain noise because water layers on roof elements are typically <6 mm deep and the radiated sound only tends to be assessed at frequencies below 6.5k Hz.

When the response signal has low SNR value (<10 dB), wavelet deconvolution becomes less robust and results in significant estimation error, which only occurs for the 2 mm drop at the lowest drop velocity. However, it is possible to use the sparse representation method to improve the estimation accuracy and meanwhile preserve

the shape edge at initial phase of the impact force from water drop. It is shown that l_0 norm regularization is better in the edge-preserving and noise suppression than l_1 norm regularization for single drop impact when the optimal wavelet basis has been selected (coif1 in the thesis).

When SNR >15 dB, wavelet deconvolution, sparse representation and the force transducer measurement have <1.6 dB difference for the initial impact force estimation on the dry surface.

7. Development and assessment of empirical models for the force from a single drop impact on dry and wet surfaces

7.1. Introduction

In this chapter, the experimental data are used to create empirical models for the time-dependent force on dry and wet surfaces. At present, there are only theoretical models for drop impact on a dry surface; hence, the validity of these models is assessed through direct comparison with measured data and the empirical models.

Section 7.2 describes the approach used to determine empirical models for the impact force on a dry surface.

Section 7.3 compares the dry surface results between the measured time-dependent force, empirical formulae, and theoretical models.

Section 7.4 describes the empirical formulae determined from the wavelet deconvolution measurement for the drop impact force on a glass plate with and without a shallow water layer.

Section 7.5 assesses whether the use of sparse representation methods for the 2 mm drop at a drop velocity of 2.57 m/s changes the empirical model developed using wavelet deconvolutions.

In Section 7.6, an angle-corrected empirical model is developed for oblique angle impacts, which is assessed by comparison with measurements.

7.2. Empirical formulae for the dry surface

In the previous chapter the wavelet approach was validated by the agreement with the force transducer, however, because the transducer-disc system can be adversely affected by ringing from the first structural mode, only the wavelet approach is used to determine the empirical formulae.

Based on the shape of the measured force profiles, the following empirical formula is proposed for the time-dependent force which is dependent on three parameters, C, α, β:

$$F(t) = F(t; C, \alpha, \beta) = C \exp[-(\ln(1000t) + \alpha)^2/\beta^2] \quad 7\text{-}1$$

The absolute error (2-norm) between this formula and the wavelet approach is minimized to give optimized parameters C, α, β in the frequency domain to cover one-third octave bands between 12.5 and 5k Hz using:

$$\underset{C,\alpha,\beta}{\operatorname{argmin}} \|F(f;C,\alpha,\beta) - F_{\text{wavelet}}(f)\|_2 \quad 7\text{-}2$$

A least squares approach is then used to give a linear relationship between the parameters ln(C), α, β and drop velocity, v_d, where

$$\ln(C) = v_d a_C + b_C \quad 7\text{-}3$$

$$\alpha = v_d a_\alpha + b_\alpha \quad 7\text{-}4$$

$$\beta = v_d a_\beta + b_\beta \quad 7\text{-}5$$

The empirical formula for the time-dependent force is given by Eq. 7-1, where

$$\ln(C) = 0.4507 v_d - 4.7951 \quad 7\text{-}6$$

$$\alpha = 0.1848 v_d + 1.3576 \quad 7\text{-}7$$

$$\beta = -0.0447 v_d + 1.2157 \quad 7\text{-}8$$

for 2 mm drops with drop velocities between 2.57 and 6.55 m/s, and

$$\ln(C) = 0.449 v_d - 3.0538 \quad 7\text{-}9$$

$$\alpha = 0.3386 v_d + 0.2325 \quad 7\text{-}10$$

$$\beta = 0.0417 v_d + 1.1023 \quad 7\text{-}11$$

for 4.5 mm drops with drop velocities between 2.69 and 9.17 m/s.

7.3. Comparison of measurements with the empirical formulae and idealized drop shape models for the dry surface

For 2 and 4.5 mm drops, Figure 7.1 shows a time domain comparison of the measured forces in Figure 7.1 (a) with empirical formulae in Figure 7.1 (b), and idealized drop shape models in Figure 7.1 (c) and the models from Roisman *et al*, Marengo *et al* and Mitchell *et al* in Figure 7.1 (d). To facilitate the comparison of these results, dimensionless force, $f(t)/(\rho_w v^2 D^2)$, and dimensionless time, $t/(D/v)$, are used as described by Zhang *et al* [165]. In the frequency domain the difference between the measured one-third octave band ESD and the empirical formulae, idealized drop shape models and the model from Roisman *et al*, Marengo *et al* and Mitchell *et al* are shown in Figure 7.2 .

In the time domain there is close agreement between measurements and the empirical formula, which justifies the shape chosen in Eq. 7-1. In the frequency domain, Figure 7.2 (a) shows that the difference between the wavelet measurements and the empirical formula is <±1 dB between 12.5 and 250 Hz, and <±4 dB between 315 and 5k Hz. For most noise control applications the empirical models can be considered to provide suitable accuracy.

Zhang *et al* [75] showed that dimensionless force and time resulted in a universal curve for the time-dependent force when *Re*>230 (described as an 'inertia-dominated zone' for the impact force). However, they used low drop velocities between 1.36 and 2.99 m/s (water drop diameters between 2.7 and 3.53 mm) whilst this thesis mainly considers higher drop velocities. The results in Figure 7.1(a) indicate that the concept of a universal curve is reasonable for all the 2 mm drops up to terminal velocity but only up to a drop velocity of 5.18 m/s for 4.5 mm drops. For 4.5 mm drops it is seen that at velocities up to terminal velocity (6.73, 8.20, and 9.17 m/s) the dimensionless force differs significantly from the other curves. This might be caused by the flattened underside of the drop which occurs at high velocities, and would be a topic for further research.

The idealised drop shape models in Figure 7.1(c) tend to show less agreement with the measured force than the empirical formulae. In the time domain, the force increases rapidly when the water drop hits the surface of the glass, then decreases as the liquid begins to spread outward. The initial rapid rise in the force is approximated by the paraboloidal, cylindrical-hemispherical, and ellipsoidal drop shape models. However, the measured peak force for 4.5 mm drops is significantly higher than all the drop shape models with the three highest drop velocities (9.17, 8.20 and 6.73 m/s) although it is a reasonable estimate for lower drop velocities (5.18, 3.77 and 2.69 m/s). For 2.5 mm drops the measured peak force is reasonably estimated by the models for the four highest drop velocities (6.55, 5.71, 4.62, 3.49 m/s) but not for the lowest drop velocity (2.57 m/s). Note that these seemingly large errors in the time domain tend to be relatively insignificant in the frequency domain (i.e. < ±2 dB) at low-frequencies (i.e. below 200 Hz) - see Figure 7.2(b) and Figure 7.2(c).

The models from Roisman *et al* and Marengo *et al* (see Figure 7.2(d)) have an offset error of ≈5 dB below 200 Hz which is significantly larger than the error with the idealised drop shape models. Above 1k Hz the agreement with measurements is no better than the idealised drop shape models. The model from Mitchell *et al* (see Figure 7.2(d)) has better agreement with the measurement data compared with other theoretical models, (e.g. <±2 dB) below the 1k Hz. Above 3k Hz, Mitchell *et al*'s model also has >5 dB error in the force prediction. This is because the 4.5mm drop

with high velocities has a flattened bottom, which is different from the spherical drop shape assumption made by Mitchell *et al*.

The motivation to develop empirical formulae comes from the fact that the idealised drop shape models, the Roisman *et al*, and Marengo *et al* model are not able to reproduce the measured spectrum to <±1 dB up to 250 Hz.

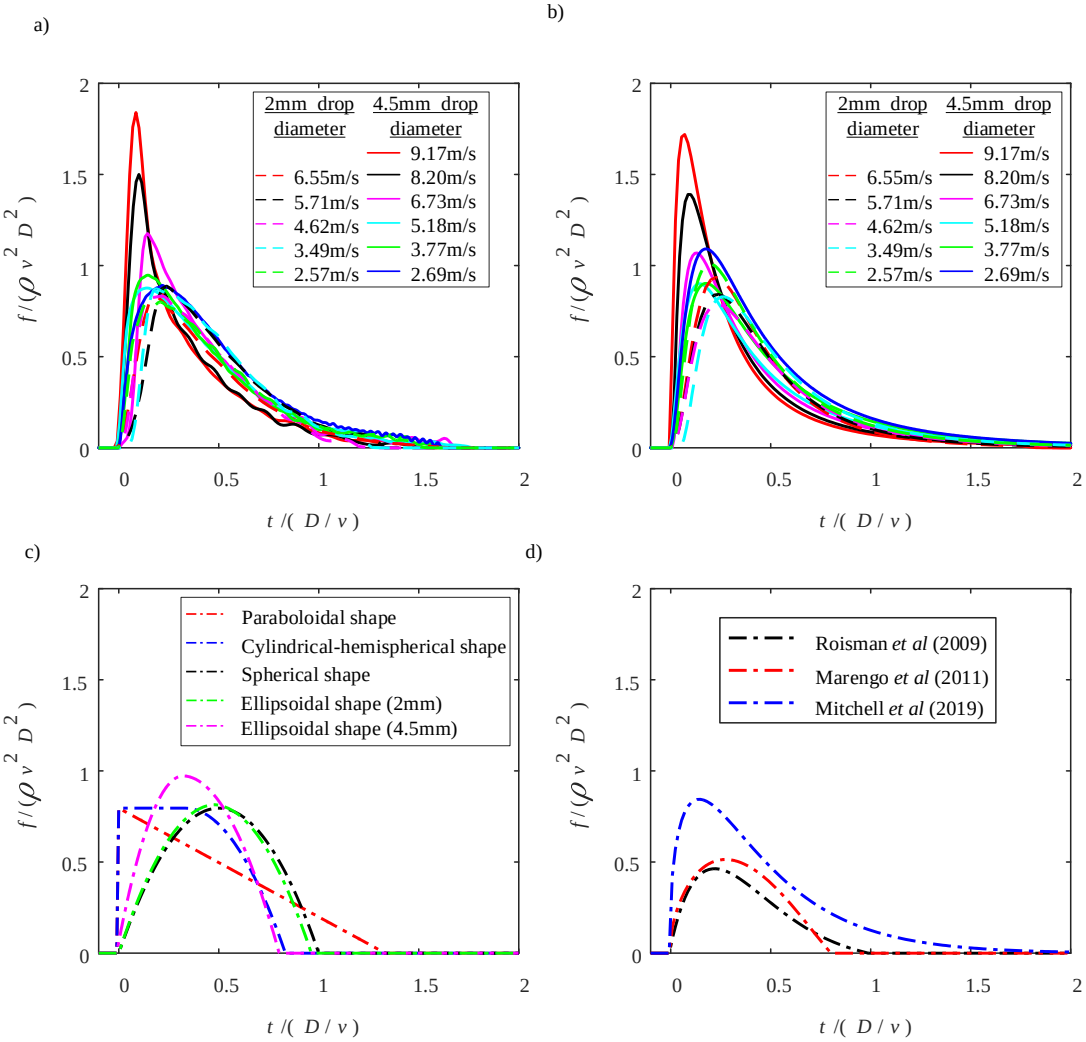

Figure 7.1. Comparison of dimensionless force between measurements using the wavelet deconvolution and different models for 2 and 4.5 mm drops with the different drop velocities impacting a dry glass surface. (a) wavelet measurement (b) empirical model (c) idealized drop shape model (d) Roisman *et al* (2009), Marengo *et al* (2011) and Mitchell *et al* (2019) models.

In the time domain there is close agreement between measurements and the empirical formula. In the frequency domain, the difference between measurements and the empirical formula is typically <2 dB for 2 and 4.5 mm drops, with the larger differences occurring above 800 Hz.

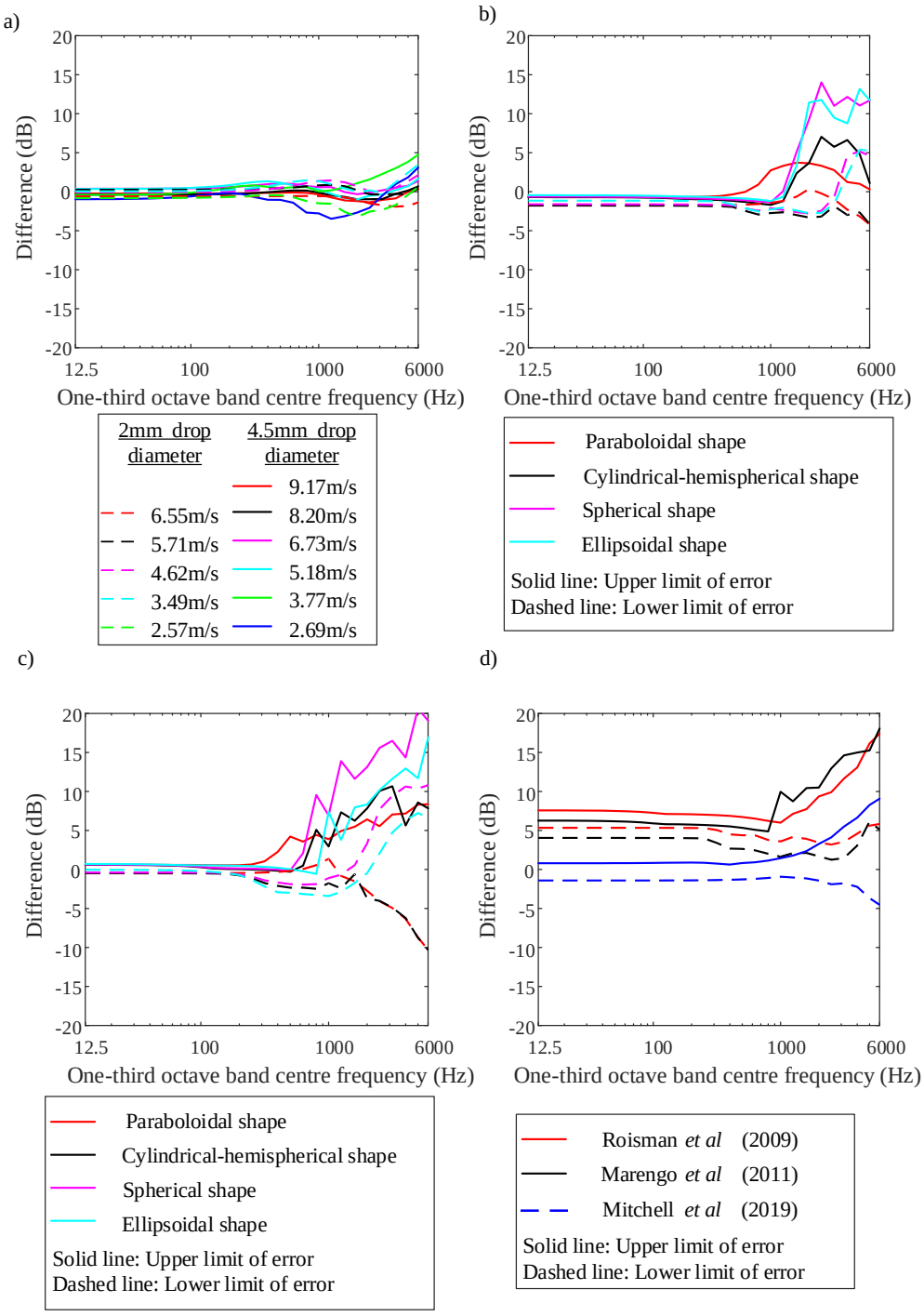

Figure 7.2. Difference in the ESD (one-third octave bands) between (a) the wavelet deconvolution measurement and the empirical formula for different drop velocities, (b) the wavelet deconvolution and idealised drop shape models for 2 mm drops in terms of the upper and lower limit from different drop velocities, (c) the wavelet measurement and idealised drop shape models for 4.5 mm drops in terms of the upper and lower limit from different drop velocities, and (d) the wavelet deconvolution measurement and Roisman *et al* (2009), Marengo *et al* (2011) and Mitchell *et al* (2019) models in terms of the upper and lower limit from different drop velocities for the 2 and 4.5 mm drops

7.4. Empirical formulae for the glass plate with and without a shallow water layer

In Sections 7.2 and 7.3, empirical formulae were determined for 2 and 4.5 mm drops on dry glass for the full range of measured drop velocities. This section determines one set of empirical formulae with a practical application to rainfall where the drops impact at terminal velocity, and another set for lower drop velocities (between 2.57 and 5.71 m/s for 2 mm drops, and between 2.69 and 8.20 m/s for 4.5 mm drops). The advantage of this approach is that it is possible to minimise the errors for the practical application to rainfall at terminal velocity.

Table 7-1. Empirical formulae constants for 2 mm drops at terminal velocity.

Water depth, *d* (mm)	***C***	α	β
0	0.1389	2.5912	0.9867
1	0.1504	2.0231	1.1196
2	0.1553	1.6889	1.1136
4	0.1504	1.5910	1.2567
6	0.1496	1.4639	1.3171
8	0.1534	1.4308	1.3934
10	0.1447	1.3864	1.3251

For 2 mm drops falling at terminal velocity onto a glass plate with or without a water layer, Eq. 7-1 is used with the empirical constants (C, α, and β) in Table 7-1.

For 4.5 mm drops falling at terminal velocity onto a glass plate with or without a water layer, the following equation is used:

$$F(t) = C_1 \exp\left[-\frac{(\ln(1000t) + \alpha_1)^2}{{\beta_1}^2}\right] + C_2 \exp[-(\ln(1000t) + \alpha_2)^2/{\beta_2}^2] \quad 7\text{-}12$$

where the empirical constants C_i, α_i, β_i; i=1,2 are given in Table 7-2.

Table 7-2. Empirical formulae constants for 4.5 mm drops at terminal velocity.

Water depth, d (mm)	C_1	C_2	α_1	α_2	β_1	β_2
0	2.7186	0	3.3367	0	1.5027	0
1	1.7168	1.5693	2.0703	2.8439	1.3129	0.4645
2	1.7673	1.2078	1.8683	2.8984	1.4361	0.509
4	1.7673	1.2220	1.6663	2.8479	1.5391	0.4787
6	1.7067	1.1250	1.5653	2.7873	1.5371	0.4403
8	1.6885	1.1008	1.4139	2.7408	1.5391	0.4726
10	1.6663	0.9756	1.3129	2.5934	1.3916	0.4141

For 2 and 4.5 mm drops falling at velocities lower than terminal velocity onto a glass plate with or without a water layer, the empirical constants (a_C, b_C, a_α, b_α, a_β, b_β) are given in Table 7-3 and Table 7-4 respectively to determine C, α and β as described by Eqs. 7-3, 7-4 and 7-5.

Table 7-3. Empirical formulae constants for 2 mm drops at drop velocities that are lower than terminal velocity.

Water depth, d (mm)	a_C	b_C	a_α	b_α	a_β	b_β
0	0.5088	–5.001	0.1748	1.3930	–0.0727	1.3148
1	0.4728	–4.7645	0.2003	0.5220	0.0270	0.9816
2	0.4402	–4.5871	0.2266	0.1213	0.0584	0.9180
4	0.4654	–4.6779	0.2605	0.0738	0.0082	1.1615
6	0.4976	–4.8194	0.1749	0.2685	0.0918	0.9180
8	0.6225	–5.1825	0.2988	–0.3846	0.1187	0.7678
10	0.5801	–5.0568	0.3165	–0.5613	0.1493	0.5681

Table 7-4. Empirical formulae constants for 4.5 mm drops at drop velocities that are lower than terminal velocity.

Water depth, d (mm)	a_C	b_C	a_α	b_α	a_β	b_β
0	0.4616	–3.1084	0.3391	0.2307	0.0381	1.1176
1	0.4227	–2.9358	0.3672	–0.7840	0.1314	0.5461
2	0.4153	–2.9193	0.3703	–0.9777	0.1392	0.4741
4	0.4035	–2.8740	0.3112	–0.9527	0.1106	0.5509
6	0.4011	–2.8439	0.2451	–0.7966	0.0654	0.8094
8	0.4023	–2.7031	0.2691	–0.9317	0.0796	0.8505
10	0.3947	–2.8019	0.2508	–0.8405	0.0875	0.8845

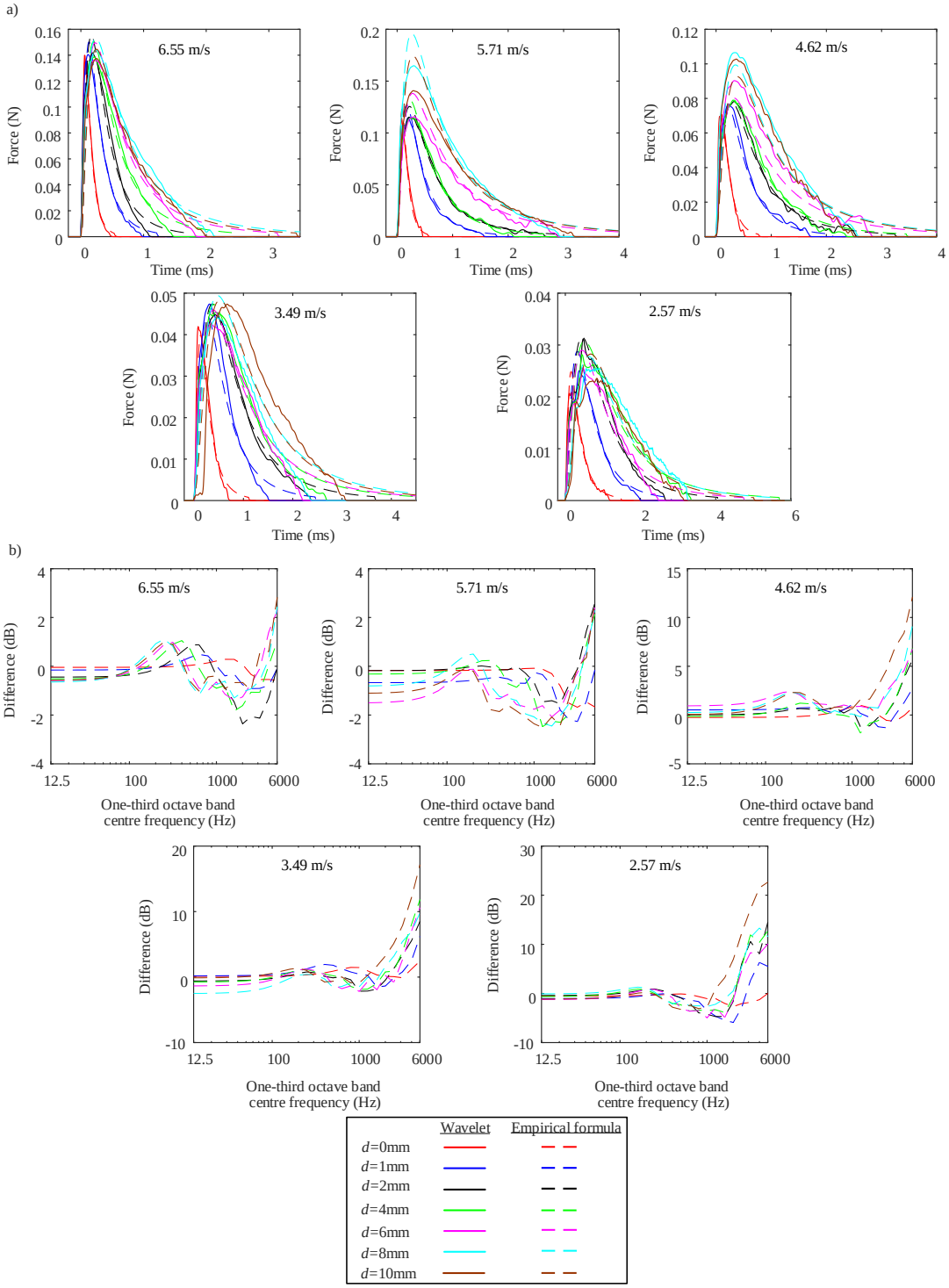

Figure 7.3. (a) Measured time dependent force and (b) difference in the ESD between wavelet deconvolution measurements and the empirical model for 2 mm drops with different drop velocities impacting the dry glass surface (d=0 mm) and different water layer depths on the glass from d=1 mm to d=10 mm.

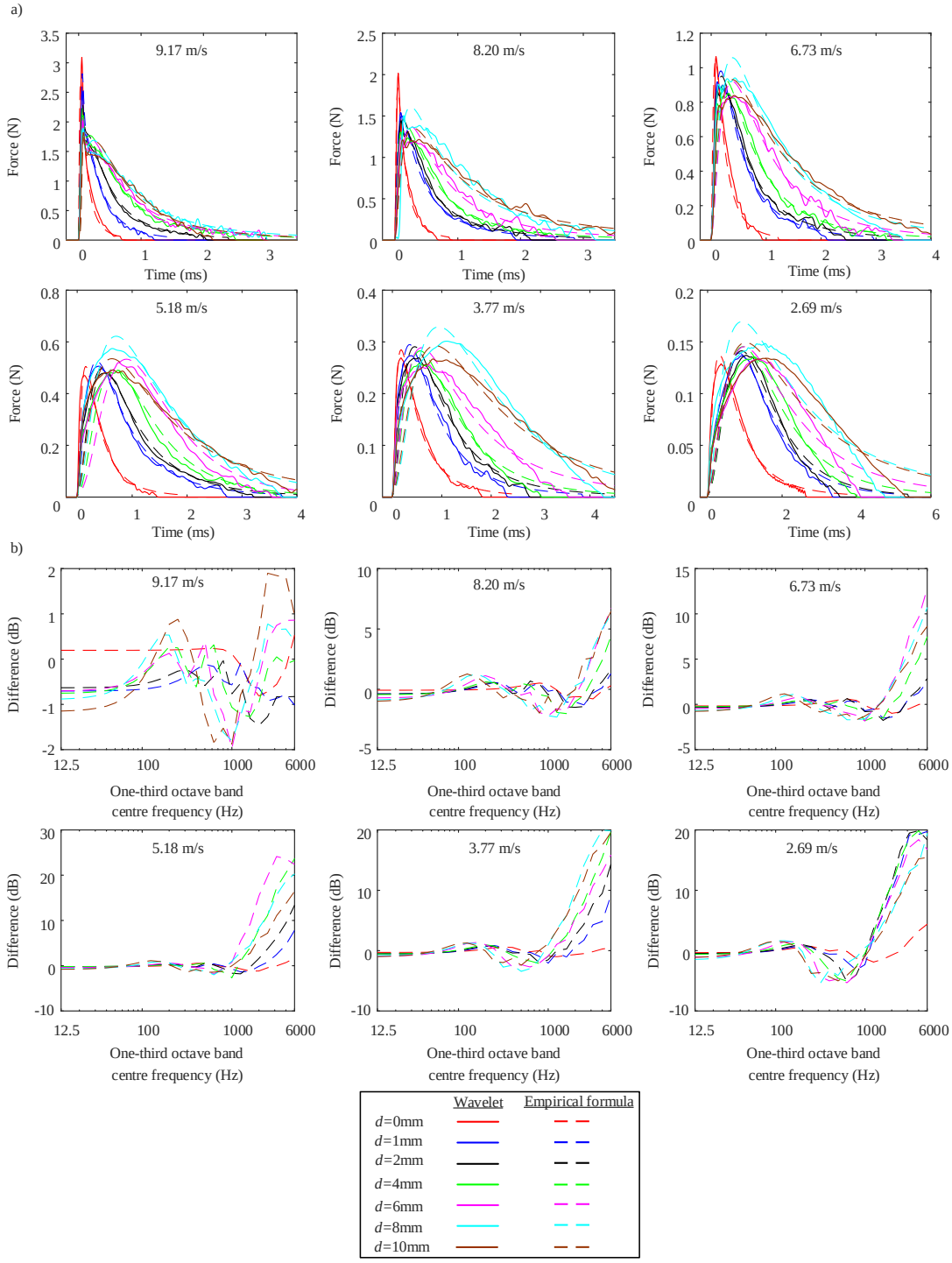

Figure 7.4. Measured (a) time dependent force and (b) difference in the ESD between wavelet deconvolution measurements and the empirical model for 4.5 mm drops with different drop velocities impacting the dry glass surface (d=0 mm) and different water layer depths on the glass from d=1 mm to d=10 mm.

For comparison with the empirical formulae, the time-dependent forces and ESD measured with the wavelet approach are shown on Figure 7.3 and Figure 7.4 for 2 and 4.5 mm drops respectively. At terminal velocity the empirical formulae for

frequencies up to 1k Hz give an error <0.5 dB for the dry surface (NB This is a lower error than was achieved with the empirical formula in section 4.2.3) and <2 dB for the shallow water layers. For drop velocities below terminal velocity, the error is typically <5 dB below 1kHz but this increases significantly at higher frequencies due to the empirical formula not accounting for ripples in the shallow water layer in the time-domain that contain high-frequency energy.

7.5. Empirical model determined by the sparse representation estimation

In Section 3.4, the sparse representation methods were shown to be more robust and accurate for the impact force estimation when the response signal has a low SNR. The SNR assessment in Section 6.2 shows that for a 2 mm drop impacts on a dry surface with a drop velocity of 2.57 m/s, the acceleration signal has <10 dB SNR, which results in the estimation error of wavelet deconvolution (refer back to Figure 6.7). Since the sparse representation method results in better estimation accuracy in low SNR situation, an empirical model based on the sparse representation results has also been developed to compare with the empirical model obtained from wavelet deconvolution.

The empirical model from these two methods have similar time dependant curves (see Figure 6.7), and as shown in Figure 7.5, the empirical model determined from the sparse representation estimation has less than 0.4 dB difference from the empirical model by wavelet deconvolution over the frequency range from 10 Hz to 6 kHz. Therefore any improvement by using sparse representation estimation method compared with the wavelet deconvolution can be considered to be negligible.

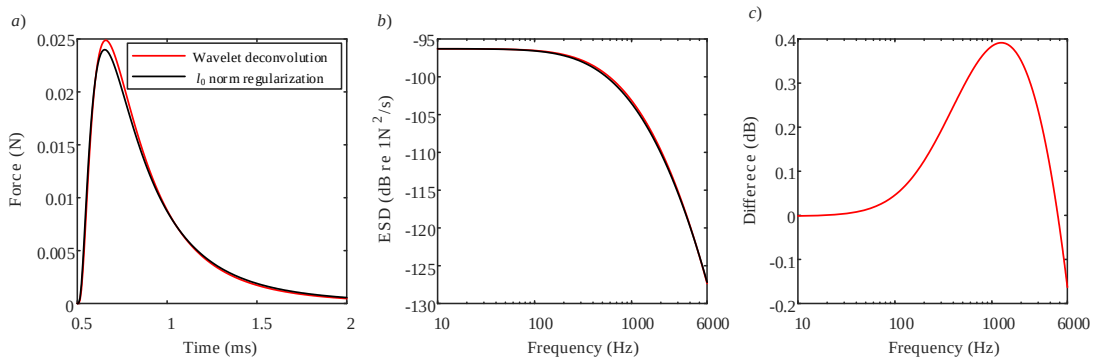

Figure 7.5. Empirical model difference determined from wavelet deconvolution and the l_0 norm regularization of 2 mm drop impact on dry surface with 2.57 m/s: a) in the time domain and b) in the frequency domain and c) the ESD difference.

7.6. Angle-corrected empirical model

The validated empirical model for drop impacts on a horizontal plate now needs to be adapted to allow oblique angle drop impacts.

In terms of the angled impact, the force pulse is mainly applied by the perpendicular component of the velocity according to the momentum theory (see Section 2.7). However, since the shape of a 4.5 mm drop at terminal velocity is not spherical (see Section 2.3 and Section 5.2.2) but has a flattened bottom, the force measured on the flat glass plate needs to be corrected to apply to oblique angles. As discussed in Section 2.7 the projection area of the oblique impact is smaller than in the horizontal situation, which results in lower peak force in the time domain. Moreover, the irregular projection area of the drop can also delay the occurrence time of the force peak.

The correction of the angled impact force is calculated using the perpendicular drop velocity as given by Eq. 2-20. Therefore the angle-corrected empirical model for 4.5 mm drops can be calculated by substituting the perpendicular drop velocity into Eqs. 7-9, 7-10 and 7-11. Figure 7.6(a) shows that the peak force in the time domain estimated by the angle-corrected empirical model is similar to the measured force and the impact force from the angle-corrected empirical model is in close agreement with the measured force (<4 dB difference over the frequency range 10 Hz to 6k Hz).

When the drop velocity increases to 9.08 m/s, the angle-corrected empirical model tends to overestimate the high-frequency energy (above 2k Hz) and underestimate the low-frequency energy (below 200 Hz) of the angled drop impact force as shown in Figure 7.6(b). This becomes more significant when the drop impact is at terminal velocity in Figure 7.6(c). The drop has a flattened bottom and therefore the projection area is smaller than the horizontal situation; hence, the force peak estimated using the angle-corrected empirical model gives rise to this error.

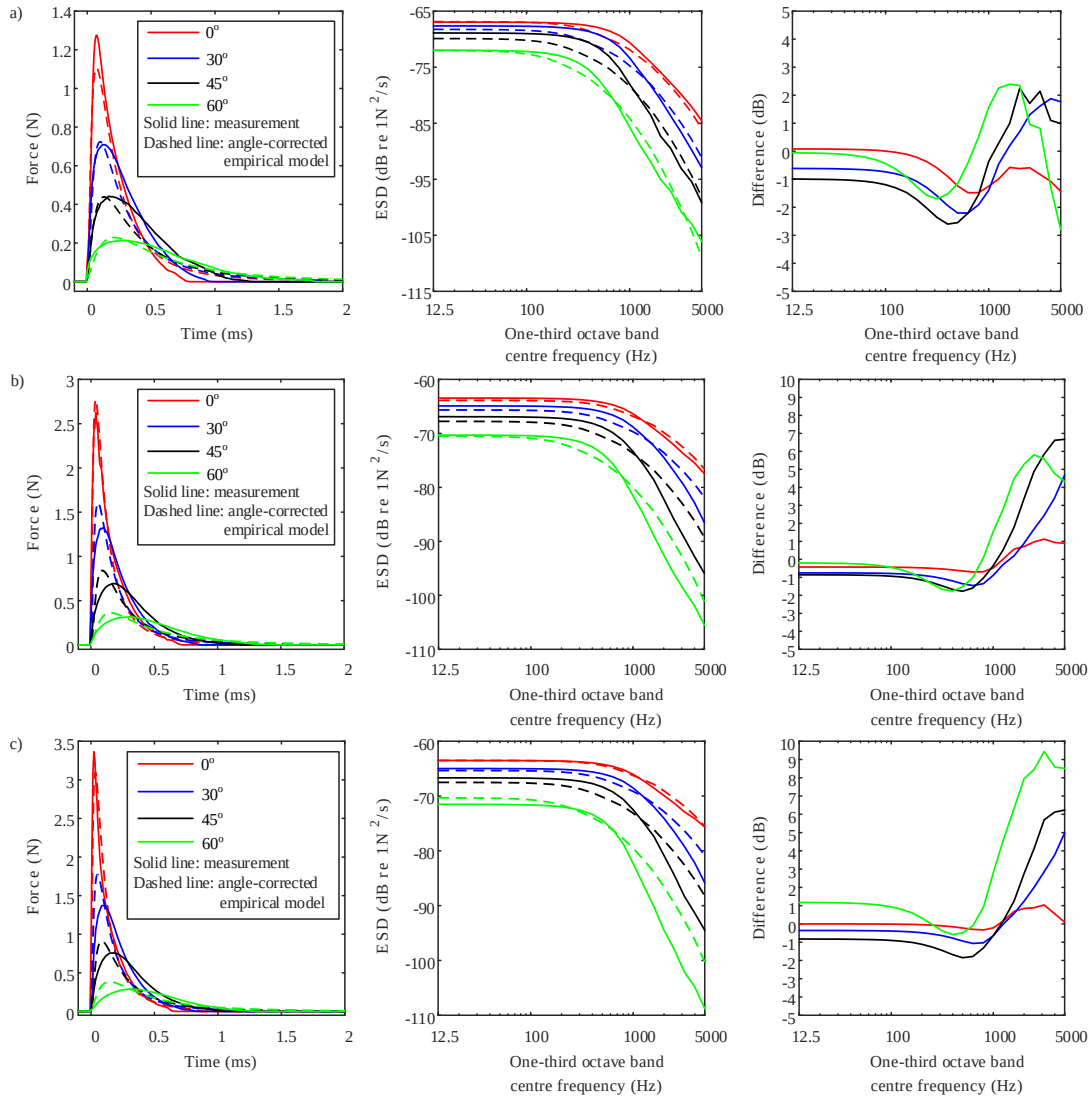

Figure 7.6. Effect of oblique angle impacts: comparison of the impact force from measurement using wavelet deconvolution (solid line) and the angle-corrected empirical model (dashed line) by 4.5 mm drops with different drop velocities: (a) 7.03 m/s (b) 9.08 m/s (c) 9.31 m/s impacting on a dry glass plate with different angles. The first column contains the time-dependent zero-padded initial impact force, the second column contains the ESD in narrow bands, the third column contains the difference between the ESD from wavelet deconvolution and the angle-corrected empirical formula.

Compared with the horizontal plate shown in Figure 7.2(a), the errors of the empirical model for an oblique angle plate in Figure 7.6 are not significantly larger below 1k Hz. Figure 7.6 shows that the difference between the wavelet measurement and the empirical formula is <±2 dB between 12.5 and 250 Hz, and <±10 dB between 315 and 5k Hz.

In order to predict the rain noise from artificial rainfall with 4.5mm drops at velocities of 9.08 and 7.03 m/s (corresponding to 11.4 and 3.65 m drop heights in

Figure 5.11), the corrected empirical model for 30^o oblique plate can lead to prediction errors which increase at high frequencies up to approximately 5 dB and 2 dB at 5k Hz for drop heights of 11.4 and 3.65 m, respectively. This angle corrected empirical model will be used in Chapter 8 for the prediction of artificial rainfall.

7.7. Conclusions

Using the measured force for water drops at different drop velocities, an assessment was made of the validity of theoretical models for the water drop impact force on a dry glass surface. At relatively high velocities (including terminal velocity) the measured peak force is significantly higher than predicted by the paraboloidal, cylindrical-hemispherical, spherical, and ellipsoidal drop shape models, and the model from Roisman *et al* (which takes the lamella into account) gives no significant improvement in the predicted force particularly for 4.5 mm drops. The inability of these prediction models to describe the time-dependent force provided the motivation to develop empirical formulae.

For a horizontal glass plate, empirical formulae have been developed for 2 and 4.5 mm drops falling at (a) different velocities up to and including terminal velocity onto a dry glass surface, (b) terminal velocity onto dry glass or glass with a shallow water layer up to 10 mm and (c) different velocities below terminal velocity onto dry glass or glass with a shallow water layer up to 10 mm. This allowed the errors to be minimised for different applications. For drops on dry glass, the empirical formulae are only strictly applicable to a glass plate or a composite layered plate with a glass surface, although they apply to any other thickness of plate. All the empirical formulae can reasonably be applied to any plate material with a similar surface roughness and wettability.

The empirical model determined from the sparse representation measurement had <0.4 dB difference when compared with the empirical model from the wavelet deconvolution measurement data. This difference is not considered significant; hence, the empirical formulae from the wavelet deconvolution measurement will be applied in Chapter 8 for artificial rainfall prediction.

For oblique angle impacts, an empirical model correction is accounted for by using the perpendicular velocity component. Comparison of the differences between the wavelet measurements for 30^o, 45^o and 60^o angles and the angle-corrected empirical formulae are not significantly larger than with empirical formulae for the

horizontal plate below 1k Hz. For 4.5 mm drop impacts at terminal velocity on a plate with 30^{o} slope, the error of the angle-corrected empirical model is $<\pm 1$ dB between 12.5 to 2k Hz, and $<\pm 5$ dB between 2k to 5k Hz.

8. Experimental validation and numerical simulation results with artificial rainfall

8.1. Introduction

This chapter uses the angle-corrected empirical model for the drop impact force with FTMM to predict vibration and sound radiation under artificial rain excitation.

Section 8.2 describes the experimental and numerical results for the vibration and sound radiation from a glass plate at an angle of 30^o under artificial rainfall at two different drop heights (including terminal velocity). The numerical models are validated using SEA and FTMM which incorporate the angle-corrected empirical model.

In Section 8.3, FTMM is used to predict the vibration and sound radiation from a multilayer plate (plate-limp porous material-plate) under artificial rainfall excitation at terminal velocity.

8.2. Glass plate at 30^o angle

8.2.1. Using SEA and FTMM to predict the plate vibration

The vibration of a plate at a 30^o angle is predicted using the force from the angle-corrected empirical model for two different drop heights, 11.4 m and 3.65 m. For the 11.4 m height in Figure 8.1, the prediction of the mean-square velocity from a glass plate using SEA and FTMM are the same to within ±0.1 dB. At low frequencies (up to 500 Hz), the prediction models with 1 mm water layer over-estimated the vibration energy, whereas dry surface model results in closer agreement with the measurement (<5 dB difference). At high frequencies (from 2k to 5k Hz), the predicted vibration has higher energy (<3dB difference) than the measurement for 4.5mm drops at terminal velocity, because of the error of the angle-corrected empirical model (refer back to Figure 7.6). However, with the 3.65m height in Figure 8.2, the empirical model has closer agreement with the measurement data at high frequencies (from 1k to 5k Hz).

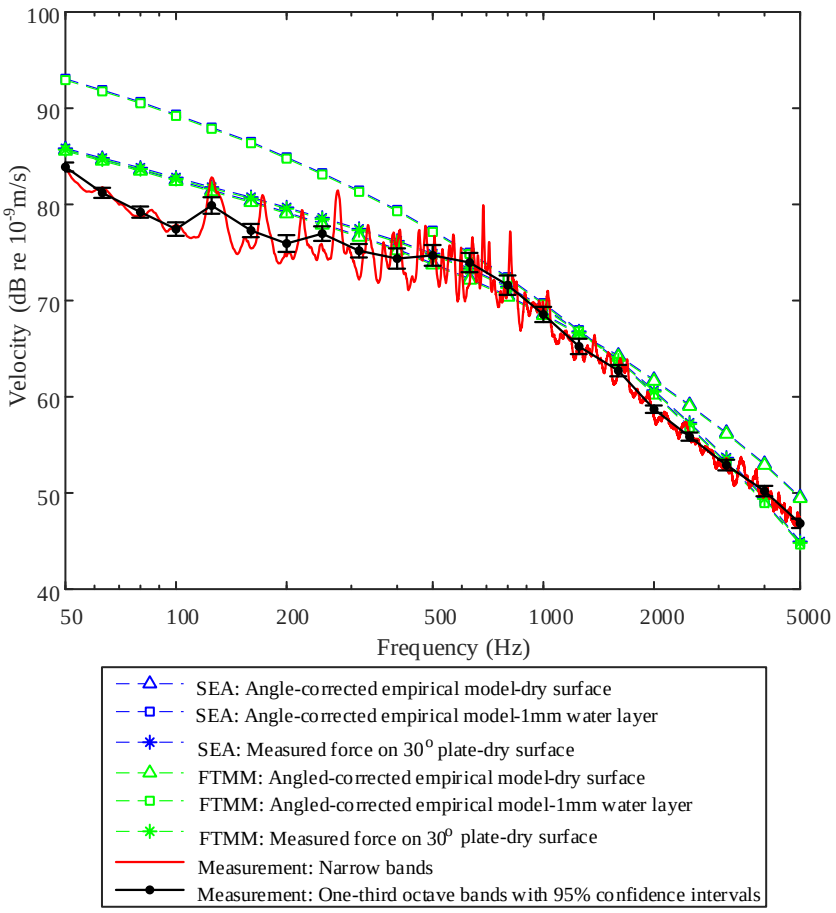

Figure 8.1. Comparison between the plate velocity prediction using SEA and FTMM (one-third octave bands) and measurement (narrow bands and one-third octave bands) of a glass plate under artificial rainfall from 11.4 m.

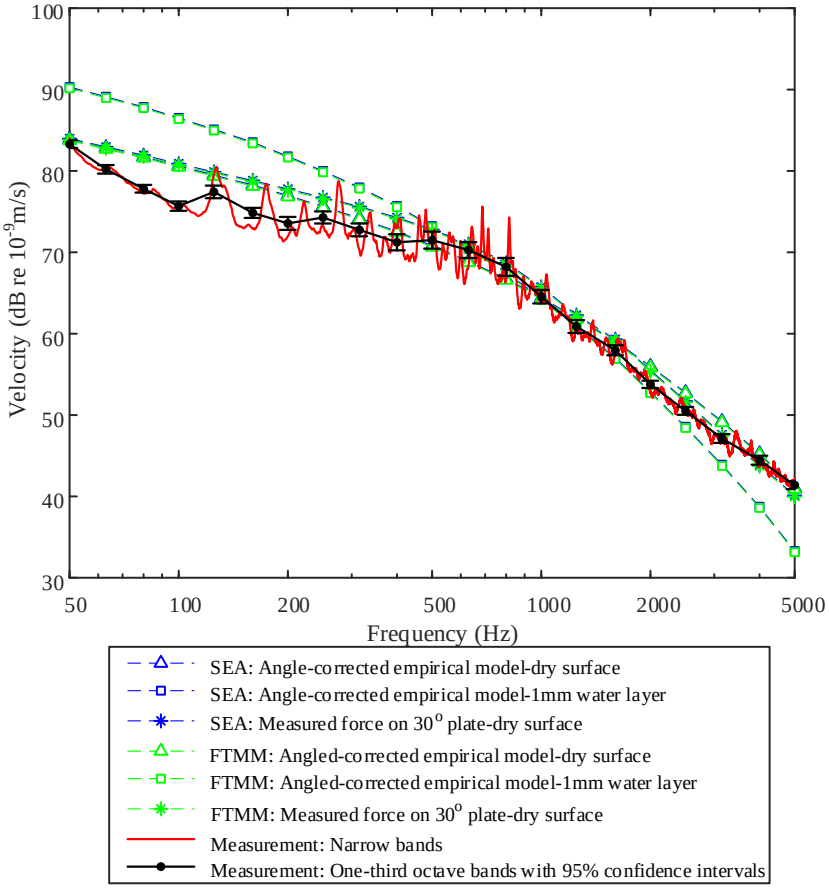

Figure 8.2. Comparison between the plate velocity prediction using SEA and FTMM (one-third octave bands) and measurement (narrow bands and one-third octave bands) of a glass plate under artificial rainfall from 3.65 m.

The difference in the power input applied by the artificial rainfall at two different heights is shown in Figure 8.3. The empirical model for the dry surface shows better agreement with the measured mean-square velocity than the empirical model for a 1 mm water layer. The agreement between the measurement and the prediction using the dry surface angle-corrected empirical model is less than 1 dB between 63 and 3.15k Hz. At 4k and 5k Hz, the error is due to the empirical model (refer back to Figure 7.6). The finding that it is possible to predict the change in power input for different drop heights has practical implications for ISO 10140 [12] which uses a drop height of ≈3.5 m and therefore does not provide terminal velocity as would occur with natural rainfall. This model would allow measured data to be adjusted to represent artificial rain at terminal velocity.

The measured oblique impact force (30^o slope) from wavelet deconvolution has also been used to calculate the difference in power input, which is within 1 dB of the

measured plate velocity difference. This confirms that for a 40 mm/h rainfall rate and 4.5 mm drops, it is reasonable to predict the power input into 30^{o} angled glass by assuming a dry surface.

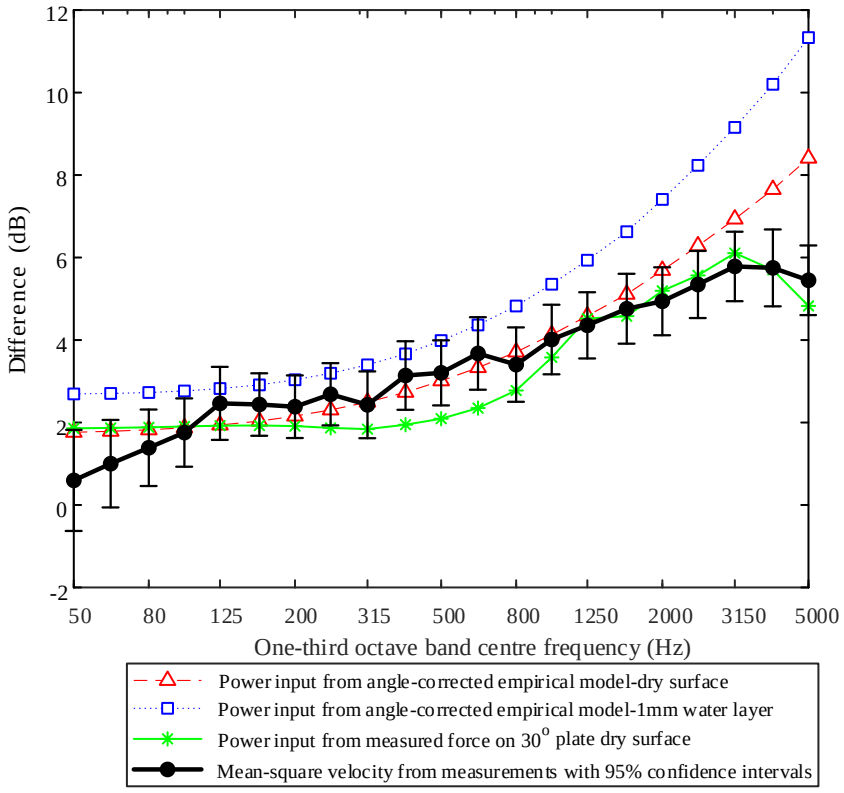

Figure 8.3. Comparison of the difference between the power input applied by artificial rainfall at two different falling heights (11.4 m and 3.65 m) with the difference in the measured mean-square velocity (spatial average).

8.2.2. Radiated sound power

The radiated sound power has been predicted using (a) SEA with Leppington *et al*'s frequency-average radiation efficiency from Eq. 4-11, and (b) the FTMM method from Eq. 4-36. As discussed in Section 4.5.2, Leppington *et al*'s formula leads to ≈3 dB higher values of radiated sound power below the critical frequency compared to the travelling wave method (see Figure 4.5). This difference between the SEA and FTMM predictions is seen in Figure 8.4.

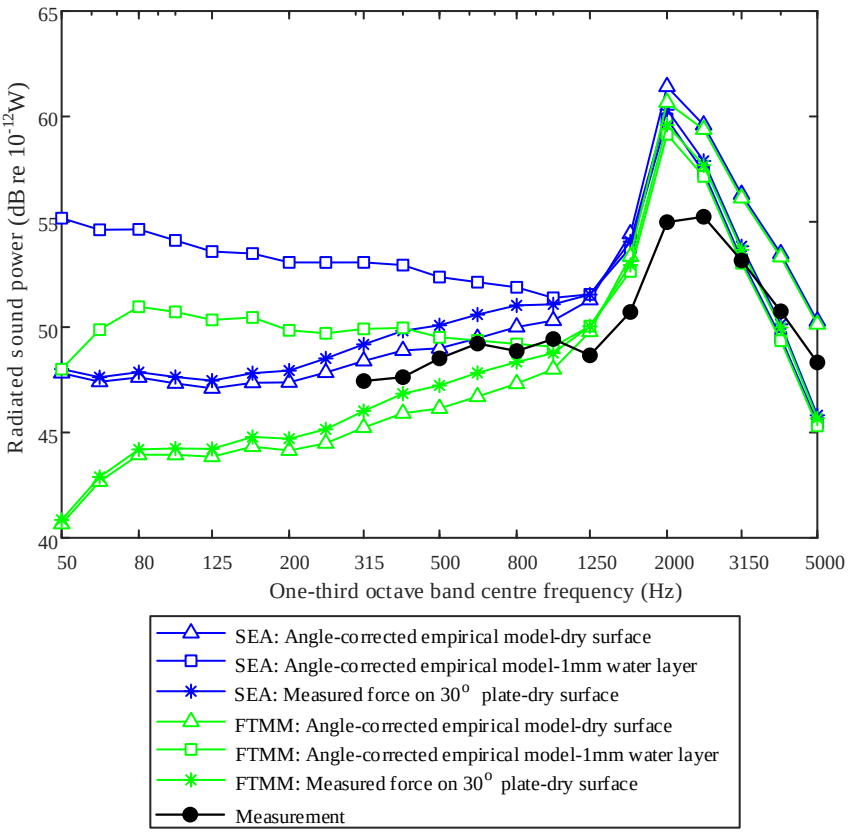

Figure 8.4. Comparison between the prediction of the radiated sound power from a glass plate using FTMM method and SEA method, and the measurement for artificial rainfall from 11.4 m.

In Figure 8.4, the prediction of the radiated sound power using the dry surface angle-corrected empirical model in SEA shows close agreement (<2 dB difference) with measurements over the frequency range from 315 to 1k Hz. The FTMM prediction based on the travelling wave method underestimated the radiated sound power below 1k Hz (<4 dB difference compared with the measurement). From 1.25k to 2.5k Hz (which includes the critical frequency at 2k Hz), both SEA and FTMM overestimate the radiated sound power assuming a dry or 1 mm water layer surface. Above the critical frequency from 3.15k to 5k Hz, the angle-corrected dry surface empirical model leads to 3 dB higher values than the measurement which is expected due to the error in the empirical model discussed in Section 4.5.2.

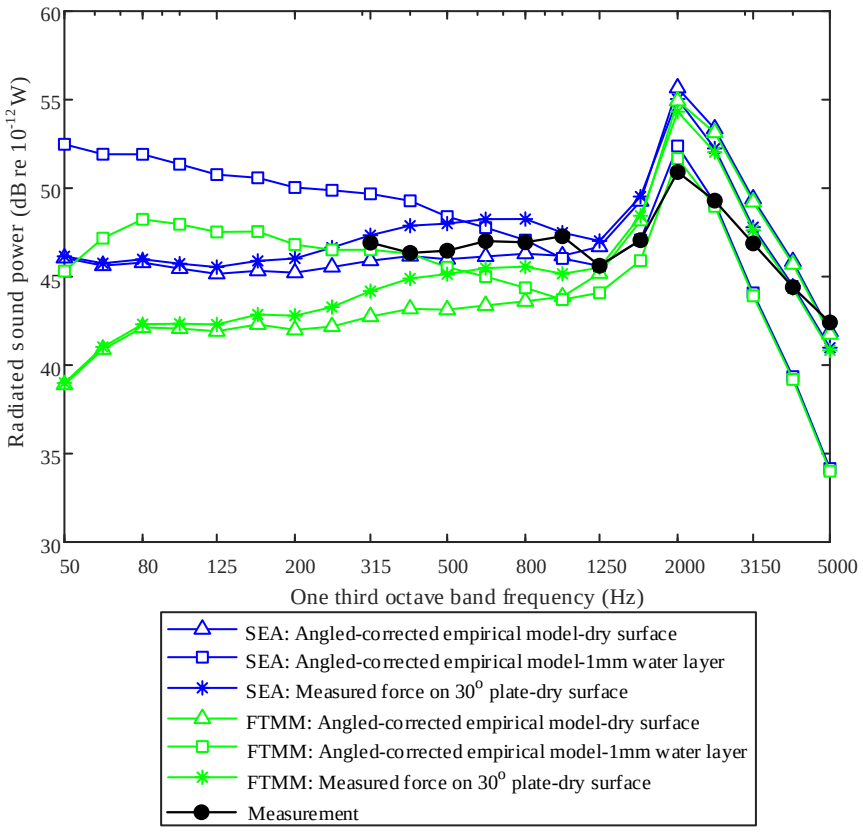

Figure 8.5. Comparison between the prediction of the radiated sound power from a glass plate using FTMM method and SEA method, and the measurement for artificial rainfall from 3.65 m.

Figure 8.5 allows comparison of the predicted radiated sound power using FTMM and SEA and the measurement with artificial rainfall at a drop height of 3.65 m. Below the critical frequency, the SEA model using the dry surface empirical model shows closer agreement with the measurement than FTMM. However, both SEA and FTMM overestimates the radiated sound power at the critical frequency by ≈5 dB. Between 3.15k and 5k Hz, SEA and FTMM were similar and had <3 dB difference compared with the measurement.

Figure 8.4 and Figure 8.5 show the discrepancy between the measurement and prediction of the radiated sound power around the critical frequency (2k Hz). This is mainly due to the error of the predicted radiation efficiency as shown in Figure 8.6. During the measurement, the sound intensity probe was perpendicular to the glass surface with 150mm distance. However, sound propagates through this gap to the wall of the baffle box with sound absorption materials can cause the measurement error of the radiated sound power. Furthermore, the empirical model, damping, water

layer, or other possible measurement uncertainties can also cause some error in the predicted vibration and sound radiation of the plate.

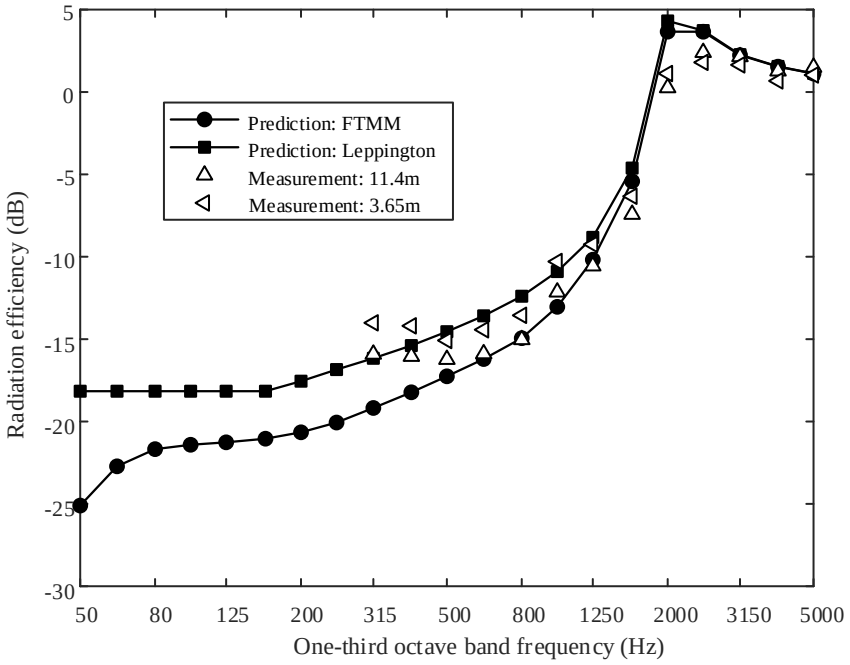

Figure 8.6. Comparison of radiation efficiency of the glass plate between the prediction using FTMM and Leppington *et al* formula and the measurement using the measured vibration and radiated sound power.

8.3. Multilayer plate at 30^o angle

8.3.1. Sensitivity function and the FTMM model

This section describes the measurement of the sensitivity function of the multilayer plate to assess the nearfield vibration phenomenon under point force excitation.

The sensitivity function is defined here as the frequency-domain transfer function from point force excitation on the source side (aluminium) of the multilayer plate to the mean-square velocity on the receiving side (Perspex) of the plate. The sensitivity function has been measured using a point force at five randomly chosen positions to a grid of accelerometer positions (125 mm grid spacing).

The nearfield vibration can affect the sound radiation prediction, as discussed in Section 4.5.3.3. To account for the point force acting over a finite circular contact area with radius, *r*, the radiated power from the nearfield can be represented by radiation from a piston with a radius $r + \lambda_B/4$ [48, 166], where λ_B is the bending wavelength. The near field radiation (also referred to as the damping effect in sound power radiation) can be taken into account in the radiation efficiency [132], where

this phenomenon is mainly significant below the critical frequency (refer back to Figure 4.8). The critical frequency of the Perspex plate is about 10 kHz.

Contour plots of the velocity on the receiving side of the multilayer plate (Perspex) are shown for 100, 1k and 5k Hz in Figure 8.7, Figure 8.8 and Figure 8.9, respectively.

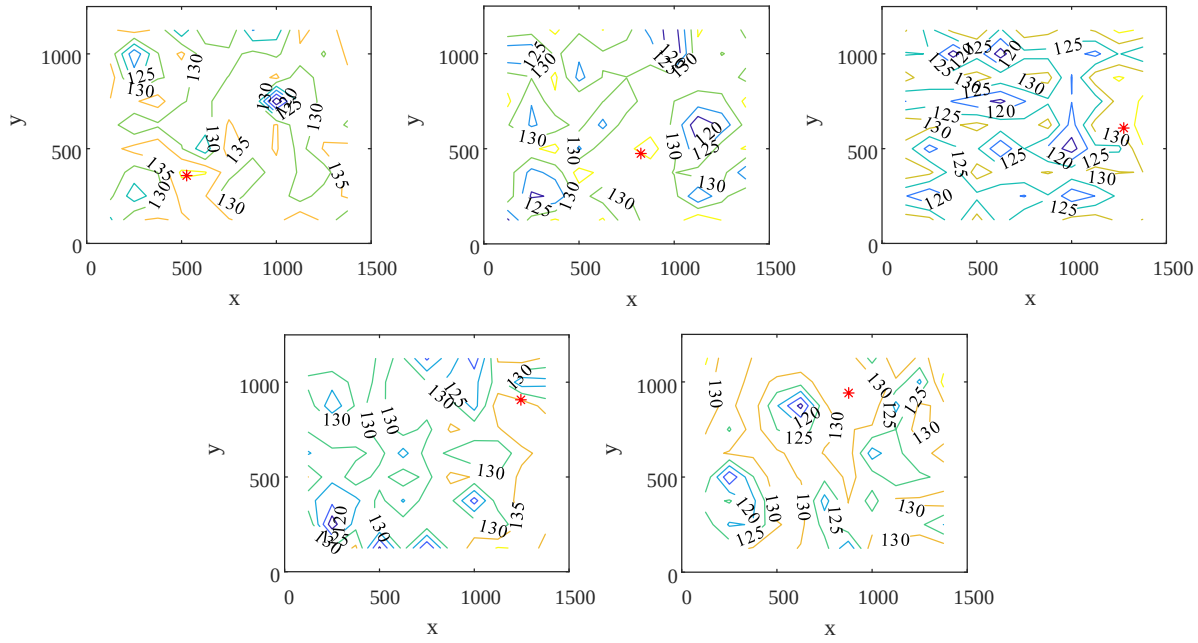

Figure 8.7. Contour plot of the velocity level (dB re 10^{-9}m/s) at 100 Hz of the receiving side of the multilayer plate (Perspex) with unit force excitation at the positions indicated by red * on the source side of the plate (aluminium).

The Perspex plate is highly damped by the foam layer, such that the vibration energy tends to be concentrated around the excitation position at and above 1k Hz (rather than at 100 Hz as seen in Figure 8.7). Therefore, it is necessary to consider the nearfield effect in the prediction of the sound radiation between 1k Hz and 6 kHz.

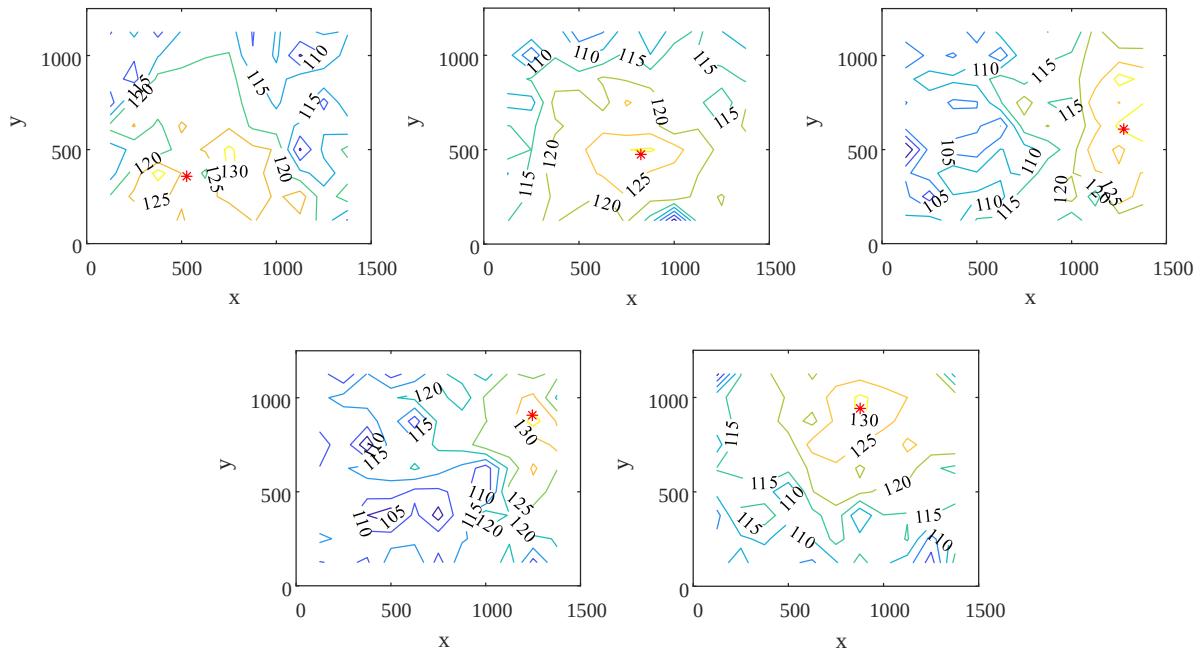

Figure 8.8. Contour plot of the velocity level (dB re 10^{-9}m/s) at 1k Hz of the receiving side of the multilayer plate (Perspex) with unit force excitation at the positions indicated by red * on the source side of the plate (aluminium).

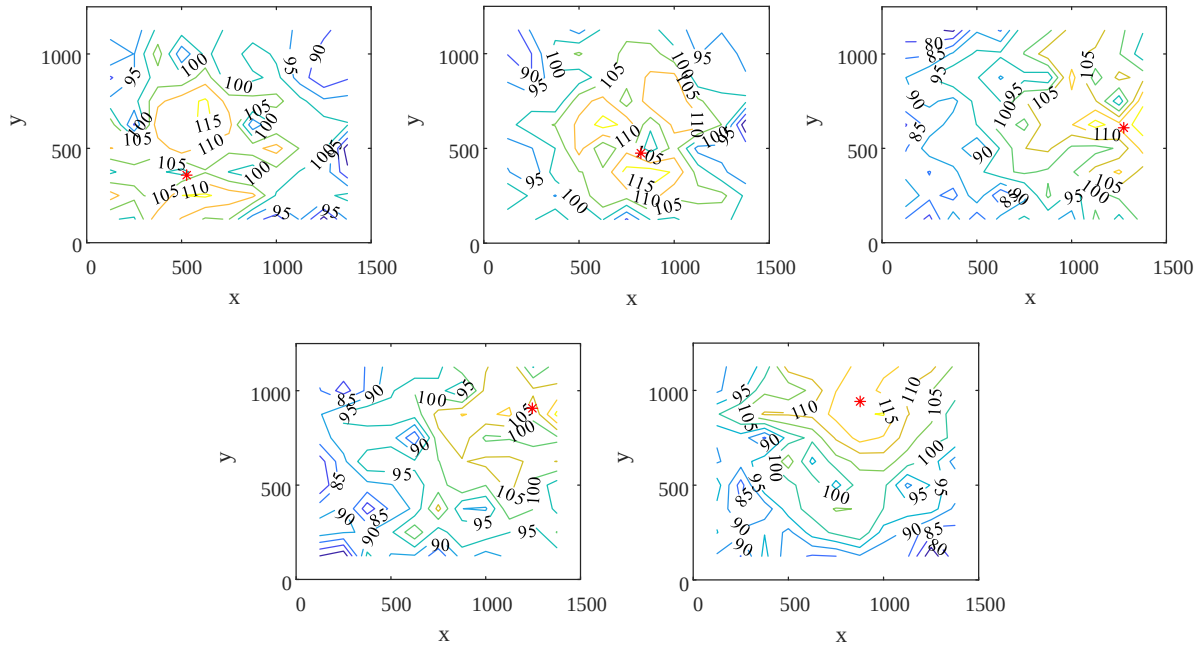

Figure 8.9. Contour plot of the velocity level (dB re 10^{-9}m/s) at 5k Hz of the receiving side of the multilayer plate (Perspex) with unit force excitation at the positions indicated by red * on the source side of the plate (aluminium).

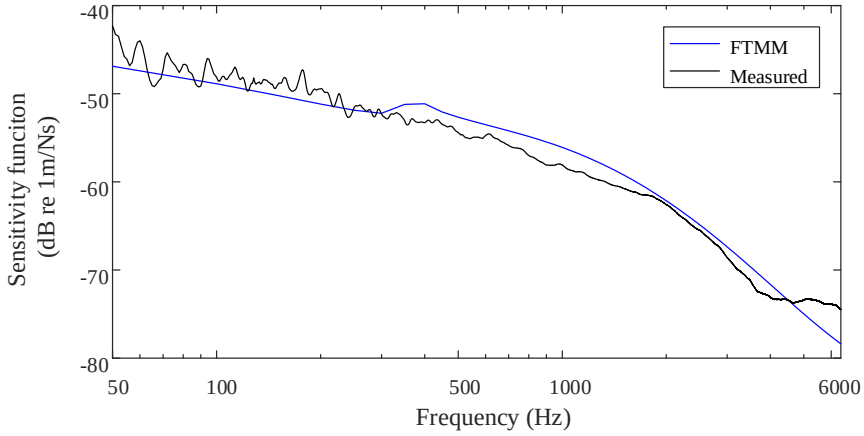

Figure 8.10. Comparison of the sensitivity function from FTMM and measurement of the multilayer plate for mean-square velocity at the receiving side (Perspex) and excitation on the source side of the plate (aluminium).

Figure 8.10 shows comparison of the averaged transfer mobility measurement from five point force excitation and prediction of the sensitivity function by FTMM method. The difference between the prediction and the measured data is less than 3 dB between 50 to 6k Hz, which provides validation of the FTMM model.

8.3.2. FTMM for the prediction of plate vibration

In Figure 8.11, the angle-corrected empirical model with a dry surface or a surface with 1 mm water layer has been applied to FTMM to predict the vibration of the plate. The dry surface model prediction shows close agreement with the measurement within <4 dB. At high frequencies, the predicted vibration is expected to be higher than the measurement due to the error of the empirical model discussed in Section 4.5.2. However, for this multilayer plate, FTMM slightly overestimates the sensitivity function from 315 to 2k Hz and underestimates the vibration above 4.5k Hz as shown in Figure 8.10. Therefore, there is a cancellation of errors which results in closer agreement between the measurement and FTMM prediction in Figure 8.11.

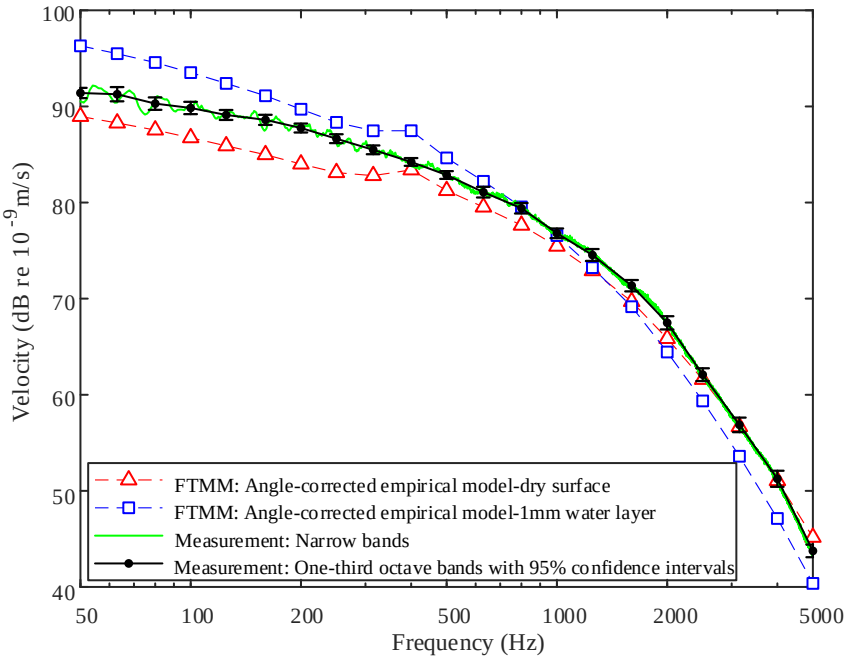

Figure 8.11. Comparison between the prediction of the mean-square velocity of the multilayer plate using FTMM incorporating the angle-corrected empirical model and measurements with artificial rainfall from 11.4 m.

8.3.3. Radiated sound power

The radiated sound power from the multilayer plate is assessed using the measured velocity and radiation efficiency from Leppington *et al* formula (Eq. 4-11) and FTMM radiation efficiency (Eq. 4-52). These two methods are within 3.5 and 2 dB of each other with and without consideration of the nearfield radiation respectively. The nearfield radiation is accounted for in the radiation efficiency as discussed in Section 4.5.3.3 (refer back to Eq. 4-55, where σ_0 is the radiation efficiency without nearfield that can be calculated using Leppington *et al* formula (Eq. 4-11) or the travelling wave method in FTMM (Eq. 4-52)).

From Figure 8.12, the prediction models using Leppington *et al* formulae with or without nearfield radiation and FTMM radiation with nearfield radiation show close agreement with the measurement at low frequencies (within 4 dB between 80 and 800 Hz). When nearfield radiation is not included, the radiated sound power predicted using these two formulae is underestimated above 800 Hz, where the nearfield radiation becomes significant as discussed in Section 8.3.1.

There is <3 dB difference between the measurement and the radiated sound power from the prediction model using FTMM radiation efficiency with

consideration of the nearfield radiation. Leppington *et al* formulae (Eq. 4-11) overestimate the radiated sound power by ≈3.5 dB over the frequency range between 200 and 1.25k Hz.

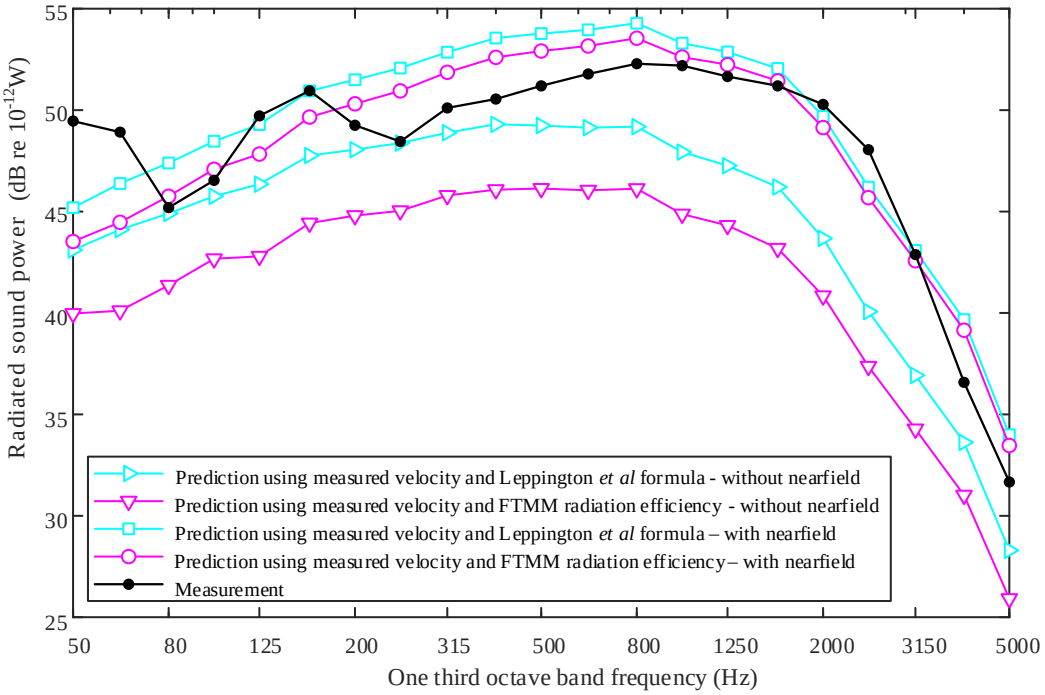

Figure 8.12. Comparison of the radiated sound power from the multilayer plate between the measurement with artificial rainfall at 11.4 m height and the prediction using measured velocity and the radiation efficiency calculated from Leppington's formula and the FTMM travelling wave method.

Figure 8.13 shows the prediction using FTMM with the angle-corrected empirical model for a dry surface and surface with 1 mm water layer. The measured radiated sound power lies between the dry surface model and the wet surface model with 1 mm water layer, and it shows closer agreement with the dry surface model between 200 and 3.15k Hz. However, the radiated sound power is overestimated by ≈2.5 dB from 3.15k to 5k Hz, because of the error of the angle-corrected empirical model at terminal velocity for 4.5 mm drops (discussed in Section 7.6).

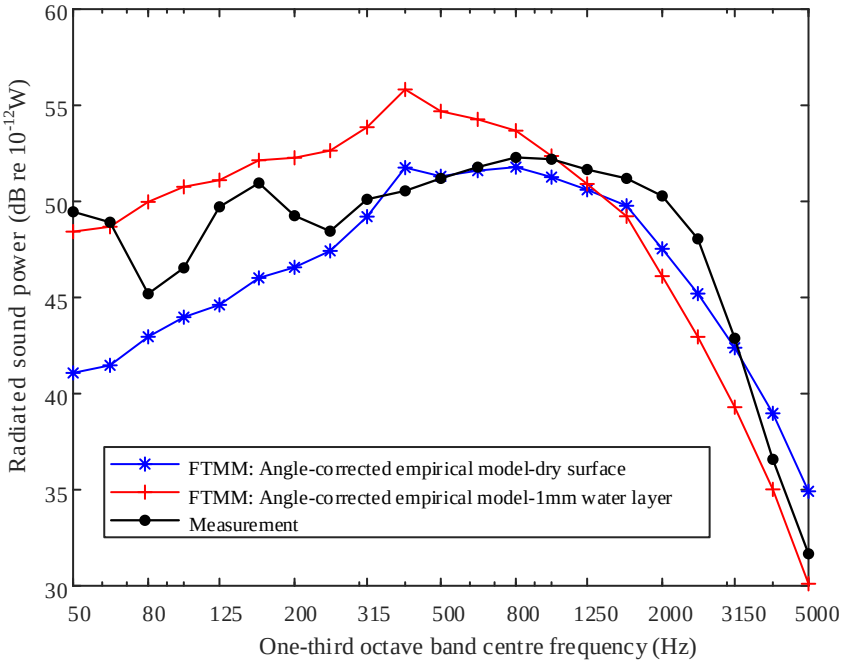

Figure 8.13. Comparison of the radiated sound power from the FTMM prediction and the measurement with artificial rainfall at 11.4 m height.

8.4. Conclusions

This chapter validated vibro-acoustic prediction models using SEA and FTMM which incorporate the empirical model to estimate the structure-borne sound power input into a single glass plate and a multilayer plate system from artificial rainfall. The angle-corrected empirical model for a dry surface shows closer agreement with the measurement data than for a model assuming 1 mm surface water layer. This justifies the approach in the literature for rain noise which does not account for water on a roof surface when predicting the power input. However, for artificial rainfall at terminal velocity, the dry surface model overestimates the vibration and sound radiation of the glass plate at high frequencies (above 3.15 Hz). This is due to the error of the angle-corrected empirical model generated from the irregular shape of 4.5 mm drops.

The FTMM and SEA predictions for the vibration of a glass plate under artificial rainfall excitation are similar. However, the radiated sound power, the measured data lies between the SEA model prediction using Leppington *et al* formula for radiation efficiency and the FTMM model using spatial windowing for the radiation efficiency (Eq. 4-52).

The FTMM method is used for the prediction of vibration and sound radiation from a multilayer plate under artificial rainfall at terminal velocity, which is within 2.5 dB of measurement data between 200 and 4k Hz.

The main finding for the prediction of artificial (and natural) rainfall is that it is reasonable to use the angle-corrected empirical model for a dry surface rather than a 1 mm surface water layer. This is only validated for a glass plate at a 30^{o} angle, but importantly this will allow measured data from laboratory measurements to ISO 10140 at drop velocities lower than terminal velocity to be corrected to the level that would be expected for terminal velocity.

9. Numerical experiments to simulate natural rainfall

9.1. Introduction

In this chapter, the rain drop size distribution for natural rainfall has been used with the empirical model to calculate power injection to a horizontal glass plate assuming terminal velocity.

In Section 9.2, the empirical model of impact force from 2 and 4.5 mm drops is extended to a distribution of raindrop sizes from 0.1 mm up to 6 mm diameter.

In Section 9.3, the power input from natural rainfall on dry and wet glass plates is calculated and assessed.

9.2. Empirical model for different size rain drops at terminal velocity

The empirical model from Chapter 7 cannot be used directly to estimate the natural raindrop impact forces because it was derived for two specific drop diameters. In this section, the empirical model is extended to a range of drop sizes from 0.03 mm up to 6 mm diameter based on the factor $v_{\mathrm{d}}^2 D^2$.

The empirical formula for different drop diameter is assumed as a combination of two exponential functions:

$$f(t) = C_1 \exp\left[-\frac{(\ln(1000t) + \alpha_1)^2}{{\beta_1}^2}\right] + C_2 \exp\left[-\frac{(\ln(1000t) + \alpha_2)^2}{{\beta_2}^2}\right] \qquad 9\text{-}1$$

The first term at the right side of Eq. 9-1 has the dominant energy in the empirical force model, and the second term is for large rain drops correction due to the effect of ellipsoidal drop shape with flatten bottom. The amplitude of the force pulse is strongly related to the dimensionless force $\rho_{\mathrm{w}} v_{\mathrm{d}}^2 D^2$ as discussed in Section 2.6; hence, it is reasonable to assume that the extension of the parameter C_1 is a second order polynomial function with respect to $v_{\mathrm{d}}^2 D^2$.

Therefore, C_1 is given by a piecewise function according to the drop diameter, and the terminal velocity of raindrops is used:

$$C_1 = \begin{cases} C_{a1}({v_T}^2 D^2)^2 + C_{a2}({v_T}^2 D^2) + C_{a3} & \text{for } 0 \le D < 2 \text{ mm} \\ C_{b1}({v_T}^2 D^2)^2 + C_{b2}({v_T}^2 D^2) + C_{b3} & \text{for } 2 \text{ mm} \le D \le 6 \text{ mm} \end{cases} \qquad 9\text{-}2$$

where v_{T} is the terminal velocity, which is given by an empirical equation [167]:

$$v_{\mathrm{T}} = 9.58\left\{1 - \exp\left[-\left(\frac{D}{1.77}\right)^{1.147}\right]\right\} \qquad 9\text{-}3$$

where D is the drop diameter in millimetres.

From the empirical model given by Eq. 7-1 and Eq. 7-12, the parameter C is given for 2 and 4.5 mm drop diameters with different falling velocity (including the terminal velocity). Additionally, for 0mm drops, the amplitude of the impact force is set to zero $C_1|_{D=0} = 0$. The empirical formula can now be extended to all drop sizes up to 6mm diameter from the 0, 2 and 4.5 mm drops formulae. As shown in Figure 9.1, the blue and red solid lines correspond to 2 and 4.5 mm drops respectively using the empirical models at different velocities (see Table 7-1 and Table 7-3 for 2 mm drops, Table 7-2 and Table 7-4 for 4.5 mm drops). Black dashed-dotted and dashed lines correspond to the second order polynomial curve fit of C_1 respected to $v_d^2 D^2$ from 2 and 4.5 mm drops respectively.

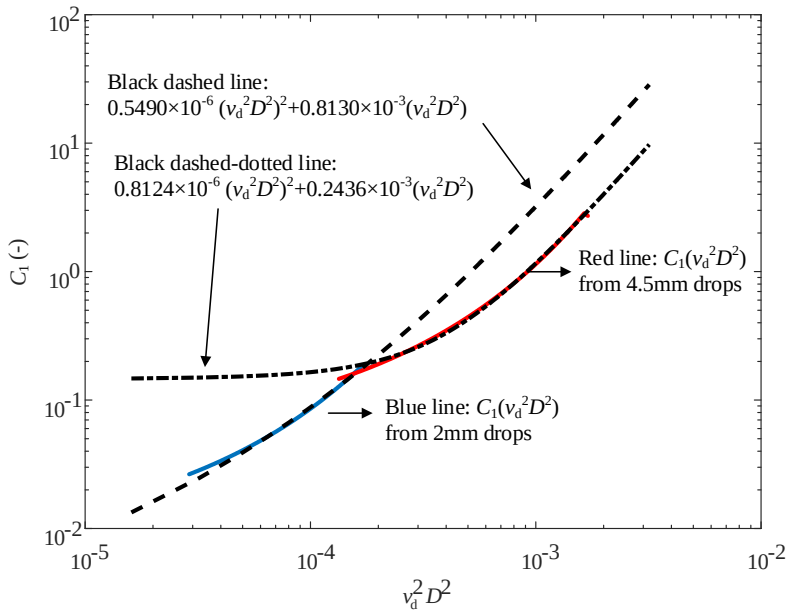

Figure 9.1. Determination of parameter C_1 for the dry surface.

α_1 and β_1 can also be determined using the same process as C_1 using the empirical model from 2 and 4.5 mm drops by a linear regression respected with D:

$$\alpha_1 = 0.2982D + 1.9948$$
$$\beta_1 = 0.2064D + 0.573 \qquad 9\text{-}4$$

The correction term in Eq. 9-1 is concerned for large drops ($D > 2.5$ mm in this section)

$$C_2 = \begin{cases} 0 & \text{for } 0 \le D < 2.5 \text{ mm} \\ K_{4.5}\dfrac{v_T{}^2D^2|_{D=4.5} - v_T{}^2D^2|_{D=2.5}}{v_T{}^2D^2|_{D=4.5} - v_T{}^2D^2|_{D=2.5}} & \text{for } 2.5 \text{ mm} \le D \le 6 \text{ mm} \end{cases} \quad 9\text{-}5$$

Due to the lack of data for drop diameters above 4.5 mm, $K_{4.5}$, α_2 and β_2 use the empirical model for 4.5 mm drops at terminal velocity (see Table 7-2). The parameters of Eq. 9-1 are given in Table 9-1.

Table 9-1. Parameters of the empirical model for the impact force of any raindrop diameter at terminal velocity.

Water depth, d (mm)	C_{a1}	C_{a2}	C_{a3}	C_{b1}	C_{b2}	C_{b3}	$K_{4.5}$	α_2	β_2
0	5.49E-07	8.13E-04	0	8.12E-07	2.44E-04	0.1107	0	0	0
1	2.87E-07	8.77E-04	0	3.24E-07	7.29E-04	0.0125	1.5693	2.8439	0.4645
2	-4.45E-08	9.03E-04	0	3.52E-07	6.36E-04	0.0362	1.2078	2.8984	0.509
4	-7.84E-08	9.60E-04	0	3.51E-07	5.75E-04	0.0559	1.222	2.8479	0.4787
6	1.96E-07	9.64E-04	0	3.13E-07	6.38E-04	0.0454	1.125	2.7873	0.4403
8	9.38E-07	1.26E-03	0	2.31E-07	9.29E-04	0.0045	1.1008	2.7408	0.4726
10	3.96E-07	1.20E-03	0	2.87E-07	6.61E-04	0.0457	0.9756	2.5934	0.4141

From Eq. 9-1 and the parameters in Table 9-1, the impact force for a dry surface can be obtained as shown in Figure 9.2. The highest dimensionless force for a 3 mm water drop is slightly lower than the 2 mm drops. This is because of the slight overestimation of 2 mm drop impact force from the empirical model. However, the highest dimensionless force for a 2 mm drop is 0.9±0.2 according to [168]; hence it is assumed to be a reasonable representation.

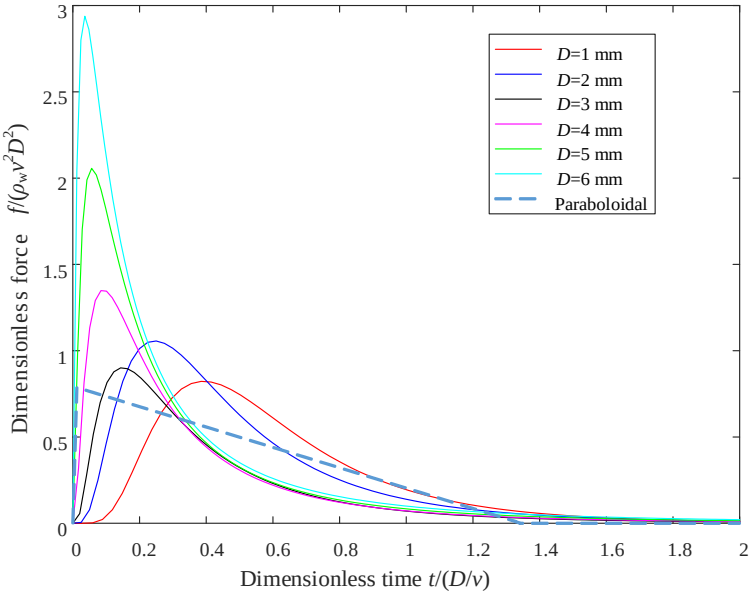

Figure 9.2. Dimensionless impact force applied by different size rain drops at terminal velocity from the empirical model and the paraboloidal drop shape model.

9.3. Power input from natural rainfall

This section assessed the power input from natural rainfall to a horizontal dry glass plate with the same rainfall rate as the artificial rainfall described in [7, 12]. The natural rainfall has a statistical distribution of raindrop diameters by Marshall and Palmer [13] as discussed in Section 2.2. Using the raindrop diameter distribution and the force equations from the empirical model, the power input can be calculated.

Figure 9.3 shows the power input from rain drops at three different rainfall rates (heavy, intense and moderate rainfall according to [12]) impacting on a horizontal dry 6 mm glass plate using the empirical model and the idealized paraboloidal drop shape model and the Mitchell *et al* model. As shown in Figure 9.3, all three models are within 1.5 dB of each other below 1.6k Hz. The empirical model has less low frequency energy for moderate and intense natural rainfall than the paraboloidal model and Mitchell *et al* model. This is possibly because the small drops dominates the impact energy and the empirical model for small drops has less low-frequency energy than the paraboloidal drop shape model and Mitchell *et al* model.

However, at high frequencies, the empirical model predicts a higher power input than the paraboloidal drop shape model and the Mitchell *et al* model. This is because the high frequency energy introduced by large raindrops is underestimated by the paraboloidal drop shape model as it does not consider the spreading lamella effect. Although the Mitchell *et al* model was seen to give a reasonable representation of the time domain force (refer back to Figure 7.1), the spherical drop shape is assumed in their theory which is not suitable for large raindrops at terminal velocity with a flattened bottom (as discussed in Section 2.6 and 7.3). At high frequencies, the difference between the empirical model, paraboloidal drop shape model or the Mitchell *et al* model increases when the rainfall rate increases, because the energy from larger drops becomes dominant when the rainfall rate increases.

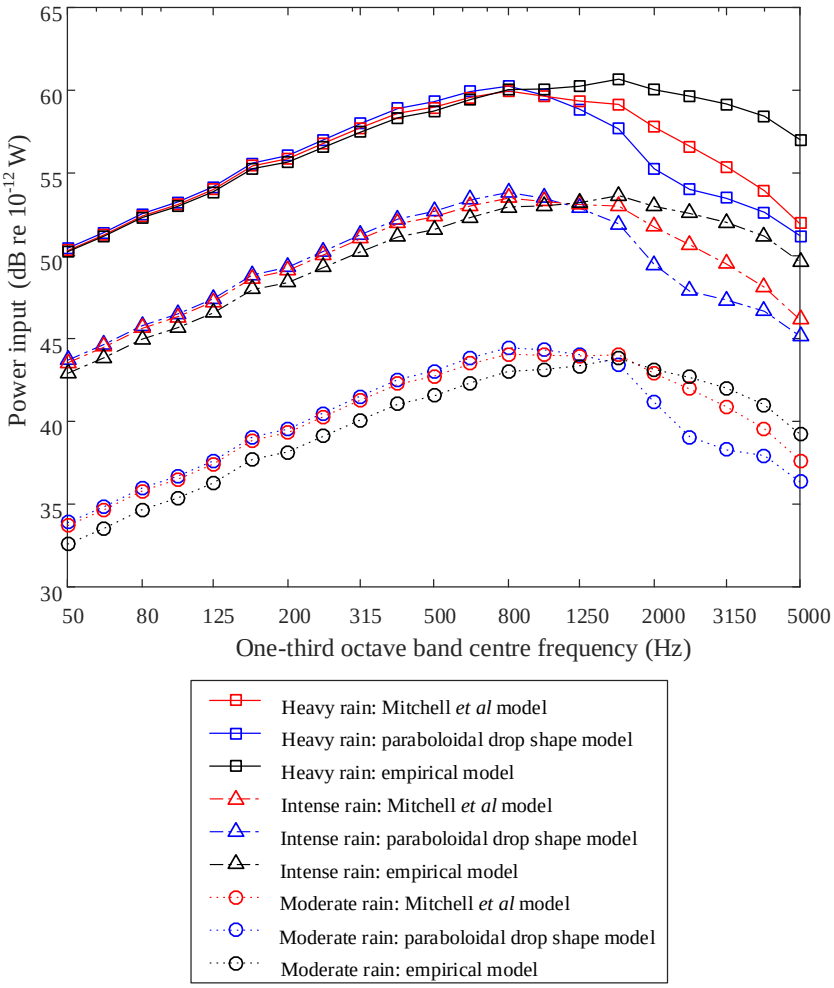

Figure 9.3. Power input from rain drops with different natural rainfall rates onto a horizontal dry glass plate.

Figure 9.4 shows the power input from rain drop impact at different rainfall rates on a glass plate with different depths of water layer. The water layer can increase the low frequency component of the power input and decrease the high frequency component, as discussed in Chapter 4. Note that with the water layer, lower rainfall rates can reach and even exceed the power input level from higher rainfall rates at low frequencies (i.e. below 500 Hz).

Note that the simulation results of wet surfaces shown in Figure 9.4 consider the initial impact power and not features after the initial impact such as ripples, splash, and bubble entrainment (as discussed in Section 6.4).

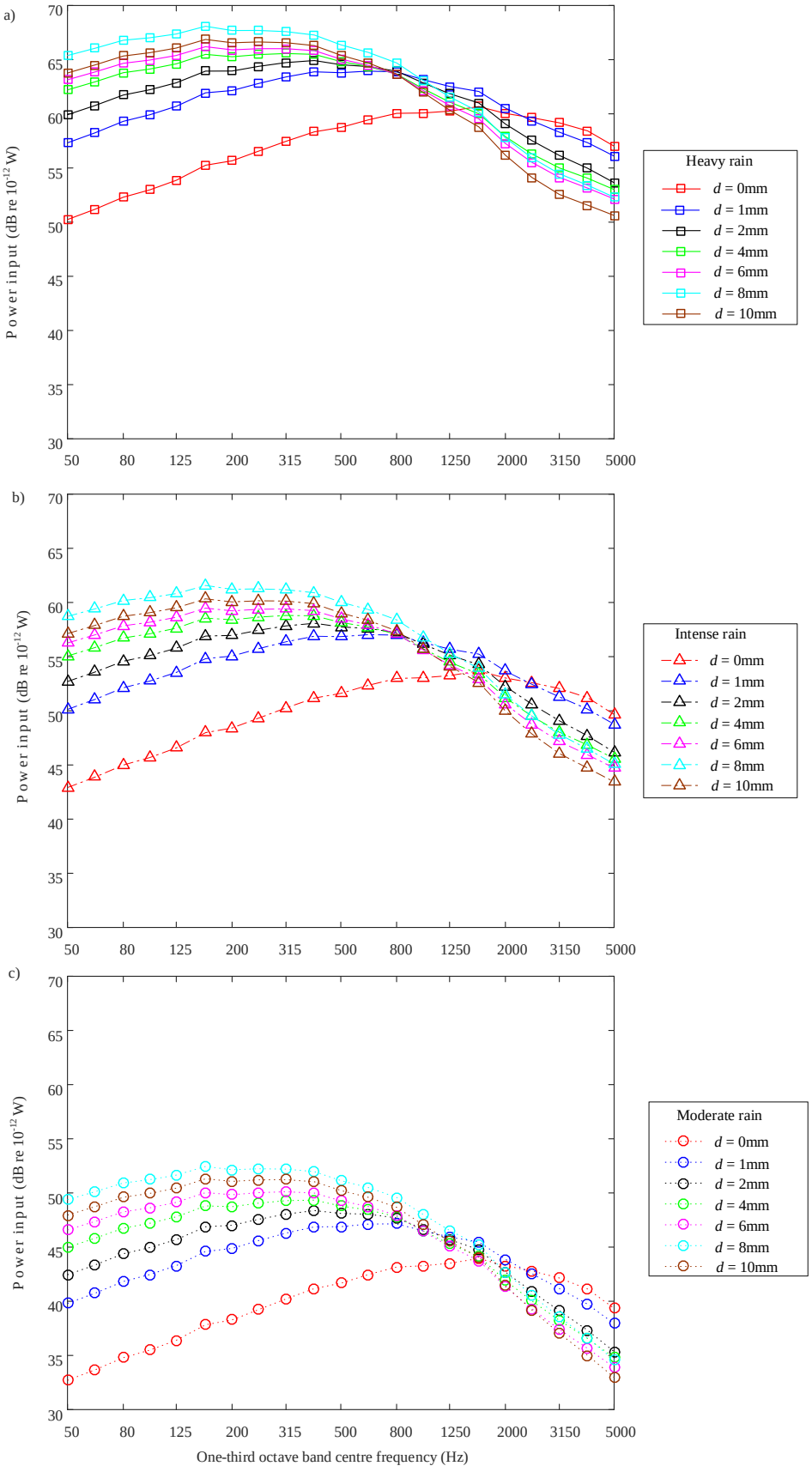

Figure 9.4. Power input from different natural rainfall rates a) heavy rain, b) intense rain and c) moderate rain, onto a glass plate with different water layer depths.

The distribution of power input from different raindrop sizes is estimated by calculating the power input ratio density using the empirical model. In this estimation, the power input ratio density is defined as the ratio of power input by a number of raindrops within a chosen diameter step δD (δD is assumed to be 0.03mm in this prediction model):

$$\mathcal{R}_W = \frac{W_{\text{in},\delta D}}{\delta D W_{\text{in,total}}} \qquad 9\text{-}6$$

The power input distribution varies for different frequencies, different rainfall rates and different water layer depths. In Figure 9.5, 50 and 5k Hz are used to assess the low frequency and high frequency power input distribution respectively. It is seen that the power input from raindrops with diameter D<1 mm is negligible for these three different rainfall rates with or without consideration of water layer. For heavy natural rainfall, the combined power input from the large raindrops (3 mm<D<6 mm) is dominant at both 50 and 5k Hz with or without water layer (1 and 2 mm) compared to small raindrops (D<3 mm), although the number of large raindrops is less than the small ones; whereas for moderate rain, small raindrops introduce more power than large raindrops, as shown in Figure 9.5.

On a dry surface, the power input distribution at 50 Hz is similar to 5k Hz for the three different rainfall rates. For moderate rainfall, the power input is mainly determined by a range of raindrops with 1.5 to 3.5 mm diameters. When the rain fall is intense or heavy, the number of large drops (D>3 mm) increases significantly to dominate the power input to the structure.

The existence of a 1 or 2 mm water layer on the glass surface gives rise to different power input distributions at 50 and 5k Hz. At 5k Hz, power is dominated by 2.5 to 4 mm drops for moderate rainfall. The reason that the distribution curve shifts to larger drop size is because the water layer reduces the high frequency power for smaller drops.

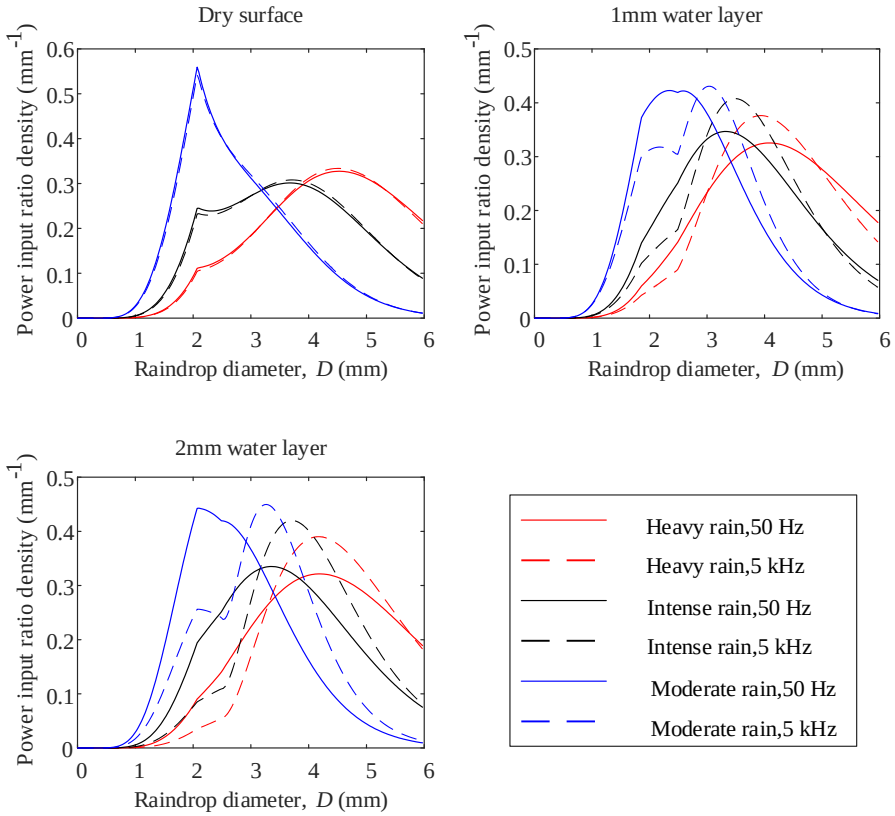

Figure 9.5. Power input ratio density distribution for different size drops and different water layer depth.

9.4. Conclusions

This chapter described numerical experiments to quantify the power input from natural rainfall. The empirical model based on the measurement of 2 and 4.5 mm drops with different velocities was modified to account for drop sizes ranging from 0mm to 6mm diameter. The empirical model has been used to predict the power input of natural rainfall at three different rainfall rates (heavy, intense and moderate rainfall) onto a horizontal glass plate with or without water layer.

For the dry surface, the empirical model prediction has <1.5 dB difference below 1.25k Hz compared with the paraboloidal drop shape model and Mitchell *et al* model. At higher frequencies above 1.6k Hz, the empirical model has higher power input prediction than the other two models, especially for heavy rainfall due to neglecting the lamella effect in the paraboloidal drop shape model and the inaccuracy of the assumption of a spherical drop shape in the Mitchell *et al* model.

A thin layer of water gives rise to increased power input from natural rainfall at low frequencies (<500 Hz), and decreased power input at high frequencies.

For heavy, intense or moderate natural rainfall, the power input from raindrops with diameter D<1 mm is negligible with or without a water layer. For heavy natural rainfall, the power input from the large raindrops (3 mm<D<6 mm) is dominant at both 50 and 5k Hz with or without water layer (1 and 2 mm) compared to small raindrops (D<3 mm); whereas for moderate rain, small raindrops introduce more power than large raindrops.

10. Conclusion and further work

10.1. Conclusions

The time-dependent force applied by a liquid water drop with 2mm and 4.5mm diameter impacting a glass plate (at normal and oblique angles) at a range of drop velocities when the plate is dry and with a shallow water layer has been experimentally quantified using wavelet deconvolution of accelerometer signals in order to overcome limitations of other measurement techniques.

For drops on dry glass, the peak force increases and the pulse width of the impact force decreases with increasing drop velocity. Wavelet deconvolution was validated by its close agreement with force transducer measurements in the frequency domain. For drops on a shallow water layer, high-speed camera images were used to identify distinct features relating to the splash that apply forces on the plate that occur after the initial impact, such as the crater, crown, and jet as well as bubble entrainment underneath the surface of the water. This leads to measurement problems when using a force transducer with contained water layer because some features of the splash such as crater formation and outgoing capillary waves are no longer representative of the natural phenomena. Analysis of the measurement errors indicates that the wavelet approach can be used to estimate forces applied by the crater, crown, jet, vortex ring, or oscillating bubbles within 1 dB. However, there will be some low-level forces that cannot be accurately determined such as those from rebounding drops falling far from the original impact position, or capillary waves propagating away from the crater; fortunately their low-level makes them of little relevance for the purpose of noise control in cars and buildings. For 2 mm drops falling on 6, 8, and 10 mm layers, bubbles are regularly entrained in the water layer. Whilst the force from the initial impact tends to be significantly higher than the bubble-induced force below 200 Hz, the bubble-induced force above 700 Hz tends to become significantly higher than that from the initial impact with high peak levels at or above 6.5k Hz. Whilst these high forces from entrained bubbles are noteworthy, they are less critical when evaluating rain noise because water layers on roof elements are typically <6 mm deep and the radiated sound only tends to be assessed at frequencies below 6.5k Hz.

When the response signal has low SNR value (<10 dB), wavelet deconvolution becomes less robust and results in a significant estimation error. This occurred for

the 2mm drop at the lowest drop velocity (2.57 m/s). To overcome this problem, the sparse representation method was used to improve the estimation accuracy and preserve the shape edge in the initial phase of the impact. It is shown that the l_0-norm regularization is better in edge-preserving and noise suppression than l_1-norm regularization for single drop impact when the optimal wavelet basis has been selected (*coif1*). When there is a sufficiently high SNR (>15 dB), the wavelet deconvolution, sparse representation and the force transducer measurement have <1.6 dB difference for the initial impact force estimation on a dry surface.

The validity of theoretical models has been assessed through comparison with experimental data for the water drop impact force prediction on a dry surface. At relatively high velocities (including terminal velocity) the measured peak force is significantly higher than predicted by all the paraboloidal, cylindrical-hemispherical, spherical, and ellipsoidal drop shape models, and the model from Roisman *et al* which takes the lamella into account gives no significant improvement in the predicted force particularly for 4.5 mm drops. The inability of these prediction models to describe the time-dependent force provided the motivation to develop empirical formulae.

Empirical formulae were developed for 2 and 4.5 mm drops falling at (a) different velocities up to and including terminal velocity onto a dry glass surface, (b) terminal velocity onto dry glass or glass with a shallow water layer up to 10 mm and (c) different velocities below terminal velocity onto dry glass or glass with a shallow water layer up to 10 mm. This allowed the errors to be minimised for different applications. For drops on dry glass, the empirical formulae are only strictly applicable to a glass plate or a composite layered plate with a glass surface, although they apply to any other thickness of plate. All the empirical formulae can reasonably be applied to any plate material with a similar surface roughness and wettability. The empirical model determined from the sparse representation measurement has < 0.4dB difference compared with the model from the wavelet deconvolution measurement data. Therefore, the empirical formulae from the wavelet deconvolution measurement can be used for rain noise prediction. The empirical model correction for the impact of a drop on an angled plate is accounted by using the perpendicular velocity component. The difference between the wavelet measurements and the angle-corrected empirical formulae are not significantly larger than the flat plate

below 1k Hz. For 4.5mm drops impact at terminal velocity on a plate with 30^o slope, the error of the angle-corrected empirical model is <±1 dB between 12.5 and 2k Hz, and <±5 dB between 2k and 5k Hz.

Numerical models have been validated via experiments using SEA and FTMM which incorporate the empirical model to estimate the vibration and sound radiation from a glass plate and a multilayer plate (plate-limp porous material-plate). The angle-corrected empirical model for a dry surface showed closer agreement with measurements than the wet surface model, apart from high-frequencies (above 3.15k Hz) due to the non-spherical shape of 4.5 mm drops at terminal velocity. FTMM prediction for the vibration prediction of a glass plate under artificial rainfall excitation was similar to the SEA model. However, for the radiated sound power prediction, the measured data is between the SEA model prediction using Leppington *et al*'s formula for radiation efficiency and the FTMM model using the spatial windowing for radiation efficiency. The FTMM method is also used for the prediction of vibration and sound radiation from a multilayer plate under artificial rainfall at terminal velocity, which is within 2.5 dB of measurements between 200 and 3.15k Hz.

Natural rain noise has been assessed using numerical experiments. The empirical model based on the measurement of 2 and 4.5 mm drops with different velocities has been developed for natural rain drop sizes from 0.03 to 6 mm diameter. The Marshall-Palmer distribution has been used to predict the power input from natural rainfall into a 6mm glass plate. This shows that the water layer can significantly increase the power input at low frequencies and reduce the high frequency power input. It also allows an assessment of what raindrop diameters are responsible for injecting the most power at different frequencies.

10.2. Further work

10.2.1. Force applied by raindrops with a horizontal velocity component

For raindrops impacting on car windscreens when the car is in motion and wind driven rainfall impacting on the facade of a building, the impact force will be affected by the horizontal velocity component that could also determine the drop shape. Building on the work in this thesis, laboratory experiments could also use the wavelet approach for drops released under horizontal airflow. However, the

experimental validation of wind driven rain under different wind speeds could be challenging if the airflow generated by a fan caused signal to noise problems on the plate

10.2.2. Energy harvesting of raindrops

Energy Harvesting (EH) is a process whereby energy is derived from external sources (such as solar, wind or other means) captured and stored for micro to macro level applications. EH from the impact of raindrops has attracted significant research interest over recent years, and the potential still has not been fully unlocked. To the author's knowledge, the maximum output reached experimentally using Piezoelectric devices is 12 mW as detailed in [9], which is less than 1% of the raindrop kinetic energy. Using the energy harvesting equipment could capture clean and renewable energy from raindrops, but could also reduce the vibration level of the structure by applying the damping to the structure essentially. The empirical model proposed in this thesis can help estimate the efficiency of EH and optimize the properties of the structure (e.g. glass plate) to compromise the trade-off between the harvested energy, the structural vibration and noise radiation.

11. Appendices

Appendix A: baffle box diagrams

The baffle box is made of chipboard with 18mm thickness. The air gap between the internal and external box is 12mm.

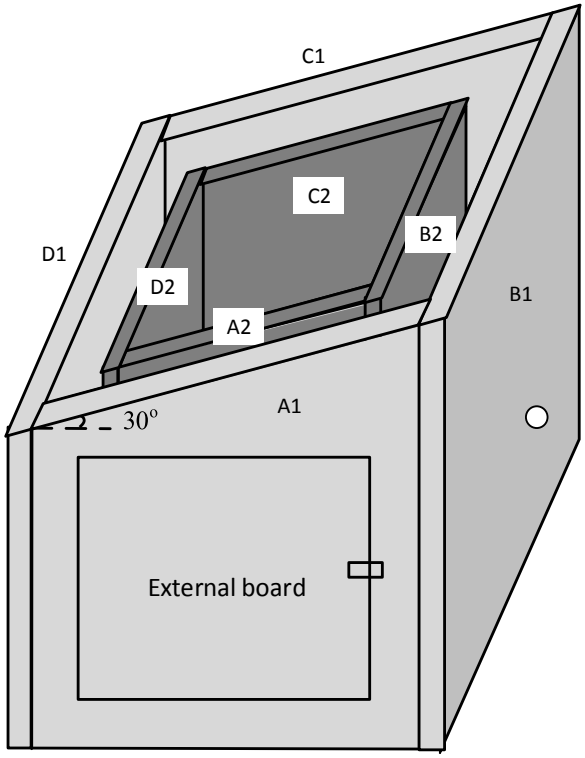

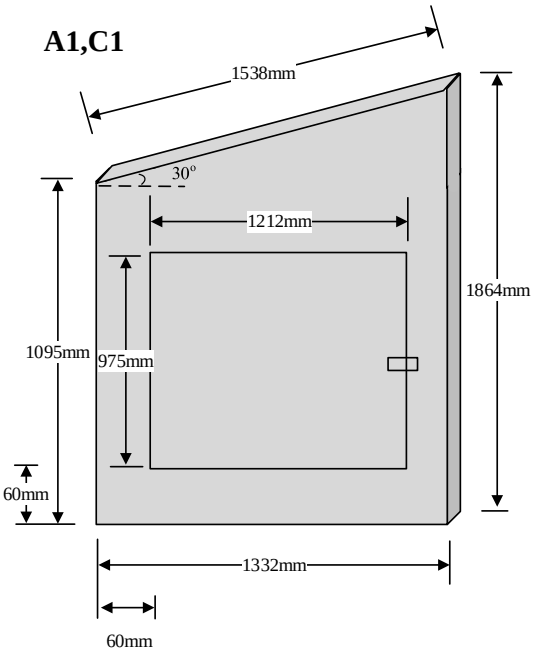
A1,C1
1538mm
30°
1212mm
1864mm
1095mm
975mm
60mm
1332mm
60mm

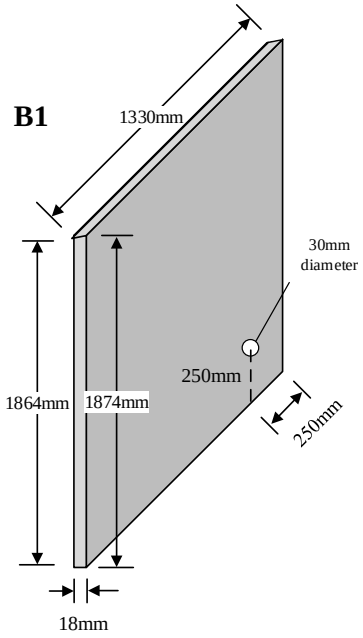
B1
1330mm
30mm
diameter
250mm
1864mm
1874mm
250mm
18mm

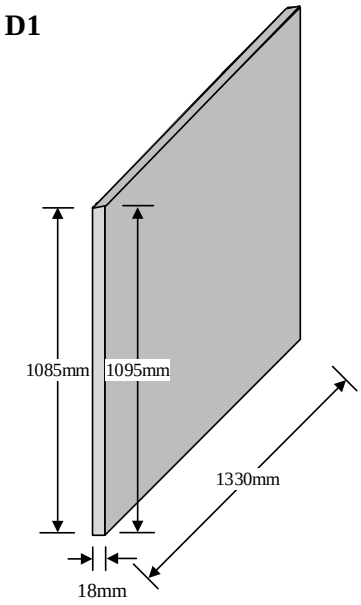
D1
1085mm
1095mm
1330mm
18mm

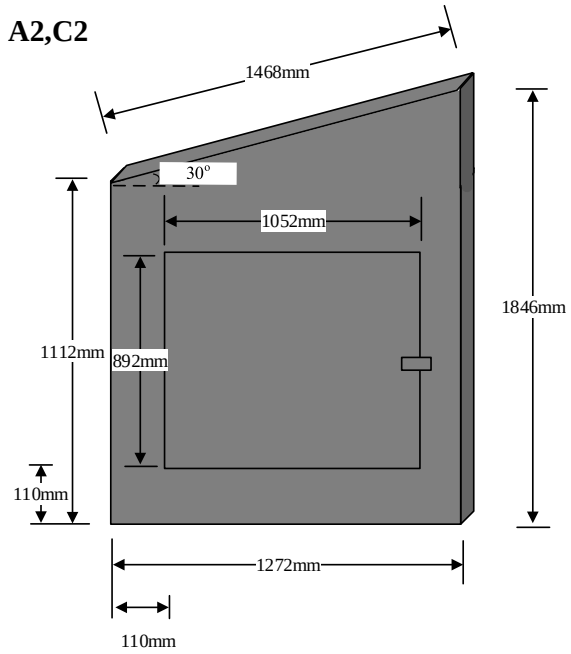
A2,C2
1468mm
30°
1052mm
1846mm
1112mm
892mm
110mm
1272mm
110mm

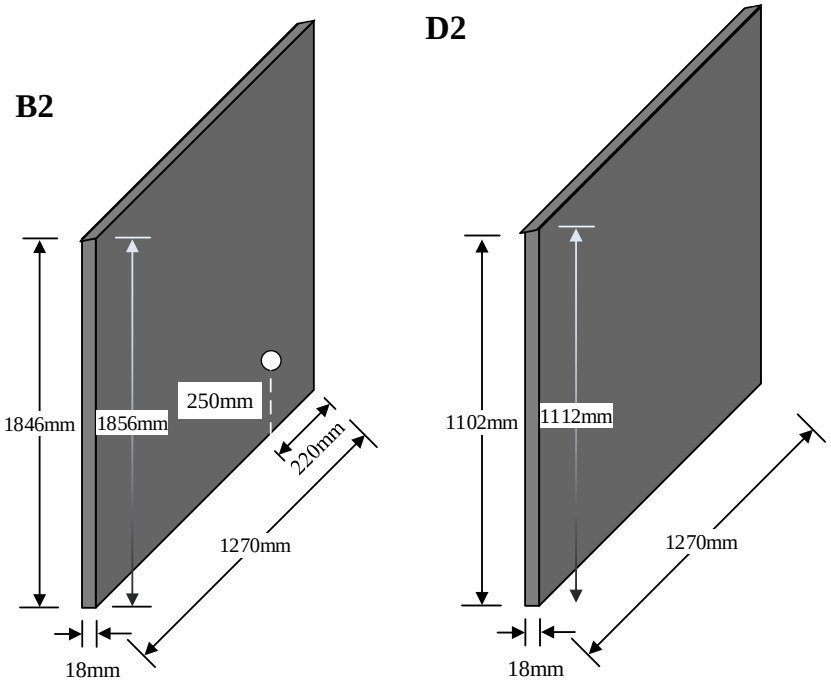
B2
1846mm
1856mm
250mm
220mm
1270mm
18mm
D2
1102mm
1112mm
1270mm
18mm

12. References

[1] Nearing M. A. and Bradford J. M. (1987) Relationships between waterdrop properties and forces of impact. Soil Science Society of America Journal. 51(2):425-430.

[2] Nearing M. A., Bradford J. M., Holtz R. D. (1986) Measurement of force vs. time relations for waterdrop impact. Soil Science Society of America Journal. 50(6), 1532-1536.

[3] Imeson, A. C., Vis, R., and de Water, E., 1981, "The measurement of water-drop impact forces with a piezo-electric transducer," CATENA, 8(1), pp. 83-96.

[4] Petersson, B. A. T., 1995, "The Liquid Drop Impact as a Source of Sound and Vibration," Building Acoustics, 2(4), pp. 585-621.

[5] Suga, H., and Tachibana, H., 1994, "Sound Radiation Characteristics of Lightweight Roof Constructions Excited by Rain," Building Acoustics, 1(4), pp. 249-270.

[6] McLoughlin, J., Saunders, D. J., and Ford, R. D., 1994, "Noise generated by simulated rainfall on profiled steel roof structures," Applied Acoustics, 42(3), pp. 239-255.

[7] Hopkins, C., 2007, Sound Insulation, Elsevier / Butterworth-Heinemann.

[8] Romain, G., Jean-Jacques, C., Thomas, J., and Ghislain, D., 2008, "Harvesting raindrop energy: theory," Smart Materials and Structures, 17(1), p. 015038.

[9] Romain, G., Jean-Jacques, C., Thomas, J., and Ghislain, D., 2008, "Harvesting raindrop energy: experimental study," Smart Materials and Structures, 17(1), p. 015039.

[10] Guigou-Carter, C., Villot, M., and Horlaville, C., 2002 "Study of simulated rainfall noise of roofs and glazings," Proc. Forum Acusticum.

[11] https://www.homebuilding.co.uk/getting-the-right-pitch/.

[12] ISO 10140-5:2010+A1:2014 Acoustics - Laboratory measurement of sound insulation of building elements.

[13] Marshall, J. S., and Palmer, W. M. K., 1948, "The distribution of raindrops with size," Journal of meteorology, 5(4), pp. 165-166.

[14] IEC 60721-2-2:2013 Classification of environmental conditions – Part 2-2: Environmental conditions appearing in nature – Precipitation and wind. International Electrotechnical Commission.

[15] Clift, R., Grace, J. R., Weber, M. E., 1978, Bubbles, drops, and particles, Academic press.

[16] Beard, K. V., Bringi, V. N., and Thurai, M., 2010, "A new understanding of raindrop shape," Atmospheric Research, 97(4), pp. 396-415.

[17] IEC 721-2-2:1988 Classification of environmental conditions – Part 2-2: Environmental conditions appearing in nature – Precipitation and wind. International Electrotechnical Commission.

[18] Ballagh, K. O., 1990, "Noise of simulated rainfall on roofs," Applied Acoustics, 31(4), pp. 245-264.

[19] Levy, S., 1999, Two-phase flow in complex systems, John Wiley & Sons.

[20] Mitchell, B. R., Nassiri, A., Locke, M. R., Klewicki, J. C., Korkolis, Y. P., and Kinsey, B. L., 2016, "Experimental and numerical framework for study of low velocity water droplet impact dynamics," In: ASME 2016 11th international manufacturing science and engineering conference. ASME(49897), p. V001T002A047.

[21] Rioboo, R., Marengo, M., and Tropea, C., 2002, "Time evolution of liquid drop impact onto solid, dry surfaces," Experiments in Fluids, 33(1), pp. 112-124.

[22] Roisman, I. V., Rioboo, R., and Tropea, C., 2002, "Normal impact of a liquid drop on a dry surface: model for spreading and receding," Proceedings of the Royal Society of London. Series A: Mathematical, Physical and Engineering Sciences, 458(2022), pp. 1411-1430.

[23] Anantharamaiah N, Vahedi Tafreshi HV, Pourdeyhimi B (2006) A study on hydroentangling waterjets and their impact forces. Experiments in Fluids 41(1):103.

[24] Marco, M., Carlo, A., V, R. I., and Cameron, T., 2011, "Drop collisions with simple and complex surfaces," Current Opinion in Colloid & Interface Science, 16(4), pp. 292-302.

[25] Roisman, I. V., Berberović, E., and Tropea, C., 2009, "Inertia dominated drop collisions. I. On the universal flow in the lamella," Physics of Fluids, 21(5), p. 052103.

[26] Philippi, J., Lagrée, P.-Y., and Antkowiak, A., 2016, "Drop impact on a solid surface: short-time self-similarity," Journal of Fluid Mechanics, 795, pp. 96-135.

[27] Gordillo, L., Sun, T.-P., and Cheng, X., 2018, "Dynamics of drop impact on solid surfaces: evolution of impact force and self-similar spreading," Journal of Fluid Mechanics, 840, pp. 190-214.

[28] Mitchell, B. R., Klewicki, J. C., Korkolis, Y. P., and Kinsey, B. L., 2019, "The transient force profile of low-speed droplet impact: measurements and model," Journal of Fluid Mechanics, 867, pp. 300-322.

[29] Grinspan, A. S., and Gnanamoorthy, R., 2010 "Impact force of low velocity liquid droplets measured using piezoelectric PVDF film," Colloids and Surfaces A, pp. 162-168.

[30] Soto D., De Lariviere A. B., Boutillon X., Clanet C., Quéré D., 2014, "The force of impacting rain", Soft Matter 10(27):4929-4934.

[31] Li, J., Zhang, B., Guo, P., and Lv, Q., 2014, "Impact force of a low speed water droplet colliding on a solid surface," Journal of Applied Physics, 116(21), p. 214903.

[32] Inoue, H., Harrigan, J. J., and Reid, S. R., 2001, "Review of inverse analysis for indirect measurement of impact force," Applied Mechanics Reviews, 54(6), pp. 503-524.

[33] Doyle, J. F., 1997, "A wavelet deconvolution method for impact force identification.," Experimental Mechanics, 37(4), pp. 403-408.

[34] Martin, M. T., and Doyle, J. F., 1996, "Impact force identification from wave propagation responses," International Journal of Impact Engineering, 18(1), pp. 65-77.

[35] Wu, E., Yeh, J.-C., and Yen, C.-S., 1994, "Impact on composite laminated plates: an inverse method," International Journal of Impact Engineering, 15(4), pp. 417-433.

[36] Wu, E., Tsai, T.-D., and Yen, C.-S., 1995, "Two methods for determining impact-force history on elastic plates," Experimental Mechanics, 35(1), pp. 11-18.

[37] Khoo, S. Y., Ismail, Z., Kong, K. K., Ong, Z. C., Noroozi, S., Chong, W. T., and Rahman, A. G. A., 2014, "Impact force identification with pseudo-inverse method on a lightweight structure for under-determined, even-determined and over-determined cases," International Journal of Impact Engineering, 63, pp. 52-62.

[38] Groetsch, C. W., and Groetsch, C., 1993, Inverse problems in the mathematical sciences, Springer.

[39] Inoue, H., Kishimoto, K., Shibuya, T., and Koizumi, T., 1992, "Estimation of impact load by inverse analysis: Optimal transfer function for inverse analysis," JSME International Journal. Ser. 1, Solid Mechanics, Strength of Materials, 35(4), pp. 420-427.

[40] Ma, C. K., Chang, J. M., and Lin, D. C., 2003, "Input forces estimation of beam structures by an inverse method," Journal of Sound and Vibration, 259(2), pp. 387-407.

[41] Lourens, E., Reynders, E., De Roeck, G., Degrande, G., and Lombaert, G., 2012, "An augmented Kalman filter for force identification in structural dynamics," Mechanical Systems and Signal Processing, 27, pp. 446-460.

[42] Bateman, V. I., Carne, T. G., Gregory, D. L., Attaway, S. W., and Yoshimura, H. R., 1991, "Force Reconstruction for Impact Tests," Journal of Vibration and Acoustics, 113(2), pp. 192-200.

[43] Williams, M. E., and Hoit, M. I., 2004, "Bridge pier live load analysis using neural networks," Advances in Engineering Software, 35(10), pp. 645-652.

[44] Yan, G., and Zhou, L., 2009, "Impact load identification of composite structure using genetic algorithms," Journal of Sound and Vibration, 319(3), pp. 869-884.

[45] Ghajari, M., Sharif-Khodaei, Z., Aliabadi, M., and Apicella, A., 2013, "Identification of impact force for smart composite stiffened panels," Smart Materials and Structures, 22(8), p. 085014.

[46] Mao, B. Y., Xie, S. L., Xu, M. L., Zhang, X. N., and Zhang, G. H., 2014, "Simulated and experimental studies on identification of impact load with the transient statistical energy analysis method," Mechanical Systems and Signal Processing, 46(2), pp. 307-324.

[47] Vermeir, G., Mees, P., and Bosmans, I., 1996, "Prediction of rainfall noise on single and double glazing," Proc. INTER. NOISE 96, pp. 523-528.

[48] Cremer, L., Heckl, M., and Pertersson, B. A. T., 2013, Structure-borne sound: structural vibrations and sound radiation at audio frequencies, Springer Science & Business Media.

[49] Lyon, R. H., and DeJong, R. G., 1995, "Theory and application of statistical energy analysis," Butterworth-Heinemann.

[50] Jean, A., and Atalla, N., 2009, Propagation of sound in porous media: modelling sound absorbing materials, John Wiley & Sons.

[51] Rhazi, D., and Atalla, N., 2010, "Transfer matrix modeling of the vibroacoustic response of multi-materials structures under mechanical excitation," Journal of Sound and Vibration, 329(13), pp. 2532-2546.

[52] Villot, M., Guigou, C., and Gagliardini, L., 2001, "Predicting the acoustical radiation of finite size multi-layered structures by applying spatial windowing on infinite structures," Journal of Sound and Vibration, 245(3), pp. 433-455.

[53] Worthington, A. M., 1895, The splash of a drop, Society for Promoting Christian Knowledge.

[54] Worthington, A. M., 1908, A study of splashes. , Longmans, Green, and Company.

[55] Rein, M., 1993, "Phenomena of liquid drop impact on solid and liquid surfaces," Fluid Dynamics Research, 12(2), p. 61.

[56] Yarin, A. L., 2006, "Drop impact dynamics: Splashing, Spreading, Receding, Bouncing…," Annual Review of Fluid Mechanics, 38(1), pp. 159-192.

[57] Rioboo, R., Cameron T., Marco M., 2001, "Outcomes from a drop impact on solid surfaces. ," Atomization and Sprays 11.2

[58] Pumphrey, H. C., and Elmore, P. A., 2006, "The entrainment of bubbles by drop impacts," Journal of Fluid Mechanics, 220, pp. 539-567.

[59] Antonini, C., Amirfazli, A., and Marengo, M., 2012, "Drop impact and wettability: From hydrophilic to superhydrophobic surfaces," Physics of Fluids, 24(10), p. 102104.

[60] Rioboo, R., Voué, M., Vaillant, A., and De Coninck, J., 2008, "Drop Impact on Porous Superhydrophobic Polymer Surfaces," Langmuir, 24(24), pp. 14074-14077.

[61] Range, K., and Feuillebois, F., 1998, "Influence of Surface Roughness on Liquid Drop Impact," Journal of Colloid and Interface Science, 203(1), pp. 16-30.

[62] Reynolds, O., 1881, "On the floating of drops on the surface of water depending only on the purity of the surface," Proc. Lit. Phil. Soc. Manchester, 21(1).

[63] Rodriguez, F., and Mesler, R., 1985, "Some drops don't splash," Journal of Colloid and Interface Science, 106(2), pp. 347-352.

[64] Leighton, T., 2012, The acoustic bubble, Academic press.

[65] Hobbs, P., and Osheroff, T., 1967, "Splashing of drops on shallow liquids," Science, 158(3805), pp. 1184-1186.

[66] Macklin, W., and Hobbs, P., 1969, "Subsurface phenomena and the splashing of drops on shallow liquids," Science, 166(3901), pp. 107-108.

[67] Wang, A.-B., and Chen, C.-C., 2000, "Splashing impact of a single drop onto very thin liquid films," Physics of Fluids, 12(9), pp. 2155-2158.

[68] Beard, K. V., and Chuang, C., 1987, "A new model for the equilibrium shape of raindrops," Journal of the Atmospheric sciences, 44(11), pp. 1509-1524.

[69] Gunjal, P. R., Ranade, V. V., and Chaudhari, R. V., 2005, "Dynamics of drop impact on solid surface: Experiments and VOF simulations," AIChE Journal, 51(1), pp. 59-78.

[70] Roux, D. C. D., and Cooper-White, J. J., 2004, "Dynamics of water spreading on a glass surface," Journal of Colloid and Interface Science, 277(2), pp. 424-436.

[71] Josserand, C., and Zaleski, S., 2003, "Droplet splashing on a thin liquid film," Physics of fluids, 15(6), pp. 1650-1657.

[72] Eggers, J., Fontelos, M. A., Josserand, C., and Zaleski, S., 2010, "Drop dynamics after impact on a solid wall: Theory and simulations," Physics of Fluids, 22(6), p. 062101.

[73] Hattori, S., and Kakuichi, M., 2013, "Effect of impact angle on liquid droplet impingement erosion," Wear, 298-299, pp. 1-7.

[74] Ahmad, M., Casey, M., and Sürken, N., 2009, "Experimental assessment of droplet impact erosion resistance of steam turbine blade materials," Wear, 267(9), pp. 1605-1618.

[75] Zhang, B., Lv, Q., Guo, P., and Li, J., "Experimental Study of Impact Force of a Low-Speed Droplet Colliding on the Solid Surface at Different Impact Angles," Proc. ASME 2017 International Mechanical Engineering Congress and Exposition, American Society of Mechanical Engineers, pp. V007T009A022-V007T009A022.

[76] Zhang, R., Zhang, B., Lv, Q., Li, J., and Guo, P., 2019, "Effects of droplet shape on impact force of low-speed droplets colliding with solid surface," Experiments in Fluids, 60(4), p. 64.

[77] Chang, C., and Sun, C. T., 1989, "Determining transverse impact force on a composite laminate by signal deconvolution," Experimental Mechanics, 29(4), pp. 414-419.

[78] Hansen, P. C., 1998, "Rank-deficient and discrete ill-posed problems: SIAM," Philadelphia, PA, pp. 175-206.

[79] Uhl, T., 2007, "The inverse identification problem and its technical application," Archive of Applied Mechanics, 77(5), pp. 325-337.

[80] Holzer, A. J., 1978, "A technique for obtaining compressive strength at high strain rates using short load cells," International Journal of Mechanical Sciences, 20(9), pp. 553-560.

[81] Inoue, H., Kamibayashi, M., Kishimoto, K., Shibuya, T., and Koizumi, T., 1992, "Numerical Laplace Transformation and Inversion using Fast Fourier Transform," JSME International Journal. Ser. 1, Solid Mechanics, Strength of Materials, 35(3), pp. 319-324.

[82] Inoue, H., Kishimoto, K., Shibuya, T., and Harada, K., 1998, "Regularization of Numerical Inversion of the Laplace Transform for the Inverse Analysis of Impact Force," JSME International Journal Series A, 41(4), pp. 473-480.

[83] Liu, Y., and Shepard Jr, W. S., 2005, "Dynamic force identification based on enhanced least squares and total least-squares schemes in the frequency domain," Journal of Sound and Vibration, 282(1-2), pp. 37-60.

[84] Thite, A. N., and Thompson, D. J., 2003, "The quantification of structure-borne transmission paths by inverse methods. Part 1: Improved singular value rejection methods," Journal of Sound and Vibration, 264(2), pp. 411-431.

[85] Mallat, S., 1999, A wavelet tour of signal processing, Elsevier.

[86] Li, Z., Feng, Z., and Chu, F., 2014, "A load identification method based on wavelet multi-resolution analysis," Journal of Sound and Vibration, 333(2), pp. 381-391.

[87] Qiao, B., Chen, X., Xue, X., Luo, X., and Liu, R., 2015, "The application of cubic B-spline collocation method in impact force identification," Mechanical Systems and Signal Processing, 64-65, pp. 413-427.

[88] Qiao, B., Zhang, X., Luo, X., and Chen, X., 2015, "A force identification method using cubic B-spline scaling functions," Journal of Sound and Vibration, 337, pp. 28-44.

[89] Paige, C. C., and Saunders, M. A., 1982, "LSQR: An Algorithm for Sparse Linear Equations and Sparse Least Squares," ACM Transactions on Mathematical Software, 8(1), pp. 43-71.

[90] Vaseghi, S. V., 2008, Advanced digital signal processing and noise reduction, John Wiley & Sons.

[91] Vaseghi S.V. (2013) Chapter 4 Bayesian estimation. In: Vaseghi SV Advanced signal processing and digital noise reduction, 2nd edn. Springer-Verlag. ISBN: 0-471-62692-9.

[92] Qiao, B., Zhang, X., Wang, C., Zhang, H., and Chen, X., 2016, "Sparse regularization for force identification using dictionaries," Journal of Sound and Vibration, 368, pp. 71-86.

[93] Tran, H., and Inoue, H., 2018, "Development of wavelet deconvolution technique for impact force reconstruction: Application to reconstruction of impact force acting on a load-cell," International Journal of Impact Engineering, 122, pp. 137-147.

[94] Qiao, B., Chen, X., Luo, X., and Xue, X., 2015, "A Novel Method for Force Identification Based on the Discrete Cosine Transform," Journal of Vibration and Acoustics, 137(5), pp. 051012-051012-051015.

[95] Gunawan, F. E., Homma, H., and Kanto, Y., 2006, "Two-step B-splines regularization method for solving an ill-posed problem of impact-force reconstruction," Journal of Sound and Vibration, 297(1), pp. 200-214.

[96] Gunawan, F. E., Homma, H., and Morisawa, Y., 2008, "Impact-Force Estimation by Quadratic Spline Approximation," Journal of Solid Mechanics and Materials Engineering, 2(8), pp. 1092-1103.

[97] Qiao, B., Zhang, X., Gao, J., Liu, R., and Chen, X., 2017, "Sparse deconvolution for the large-scale ill-posed inverse problem of impact force reconstruction," Mechanical Systems and Signal Processing, 83, pp. 93-115.

[98] Rezayat, A., Nassiri, V., De Pauw, B., Ertveldt, J., Vanlanduit, S., and Guillaume, P., 2016, "Identification of dynamic forces using group-sparsity in frequency domain," Mechanical Systems and Signal Processing, 70-71, pp. 756-768.

[99] Aucejo, M., and De Smet, O., 2016, "Bayesian source identification using local priors," Mechanical Systems and Signal Processing, 66-67, pp. 120-136.

[100] Li, Q., and Lu, Q., 2018, "Time domain force identification based on adaptive ℓq regularization," Journal of Vibration and Control, 24(23), pp. 5610-5626.

[101] Li, Q., and Lu, Q., 2018, "A hierarchical Bayesian method for vibration-based time domain force reconstruction problems," Journal of Sound and Vibration, 421, pp. 190-204.

[102] Zhang, Z., Xu, Y., Yang, J., Li, X., and Zhang, D., 2015, "A survey of sparse representation: algorithms and applications," IEEE access, 3, pp. 490-530.

[103] Foucart, S., and Rauhut, H., 2013, A mathematical introduction to compressive sensing, Birkhäuser Basel.

[104] Bruckstein, A. M., Donoho, D. L., and Elad, M., 2009, "From sparse solutions of systems of equations to sparse modeling of signals and images," SIAM review, 51(1), pp. 34-81.

[105] Tropp, J. A., and Gilbert, A. C., 2007, "Signal recovery from random measurements via orthogonal matching pursuit," IEEE Transactions on Information Theory, 53(12), pp. 4655-4666.

[106] Needell, D., and Tropp, J. A., 2009, "CoSaMP: Iterative signal recovery from incomplete and inaccurate samples," Applied and Computational Harmonic Analysis, 26(3), pp. 301-321.

[107] Aucejo, M., and De Smet, O., 2017, "A multiplicative regularization for force reconstruction," Mechanical Systems and Signal Processing, 85, pp. 730-745.

[108] Wright, S. J., Nowak, R. D., and Figueiredo, M. A., 2009, "Sparse reconstruction by separable approximation," IEEE Transactions on Signal Processing, 57(7), pp. 2479-2493.

[109] Hansen, P. C., and O'Leary, D. P., 1993, "The use of the L-curve in the regularization of discrete ill-posed problems," SIAM Journal on Scientific Computing, 14(6), pp. 1487-1503.

[110] Mehrotra, S., 1992, "On the implementation of a primal-dual interior point method," SIAM Journal on Optimization, 2(4), pp. 575-601.

[111] Pan, C.-D., Yu, L., Liu, H.-L., Chen, Z.-P., and Luo, W.-F., 2018, "Moving force identification based on redundant concatenated dictionary and weighted l1-norm regularization," Mechanical Systems and Signal Processing, 98, pp. 32-49.

[112] Qiao, B., Liu, J., Liu, J., Yang, Z., and Chen, X., 2019, "An enhanced sparse regularization method for impact force identification," Mechanical Systems and Signal Processing, 126, pp. 341-367.

[113] Pasti, L., Walczak, B., Massart, D. L., and Reschiglian, P., 1999, "Optimization of signal denoising in discrete wavelet transform," Chemometrics and Intelligent Laboratory Systems, 48(1), pp. 21-34.

[114] Belge, M., Kilmer, M. E., and Miller, E. L., 2000, "Wavelet domain image restoration with adaptive edge-preserving regularization," IEEE Transactions on Image Processing, 9(4), pp. 597-608.

[115] Beck, A., and Teboulle, M., 2009, "A fast iterative shrinkage-thresholding algorithm for linear inverse problems," SIAM Journal on Imaging Sciences, 2(1), pp. 183-202.

[116] Xu, Z., Chang, X., Xu, F., and Zhang, H., 2012, "$l_{1/2}$ regularization: A thresholding representation theory and a fast solver," IEEE Transactions on Neural Networks and Learning Systems, 23(7), pp. 1013-1027.

[117] Zeng, J., Lin, S., Wang, Y., and Xu, Z., 2014, "$l_{1/2}$ regularization: Convergence of iterative half thresholding algorithm," IEEE Transactions on Signal Processing, 62(9), pp. 2317-2329.

[118] Blumensath, T., and Davies, M. E., 2009, "Iterative hard thresholding for compressed sensing," Applied and Computational Harmonic Analysis, 27(3), pp. 265-274.

[119] Lee, J. K., and Park, Y.-S., 1994, "Response selection and dynamic damper application to improve the identification of multiple input forces of narrow frequency band," Mechanical Systems and Signal Processing, 8(6), pp. 649-664.

[120] Inoue, H., Kishimoto, K., Shibuya, T., and Koizumi, T., 1992, "Estimation of Impact Load by Inverse Analysis : Optimal Transfer Function for Inverse Analysis," JSME international journal. Ser. 1, Solid mechanics, strength of materials, 35(4), pp. 420-427.

[121] Vetterli, M., 2001, "Wavelets, approximation, and compression," IEEE Signal Processing Magazine, 18(5), pp. 59-73.

[122] Coifman, R. R., and Wickerhauser, M. V., 1992, "Entropy-based algorithms for best basis selection," IEEE Transactions on Information Theory, 38(2), pp. 713-718.

[123] Chen, S. S., Donoho, D. L., and Saunders, M. A., 2001, "Atomic decomposition by basis pursuit," SIAM review, 43(1), pp. 129-159.

[124] Singh, B. N., and Tiwari, A. K., 2006, "Optimal selection of wavelet basis function applied to ECG signal denoising," Digital Signal Processing, 16(3), pp. 275-287.

[125] Maidanik, G., 1962, "Response of Ribbed Panels to Reverberant Acoustic Fields," The Journal of the Acoustical Society of America, 34(6), pp. 809-826.

[126] Wallace, C., 1972, "Radiation resistance of a rectangular panel," The Journal of the Acoustical Society of America, 51(3B), pp. 946-952.

[127] Gomperts, M., 1974, "Radiation from rigid baffled, rectangular plates with general boundary conditions," Acta Acustica united with Acustica, 30(6), pp. 320-327.

[128] Gomperts, M., 1977, "Sound radiation from baffled, thin, rectangular plates," Acta Acustica united with Acustica, 37(2), pp. 93-102.

[129] Leppington, F. G., Broadbent, E. G., and Heron, K., 1982, "The acoustic radiation efficiency of rectangular panels," Proceedings of the Royal Society A, 382(1783), pp. 245-271.

[130] Leppington, F., Broadbent, E. G., and Heron, K., 1984, "Acoustic radiation from rectangular panels with constrained edges," Proceedings of the Royal Society A, 393(1804), pp. 67-84.

[131] Li, W., and Gibeling, H., 2000, "Determination of the mutual radiation resistances of a rectangular plate and their impact on the radiated sound power," Journal of Sound and Vibration, 229(5), pp. 1213-1233.

[132] Xie, G., Thompson, D., and Jones, C., 2005, "The radiation efficiency of baffled plates and strips," Journal of Sound and Vibration, 280(1-2), pp. 181-209.

[133] Decraene, C., Dijckmans, A., and Reynders, E. B., 2018, "Fast mean and variance computation of the diffuse sound transmission through finite-sized thick and layered wall and floor systems," Journal of Sound and Vibration, 422, pp. 131-145.

[134] Cherif, R., Wareing, A., and Atalla, N., 2017, "Evaluation of a hybrid TMM-SEA method for prediction of sound transmission loss through mechanically coupled aircraft double-walls," Applied Acoustics, 117, pp. 132-140.

[135] Folds, D., and Loggins, C., 1977, "Transmission and reflection of ultrasonic waves in layered media," The Journal of the Acoustical Society of America, 62(5), pp. 1102-1109.

[136] Brouard, B., Lafarge, D., and Allard, J. F., 1995, "A general method of modelling sound propagation in layered media," Journal of Sound and Vibration, 183(1), pp. 129-142.

[137] Panneton, R., 2007, "Comments on the limp frame equivalent fluid model for porous media," The Journal of the Acoustical Society of America, 122(6), pp. EL217-EL222.

[138] Doutres, O., Dauchez, N., Génevaux, J.-M., and Dazel, O., 2007, "Validity of the limp model for porous materials: A criterion based on the Biot theory," The Journal of the Acoustical Society of America, 122(4), pp. 2038-2048.

[139] Guyader, J. L., Boisson, C., and Lesueur, C., 1982, "Energy transmission in finite coupled plates, part I: Theory," Journal of Sound and Vibration, 81(1), pp. 81-92.

[140] Ghinet, S., and Atalla, N., 2001, "Sound transmission loss of insulating complex structures," Canadian Acoustics, 29(3), pp. 26-27.

[141] Rhazi, D., and Atalla, N., 2010, "A simple method to account for size effects in the transfer matrix method," The Journal of the Acoustical Society of America, 127(2), pp. EL30-EL36.

[142] Bonfiglio, P., Pompoli, F., and Lionti, R., 2016, "A reduced-order integral formulation to account for the finite size effect of isotropic square panels using the transfer matrix method," The Journal of the Acoustical Society of America, 139(4), pp. 1773-1783.

[143] Davy, J. L., Larner, D. J., Wareing, R. R., and Pearse, J. R., 2015, "The acoustic radiation impedance of a rectangular panel," Building and Environment, 92, pp. 743-755.

[144] Vigran, T., 2009, "Predicting the sound reduction index of finite size specimen by a simplified spatial windowing technique," Journal of Sound and Vibration, 325(3), pp. 507-512.

[145] ESDU Data Item 00002, Radiation efficiencies of isotropic plates, ESDU International plc, London, UK, 2000.

[146] Leppington, F. G., 1996, "Acoustic radiation from plates into a wedge-shaped fluid region: application to the free plate problem," Proceedings of the Royal Society of London. Series A: Mathematical, Physical and Engineering Sciences, 452(1951), pp. 1745-1764.

[147] Squicciarini, G., Thompson, D. J., and Corradi, R., 2014, "The effect of different combinations of boundary conditions on the average radiation efficiency of rectangular plates," Journal of Sound and Vibration, 333(17), pp. 3931-3948.

[148] Liu, B., "Influence of baffle size and curvature on sound radiated by vibrating panels," Proc. Proceedings of the 11th International Congress on Sound and Vibration, pp. 1871-1878.

[149] Williams, E. G., and Maynard, J. D., 1982, "Numerical evaluation of the Rayleigh integral for planar radiators using the FFT," The Journal of the Acoustical Society of America, 72(6), pp. 2020-2030.

[150] Rhazi, D., and Atalla, N., 2014, "Acoustic and vibration response of a structure with added noise control treatment under various excitations," The Journal of the Acoustical Society of America, 135(2), pp. 693-704.

[151] Dijckmans, A., and Vermeir, G., 2013, "Development of a hybrid wave based–transfer matrix model for sound transmission analysis," The Journal of the Acoustical Society of America, 133(4), pp. 2157-2168.

[152] Kou, Y., Liu, B., and Tian, J., 2015, "Radiation efficiency of damped plates," The Journal of the Acoustical Society of America, 137(2), pp. 1032-1035.

[153] Scheller, B. L., and Bousfield, D. W., 1995, "Newtonian drop impact with a solid surface," AIChE Journal, 41(6), pp. 1357-1367.

[154] Li J, Z. B., Guo P, Lv Q 2014, " Impact force of a low speed water droplet colliding on a solid surface.," Journal of Applied Physics, 116(214903), pp. 1-11.

[155] Widrow, B., Glover, J. R., McCool, J. M., Kaunitz, J., Williams, C. S., Hearn, R. H., Zeidler, J. R., Dong, J. E., and Goodlin, R. C., 1975, "Adaptive noise cancelling: Principles and applications," Proceedings of the IEEE, 63(12), pp. 1692-1716.

[156] Fuks, N. A., 1989, The mechanics of aerosols, Dover Publications.

[157] ISO 9614-1:2009 Acoustics - Determination of sound power levels of noise sources using sound intensity.

[158] www.acefoam.co.uk/store/products/1559-2/.

[159] Robinson, M., 2012, "Prediction of sound and vibration response using Transient Statistical Energy Analysis," PhD, University of Liverpool.

[160] ISO/PAS 16940:2004 Glass in building-Glazing and airborne sound insulation-Measurement of the mechanical impedence of laminated glass. International Organization for Standardization. .

[161] ISO 3382: 1997 Acoustics--Measurement of the reverberation time of rooms with reference to other acoustical parameters. International Organization for Standardization.

[162] Schroeder, M. R., 1965, "New Method of Measuring Reverberation Time," The Journal of the Acoustical Society of America, 37(3), pp. 409-412.

[163] Jacobsen, F., 1987, "A note on acoustic decay measurements," Journal of Sound and Vibration, 115(1), pp. 163-170.

[164] Lee, S.-K., 2002, "An acoustic decay measurement based on time-frequency analysis using wavelet transform," Journal of Sound and Vibration, 252(1), pp. 141-153.

[165] Zhang, B., Li, J., Guo, P., and Lv, Q., 2017, "Experimental studies on the effect of Reynolds and Weber numbers on the impact forces of low-speed droplets colliding with a solid surface," Experiments in Fluids, 58(9), p. 125.

[166] Fahy, F. J., and Gardonio, P., 2007, Sound and structural vibration: radiation, transmission and response, Elsevier.

[167] Best, A. C., 1950, "Empirical formulae for the terminal velocity of water drops falling through the atmosphere," Quarterly Journal of the Royal Meteorological Society, 76(329), pp. 302-311.

[168] Gordillo, L., and Cheng, X., 2017, "Self-similar dynamics of inertia-driven drop impacts: impact force and drop shape," arXiv preprint arXiv:1706.07541.